Universidad de Granada

Facultad de Ciencias

Departamento de Electrónica y Tecnología de Computadores

Tesis doctoral

CHARACTERIZATION AND MODELING OF RESISTIVE MEMORIES BASED ON MIS AND MIM STRUCTURES

Programa de Doctorado en Tecnologías de la Información y la Comunicación

Doctorando:
David Maldonado Correa

Directores:
Juan Bautista Roldán Aranda
Andrés Roldán Aranda

Granada 2022

Editor: Universidad de Granada. Tesis Doctorales
Autor: David Maldonado Correa
ISBN: 978-84-1117-432-9
URI: http://hdl.handle.net/10481/75969

A mi familia, por la confianza depositada en mí y ayudar a superarme cada día.

A mis abuelos, por su sacrificio y continuo apoyo durante toda una vida.

A mis padres, por inculcarme los valores de esfuerzo y trabajo que poseen y hoy estoy orgulloso de tener. Sin ellos nada de esto hubiera sido posible.

A mi hermano, por su ayuda incondicional e infinita paciencia para aguantarme.

A Alejandra, por acompañarme, escucharme y entenderme en todo momento.

A mis amigos, por estar siempre cuando los necesito.

Todos son igualmente partícipes de este trabajo.

Agradecimientos

En primer lugar, me gustaría agradecer la labor y dedicación de Dr. Juan Bautista Roldán Aranda y Dr. Andrés María Roldán Aranda como directores y tutores; por la continua ayuda, paciencia, dedicación y sobre todo trabajo, tareas indispensables para el correcto desarrollo y término de esta tesis doctoral.

Quiero agradecer la colaboración de los miembros del grupo de investigación "Nanoestructuras, propiedades cuánticas y aplicaciones tecnológicas" del Departamento de Electrónica y Tecnología de Computadores de la Universidad de Granada, especialmente al Dr. Francisco Jiménez Molinos por la participación en los artículos [Maldonado2019, Maldonado2019b, Maldonado2020, Maldonado2021, Maldonado2022, Rodríguez2019, Roldán2021b] y al Dr. Francisco Manuel Gómez Campos, por la contribución en el artículo [Maldonado2022], por el desarrollo de un vídeo para la divulgación de resultados.

Quiero agradecer además la colaboración de los miembros del grupo de investigación "Pervasive Electronics Advanced Research Laboratory" del Departamento de Electrónica y Tecnología de Computadores de la Universidad de Granada, en especial al Dr. Noel Rodríguez Santiago por la realización y revisión del artículo [Rodríguez2019].

Agradecer también la colaboración de otros departamentos de la Universidad de Granada, al Dr. Manuel Calixto Molina del Departamento de Matemática Aplicada por la realización y revisión del artículo [Calixto2020], a la Dra. Ana María Aguilera del Pino, al Dr. Francisco Javier Alonso Morales, al Dr. Christian Acal y al Dr. Juan Eloy Ruiz Castro del Departamento de Estadística e Investigación Operativa por su participación en los artículos [Rodríguez2019, Roldán2019, Roldán2021b].

Deseo agradecer también la participación y ayuda de distintos grupos de investigación pertenecientes a otras universidades y entidades:

- Dra. Francesca Campabadal Segura y Dra. Mireia Bargalló González, del Institut de Microelectrònica de Barcelona IMB-CNM (CSIC) Bellaterra en España, por las muestras y medidas de los dispositivos TiN/Ti/HfO_2/W y Ni/HfO_2/Si-n^{++} así como la colaboración en la redacción y revisión de los artículos [Maldonado2019, Maldonado2019b, Maldonado2020, Maldonado2021, Maldonado2022].
- Dr. Mario Lanza, del King Abdullah University of Science and Technology de Arabia Saudi, por las muestras de los dispositivos basados en h-BN y la colaboración y revisión de los artículos [Roldán2019, Roldán2021b].
- Dr. Enrique Miranda Castellano del Departament d'Enginyeria Electrònica de la Universitat Autònoma de Barcelona, por la colaboración y revisión de los artículos [Maldonado2021] y [Calixto2020] respectivamente.

- Dr. Rodrigo Picos Gayá del Departament de Física de la Universitat de les Illes Balears, por la colaboración y revisión del artículo [Maldonado2020].

Agradezco también la financiación ofrecida por el Ministerio de Economía y Competitividad de España, con fondos de la Unión Europea del programa FEDER, a través de los proyectos TEC2014-52152-C3-2-R y TEC2017-84321-C4-3-R, a la Junta de Andalucía que junto al programa FEDER han financiado los proyectos A-TIC-117-UGR18 y B-TIC-624-UGR20.

D. Maldonado Correa

Granada, a 10 de mayo de 2022

Index

Agradecimientos v
Index vii
List of Figures ix
List of Tables xiii
List of Videos xv
List of abbreviations xvii
Contributions included in this work xix
Journal papers xix
Proceedings of IEEE Xplore Digital Library xx
International conferences xx
Other contributions related to the subject of this thesis xx
Book chapters xxi
Videos
Abstract xxiii
Introduction xxvii
Objectives xxix
Methodology xxxi
1. Introduction to RRAM technology. Overview and state of the art 1
1.1. Memristors. Applications 5
1.2. Actual technology and limitations 7
1.3. New devices in the framework of non-volatile memories 8
1.4. RRAM Technology 11
1.4.1. RRAM Structure 11
1.4.2. Device fabrication 12
1.4.3. Operation 14

1.4.4. State of the art and challenges 16
1.5. RRAM Simulation and Modeling 18
1.5.1. Atomistic simulators 19
1.5.2. Microscopic simulators (kinetic Monte Carlo simulators) 20
1.5.3. Macroscopic simulators (finite element method) 21
1.5.4. Compact modeling 22
2. Electrical characterization of resistive memories 25
2.1. Measurement of resistive memories under the effects of the magnetic field 25
2.2. Statistical procedures to analyze resistive switching 39
3. Time series analysis for the study of variability in resistive memories 47
3.1. Introduction and application of the technique 47
3.2. TSSA in h-BN memristors 77
3.3. TSSA in graphene oxide memristors 89
4. Enhanced compact modeling in resistive memories 103
4.1. Series resistance extraction and inclusion in the Stanford model 103
4.2. Inclusion of thermal effects on the quantum point contact model 121
5. Use of dynamic route maps to understand resistive memories operation
5.1. Introduction 141
6. A resistive memory simulator based on circuit breakers 161
6.1. Introduction 161
6.2. Description 162
6.3. Operation 164
6.4. Functionalities 165
7. Conclusions 187
References 191

List of Figures

Figure 1.1. a) Schematic of a metal-insulator-metal or metal-insulator-semiconductor RRAM device. Typical I-V curves showing b) unipolar mode, c) bipolar mode. A CC is stablished to prevent the device from reaching the electric breakdown [Pan2014]. 3
Figure 1.2. TEM examination of the evolution of a CF during a forming and a reset process on a unipolar CBRAM Pt/ZnO/Pt device. a-b) detail of the formation of the filament from the bottom to the top electrode, c) fully formed cylindrical shape filament after set, d) partially broken filament after reset [Pan2014]. 5
Figure 1.3. a) Diagram of the four basic passive elements (resistor, capacitor, inductor and memristor) and their association with the basic electrical magnitudes (voltage, intensity, charge and flux). b) Classical current versus voltage plot of a memristor element. Inset: charge versus flux function [Strukov2008]. 6
Figure 1.4. Graph of a FAMOS transistor (Floating Gate Avalanche-injection MOS) [Villena2015].7
Figure 1.5. *"More than Moore"* technology allows the communication between the digital processing & storage of an integrated system and the users in the outside world. 9
Figure 1.6. Diagram including all the different types of memories underway. In this work, all the efforts will be focused on emerging NVMs, precisely on RRAMs. 10
Figure 1.7. Crossbar Inc. RRAM technology highlights compared to traditional NAND Flash technology [Crossbar2021]. 11
Figure 1.8. Sketch of a RRAM memory crossbar array. (a) Structure of a single cell, b), crossbar architecture formed by multiple cells driven at the same polarity at the same time [Wei2020]. 12
Figure 1.9. Design of a 3D a) horizontal cross-point array (HRRAM) where the memory cell is positioned at the intersection between bit line and world line, b) vertical cross-point array (VRRAM) where the memory cell is located at the intersection between pillar electrode and word line [Yu2016]. 12
Figure 1.10. Typical RRAM structures to study the RS mechanism, SEM images are presented. a) Multiple top electrodes of different sizes with a common bottom electrode, b) device built on a horizontal cross-point structure, c) crossbar structure, d) section of a MIM structure showing its different layers, TEM image [Lanza2019]. 13
Figure 1.11. Sketch of resistive switching in ECM devices taking as example an Ag/ZnO:Mn/Pt structure. a) At the top electrode, Ag oxidize to ions (Ag → $Ag^+ + e^-$) when an electric field high enough is applied, b) Ag^+ is reduced after moving to the bottom electrode ($Ag^+ + e^-$ → Ag), c) a conductive filament is created as precipitations of Ag are deposited at the bottom electrode creating a percolation path to the top electrode and the cell reaches the LRS, d) when electric field is inverted the cell switches back to the HRS as a consequence of an electrochemical dissolution of the conductive filament which breaks the percolation path. Adapted from [Ye2016]. 14
Figure 1.12. Schematic of resistive switching in VCM devices [Wong2012a]. 15

Figure 1.13. Sketch of the most important RRAM features including endurance, retention, scalability, switching time and energy consumption; and hurdles to be addressed, such as variability and the lack of EDA tools. 16
Figure 1.14. Schematic of the different simulation models employed for the characterization of RRAM devices depending on the scale. As the physical detail level increases, the corresponding computational cost is increased in concordance. 19
Figure 1.15. Example of a microscopic simulation of a Cu/a-SiO_2 RRAM device accounting for a (a-d) forming, (e) reset and (f-h) set processes. Note that each capture is displayed as a function of the simulation elapsed time [Onofrio2015]. 20
Figure 1.16. Kinetic Monte Carlo simulation of a forming process presenting different stages depending on the external applied voltage. Red balls represent Ni atoms while blue balls mean Ni cations. In h) the conductive filament is fully formed and the process concluded [Aldana2017]. 21
Figure 1.17. Example of a Pt/Ta_2O_5/TaO_x/W RRAM simulated device making use of a properly configured FEM model, a) cross section, b) I-V measured and simulated curve comparison [Ielmini2017]. 22
Figure 1.18. 3D representation of the geometrical aspect of a RRAM conductive filament to be modeled, a) square shaped, b) cylindrical shape, c) conical shape. Obtained I-V simulated curves considering different d) oxide thickness, e) thermal resistances [González-Cordero2016c]. 23
Figure 2.1. a) Scheme of Lorentz force produced as a result of the combination of electric and magnetic force, b) 3D CF shunting both top and bottom electrodes when no MF is applied, c) 3D CF when the action of a MF is activated resulting in a clustering of the atoms on one side [Maldonado2020b]. 26
Figure 4.1. Example of a TiN/Ti/HfO_2/W experimental I-V curve (in blue) showing a rapid increase in the voltage compared to a typical one (in black). This is known as the snapback effect. 104
Figure 4.2. Diagram of a variable width CF including the energy band description. See that as the potential barrier height increases, the constriction width of the CF decreases and vice versa [Lian2012]. 121
Figure 6.1. Sketch of the network composed of circuit breakers. An external voltage is applied to the nodes in the top electrode while the nodes in the bottom electrode are grounded. 162
Figure 6.2. Graphical user interface of the simulator as it is initialized. 163
Figure 6.3. a) Voltage level in each node of the grid for an external applied voltage of 0.8 V. At this point, the total current flowing through the network is 0.3081 mA and the equivalent resistance 2.6 kΩ. b) Level of the resistances as a function of the voltage across the nodes, see the color code to describe the resistance state of each circuit breaker. 164
Figure 6.4. Graphical interface of the simulator when simulations are completed. 165
Figure 6.5. Loading cycles tab location. 166
Figure 6.6. Selection of experimental measurements folder window. 166
Figure 6.7. Experimental curves selection window 166
Figure 6.8. Graphical interface aspect when experimental cycles are loaded. 167
Figure 6.9. Graphical interface with a) one cycle loaded, b) two cycles loaded by means of hold button. 167

Figure 6.10. a) Plot step-by-step tab, b) manipulate tab location.....167
Figure 6.11. Manipulate menu with two different sets of parameters, a) alpha = 9.66, beta = 0.53, phi = 0.67, N = 1, b) alpha = 4.43, beta = 0.76, phi = 0.83, N = 1. In both cases, the experimental curve is fixed (dark blue), while the modified curve varies depending on the sliders position (light blue).....168

List of Tables

Table 1.1. Comparison among various RRAM devices. The most representative parameters such as the ON-OFF ratio, between the LRS and HRS operation, data retention and operation speed are displayed along with the type of device. 4
Table 1.2. Comparison of the typical main features in RRAM memories between ECM and VCM. The best parameters of each of the references are considered. Adapted from [Zahoor2020] 16

List of Videos

Video 1.1 Video detailing the principles of the presented simulator [videoSimulator]. 165

List of abbreviations

Abbreviation	Description
ACF	Autocorrelation function
ALD	Atomic Layer Deposition
BE	Bottom Electrode
BEOL	Back-End-Of-Line
CBRAM	Conductive Bridge Random Access Memory
CC	Compliance Current
CDF	Cumulative Distribution Function
CF	Conductive Filaments
CG	Control Gate
CMOS	Complementary Metal-Oxide-Semiconductor
CVS	Constant Voltage Stress
DFT	Density Functional Theory
DRAM	Dynamic Random-Access Memory
DRM	Dynamic Route Map
ECM	Electrochemical Metallization Memory
ED	Erlang distribution
EDA	Electronic Design Automation
EMC	Electrochemical Metallization Cells
FAMOS	Floating Gate Avalanche-injection MOS
FeFET	Ferroelectric Field-Effect Transistor
FEM	Finite Element Method
FeRAM	Ferroelectric RAM
FET	Field Effect Transistor
FG	Floating Gate
FTJ	Ferroelectric Tunnel Junction
HRS	High Resistance State
IMB-CNM (CSIC)	Institut de Microelectrònica de Barcelona - Centro Nacional de Microelectrónica (Consejo Superior de Investigaciones Científicas)
IoT	Internet of Things
KMC	Kinetic Monte Carlo
LRS	Low Resistance State
MF	Magnetic Field
MIM	Metal-Insulator-Metal
MIS	Metal-Insulator-Semiconductor
MOSFET	Metal – Oxide – Semiconductor – Field - Effect Transistor
MRAM	Magnetic RAM
MTJ	Magnetic Tunnel Junction
NAND	Not And

Abbreviation	Description
NOR	Not Or
NVM	Non-Volatile Memories
ODE	Ordinary Differential Equations
PACF	Partial Autocorrelation Function
PCM	Phase Change Memories
PDE	Partial Differential Equations
PHD	Phase type Distribution
PVD	Physical Vapor Deposition
PVS	Pulsed Voltage Stresses
QPC	Quantum Point Contact
RNG	Random number generator
RRAM	Resistive Random Access Memory
RS	Resistive Switching
RTN	Random Telegraph Noise
RVS	Ramped Voltage Stress
SEM	Scanning Electron Microscope
SILC	Stress Induced Leakage Current
SPICE	Simulation Program with Integrated Circuits Emphasis
SRAM	Static Random-Access Memory
SSD	Solid-State Drives
STT-RAM	Spin-Transfer Torque RAM
TDMAH	Tetrakis (Dimethylamido)-Hafnium
TE	Top electrode
TMO	Transition Metal Oxides
TSSA	Time series statistical analyses
VCM	Valence Change Memory
WD	Weibull distribution

Contributions included in this work

Journal papers

[1] **D. Maldonado**, F. Gómez-Campos, M.B. González, A. Roldán, F. Jiménez-Molinos, F. Campabadal, J. B. Roldán, “Comprehensive study on unipolar RRAM charge conduction and stochastic features, a simulation approach”, Journal of Physics D: Applied Physics, 55, 155104, 2022, doi: 10.1088/1361-6463/ac472c.

Web of Science: Impact factor: 3.2, Q2 Scimago: SJR: 0.86, Q1

[2] **D. Maldonado**, F. Aguirre, G. González-Cordero, A.M. Roldán, M.B. González, F. Jiménez-Molinos, F. Campabadal, E. Miranda, J.B. Roldán, "Experimental study of the series resistance effect and its impact on the compact modeling of the conduction characteristics of HfO2-based resistive switching memories", Journal of Applied Physics, 130(5), 054503, 2021, doi: 10.1063/5.0055982.

Web of Science: Impact factor: 2.55, Q2 Scimago: SJR: 0.7, Q2

[3] **D. Maldonado**, M.B. González, F. Campabadal, F. Jiménez-Molinos, M. Chawa, S.G. Stavrinides, JB. Roldán, R. Picos, R. Tetzlaff, L. O. Chua, "Experimental evaluation of the dynamic route map in the reset transition of memristive ReRAMs", Chaos, Solitons & Fractals, 139, 110288, 2020, doi: 10.1016/j.chaos.2020.110288

Web of Science: Impact factor: 5.94, Q1 Scimago: SJR: 1.04, Q1

[4] **D. Maldonado**, A. M. Roldán, M. B. González, F. Jiménez-Molinos, F. Campabadal, J. B. Roldán, "Influence of magnetic field on the operation of TiN/Ti/HfO2/W resistive memories", Microelectronics Engineering, 215, 110983, 2019, doi: 10.1016/j.mee.2019.110983.

Web of Science: Impact factor: 2.52, Q2 Scimago: SJR: 0.55, Q2

[5] M. Calixto, **D. Maldonado**, E. Miranda, J. B. Roldán, "Modeling of the temperature effects in filamentary-type resistive switching memories using quantum point-contact theory”, Journal of Physics D: Applied Physics, 53, 295106, 202, doi: 10.1088/1361-6463/ab85e5.

Web of Science: Impact factor: 3.2, Q2 Scimago: SJR: 0.86, Q1

[6] N. Rodriguez, **D. Maldonado**, F.J. Romero, F.J. Alonso, A.M. Aguilera, A. Godoy, F. Jimenez-Molinos, F.G. Ruiz, J.B. Roldan, "Resistive switching and charge transport in laser-fabricated graphene oxide memristors: a Time Series and Quantum Point Contact modelling approach”, Materials, 12, 3734, 2019, doi: 10.3390/ma12223734.

Web of Science: Impact factor: 3.62, Q2 Scimago: SJR: 0.68, Q2

[7] J.B. Roldán, F.J. Alonso, A.M. Aguilera, **D. Maldonado**, M. Lanza, "Time series statistical analysis: a powerful tool to evaluate the variability of resistive switching memories", Journal of Applied Physics, 125, 174504, 2019, doi: 10.1063/1.5079409.

Web of Science: Impact factor: 2.55, Q2 Scimago: SJR: 0.7, Q2

Proceedings of IEEE Xplore Digital Library

[1] J. B. Roldán, **D. Maldonado**, F. J. Alonso, A. M. Roldán, F. Hui, Y. Shi, F. Jiménez-Molinos, AM. Aguilera, M. Lanza, "Time series modeling of the cycle-to-cycle variability in h-BN based memristors", 2021 IEEE International Reliability Physics Symposium (IRPS), doi: 10.1109/irps46558.2021.9405100.

Scimago Journal & Country Rank h-index: 52

International conferences

[1] **D. Maldonado**, C. Acal, M.B. González, J.E. Ruiz-Castro, A.M. Aguilera, R. Picos, F. Jiménez-Molinos, F. Campabadal, J.B. Roldán. An in-depth statistical study of resistive switching energies in unipolar RRAMs. 21th Conference on "Insulating Films on Semiconductors", Cambridge (UK), 2019.

Other contributions related to the subject of this thesis

[1] **D. Maldonado**, S. Aldana, M.B. González, F. Jiménez-Molinos, M.J. Ibáñez, D. Barrera, F. Campabadal, J.B. Roldán, "Variability estimation in resistive switching devices, a numerical and kinetic Monte Carlo perspective ", Microelectronics Engineering, 257, 111736, 2022.

[2] **D. Maldonado**, JB. Roldán, AM. Roldán, F. Jiménez-Molinos, F. Hui, Y. Shi, Xu. Jing, C. Wen, M. Lanza, "Influence of the magnetic field on dielectric breakdown in memristors based on h-BN stacks", 2020 IEEE International Reliability Physics Symposium (IRPS), Dallas, TX, USA, 2020, pp. 1-5, doi: 10.1109/IRPS45951.2020.9128325.

[3] E. Pérez, **D. Maldonado**, C. Acal, JE. Ruiz-Castro, AM. Aguilera, F. Jiménez-Molinos, J. B. Roldán, C. Wenger, "Advanced temperature dependent statistical analysis of forming voltage distributions for three different HfO2-based RRAM technologies", Solid-State Electronics, 176, 107961, 2021.

[4] E. Pérez, **D. Maldonado**, C. Acal, J.E. Ruiz-Castro, F.J. Alonso, A.M. Aguilera, F. Jiménez-Molinos, Ch. Wenger, J.B. Roldán, "Analysis of the statistics of device-to-device and cycle-to-cycle variability in TiN/Ti/Al:HfO2/TiN RRAM", Microelectronics Engineering, 214, pp. 104-109, 2019.

[5] FJ. Alonso, **D. Maldonado**, AM. Aguilera, J.B. Roldán, "Memristor variability and stochastic physical properties modeling from a multivariate time series approach", Chaos, Solitons & Fractals, 143, 110461, 2021.

[6] J.B. Roldán, **D. Maldonado**, F. Jiménez-Molinos, C. Acal, JE. Ruiz-Castro, AM. Aguilera, F. Hui, J. Kong, Y. Shi, X. Jing, C. Wen, MA. Villena, M. Lanza, "Reversible dielectric breakdown in h-BN stacks: a statistical study of the switching voltages", 2020 IEEE International Reliability Physics Symposium (IRPS), Dallas, TX, USA, 2020, pp. 1-5, doi: 10.1109/IRPS45951.2020.9129147.

[7] M. J. Ibáñez, D. Barrera, **D. Maldonado**, R. Yáñez, J. B. Roldán, "Non-Uniform Spline Quasi-Interpolation to Extract the Series Resistance in Resistive Switching Memristors for Compact Modeling Purposes", Mathematics, 9(17), 2159, 2021.

[8] C. Acal, J. E. Ruiz-Castro, **D. Maldonado**, J. B. Roldán, "One Cut-Point Phase-Type Distributions in Reliability. An Application to Resistive Random Access Memories", Mathematics, 9(21), 2734, 2021.

[9] J.B. Roldán; G. González-Cordero, R. Picos, E. Miranda, F. Palumbo, F. Jiménez-Molinos, E. Moreno, **D. Maldonado**, S.B. Baldomá, M. Moner Al Chawa, C. de Benito, S.G. Stavrinides, J. Suñé, L.O. Chua, "On the Thermal Models for Resistive Random Access Memory Circuit Simulation", Nanomaterials, 11(5), 1261, 2021.

[10] AN. Mikhaylov, DV. Guseinov, AI. Belov, DS. Korolev, VA. Shishmakova, MN. Koryazhkina, DO. Filatov, ON. Gorshkov, **D. Maldonado**, FJ. Alonso, JB. Roldán, AV. Krichigin, NV. Agudov, AA. Dubkov, A. Carollo, B. Spagnolo, "Stochastic resonance in a metal-oxide memristive device", Chaos, Solitons & Fractals, 144, 110723, 2021.

Book chapters

[1] M.B. González, M. Maestro-Izquierdo, S. Poblador, M. Zabala, F. Campabadal, G. González-Cordero, S. Aldana, **D. Maldonado**, F. Jiménez-Molinos, J.B. Roldán, "Synaptic devices based on HfO2 memristors", Chapter 19, In Advances in Nonlinear Dynamics and Chaos, Mem-elements for Neuromorphic Circuits with Artificial Intelligence Applications, Academic Press, 2021, Pages 383-426, ISBN 9780128211847, https://doi.org/10.1016/B978-0-12-821184-7.00028-1.

Videos

[1] Complementary material to "D. Maldonado, F. Gómez-Campos, M.B. González, A. Roldán, F. Jiménez-Molinos, F. Campabadal, J. B. Roldán, "Comprehensive study on unipolar RRAM charge conduction and stochastic features, a simulation approach", Journal of Physics D: Applied Physics, 55, 155104, 2022". Video link. URL: https://youtu.be/-kq6-5k2-HY

Abstract

The efforts in this doctoral thesis have been focused on the characterization and modeling of memristive devices fabricated using different technologies. Among all the memristive devices, we will focus on resistive random access memories (RRAM), also known as resistive memories. To do so, devices based on metal-insulator-metal and metal-insulator-semiconductor structures have been studied in depth. A simulator based on circuit breakers has also been developed and tested to analyse RRAM variability and operation.

This PhD dissertation (a compilation work) includes 7 publications in scientific journals indexed in the Journal Citation Report of Science Citation Index, one proceeding published in IEEE Xplore digital library and one contribution to an International Conference. I have also contributed to other publications outside this work, including a book chapter and a video explaining the operation of the simulator. The outline of this work is the following:

Chapter 1 exposes the state of the art of resistive memories; in particular, we will focus on the resistive switching operation and its modeling and simulation. To begin with, the fundamentals of this technology are presented along the main applications. The current situation of flash devices and their limitations is also exposed as these new devices are emerging to replace them. Therefore, the most important features to describe in RRAM devices such as structure, fabrication process and materials employed are tackled. In addition, the main hurdles to address in order to reach a full development of this technology and a massive commercial fabrication are explained. Compact modeling and simulation tools are also described in the last section of the chapter since they are of great interest in these devices because they are still in their infancy.

Chapter 2 deals with the electrical characterization of RRAMs. Additional effects like the magnetic field are included during conventional measurements processes. Besides, statistical techniques are applied to the extracted experimental RS parameters to be analyzed in the context of the charge and flux domain.

The chapter includes the following contributions:

- [Maldonado2019] **Maldonado, D.**, Roldán, A. M., González, M. B., Jiménez-Molinos, F., Campabadal, F., & Roldán, J. B. (2019). Influence of magnetic field on the operation of TiN/Ti/HfO2/W resistive memories. Microelectronic Engineering, 215(April). DOI: 10.1016/j.mee.2019.110983.
- [Maldonado2019b] **Maldonado, D.**, Acal, C., González, M. B., Ruiz-Castro, J.E., Aguilera, A.M., Picos, R., Jiménez-Molinos, F., Campabadal, F., & Roldán, J.B. (2019). An in-depth statistical study of resistive switching energies in unipolar RRAMs. 21th Conference on "Insulating Films on Semiconductors", Cambridge (UK).

Chapter 3 introduces the time series analysis for studying variability in resistive memories. By using this versatile and advanced technique, different kind of devices based on traditional 3D stacks such as Ni/HfO_2/Si-n+, Cu/HfO_2/Si-n^+ and Au/Ti/TiO_2/SiO_x/Si-n^+ are tackled. Furthermore, novel memristors based on 2D materials, namely h-BN, are also considered.

The chapter includes the following contributions:

- [Roldán2019] Roldán, J. B., Alonso, F. J., Aguilera, A. M., **Maldonado, D.**, & Lanza, M. (2019). Time series statistical analysis: A powerful tool to evaluate the variability of resistive switching memories. Journal of Applied Physics, 125(17), 174504. DOI: 10.1063/1.5079409.
- [Rodríguez2019] N. Rodriguez, **D. Maldonado**, F.J. Romero, F.J. Alonso, A.M. Aguilera, A. Godoy, F. Jimenez-Molinos, F.G. Ruiz, J.B. Roldan, "Resistive switching and charge transport in laser-fabricated graphene oxide memristors: a Time Series and Quantum Point Contact modelling approach", Materials, 12, 3734, 2019.
- [Roldán2021b] Roldán, J. B., **Maldonado, D.**, Alonso, F. J., Roldán, A. M., Hui, F., Shi, Y., ... & Lanza, M. (2021, March). Time series modeling of the cycle-to-cycle variability in h-BN based memristors. In 2021 IEEE International Reliability Physics Symposium (IRPS) (pp. 1-5). IEEE.

Chapter 4 describes the extraction of the series resistance in HfO_2 based RRAMs and the inclusion of this parameter in an enhanced version of the Stanford model (implemented in Verilog-A) to ease the fitting of some type of experimental curves. Besides, the quantum point contact model has been modified to account for thermal effects to determine their role.

The chapter includes the following contributions:

- [Maldonado2021] **Maldonado, D.**, Aguirre, F., González-Cordero, G., Roldán, A. M., González, M. B., Jiménez-Molinos, F., ... & Roldán, J. B. (2021). Experimental study of the series resistance effect and its impact on the compact modeling of the conduction characteristics of HfO2-based resistive switching memories. Journal of Applied Physics, 130(5), 054503., doi: 10.1063/5.0055982.
- [Calixto2020] Calixto, M., **Maldonado, D.**, Miranda, E., & Roldan, J. B. (2020). Modeling of the temperature effects in filamentary-type resistive switching memories using quantum point-contact theory. Journal of Physics D: Applied Physics.

Chapter 5 exposes the Dynamic Route Map as a powerful tool to study the temporal behavior of reset transitions in TiN/Ti/HfO_2 devices. Different inputs have been employed to show that a unique surface is created to define the operation regime of a device supported with experimental data.

The chapter includes the following contribution:

- [Maldonado2020] **Maldonado, D.**, Gonzalez, M. B., Campabadal, F., Jimenez-Molinos, F., Al Chawa, M. M., Stavrinides, S. G., ... & Chua, L. O. (2020). Experimental evaluation of the dynamic route map in the reset transition of memristive ReRAMs. Chaos, Solitons & Fractals, 139, 110288, doi: 10.1016/j.chaos.2020.110288.

Chapter 6 focuses on the simulation of resistive memories. In particular, a simulator tool based on circuit breakers has been developed from scratch in order to analyze variability and the stochastic behavior of these devices to explain the physics behind RS.

The chapter includes the following contribution:

- [Maldonado2022] **Maldonado, D.**, Gómez-Campos, F. M., González, M. B., Roldán, A. M., Jiménez-Molinos, F., Campabadal, F., & Roldán, J. B. (2022). Comprehensive study on unipolar RRAM charge conduction and stochastic features: a simulation approach. Journal of Physics D: Applied Physics, 55(15), 155104.

Chapter 7 compiles the main conclusions of this doctoral thesis and the future improvements.

Introduction

Nowadays, the electronics industry is increasing its interest for volatile (temporary) and non-volatile (permanent) data storage. This fact arrives from the needs connected to 5G circuits, solid-state drives (SSD), artificial intelligence, data mining, internet of things (IoT) devices and cloud storage apart from laptops and smartphones [Gupta2019]. Resistive memories or Resistive Random Access Memories (RRAM) technology is thought to fit well for these needs. RRAM devices are one of the most promising emerging technologies due to its outstanding features such as low operation voltage, low power consumption, CMOS compatibility in the Back-End-of-Line (BEOL), non-volatility, good endurance [Lanza2021] and retention and the capability to be fabricated in 3D stacks since its architecture is quite simple [Lanza2019, Gupta2019, Munjal2019, Pan2014, Ielmini2016, Xie2013, Lee2015, Spiga2020, Waser2010, Waser2012]. These properties make RRAM devices the perfect candidate so substitute the dominant technology in the current non-volatile realm: flash memories. The latter ones are part of the Non-Volatile Memories family (NVM), devices that store information without the need of an external power system to keep the information. Flash technology has advantages such as low cost, high density and reliability, but also some important constraints which might affect its future: low durability, leakage, low operation speed and the need of high operation voltages that results in high power consumption.

In the realm of NVM memories there are also other candidates to compete with RRAMs, the most relevant are Spin-Transfer Torque RAMs (STT-RAMs, a type of magnetic memories) and Phase Change Memories (PCM), both of them being thoroughly studied by the international electronic community due to the increasingly need for storage of the information all around the world [Xie2013]. This comes from the fact that current electronic devices for NVM are required to show retention times greater than a few years, to have low energy consumption and also offer low latency times.

The target on NVM is focused on two main issues:

1. **Reasonably low operation speed** in relation to DRAM and SRAM. If this hurdle is overcome, they could easily replace them in the future for some purposes, and in doing so, take leadership on part of the market [Xie2014].
2. **Low power operation** [Xie2014].

NVM are commonly employed in daily applications such as laptops, smartphones, videogames, scientific equipment, robotic components, etc. Nevertheless, flash technology, the current market leader, will come to an end sooner or later and some action is required [Gupta2019, Xie2013, Xie2014, Waser2007, Waser2010, Waser2012]. In this context, RRAM memories, which are based on a hysteretic operation called resistive switching (RS), rise as one of the most suitable replacements in contrast to another emerging technologies as PCM memories, Magnetic RAMs (MRAMs) or STT-RAM memories [Lanza2019, Xie2014, Waser2007, Waser2010].

If the upcoming devices are based on RRAMs instead on other technologies, the electronics paradigm is expected to lead to a breath-taking revolution: there would be applications never seen before due to the possibility to build and develop new computer architectures much powerful than the most commonly fabricated today following the von Neumann architecture [Wang2019]. RRAM fabrication is mainly based on two structures, Metal-Insulator-Metal (MIM), and Metal-Insulator-Semiconductor (MIS). The insulating material in between the electrodes consists of a dielectric whose properties allow its resistance to be changed, a mechanism known as resistive switching [Lanza2019, Gupta2019, Waser2012, Munjal2019, Carboni2019]. Among the materials employed are the following:

1. Transition metal oxides (TMO) as HfO_2 or TiO_2.
2. Perovskite family showing paraelectric, ferroelectric, multiferroelectric and magnetic behavior.
3. Graphene oxides as hexagonal boron nitride (h-BN) along with another two-dimensional materials.

In the past years, great results have been obtained both at device and circuit level, allowing to design and fabricate a 16 GBs integrated RRAM memory circuit [Zahurak2014] or a 4 GBs memory device in 24 nm CMOS technology [Liu2013]. The foundry TSMC has recently planned to offer embedded RRAM at both 40 nm and 22 nm nodes, this technology is capable of 10-year retention at 125ºC and over 10000 cycles of endurance (suggesting using TiO_2 as dielectric [TSMC2020]). These facts allow to consider this technology a real candidate in the near future for massive NVM industrial manufacturing, granting embedded storage class memory in processors and microcontrollers.

Even so, there are still some impediments to surpass before reaching the massive market regime for this technology: to begin with, the variability linked to the fabrication process which makes differences between two identical devices (device-to-device) along with the inherent variability during cycling in the same device (cycle-to-cycle). The latter is associated to the physics behind the RS process [Lanza2019, Pan2014]. For the characterization of RS and the study of the physics behind, both device simulators and compact models are needed. In particular, in the physical simulator context, there can be found the kinetic Monte Carlo (KMC) simulators, where the device operation is described in detail, according to the physical mechanisms involved at the atomic level [Aldana2020, Padovani2015, Dirkmann2018, Guy2015]. At the modeling level, advanced statistical modeling [Pérez2019, Mikhaylov2021, Alonso2021, Roldán2019] and the compact modeling approach for circuit simulation, where the device description is faster and compact [Huang2013, Chen2015, Bocquet2014, Picos2015, Maldonado2019, Guan2012, Jiang2016, Roldán2021, González-Cordero2017], can be found.

In this work we deal with several RRAM technologies. We perform different characterization techniques, including the electrical analysis of devices within magnetic fields. We have analysed the measurement data to obtain compact models and implement them in circuit simulators by means of SPICE macromodels and Verilog-A (including parameter extraction techniques). We have also developed a device simulator using circuit breakers. With all these measurements and software tools we have studied RS in all the devices analysed and their variability, among other issues.

Objectives

The main objective of this work consists of the measurement of different types of RRAM devices including MIS and MIM structures under several situations (temperature, electric/magnetic field…) in order to analyse the obtained data and understand resistive switching operation. First of all, the laboratory was conditioned to carry out these measurements employing magnetic field generated by Helmholtz coils and a chiller to control and fix the temperature in the sample during the procedure. Additionally, the required software to control the instrumentation was programmed to allow a fully and correct automation of the process. To do so, different numerical algorithms were implemented to grant the parameter extraction of the data, in particular, the typical resistive switching parameters, such as the set and reset voltages and currents. Then, modeling and simulation of RRAMs was performed taking into consideration the measurements obtained in the laboratory.

The objectives were subdivided into the following issues:

1. Analysis of the experimental results applying advanced statistical techniques.

2. Characterization and modeling of the experimental data employing the time series approach and the Quantum Point Contact model.

3. Modeling of quantum effects considering multiple potential barriers.

4. Development of compact models to reproduce experimental data and simulate circuits.

5. Development of a circuit breaker-based RRAM simulator.

xxx

Methodology

The following methodology and associated tasks were performed to accomplish the previous objectives, see the diagram below.

1. Analysis of the experimental results applying advanced statistical techniques:
    a. Devices fabricated in the National Microelectronics Center at Barcelona (*IMB-CNM (CSIC)*) and the University of Shoochow (China), based in MIS and MIM structures, were measured in the laboratory including external effects: magnetic field and temperature variation.
    b. Study and evaluation of the magnetic field and temperature effects on the operation of these devices. The typical parameters are analysed: set/reset voltages and currents.
    c. Study of the device-to-device and cycle-to-cycle variability considering phase-type and Weibull statistical distributions.
2. Characterization and modeling of the experimental measurements employing the time series approach and the Quantum Point Contact (QPC) model. Implementation of the time series analysis and forecasting: a mathematical tool to predict and evaluate variability on resistive memories.
3. Modeling of quantum effects considering multiple potential barriers. Simple and double potential barriers are taken into consideration.
4. Development of compact models to reproduce experimental data:
    a. Analysis of graphene-based devices using the Quantum Point Contact model.
    b. Modification of stablished models, as the Stanford model, to include additional effects like the series resistance using Verilog-A.
5. Development of device simulator implemented by circuit breakers. Forming, set and reset processes were described in terms of the rupture and creation of conductive filaments by means of circuit breakers, including the stochastic component in the device operation.

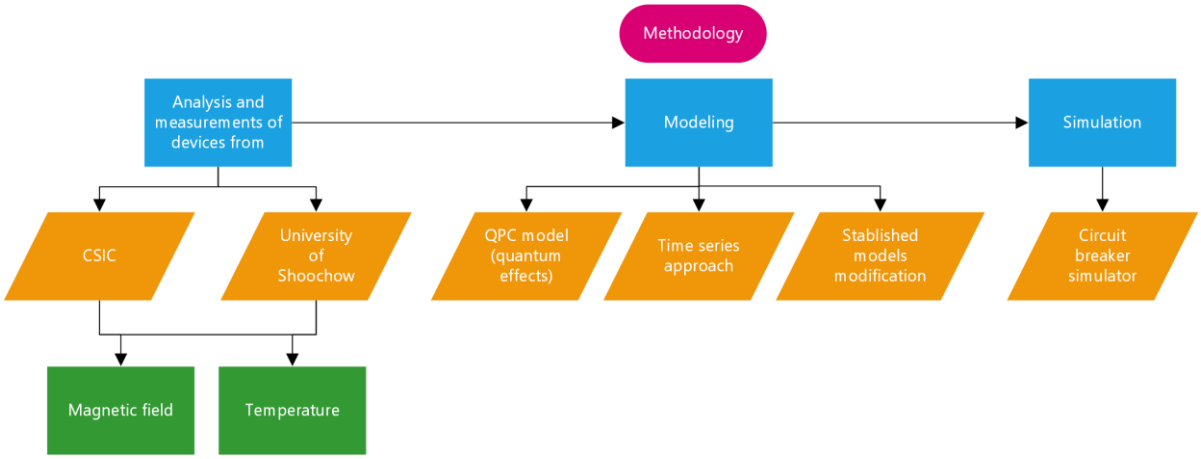

Diagram of the methodology and associated tasks

Chapter 1.

1. Introduction to RRAM technology. Overview and state of the art

For several years now, flash technology has reigned in the non-volatile memory markets both in its NOR or NAND architecture. This technology, an upgrade of the EEPROM which was invented at Toshiba in 1984 essentially consisting in a metal-oxide-semiconductor field-effect-transistor (MOSFET) structure, in addition to a floating gate in each memory cell, is largely being used in embedded applications due to its excellent properties: high density and low cost. However, there are also some important drawbacks which limit its development [Pan2014, Ielmini2015]:

1. Limited endurance (10^6 write/erase cycle).
2. Low operation speed (write/erase time: 1 ms/0.1 ms).
3. High write voltages that imply high consumption (> 10 V).

Flash memories store the information using the floating gate of the transistor to store the charge (see the diagram in **Figure 1.1**) which implies an important challenge when scaling down to 10 nm or beyond. This is associated to the loss of the stored charge at a very low scale resulting in a reliability, noise margin and performance loss. Additionally, there are some physical mechanisms such as Random Telegraph Noise, threshold voltage shift, charge trapping and Stress Induced Leakage Current (SILC) posing important objections for the design and development of future memory hierarchy [Ielmini2009, Pan2014, Villena2015, Gupta2019, Wong2015, Xie2013].

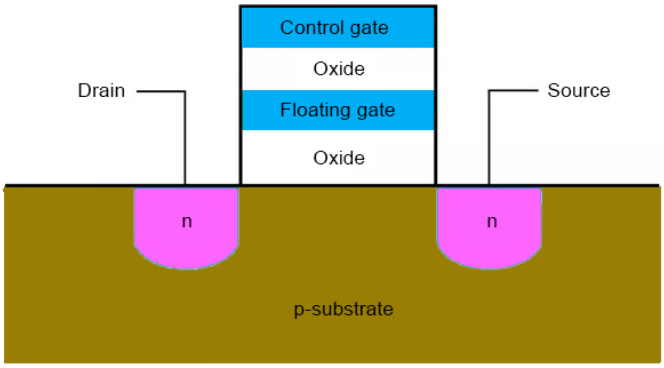

Figure 1.1. Diagram of a flash memory cell consisting of a storage transistor with a control gate and a floating gate.

Some emerging NVM technologies are currently being investigated in order to clarify and solve the issues described above. The best placed candidates are the STT-MRAM [Zhu2008], the PCM [Wong2010], and the resistive memory [Wong2012a]. These technologies are non-volatile, two-terminal devices and differentiate two states by the switching between a high resistive state (HRS) and a low resistive state (LRS) triggered by an electric field [Yang2009]. The latter, which are the objective of this work, rely, in most cases, on the formation (corresponding to the LRS) and the rupture (corresponding to the HRS) of one or more conductive filaments in the dielectric layer between two electrodes (in case they show filamentary conduction). RRAMs are seen as a possible replacement of flash memories because of its lower programming voltage and faster read/write speed. Furthermore, some improvements offer a brilliant future for these devices [Lanza2019, Pan2014, Zahurak2014, Carboni2019, Nardi2011, Lim2015, Ielmini2016]:

1. Outstanding scalability.
2. Long data retention.
3. Easy fabrication in a metal-insulator-metal or metal-insulator-semiconductor structure.
4. Sub-ns operation speed.
5. CMOS compatibility.

Figure 1.2a depicts the classic MIM (or MIS) RRAM structure accounting for two electrodes, top and bottom, including a dielectric layer sandwiched in between. Depending on the internal physical and chemical mechanisms that take place to control the resistance of the devices, several classifications can be determined [Pan2014, Lee2015, Ielmini2015]. The switching event from HRS to LRS is called **set process** and, the switching event from LRS to HRS is called **reset process**. When the sample is in the pristine state[1], a large voltage is needed to achieve the LRS state, this first cycle is known as **forming process**. There are two classifications depending on the switching operation: unipolar and bipolar. In **Figure 1.2a,** a diagram of the I-V characteristics is presented for both mechanisms. **Figure 1.2b** shows the unipolar mode, where the resistive switching calls on the amplitude of the external voltage instead of the polarity applied. This means that the set and reset processes arise in the same polarity (positive or negative). On the other hand, **Figure 1.2c** shows bipolar switching, switching directly depends on the polarity of the applied voltage. Consequently, the set process may

[1] Initial state of the device previous to the measurement

only result at one determined polarity and the reset process may only result at the opposite polarity. Both processes are limited to reach a certain current level called compliance current (CC) to prevent the device to get to a hard dielectric breakdown (a permanent damage that shorts the electrodes).

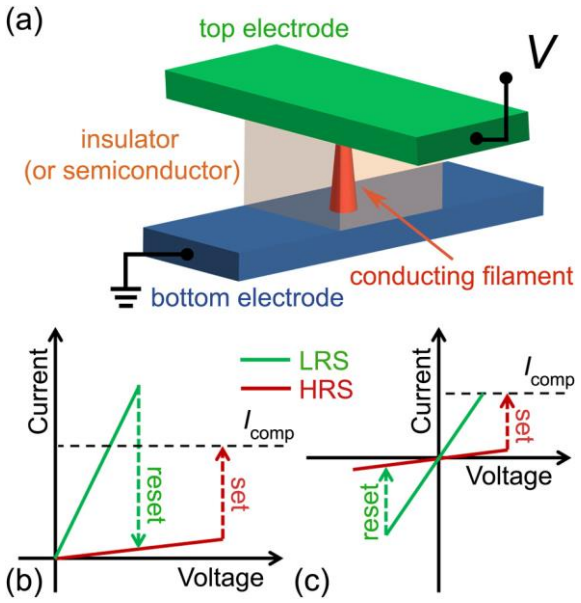

Figure 1.2. a) Schematic of a metal-insulator-metal or metal-insulator-semiconductor RRAM device**.** Typical I-V curves showing b) unipolar mode, c) bipolar mode. A CC is stablished to prevent the device from reaching the electric breakdown [Pan2014].

One key-factor here is the election of the materials when fabricating the devices because of the impact they have in the performance. Resistive switching is the result of the mechanisms produced by the combination between both electrodes and the oxide. For unipolar devices, noble metals such as Pt and Cu can be used in both electrodes, while bipolar switching can be obtained by combining a noble metal in one electrode and an oxidizable material such as TiN in the other electrode. Some common structures are TiN/metal/oxide/TiN, eg., TiN/Ti/HfO_2/W [Maldonado2019] where the electrode/oxide interface works as an oxygen reservoir. Typically, unipolar switching presents more variability and requires a higher current than bipolar switching during the reset process. In **Table 1.1** some examples of different RRAMs are presented. Note that the on/off ratio is the ratio between the value of the resistance measured in the HRS and in the LRS, and it is always recommended to be as high as possible; retention is the time a device can keep a certain resistance level and the operation speed is linked to the device read and write times. As could be seen, results are very promising.

Structure	ON-OFF ratio	Retention	Operation speed	Type	Reference
Al/Ti/Al_2O_3/s-CNT	100	10^6	50 ns	VCM	[Ahn2015]
Al/PCMO/Pt	10^3	10^7	8 ns	VCM	[Liao2011]
Pt/SiN/Ti	10^7	$>10^9$	< 100 ns	Bipolar charge trap	[Kim2013]
TiN/TiO_x/HfO_x/TiN	10	10^6	10 ns	VCM	[Chen2010]
Cu/ZrO_2:Cu/Pt	10^6	10^4	50-100 ns	Nonpolar/unipolar CBRAM	[Guan2008]
TiN/ZrO_2/Pt	10^2	10^4	1 µs	Bipolar TM	[Sun2009b]
Ti/Mo-embedded	10^2	10^7	10 ns	Bipolar	[Wang2010a]
Au/HfO_2/TiN	10^4	10^2	20-120 ns	Unipolar CBRAM	[Walczyk2009]

Table 1.1. Comparison among various RRAM devices. The most representative parameters such as the ON-OFF ratio, between the LRS and HRS operation, data retention and operation speed are displayed along with the type of device.

Another less common classification could be made depending on atomic rearrangements that causes the resistance change and is linked to the devices area [Meyer2008] or to conductive filaments formed in the dielectric (in this case it is not area dependent). In this thesis we will focus on the latter, which is the predominant operation principle for most of the competitive transition-metal-oxide-based RRAMs. Filamentary conduction arises when atomic rearrangements appear as clusters typically lower than 100 nm^2, forming a percolation path in a defined part of the oxide [Lanza2019, Chen2013, Bersuker2010, Celano2013, Kwon2010, Calka2013, Cartoixa2012, Pan2014]. In **Figure 1.3** a-c) the formation of a cylindrical shape conductive filament is depicted during the forming process, showing its growth from the cathode to the anode whereas in d) the CF (conductive filament) ruptures near the anode during the reset process.

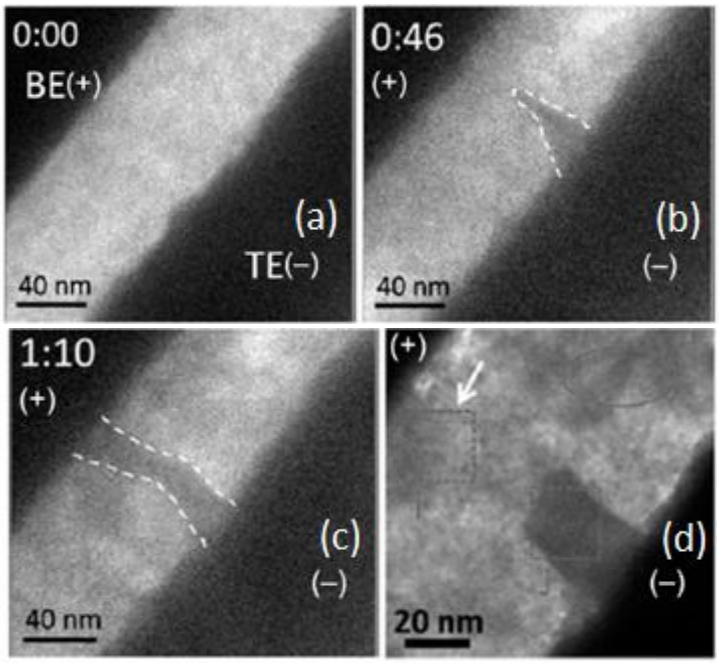

Figure 1.3. TEM examination of the evolution of a CF during a forming and a reset process on a unipolar CBRAM Pt/ZnO/Pt device. a-b) detail of the formation of the filament from the bottom to the top electrode, c) fully formed cylindrical shape filament after set, d) partially broken filament after reset [Pan2014].

1.1. Memristors. Applications

Resistive Random Access Memories belong to a wider category named memristors. The memristor, the contraction of the words "memory" and "resistor", was predicted long ago by Leon Chua in 1971 [Chua1971]. This is a new two terminal passive element that can change its internal resistance to shift between several different states when an external condition is applied (these devices are employed both for digital and analog applications). This device is known as the *missing circuit element* [Strukov2008] since it completes the classical passive electric elements: resistor, capacitor and inductor, which are linked to the essential magnitudes such as voltage, charge, flux and intensity, as shown in the scheme of **Figure 1.4a**. The typical transfer characteristic of these devices is presented in **Figure 1.4b**, note that the area within the hysteresis curve decreases as the frequency increases. The inset details that the charge is a particular function of the flux as expected in a memory device.

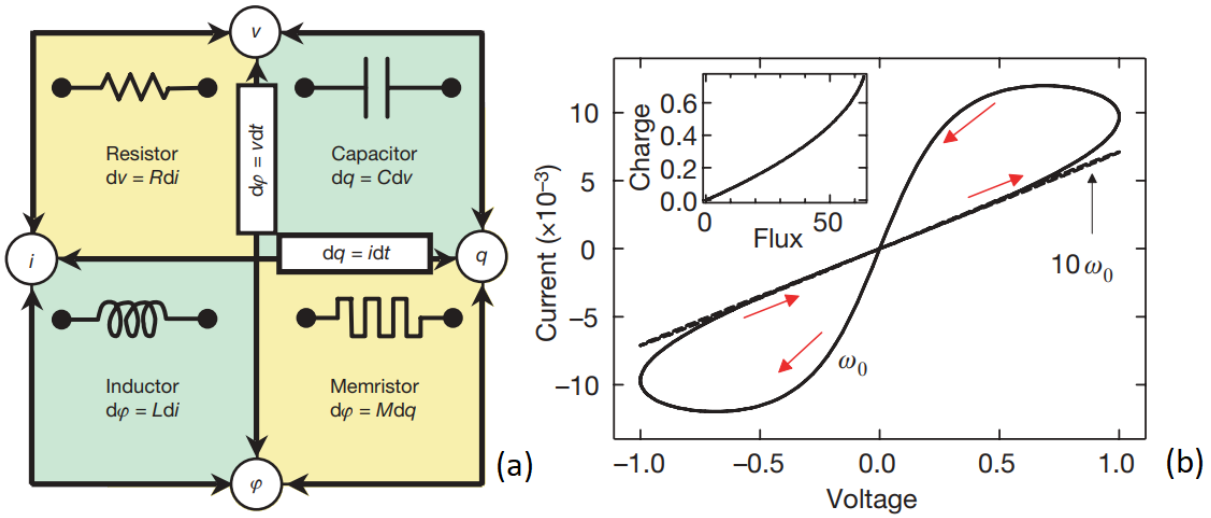

Figure 1.4. a) Diagram of the four basic passive elements (resistor, capacitor, inductor and memristor) and their association with the basic electrical magnitudes (voltage, intensity, charge and flux). b) Classical current versus voltage plot of a memristor element. Inset: charge versus flux function [Strukov2008].

Among the applications of RRAMs, and memristors in general, we can find the following:

a.- RRAMs are nowadays under scrutiny of the international scientific community due to their exceptional ability to mimic biological synapses for hardware neural networks implementation due to their controllable conductance (from an analog perspective), low power consumption, CMOS technology compatibility, retention and size [Yu2011, Wang2019, Yao2020, Villena2015, Merolla2014, Alibart2013, Prezioso2015, RomeroZaliz2021, González-Cordero2019b]. This architecture is called to replace the classical von Neumann for artificial intelligence purposes since the latter struggles when dealing with large-scale data processing which provokes the undesirable effect of a bottleneck. Neuromorphic computing is the alternative to von Neumann architecture, it allows to design and implement learning algorithms to automate tasks without the need of anybody to control, a huge advantage [Zidan2018]. This is possible since different processes are carried out in the same unit at the same time, resulting also in a low power consumption and no latency because the information is processed and stored in the same place in memory computing [Sakellaropoulos2020]. Although there is still a long way to go for this architecture [Alibart2013], neuromorphic systems could be developed to manufacture appropriate systems with higher computation sufficiency than actual ones reducing the power consumption.

b.- Physical unclonable function (PUF) implementation and random number generators (RNG) can be built based on the stochastic properties of RRAM [Huang2012]. These kinds of circuits are implemented by means of variations of RS parameters such as set and reset voltages, switching times, conductance levels and fluctuations of the current in a certain period [Zhang2018]. The latter, also known as random telegraph noise (RTN), are very interesting in order to be used as entropy sources as they do not imply the creation and disruption of a CF over the dielectric, which implies a low power implementation [Lanza2021b]. PUFs arise as an up-and-coming technology for hardware security and encryption key generation with multiple applications like the IoT, since real randomness along with robustness in functional applications could be achieved

[Lin2021, Nili2018, Pang2017]. On the other hand, true RNGs play a decisive role in cryptographic applications to generate non predictable, independent and statistically uniform data [Yang2021, Rodriguez-Montañés2021, Tseng2021].

c.- Another important characteristic of memristive devices is their use as non-volatile memories. This is possible due to their binary storage capacity (6 bits/cell) [Banerjee2020] since two differentiated resistance levels could be accomplished. In this respect, scalability along with low power operation are the main elements desired in a high density memory which make RRAMs a suitable candidate to replace flash ones. In the past years, industry has put a lot of effort in developing these technologies. In particular, commercial fabrication is offering different processes, e.g., TSMC's 40 nm RRAM [Chou2018] and Intel's 22 nm RRAM [Jain2019].

1.2. Actual technology and limitations

Non-volatile memories based on silicon, flash memories, are the dominating technology currently. In **Figure 1.5** the scheme of a MOSFET with a floating gate placed down the Control Gate (CG) noted as Floating Gate (FG) is presented. The FG is located inside the oxide, so it is electrically isolated from the other elements which allows keeping the injected electrons there for a long time (over 10 years). There are some charge carriers stored in the FG which screen the effect of the CG over the channel of the transistor, in other words, that charge somewhat cancels the electric field applied amid the CG and the transistor channel. The threshold voltage of the transistor (V_T) could be tuned by implanting hot electrons from the channel to the FG by employing a high electric field over the drain and the CG [Frohman-Bentchkowsky1974]. This results in a higher threshold voltage (V_{T2}) which means that the formation of the conduction channel inside the transistor is harder to achieve [Bez2013].

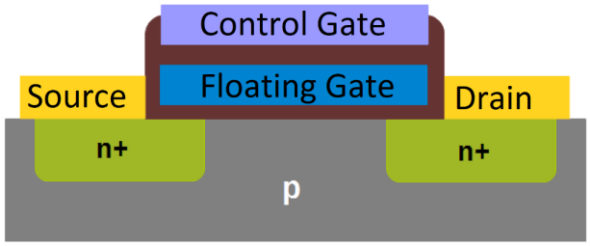

Figure 1.5. Graph of a FAMOS transistor (Floating Gate Avalanche-injection MOS) [Villena2015].

Through the charge or discharge the FG, each of the cells could store a unit of logic information (known as a 0 or a 1 logic state). If the FG is already charged, with a certain voltage V ($V_T < V < V_{T2}$) applied to the CG, the conduction channel of the transistor will not be created and there will be no current flowing across it, so a logic 0 is registered. Conversely, if the FG is discharged but with the same previous voltage, a logic 1 is registered because of the conduction in the channel.

Flash memories are reaching its physical limit since reducing the size of the cells is getting quite difficult. Currently, the scale down over 10 nm is producing several problems of loss or fluctuation of charge [Christensen2022]. Some of them are related to [Aritome1993, Atwood2004, Ielmini2009]:

- Charges trapped in the oxide: storing charge in NAND memories takes place under the effect of high electric fields that drag charges into the FG through the oxide. This produces that unavoidably some charges rest in the oxide due to the cycling, so a screening effect occurs in the FG. As a result of that, the threshold voltage of the transistor changes and that means a malfunction of the device [Lee2002].
- Random telegraph noise: appearing traps in the oxide also affects to the reading process, a carrier leak provokes random fluctuations of the current [Yang2006].
- Cross-talk (parasitic capacities): when cells are close enough, capacities between FG becomes coupled, this effect is especially relevant when a low number of electrons is involved [Atwood2004].
- Stress Induced Leakage Current (SILC): intensive programming of the cells over time produces oxide damage which makes that carrier could escape from the FG to the gate. Once again, the threshold voltage V_T is affected, and the cell does not behave properly.

1.3. New devices in the framework of non-volatile memories

The hurdles purported in the previous section 1.2 have favoured the need for researching and developing new electronic components. In general, there are several ways to go. The first one is to improve the current CMOS technology focusing on the power consumption and the increase of the speed and the storage density, this is also known as *"More Moore strategy"*. Another way is to employ CMOS technology in new architectures to enhance data treatment. The objective of this thesis is the study of novel devices based on new procedures with the potential to replace flash technology for data storing in the midterm, also known as *"More than Moore strategy"*. Note that the latter technology is not an alternative to the digital trend stated by Moore's Law, it certainly is a mixture assimilation of digital and non-digital purposes into compact systems which will be the basis of multiple applications. As depicted in **Figure 1.6**, see that *"More Moore"* is regarded as the brain of an intelligent compact system while *"More than Moore"* means interacting with the outside world and the users.

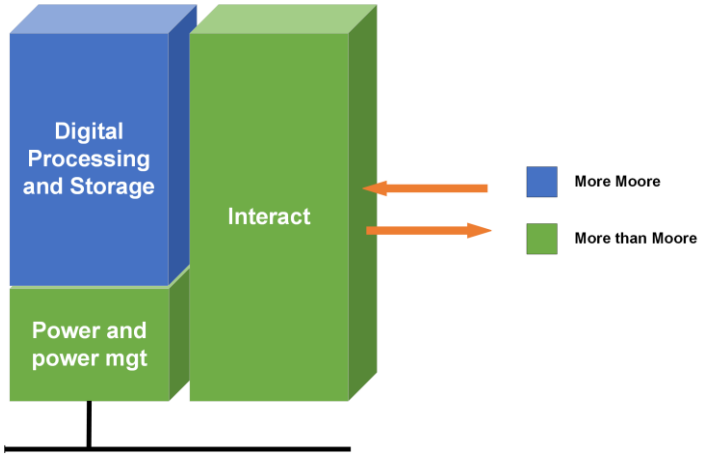

Figure 1.6. *"More than Moore"* technology allows the communication between the digital processing & storage of an integrated system and the users in the outside world.

Some of the most promising technologies capable of implementing non-volatile memories are shown in **Figure 1.7**:

1. **Phase Change Memories**. These devices are built on chalcogenide glasses and their operation is based on the change of its internal structure to reach two different conduction states: the crystalline phase (SET state), implying a low resistance and the amorphous phase (RESET state), with a high resistance [Christensen2022, Pirovano2004, Lacaita2006].
2. **Spin-transfer-torque random-access-memories**. These devices are based on spin transfer torque processes and fabricated on a magnetic tunnel junction (MTJ) with two ferromagnetic layers separated by a thin insulator barrier. The switching relies on the difference between parallel configuration (corresponding to the LRS) and the anti-parallel configuration (corresponding to the HRS) [Sebastian2020, Chen2016, Yu2016].
3. **Ferroelectric memories** as Ferroelectric Field-Effect transistor (FeFET) and the Ferroelectric Tunnel Junction (FTJ). A ferroelectric capacitor is included in the gate of the FET transistor which can be tuned to control the charge distribution in the channel, so, the output current is controlled [Zeng2019, Ma2000, Horiuchi2008]. These memories are built on two electrodes with a ferroelectric layer in between where a quantum tunnel effect induces a current. This current is fixed depending on the energy of the barrier height that is produced as result of the external voltage. [García2014, Gruverman2009]. The biggest drawback of these devices is the leakage current and the depolarization of the ferroelectric layer because of the electric fields in the common operation which implies shorter retention times.
4. **Mott memories**. These devices are typically based on a MIM structure where the dielectric is a Mott material [Xang2019b, Mott2004] that is activated by means of the carrier injection [Asamitsu1997], thermal activation [Pickett2012] or an electric field. Their operation consists of the transition between a metal and a dielectric in materials with correlated electrons.
5. **Memories fabricated with carbon-based materials**. These devices are based on amorphous carbon, nanotubes carbon or even graphene since their properties allow the switching between diamond-like (HRS) and graphite-like (LRS) phases [Zhou2019, Qin2012].

Some of them shift between both HRS and LRS states with the thermal creation and rupture of nano-holes [Kreupl2008].

6. **Molecular and macromolecular memories**. These memories are based on a simple or a little cluster of molecules which create a path between two electrical electrodes [Chen2018b]. This is carried out by applying an external electric field that changes the internal resistance, showing both unipolar and bipolar behavior [Song2011, Reed2001]. The most remarkable advantage of this technology is scalability, since the size of the cell may range from a few molecules to more efficient and complex structures [Liu2012, Bai2013].
7. **Resistive Random Access Memories**. This is one of the most promising technologies in the non-volatile realm and the objective of this work. These devices are based on a MIS or MIM structure where the resistive switching takes place in the dielectric. Dielectrics are typically made of chalcogenides, transition metal oxides, organic materials or semiconductors that change its internal resistance by means of physical mechanisms [Wong2012a, Villena2015]. There are multiple properties which make these devices such a powerful candidate: scalability under 5 nm, easy and cheap mass fabrication cost, low operation voltage (under 3 V), low power dissipation (under 64 pJ/cell), high processing speed (under 100 ns), CMOS compatibility and 3D integration [Chen2016, Yu2016, Pan2014, Villena2015]. Several classifications could be determined by the physical mechanism responsible to control the RS: Valence Change Memory (VCM) [Xue2019], thermochemical RRAM memory [Zhang2020], Conductive Bridge RAM (CBRAM) [Coll2019], and metal oxide bipolar non-filamentary RRAM memories [Zhang2020, Yu2016].

   Since the conduction of these devices is generally formed by conductive filaments formed by redox reactions, they are also named redox-based memories [Funck2021].

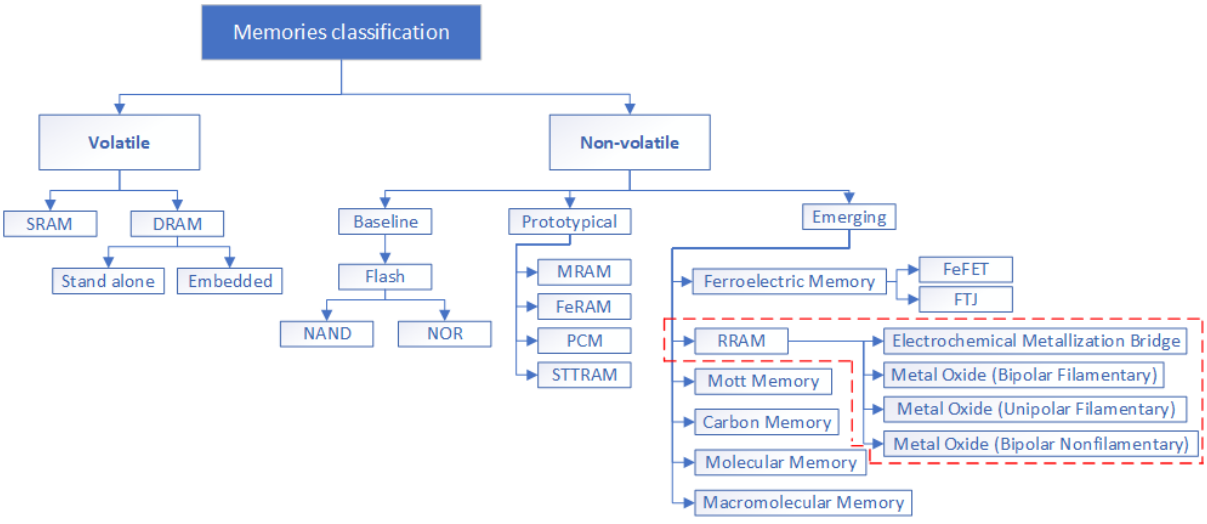

Figure 1.7. Diagram including all the different types of memories underway. In this work, all the efforts will be focused on emerging NVMs, precisely on RRAMs.

Currently, some companies are devoted to RRAM design, manufacturing and sales. One of the best known is Crossbar Inc. founded in 2010 in California with more than 190 patents issued worldwide. As stated in their website [Crossbar2021], their devices have been proved to scale below 10 nm and

compared to a traditional NAND Flash memory; they have 100 times lower read latency, 20 times better energy efficiency and 1000 times faster write performance, among other properties, see the diagram in **Figure 1.8.** Additionally, they do not need to be erased since they are capable to overwrite to bit/byte level, they are fabricated on standard CMOS production lines and their capacities could reach 1 TB/chip and more [Crossbar2021].

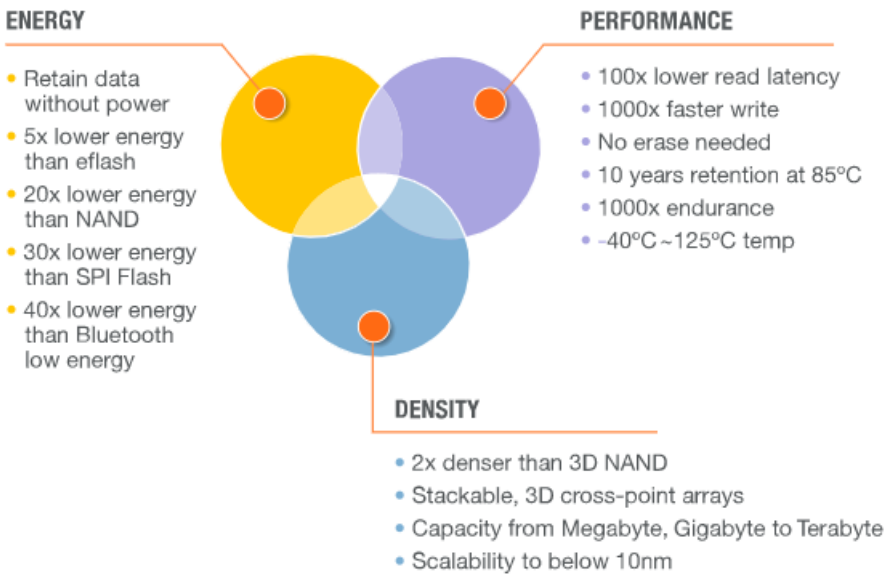

Figure 1.8. Crossbar Inc. RRAM technology highlights compared to traditional NAND Flash technology [Crossbar2021].

1.4. RRAM Technology

1.4.1. RRAM Structure

As it has been already stated, RRAM cells consists of a MIM or MIS structure, see **Figure 1.9a**. This is quite simple, so the industrial fabrication process is very competitive. The dielectric layer grants the movement of ions under the effect of an external electric field which induces an electric current [Pan2014, Waser2009]. A crossbar is needed when dealing with a high density of RRAM cells. This structure consists of a perpendicular top wire (TE) and a bottom wire (BE) with a dielectric layer in between. See in **Figure 1.9b** a crossbar example with nine cells [Wei2020].

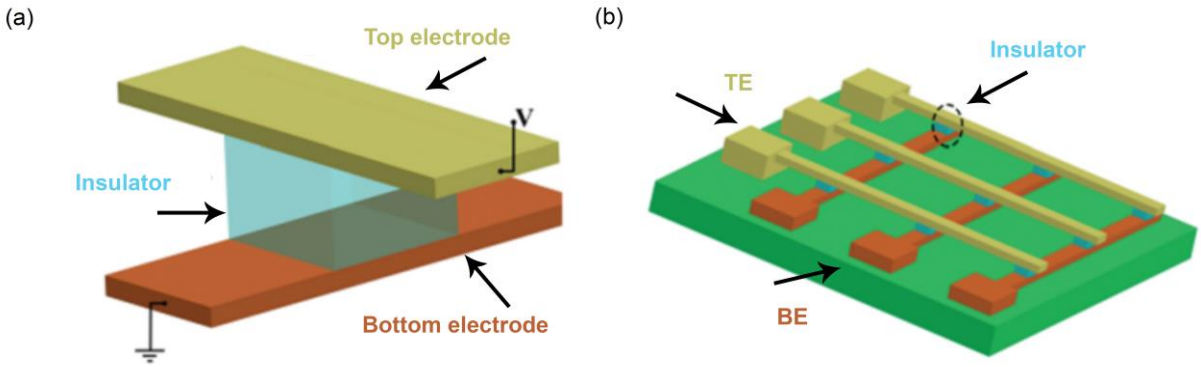

Figure 1.9. Sketch of a RRAM memory crossbar array. (a) Structure of a single cell, b), crossbar architecture formed by multiple cells driven at the same polarity at the same time [Wei2020].

If a higher level of integration is needed, this technology also gives the chance to stack the cells in a horizontal or vertical 3D cross-point architecture. The first one is based on stacking the horizontal cross-point array layer by layer as shown in **Figure 1.10a**, while the other consists of a vertical pillar structure with the RRAM sandwiched between the vertical electrodes and multilayer horizontal electrodes as shown in **Figure 1.10b**. The latter is inspired on the vertical 3D channel employed currently by NAND flash memories. Note that the fabrication process of the horizontal cross-point array is higher than the vertical one because the vertical approach only requires one critical lithography step or mask to define the pillar electrodes after the deposition of successive planes of electrodes [Pan2014, Wu2016, Yu2016]. In essence, production costs are lower as more layers are stocked.

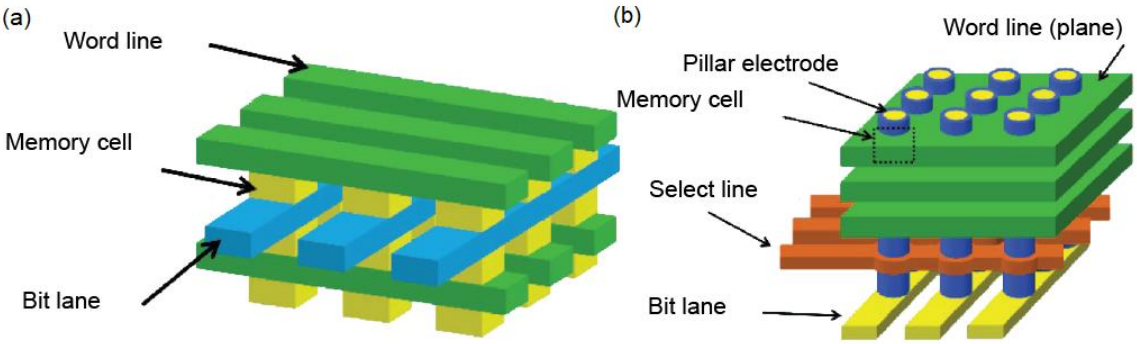

Figure 1.10. Design of a 3D a) horizontal cross-point array (HRRAM) where the memory cell is positioned at the intersection between bit line and world line, b) vertical cross-point array (VRRAM) where the memory cell is located at the intersection between pillar electrode and word line [Yu2016].

1.4.2. Device fabrication

In these devices, the election of the electrode material is key to the switching behavior. A broad diversity of them have been studied. The electrode materials can be summarized in five categories depending on their configuration: silicon-based electrodes, nitrite-based electrodes, oxide-based electrodes, alloy electrodes and elementary substance electrodes. The latter are the most usual electrodes which include Al [Maestro-Izquierdo2020], Ni [Villena2016] Ag [Huang2016], W [Prakash2014], Ti [Yang2009b], Cu [Yang2009c], Pt [Chiu2012] or graphene [Son2010]. Alloy

electrodes generally tend to balance the RS including Pt-Al [Wang2013] and Cu-Ti [Huang2013b]. Oxide-based electrodes include ZnO [Zheng2011], ITO [Kim2012], etc. In case of silicon-based electrodes p-type Si and n-type Si [Tang2013] are employed. The last group of nitrite-based electrodes is the quite frequent, for instance TiN [Poblador2020] and TaN [Tang2013b]. Regarding the dielectric layer, MIM and MIS structures could be easily assembled by employing the oxides that are typically operated in the semiconductor industry. The most common way of assembling is by physical vapor deposition and lifting-off successively. The top electrode and the dielectric layer are deposited by using physical vapor deposition (PVD) or atomic layer deposition (ALD) [Zahoor2020].

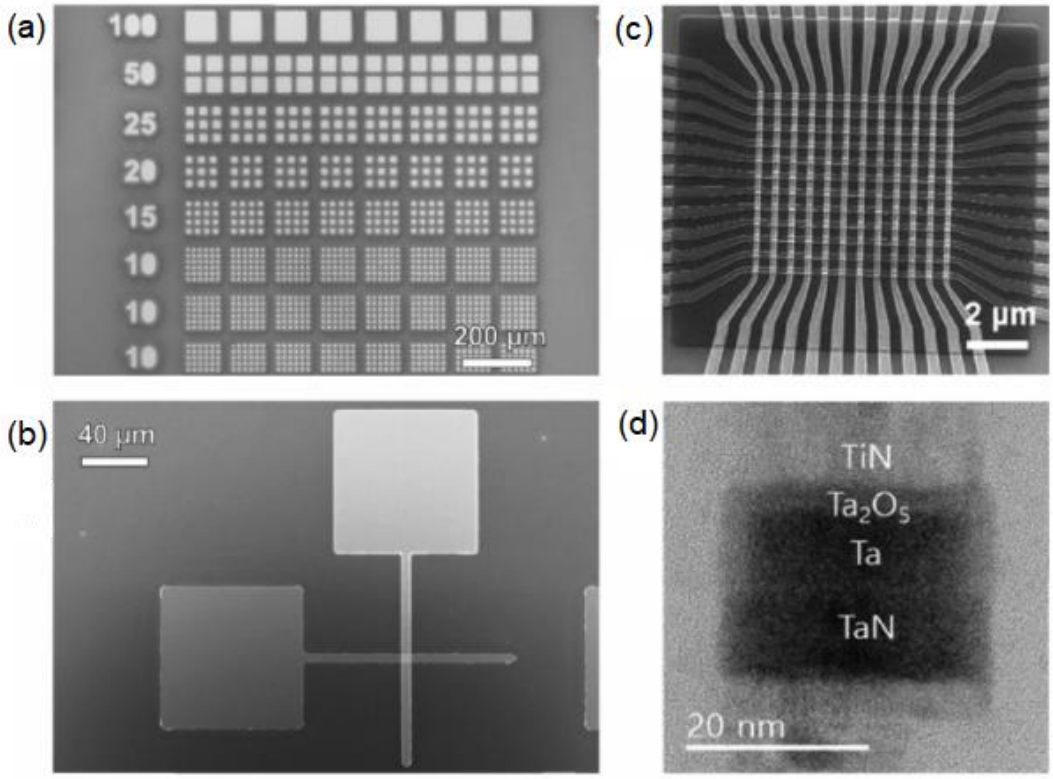

Figure 1.11. Typical RRAM structures to study the RS mechanism, SEM images are presented. a) Multiple top electrodes of different sizes with a common bottom electrode, b) device built on a horizontal cross-point structure, c) crossbar structure, d) section of a MIM structure showing its different layers, TEM image [Lanza2019].

Usually, RRAM shares the same bottom electrode as shown in **Figure 1.11a** whereas, for a crossbar architecture, separate bottom electrodes are used for each device, see **Figure 1.11b** for cross-point and **Figure 1.11c** for a 3D crossbar [Lanza2019]. It is important to highlight here that the size of the MIM cell makes HRS current depend on it when the RS is not filamentary and the LRS when the RS mechanism is distributed. Additionally, some studies demonstrated that RS is a stochastic process that always takes place at the weakest locations of the device [Pietronero1988]. Thus, as the size of the cell rises, the probability of finding defects and weaker regions is higher, which implies a variation of the set and reset threshold voltages. This fact foments that the electrical properties of the device vary a lot due to the formation of different CF sizes and shapes. Typically, smaller RS devices present lower HRS current and larger set and reset voltages [Shi2017], see in **Figure 1.11d** an example of a 28 nm diameter MIM RS device [Park2017].

1.4.3. Operation

The resistive switching operation is stochastic and takes place in the dielectric layer and in the corresponding interfaces, as reported at the beginning of the chapter. In the event of a filamentary conduction, RS takes place by means of conductive filaments that shunt both electrodes. In the case of unipolar switching, Joule heating could be the main physical mechanism involved in the conductive filament rupture while the reset process takes place. In bipolar switching the main principle involved is the migration of charged species due to the electric field, although Joule effect also accelerates the physical mechanisms (which are thermally activated) and, therefore, the resistive switching dynamics. To prevent the electric permanent breakdown of the device while successive cycling, a compliant current is stablished by a semiconductor parameter analyzer or by an external component such as a resistance, transistor or diode is employed.

Depending on the type of the resistive switching mechanism, RRAMs could be classified in two main groups: Electrochemical Metallization Cells (EMC), also known as CBRAM, and VCM.

In CBRAM memories the movement of metal ions and consecutive redox (reduction and oxidation) reactions is the physical mechanism responsible for the RS [Coll2019, Kozicki2016, Valov2011]. This structure is based on an oxidizable top electrode, commonly Cu, Ni or Ag, while bottom electrode is almost inert, such as Pt or W elements, with a metal oxide layer sandwiched in between. Regarding the creation of the filament, it is produced because of the oxidation of the active metal electrodes, generally Cu or Ag the migration of the corresponding cations Cu^+ or Ag^+ and the reduction at different parts of the dielectric [Goux2016]. Hence, RS in CBRAM memories is controlled due to creation and rupture of metallic filaments as depicted with an example in **Figure 1.12** [Ye2016].

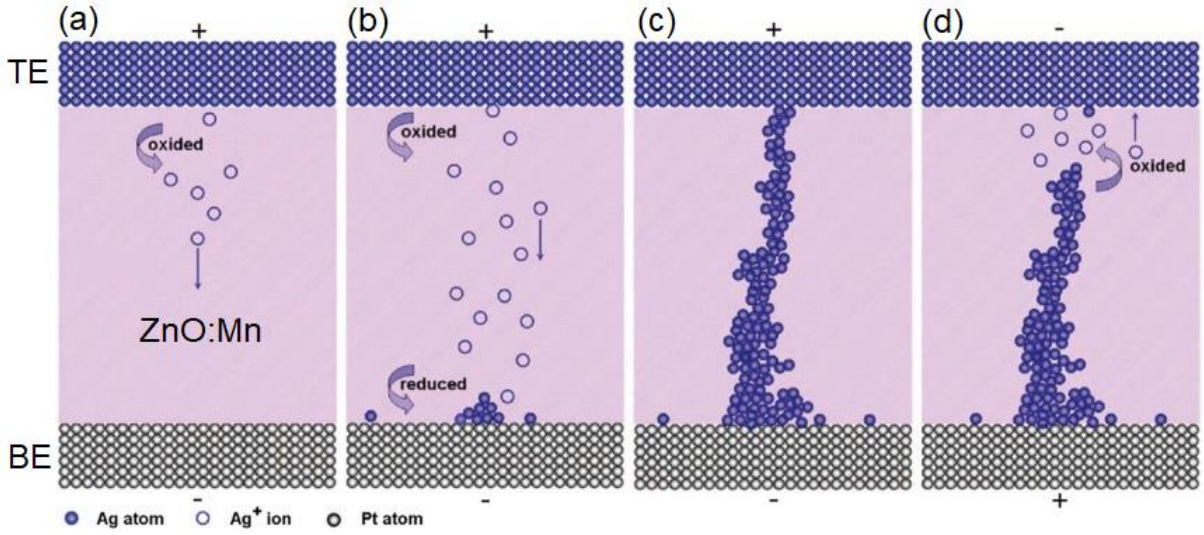

Figure 1.12. Sketch of resistive switching in ECM devices taking as example an Ag/ZnO:Mn/Pt structure. a) At the top electrode, Ag oxidize to ions (Ag → $Ag^+ + e^-$) when an electric field high enough is applied, b) Ag^+ is reduced after moving to the bottom electrode ($Ag^+ + e^-$ → Ag), c) a conductive filament is created as precipitations of Ag are deposited at the bottom electrode creating a percolation path to the top electrode and the cell reaches the LRS, d) when electric field is inverted the cell switches back to the HRS as a consequence of an electrochemical dissolution of the conductive filament which breaks the percolation path. Adapted from [Ye2016].

In case of VCM memories, the RS phenomenon involved is produced by a physical mechanism related to the generation of oxygen vacancies V_o^{2+} and consecutive movement of oxygen ions O^{2-} which produces the creation of a conductive filament from the bottom to the top electrode of the cell, see **Figure 1.13**. At the beginning, when the device is in a pristine state, this process is called forming process, **Figure 1.13a**. In this operation, if an anode forms an interfacial oxide layer created with metals, oxygen ions O^{2-} react with this or even loss their charge staying as neutral non-lattice oxygen. Thus, the electrode/oxide interface acts as the commonly called oxygen reservoir, [Chand2015]. Therefore, as oxygen vacancies V_o^{2+} agglomerate in the dielectric layer a conductive filament is created between both electrodes allowing the current to flow through it and the cell swaps from the HRS to the LRS, this is called set process, see **Figure 1.13b** and **Figure 1.13c**. On the contrary, a reset process takes place when oxygen ions O^2 return to the dielectric from the anode interface and oxidize the metallic CF or couple with oxygen vacancies V_o^{2+} which provokes the destruction of the CF and the cell switches back to the HRS [Vandelli2015] as depicted in **Figure 1.13d** and **Figure 1.13e**. In bipolar RRAMs, a positive and negative electric field is required to move oxygen ions O^{2-} in different directions.

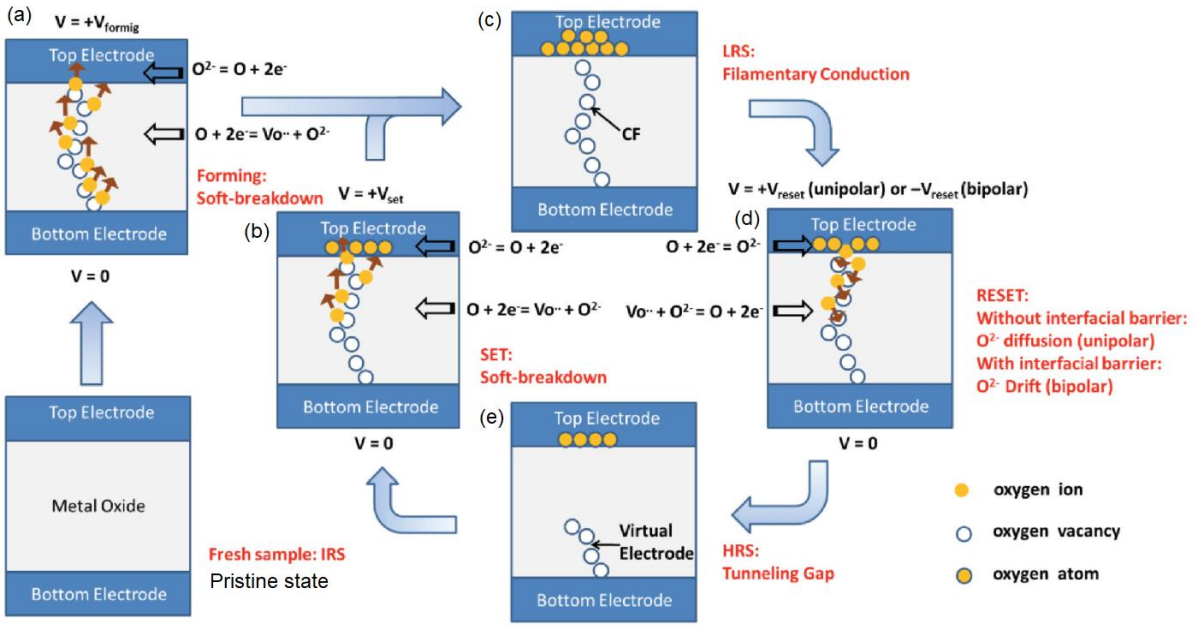

Figure 1.13. Schematic of resistive switching in VCM devices [Wong2012a].

To better describe both types of RRAM devices, in **Table 1.2** a comparison of the most representative parameters is shown. Note that the values are very similar except for the endurance, where VCM takes a huge advantage. This fact is produced because CFs of ECM devices are formed mostly by metal atoms that are easier to move and diffuse in relation to oxygen ions. Hence, a higher degradation of the components and so properties is produced in ECM devices as to VCM devices.

	RRAM type	
Parameters	ECM (CBRAM)	VCM
Operation voltage (V)	7 [Park2015]	3 [Wu2010]
Operation current (μA)	10[Woo2016]	5 [Wu2010]
Endurance (number of cycles)	10^6 [Huang2016]	10^{12} [Hsu2013]
Retention (s)	10^6 [Huang2016]	10^6 [Chiu2012]
Operation speed (ns)	1 [Goux2012]	5 [Lee2008]
On/off ratio	10^7 [Lim2016]	10^7 [Chen2017]

Table 1.2. Comparison of the typical main features in RRAM memories between ECM and VCM. The best parameters of each of the references are considered. Adapted from [Zahoor2020]

1.4.4. State of the art and challenges

Although RRAM technology presents outstanding advantages, some important hurdles need to be addressed before their massive industrial use in real-world applications. RS devices presenting two different states are being employed to build non-volatile memories, logic gates, frequency switches or stochastic computing systems. When multiple stable states are considered, these devices are being employed to hardware implementation of electronic synapses in artificial neural networks among other applications, as multiple conductance states can be maintained in the device operation [Lanza2021]. The typical figures-of-merit are endurance, retention, scalability, switching time, energy consumption and variability as shown in **Figure 1.14** diagram.

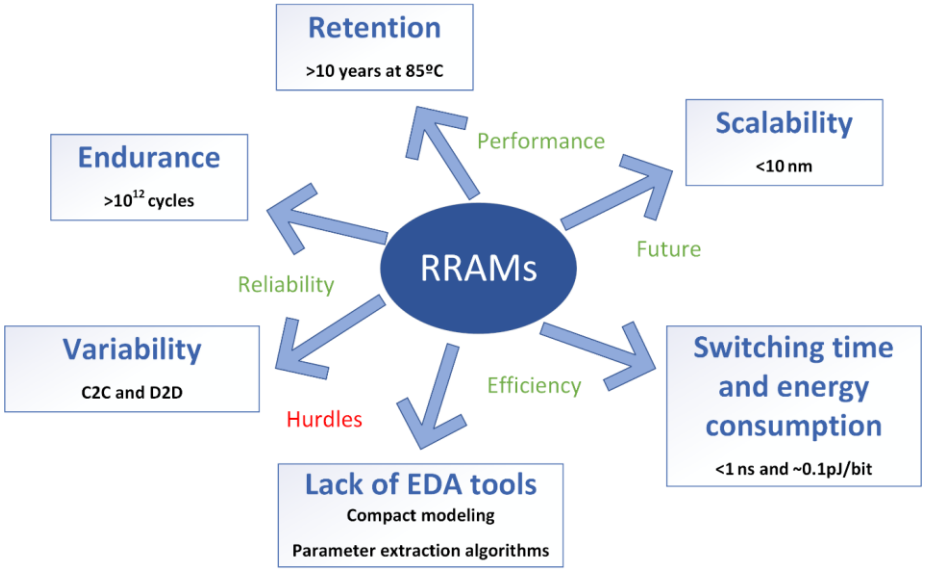

Figure 1.14. Sketch of the most important RRAM features including endurance, retention, scalability, switching time and energy consumption; and hurdles to be addressed, such as variability and the lack of EDA tools.

- **Endurance**: due to the continuous transitions in RRAM memories, from HRS to LRS and vice versa, this process produces damage in the device which implies degradation and a loss of performance. Hence, endurance measures the number of times a device is able to switch between both states granting a minimum resistance ratio amid them, this is, HRS and LRS states are still distinguishable. Endurance characteristics are obtained typically by applying a successive sequence of I-V sweeps to the device and extracting R_{HRS} and R_{LRS} at a fixed

voltage afterwards, a slow operation in most cases. The proper way of doing that is after every set/reset transition in order to have a high reliable and standard method, in addition, it is recommended to consider a large number of measured points as explained in [Lanza2021]. Measured endurances of 10^6 and 10^7 cycles are commonly achieved as reported in the literature [Yoshida2007, Wang2018] although in some cases 10^{12} cycles have been accomplished [Lee2011, Baek2004].

- **Retention**: this parameter measures the time the memory stays in a certain state after a set or reset process. Thus, the cell capacity to maintain its information could be quantified. The typical procedure to obtain this is by applying a constant voltage stress (CVS) of a low voltage (0.1 V) over the time for both HRS and LRS to measure the current versus time (I-t) curve. Note that retention in LRS is determined by the compliance current stablished while the set process takes place, for example in devices relying on CF-resistive switching as the compliance rises, the more robust and stable the conductive filament is over time. To consider a decent retention time for NVMs it should last 10 years at 85ºC [Lanza2019]. Logically, this test is not easy to carry out, so the common method to obtain retention is by applying pulses at high temperature and extrapolate the results to a 10-year period.
- **Scalability**: the RRAM area is a key parameter in this technology since it has been demonstrated the potential to hit low dimensions due to the filamentary conduction. This is not only determined by how small a useful memory could be fabricated, but also to consider the compatibility to 3D architectures. RS behavior occurs at the weakest place of the total dielectric region because of the high number of defects [Lanza2019]. As a consequence of that, it has been proved that nanoscale devices with areas under 100 nm^2 need a higher forming value in comparison to larger devices comprising areas over 25 μm^2 [Shi2017]. In addition, CFs are formed randomly on sizes and directions along the dielectric medium which provokes variations in the performance of the device.
- **Switching time and energy consumption**: to analyze these parameters, the employment of ramped voltage stress (RVS) used to perform I-V sweeps is useless, so pulsed voltage stress (PVS) with square or triangular pulses is mandatory. In this respect, energy consumption during switching transient is calculated by integrating voltage and current after each pulse which is acquired by the instrument used for the electrical characterization [Lanza2019]. Nowadays energy consumption is essential for the design and construction of portable devices such as laptops, mobile phones, or more recently, the use of electronic synapses in artificial neural networks. Typically, in RRAM devices this value ranges between 0.1 to 1 pJ/bit while in PCMs this is around 10 pJ/bit [Carboni2019]. Switching time accounts for the elapsed time in this read/write process, usually comprising the range of a nanosecond in RRAMs followed by FeRAMS (65 ns) and PCRAMs (100 ns) [Govoreanu2011, Munjal2019].
- **Variability**: this is one of the critical factors in RRAM devices [Pan2014, Lanza2019]. Set and reset voltages along HRS and LRS resistances present an important level of disparity which is not desirable. Variability can be studied when including temporal alterations (cycle-to-cycle) and spatial alterations (device-to-device) [Perez2019]. Thus, the stochastic nature of resistive switching, based on the formation and rupture of conductive filaments, is considered the main reason behind these alterations. In this sense, it is of high interest to understand

and control the form and shape of conductive filaments which is linked to the device features even on special circumstances as under the effects of an external magnetic field [Maldonado2019]. Therefore, the control and prediction of the experimental values becomes highly challenging, although some statistical techniques have been developed in order to analyse this phenomenon [Roldán2019, Roldán2021b, Acal2019]. In spite of all this, variability could also be an ally in certain occasions, leading to build true random number generators in the context of integrated circuit cryptography [Carboni2019].

- **Lack of Electronic Design Automation (EDA) tools**: it is worth to point out that there is still a lack of well-established compact models. In this respect, the latter are fundamental tools to face parameter extraction algorithms properly, another key issue not frequently tackled in these devices [Maldonado2022b]. Automatic and robust mathematical procedures are necessary to deal with high amounts of experimental data in order to process them simultaneously, a typical situation that is always necessary to carry out when studying a new device.

1.5. RRAM Simulation and Modeling

Simulation tools are one of the most important concerns in the development of any novel electron device since they are essential to understand the underlying mechanisms involved and predict its operation. In this sense, efficient and accurate models need to be addressed to establish proper working designs and normalize their utilization to provide circuit developers useful resources [Lanza2019, Panda2018]. Simulators could be classified in accord with the degree of accuracy and computational cost generally in three levels: 1) ab-initio simulation frames on the atomic scale comprising a few nm^3, 2) physically based device simulations employing finite element methods (FEM) and KMC models comprising tens of nm^3, 3) compact models comprising several μm^3 [Ielmini2017, Panda2018].

Depending on the nature of the simulation one can obtain different results [Ielmini2017, Lanza2019]:

- **Atomistic models** relying on the density functional theory (DFT) explain charge transport and the inherent phenomena which leads to resistive switching in order to understand the band structure, diffusion of ions and atoms and migration mechanisms, in addition to the energy barriers for defect generation.
- FEM models provide the typical current-voltage transfer characteristic based on differential equations to obtain the transport of charge carriers including effects such as the electric field, temperature and the concentration of defects.
- KMC **models** involve simulating the stochastic behavior of the RS operation to obtain the current-voltage transfer accounting for the possibility to describe individual defects such as the generation and recombination of oxygen vacancies and trap assisted tunneling.
- **Compact models** determine I-V characteristics by solving simplified differential equations to describe global attributes of the device such as the filament radius or the average device temperature, even in several devices at the same time.

Note that as the scale of the model decreases, the physical detail is more accurate, so it gives rise to an increase of the complexity and the computational cost. See **Figure 1.15** for a summary of the simulation tools.

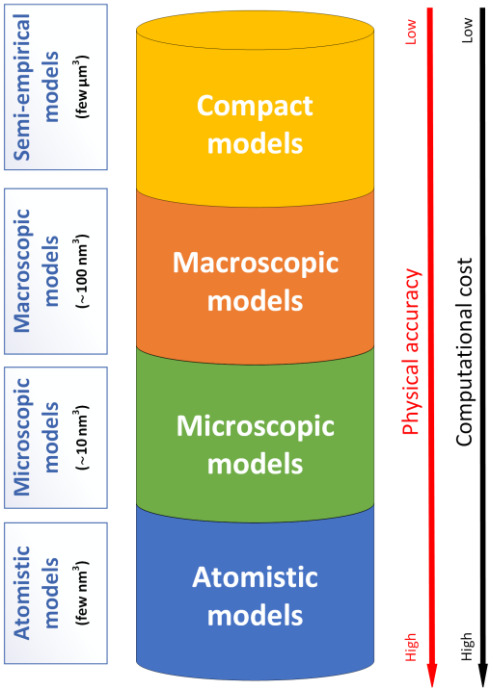

Figure 1.15. Schematic of the different simulation models employed for the characterization of RRAM devices depending on the scale. As the physical detail level increases, the corresponding computational cost is increased in concordance.

1.5.1. Atomistic simulators

Atomistic models are the most suitable for an in-depth study of the physical processes underlying in resistive switching devices such as diffusion of defect species, creation, recombination and all the effects related to charge transport mechanisms [Kamiya2012]. To properly analyse all these features, microscopic simulators must incorporate significant phenomena related with materials, defects and atoms such as structural and phase changes in the materials, generation, recombination, drift and diffusion of defects/atoms, combination of ions and thermal, electrical, or optical properties and reactions at interfaces, in addition to their combined interactions [Duncan2016]. Furthermore, other components could be added to improve the understanding in the physics involved in the inner part of the device regarding external factors like composition or materials, some of them are:

1. Defects sub-band formation.
2. Electron and ion transport models which include carrier tunnelling mechanisms.
3. Universal Landauer approach and ballistic transport.

To carry out the simulations, a KMC appliance is incorporated to explain the stochasticity of the operation in relation to the defects phenomenality and simulate its progression.

In order to reach a higher degree of efficiency and veracity, atomistic simulators could be calibrated by entering certain experimental information of chemical-physical details such as thermal and electrical conductivity, work function and crystallographic structure of the bands or the bandgap itself [Duncan2017]. To begin the simulation, ab initio or molecular models (DFT) account for the calculation of the most representative defects in the material like thermal ionization, relaxation energies and activation energies for the formation, recombination of defect species as well as their mobility within the insulator. In this way, the obtained results could be compared to experimental ones where some aspects are involved, for instance variable ramped voltage input, temperature and magnetic field switching, RTN characterization and time-dependent dielectric breakdown [Lanza2019].

Therefore, choosing the most appropriate materials depending on the applications of the device is key to tune their corresponding semi-empirical and compact models to enhance the previous design [Jung2017]. One of the advantages of this approach is that no necessary preliminary expertise of the CF shape is required and complex structures including several layers may be tested. On the other hand, one must consider that dealing with complex structures involves a very high computational cost so simulation times may take up to several days or weeks. In this sense, it is capital to know and decide which factors may be included in the simulation to achieve a trade-off between relevant results and spent time. In **Figure 1.16** an example of a simulated Cu/a-SiO_2 device is shown [Onofrio2015].

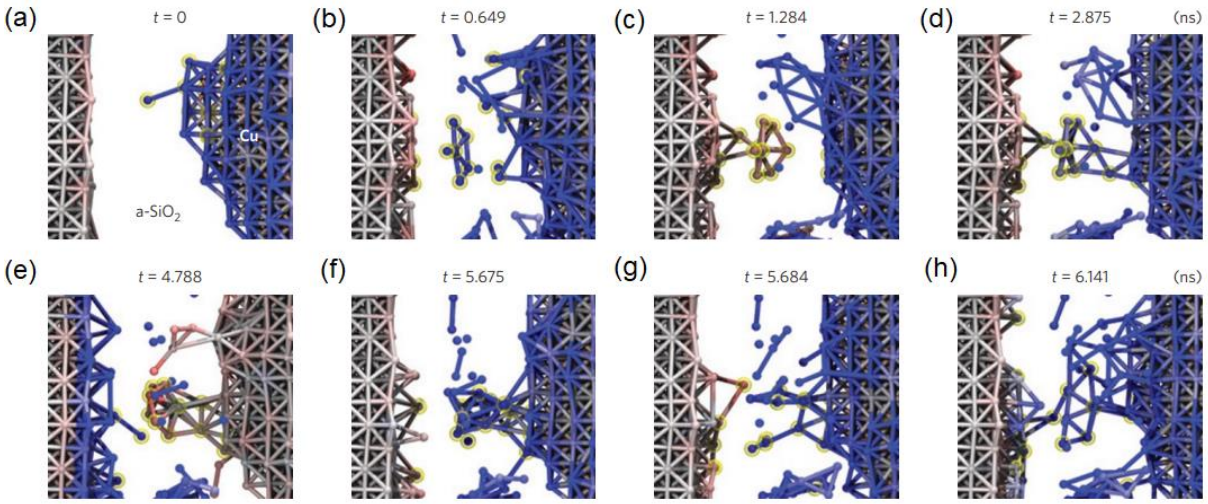

Figure 1.16. Example of a microscopic simulation of a Cu/a-SiO_2 RRAM device accounting for a (a-d) forming, (e) reset and (f-h) set processes. Note that each capture is displayed as a function of the simulation elapsed time [Onofrio2015].

1.5.2. Microscopic simulators (kinetic Monte Carlo simulators)

KMC simulators, unlike FEM simulators, base their operation on individual contributions of the ions/defects/vacancies by employing random numbers under simple rules [Aldana2020b, Aldana2017, Lanza2019, Ielmini2017]. In this manner, it is possible to consider variability and reliability of the device under study due to the generation and recombination of oxygen vacancies

which represent a decisive part during switching. Additionally, trap assisted tunneling is another important factor to be included in order to describe the main charge transport mechanism while the reset process and previous to the forming. This tool is also able to emulate current fluctuations like RTN as defects and impurities in the oxide provokes modifications in the current [González-Cordero2019, González-Cordero2019a]. In **Figure 1.17** an example of a KMC simulation of a forming process showing the microscopic distribution of ion and atoms is depicted [Aldana2017].

Note that both FEM and KMC tools present the huge advantage to solve the fundamental equations and simulate the device with a high level of detail without assuming CF sizes and shapes previously but also some hurdles need to be contemplated. One of the most important disadvantages is the lack of implementation in commercial circuit solvers such as SPICE and the corresponding Verilog-A support. This fact arises from the impossibility to solve partial differential equations (PDE) in these platforms unlike ordinary differential equations (ODE) which are tackled consistently.

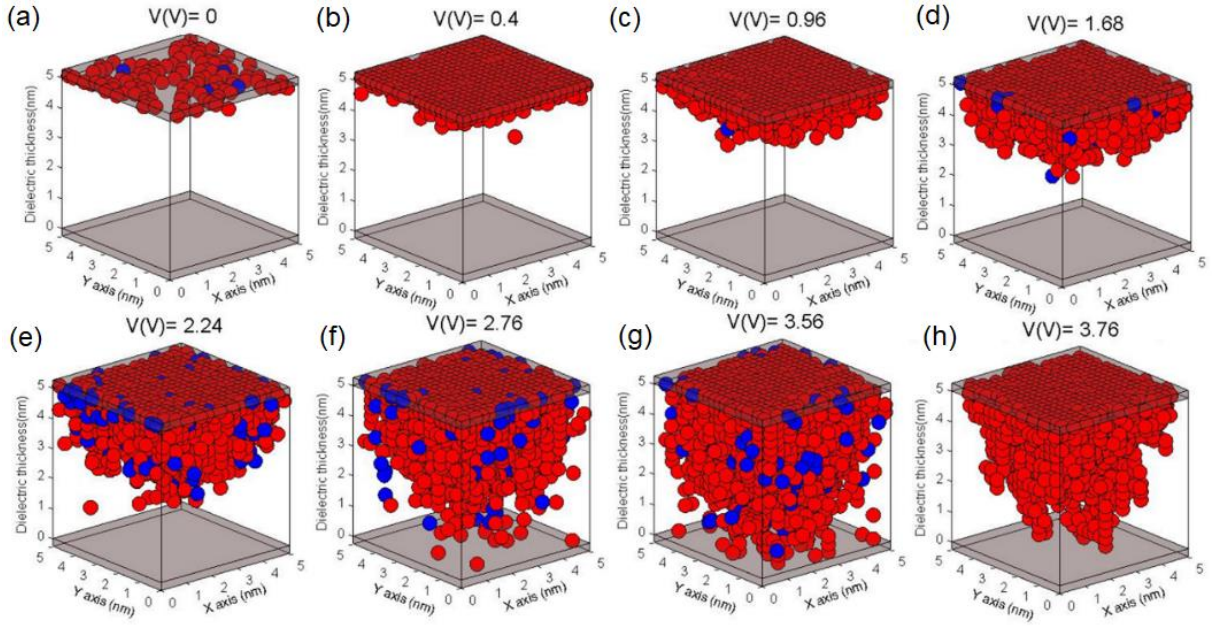

Figure 1.17. Kinetic Monte Carlo simulation of a forming process presenting different stages depending on the external applied voltage. Red balls represent Ni atoms while blue balls mean Ni cations. In h) the conductive filament is fully formed and the process concluded [Aldana2017].

1.5.3. Macroscopic simulators (finite element method)

In FEM simulators, numerical models based on heat, transport and Poisson equations are solved including boundary conditions in 2D or 3D situations where the total volume is discretized with finite elements [Lanza2019, Ielmini2015, Ielmini2017]. As is the case of RRAM devices, simulations are more complex in comparison to others such as CMOS devices where only carrier transport equations are taken into account. In this sense, ionic and thermal effects are inherent to the RS operation and must be considered for the evolution of the conductive filament [Vandelli2015, Villena2017]. Note that other components like oxygen vacancies and impurities in the layers may be included to study the modification of the CF aspect [Menzel2015, Aldana2017]. As an example of this

model, a Pt/Ta_2O_5/TaO_x/W RRAM device is simulated presenting a good accuracy with its experimental I-V characteristic as shown in **Figure 1.18** [Ielmini2017].

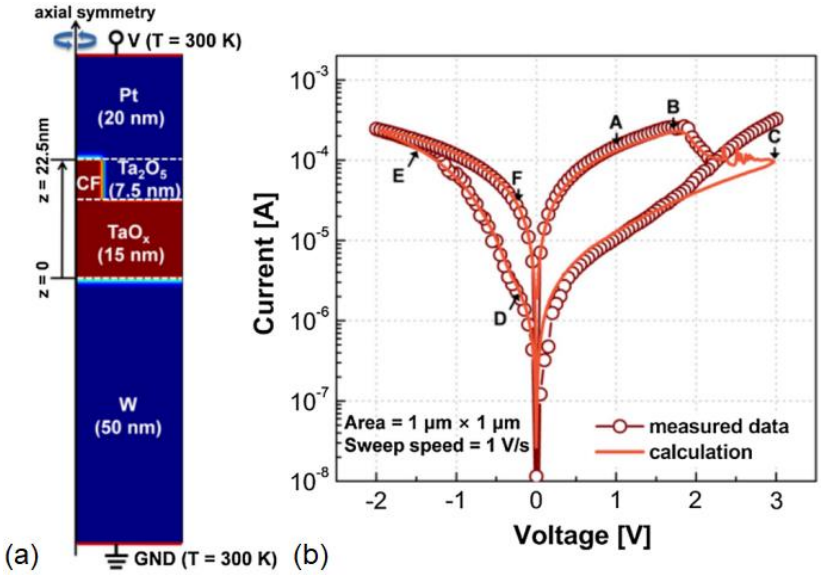

Figure 1.18. Example of a Pt/Ta_2O_5/TaO_x/W RRAM simulated device making use of a properly configured FEM model, a) cross section, b) I-V measured and simulated curve comparison [Ielmini2017].

1.5.4. Compact modeling

Compact models emerge as the need to simulate large-scale circuits and systems in SPICE-like environments established on RS devices [González-Cordero2016, Guan2012, Chen2015, Huang2013]. Thus, previous models presented in this section are not suitable for this task because the high computational cost required would suppose colossal simulation times. In this respect, the level of detail needs to be simplified to speed up the process and provide reasonable results. Typically, the solutions assumed are defining the filament shape, e.g., conical or cylindrical and assume average values along the device such as temperature, electric field or particles drift [González-Cordero2016b, González-Cordero2016c, González-Cordero2017c, González-Cordero2017d, Jiménez-Molinos2017]. The main characteristics of these models consist of integrating the most common device switching variability parameters such as set and reset voltages and resistance values corresponding with the LRS and HRS states. Thus, these analytical models are acceptable to reproduce the behavior of a circuit and grant excellent results in different routines and situations.

Sometimes, FEM and KMC approaches could be included by performing some simplifications in the differential equations destined to model ion and vacancy drift in addition to generation and recombination to account for temperature and voltage dependence of the process [Bocquet2014, Bocquet2014b, Huang2013, Kang2015]. Once properly calibrated, I-V simulations are carried out under different situations which directly rely on the chosen parameters such as Schottky/Poole-Frenkel barrier height, hopping range, number of open Landauer channels, CF resistivity thermal resistance and capacitance, among others [Lanza2019, Ielmini2017]. As an example

of a SPICE compact model simulation, in **Figure 1.19** a basic modeling scheme is presented by adapting the shape of the conductive filament obtaining different results [González-Cordero2016c].

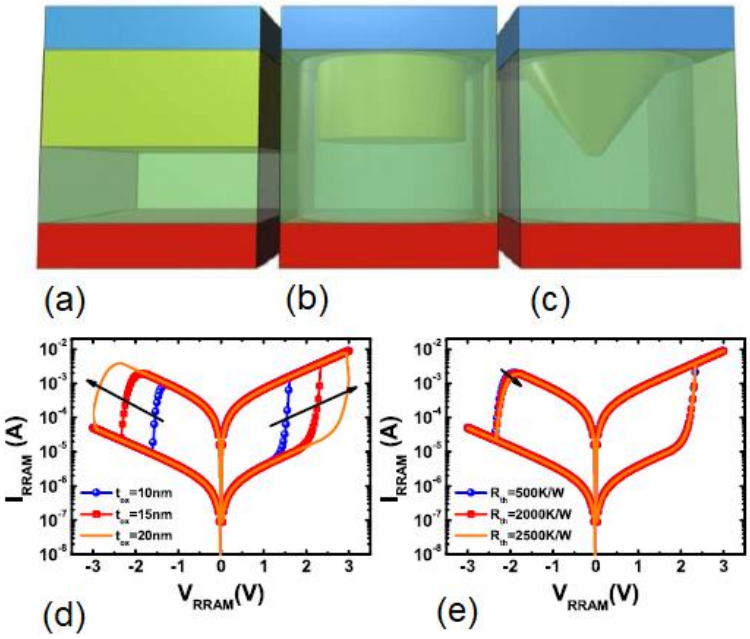

Figure 1.19. 3D representation of the geometrical aspect of a RRAM conductive filament to be modeled, a) square shaped, b) cylindrical shape, c) conical shape. Obtained I-V simulated curves considering different d) oxide thickness, e) thermal resistances [González-Cordero2016c].

Chapter 2.

2. Electrical characterization of resistive memories

2.1. Measurement of resistive memories under the effects of the magnetic field

This section focuses on the experimental characterization of RRAM devices based on TiN/Ti/HfO_2/W stacks. In particular, the role of the magnetic field (MF) has been studied in-depth in addition to traditional measurements. The main physical phenomenon involved in this situation is the inclusion of the effects of Lorentz force which have been analyzed in the RS both in the LRS and the HRS states, see **Figure 2.1**.

The effect of the MF has been proven to influence the RS parameters such as V_{set}, V_{reset}, I_{set} and I_{reset} leading to a distribution as the successive cycles are measured in a long RS series. Specifically, when the MF is enhanced, the LRS current experiments a progressive increase. This effect is also observed in the HRS current, which is also increased on average. Nevertheless, set voltages and currents are lower on average as the MF rises while reset voltages are not so influenced since cycle-to-cycle variability masks this effect. In case of reset currents a cycle-by-cycle increase for high MF values is appreciated.

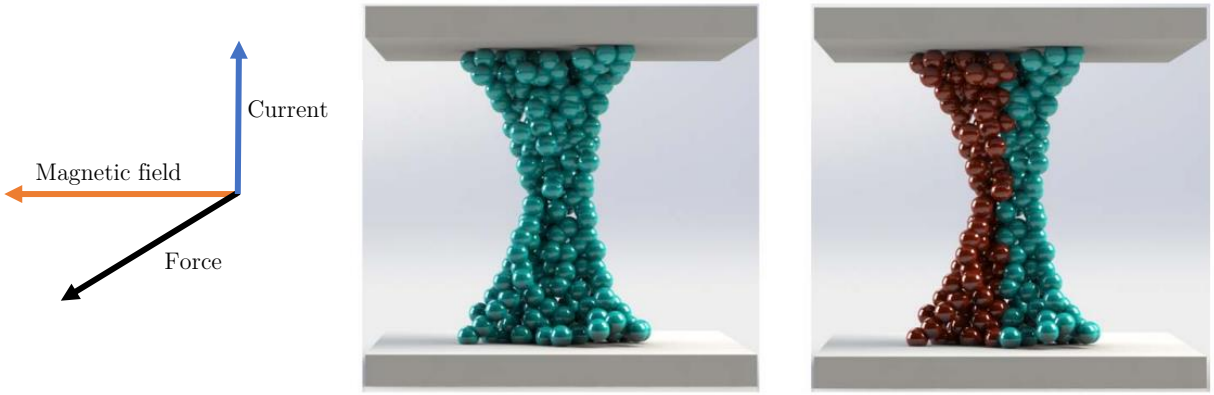

(a) (b) (c)

Figure 2.1. a) Scheme of Lorentz force produced as a result of the combination of electric and magnetic force, b) 3D CF shunting both top and bottom electrodes when no MF is applied, c) 3D CF when the action of a MF is activated resulting in a clustering of the atoms on one side [Maldonado2020b].

These measurements have been carried out in the laboratory L4 located at the second floor of the physics building of the Facultad de Ciencias de Granada, see **Figure 2.2.** More details are given in [Maldonado2017, Maldonado2019c]

The following section is an already published work [Maldonado2019].

Figure 2.2. Panoramic of the characterization system of the L4 laboratory.

D. Maldonado et al.

Microelectronic Engineering (2019)

Maldonado, D., Roldán, A. M., González, M. B., Jiménez-Molinos, F., Campabadal, F., & Roldán, J. B. (2019). Influence of magnetic field on the operation of TiN/Ti/HfO_2/W resistive memories. Microelectronic Engineering, 215, 110983. DOI: 10.1016/j.mee.2019.110983

Quality metrics

Data base	Rating	Quartile
Web of Science	Impact factor: 2.52	Q2
Scimago	Scientific journal ranking: 0.86	Q2

Publication citations (23-03-2022)

Google Scholar	Web of Science
6	**4**

Influence of magnetic field on the operation of $TiN/Ti/HfO_2/W$ resistive memories

D. Maldonado[1], A. M. Roldán[1], M. B. González[2], F. Jiménez-Molinos[1], F. Campabadal[2], J. B. Roldán[1*]

[1]*Departamento de Electrónica y Tecnología de Computadores, Universidad de Granada. Facultad de Ciencias. Avd. Fuentenueva, s/n, 18071, Granada, Spain.*

[2]*Institut de Microelectrònica de Barcelona, IMB-CNM (CSIC), Campus UAB, 08193 Bellatera, Spain.*

E-mail address of corresponding author: jroldan@ugr.es

Abstract

A characterization process for resistive RAM (RRAMs) based on $TiN/Ti/HfO_2/W$ stacks has been performed. In addition to conventional electrical measurements, the effects of the magnetic field (MF) have also been considered. The influence of the Lorenz force on resistive switching (RS) processes and on the device conduction was explored both in the Low Resistance State (LRS) and in the High Resistance State (HRS). The MF influences the set/reset voltages and current distributions, spreading the range of current values obtained in a long RS series of successive set and reset cycles and modifying set voltage values. For the reset voltage, the influence is less significant than the cycle-to-cycle variability.

Keywords: Magnetic field effects; RRAM; Resistive switching; Set voltage; Reset voltage.

1. Introduction

Resistive random access memories (RRAM) devices have shown great possibilities for applications related to non-volatile memories, neuromorphic circuits and physical unclonable functions implementation [1-8]. RRAM new designs consume much less power than traditional non-volatile NAND flash memories. In addition, read and writing speeds are higher and their technology is CMOS compatible. The scaling possibilities as well as the potential for building 3D structures based on crossbar architectures are also of great interest [1-4]. Nevertheless, the full-scale industrial use of this technology has faced several hurdles such as variability, lack of simulation and modeling tools, etc. In this respect, different facets of resistive switching (RS) physics have not been explained yet completely; therefore, there are outstanding research efforts going on [1, 3-10]. In this context, new characterization techniques are needed. Moreover, although in the last few years different results in relation to RRAM physical simulations and modeling have been published [1, 6-7, 11-17], greater efforts should be put to develop accurate and easy-to-use physical simulation tools and reliable compact models for circuit simulation.

In this manuscript we show the main results of RRAM characterization employing different magnetic fields (MFs). The use of MFs presents an advantage from the characterization viewpoint since it adds a new control variable. We have performed conventional electrical RS measurements [7, 18] while the devices are under the effects of a controlled MF perpendicular to the charge conduction direction. Different reports related to characterization including MF effects have been presented previously [19-24]. In general, these studies [21-23] show a shift of the transition voltages (set and reset voltages) towards higher absolute values. These works are based on devices made of different materials, among them only one has been performed on RRAMs with HfO_2 as dielectric [19], although this oxide shows promising RS performance both for non-volatile memories [3] and for mimicking biological synapsis in the context of neuromorphic circuits [25]. We have focused our study on HfO_2 devices; in particular, we studied the conduction levels as well as the set and reset voltages and currents (extracted as reported in Ref. [17]) for different MFs both in the HRS and LRS.

Some of the studies devoted to analyze MF effects used high MFs (several thousands Oe). However, in our case we chose lower MFs; this is a more representative situation, closer to real cases of multifunctional devices whose operation would be modulated by different physical variables (electric field, magnetic field or light intensity [23]), as it is the case of some sensor devices.

In Section 2 of this paper, the device and measurement process are described. Section 3 is devoted to explain and discuss the main results and, finally, the main conclusions are drawn in Section 4.

2. Device fabrication and measurement

The field-oxide isolated $TiN/Ti/HfO_2/W$ devices were fabricated on an N-type ($\rho = 4$ $m\Omega \cdot cm$) silicon wafer. First, a Ti adherence layer (20nm-thick) was deposited on the silicon substrate, and subsequently, a 50 nm-thick W film was deposited. The 10 nm-thick HfO_2 layer was grown by ALD at 225 °C using TDMAH and H_2O as precursors and N_2 as carrier and purge gas. The top metal electrode consists of a 200 nm-thick TiN and 10nm-thick Ti scavenging layer. The electrical contact to the bottom

* Corresponding author. Tel.:+ *34 958244071;*
E-mail address: jroldan@ugr.es (J.B. Roldán)

electrode is made through the aluminum-metallized back of the silicon wafer. The resulting TiN/Ti/HfO_2/W structures are square-shaped with an area of 15×15 μm^2.

The current-voltage (I-V) measurements were performed by means of a semiconductor parameter analyzer. The voltage was applied to the TiN/Ti top electrode, while the bottom electrode was grounded. A forming process was needed prior to the long RS series measurement with a current compliance of 0.1 mA. These series were programed with a Matlab software tool that controls the instrumentation via GPIB. The voltage ramp employed was 0.15 V/s and the voltage step was 0.02 V.

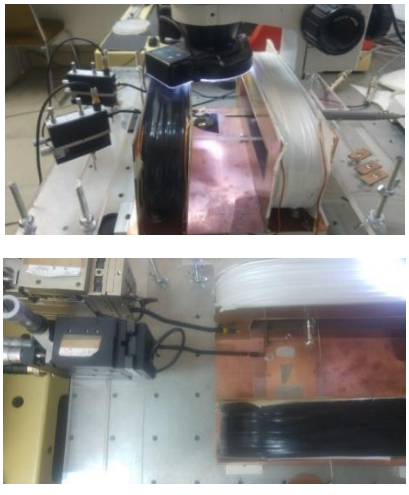

Figure 1. Measurement set-up. (a) Side view, the wafer is placed between Helmholtz coils that produce a nearly uniform magnetic field. (b) Top view, the MF created is perpendicular to the charge current direction.

The MF was generated by two Helmholtz coils (Figure 1), which are driven by a programmable current source. Sequences of 50 RS cycles were carried out at the same MF. Between the sequences of 50 RS cycles with a given MF value, 50 RS cycles were measured without an applied MF in order to allow comparison. In Figure 2 we show the magnetic field values applied during the whole experiment. By considering RS cycles for null magnetic field between every two different MF values, a representative comparison of the results can be performed.

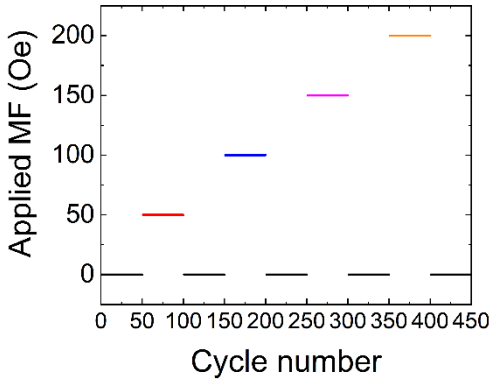

Figure 2: Applied magnetic field sequence for the 450 set/reset cycles measured during the experiment. The MF is increased in 50 Oe steps (from 0 Oe to 200 Oe) and between each MF value considered, 50 RS cycles were measured without MF.

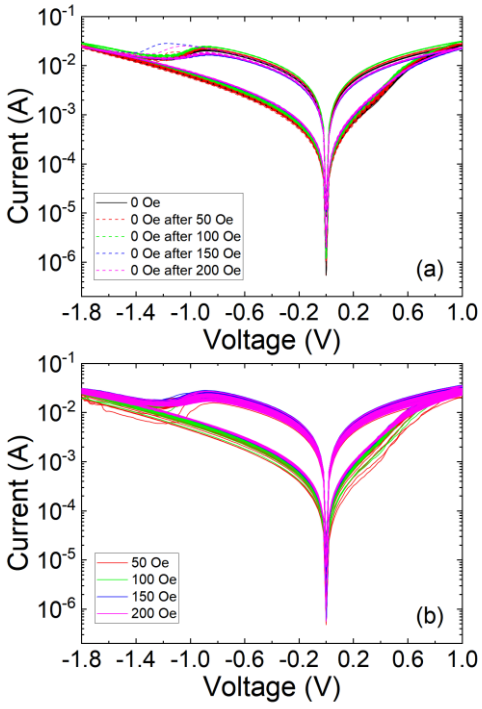

Figure 3: Experimental I-V curves for 450 set/reset cycles. The MF is increased in 50 Oe steps (from 0 Oe to 200 Oe) and between each MF value considered, 50

RS cycles are measured without MF. Figure 2a shows the 250 curves measured without MF (after applying a MF value shown in the legend), while Figure 2b shows the 200 curves obtained when applying a specific MF value.

3. Results and discussion

Figure 3 shows the measured I-V curves. Curves obtained at 0 Oe after applying a specific MF are shown in Figure 3a, while those obtained under different MFs have been plotted in Figure 3b. As can be seen, the MF spreads out the distribution of I-V curves. In order to check if there is any underlying trend, Figure 4 shows the current versus cycle number at different applied voltages.

Figures 4a and 4c show that the MF influences the HRS device resistance: a slight current increase is observed as the MF rises; therefore, the MF effects seem to affect the CF morphology during switching. Notice that the first cycle after MF removal is strongly affected by the previous MF value applied. However, the subsequent cycle-to-cycle variability measured at 0 Oe is again low, pointing out the influence of the MF during RS operation.

In Figure 4b a wider range of current values at HRS is obtained in comparison to Fig. 4c. This situation is different because the voltage considered here is close to the set voltage. At this operation point the CFs are almost formed and the conduction is ohmic.

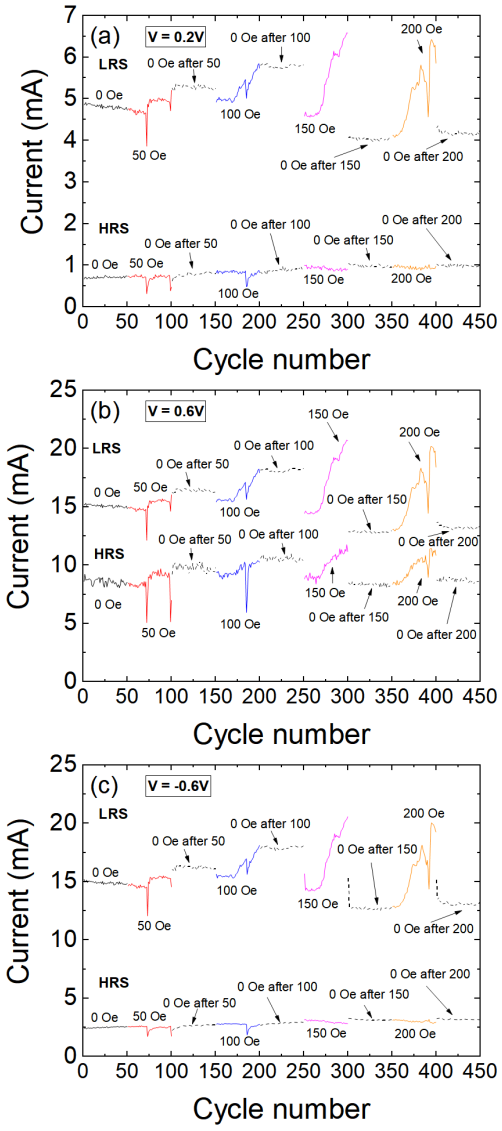

Figure 4: Experimental HRS and LRS currents measured at different applied voltages: a) 0.2 V, b) 0.6V, c) -0.6V versus cycle number for the whole experiment (curves Figs. 3a and 3b).

The results show that the MF affects the stochasticity of the RS process as indicated by the increase in set voltage variability. Regarding the LRS, the MF effects are significant, especially for values above 100 Oe. These effects seem to be cumulative, increasing the current cycle-by-cycle mean while the MF is applied (with some points out of this general trend). However, this effect is not maintained after removing the MF, where the current levels during switching are stable. In addition, it

should be noticed that only for the lowest MF values the current remains at the same level after switching off the MF, indicating that MF strongly influences CF morphology and stoichiometry.

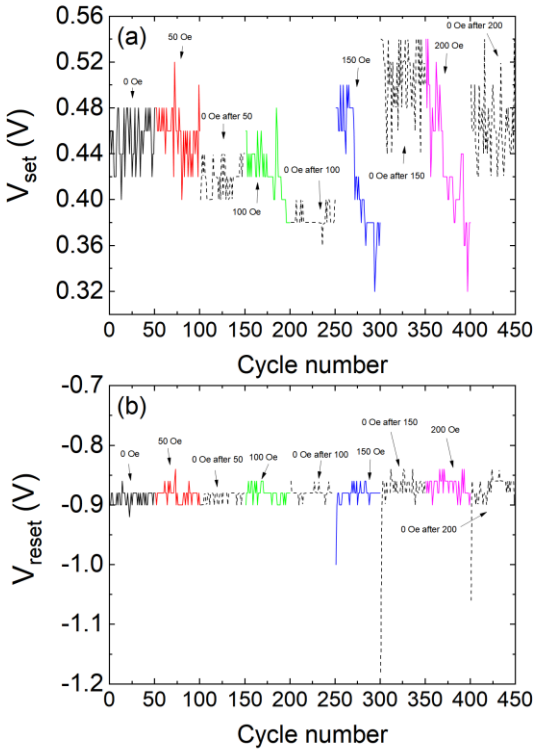

Figure 5: Experimental set (a) and reset (b) voltages obtained for each measured cycle for the whole RS series.

Once the MF effect on the current has been shown, we focus on the MF influence on the set/reset currents and voltages. Previous studies performed for much higher MFs (few thousands Oe) have revealed an increase of the reset and set voltage absolute values with the magnetic field increase [21, 23]. These results were obtained for different dielectrics (none of which was HfO_2). Our measurements show different trends (Figure 5 and Figure 6). The set voltage (Figure 5a) and set current (Figure 6a) decreasing trend on the average values is observed when they are plotted cycle-by-cycle under MF effects. Regarding the reset voltage, MF effects are not significant. Nevertheless, it is remarkable that the first cycle of the RS series for zero MF after the application of 150 Oe and 200 Oe shows an important increase in its absolute value, indicating the influence of the previous applied MF on the filamentary morphology and switching stability. Figure 6b shows the corresponding reset currents during cycling. A clear MF influence on the current levels is obtained for 150 and 200 Oe.

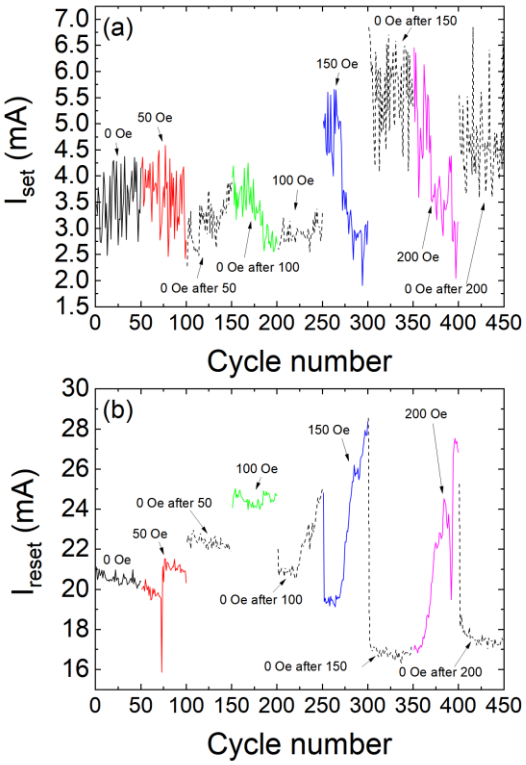

Figure 6: Experimental set (a) and reset (b) currents obtained for each measured cycle in the whole RS series.

Finally, Figure 7 shows the cumulative distribution functions of set/reset voltages and currents. Apart from the general trends commented above, a clear spreading in the measured values is observed under the MF influence in comparison with the corresponding values obtained without applying a MF. Notice that the average value for the 0 Oe curves is clearly affected by the morphological changes due to the previous MF applied.

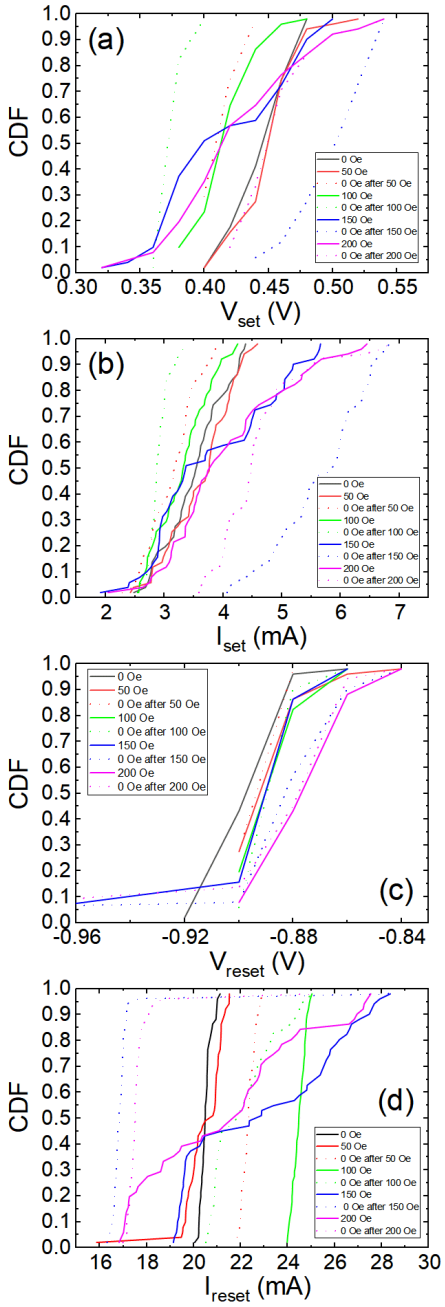

Figure 7: Cumulative distribution functions for the measured V_{set}, V_{reset}, I_{set} and I_{reset}, parameters with and without applied MF.

4. Conclusions

The influence of the magnetic field (from 0 to 200 Oe) on the operation TiN/Ti/HfO_2/W resistive memories has been investigated. The results show that MF enhances the LRS current level in a cumulative manner in a successive RS cycle series. The HRS current is also increased on average under MF effects. The set and reset voltages and currents have been also analyzed under MF influence. A decrease in the average value of the set voltages and set current with the cycle number is observed for high magnetic field values. However, the cycle-to-cycle variability of the reset voltages is larger than the influence of the MF in the range assessed, although the corresponding reset currents shows a cycle-by-cycle increase for the higher MF values assessed.

Acknowledgements

The authors thank the support of the Spanish Ministry of Science and Universities and the FEDER program through projects TEC2017-84321-C4-1-R, TEC2017-84321-C4-3-R. This work has made use of the Spanish ICTS Network MICRONANOFABS.

References

[1] F. Pan, S. Gao, C. Chen, C. Song, F. Zeng, "Recent progress in resistive random access memories: Materials, switching mechanisms, and performance", Mat. Science and Eng., 83, pp. 1-59, 2014.

[2] S. Yu, "Neuro-inspired computing using resistive synaptic devices", Springer, 2017.

[3] M. Lanza et al., "Recommended methods to study resistive switching devices", Advan. Elec. Materials, 1800143, 2018.

[4] F.M. Puglisi, L. Larcher, A. Padovani, P. Pavan, "Anomalous random telegraph noise and temporary phenomena in resistive random access memory", Solid-State Electronics, 125, pp. 204-213, 2016.

[5] S. Long, C. Cagli, D. Ielmini, M. Liu, J. Suñé, "Reset statistics ofNiO-based resistive switching memories" IEEE Electron Device Lett.,vol. 32, pp. 1570–1572, Nov. 2011.

[6] L. Larcher, A. Padovani, O. Pirrotta, L. Vandelli, and G. Bersuker, "Microscopic understanding and modeling of HfO2 RRAM device physics," in Proc. IEEE Int. Electron Devices Meeting, pp. 20.1.1–20.1.4, 2012.

[7] D. Ielmini, R. Waser. "Resistive Switching: From Fundamentals of Nanoionic Redox Processes to Memristive Device Applications", Wiley-VCH, 2015.

[8] M.A. Villena, J.B. Roldán, F. Jiménez-Molinos, E. Miranda, J. Suñé, M. Lanza, "*SIM²RRAM*: A physical model for RRAM devices simulation", Journal of Computational Electronics, 16, pp. 1095-1120, 2017.

[9] S. Menzel, P. Kaupmann, R. Waser, “Understanding filamentary growth in electrochemical metallization memory cells using kinetic Monte Carlo simulations”, Nanoscale, 7, 12673, 2015.

[10] R. Degraeve, A. Fantini, N. Raghavan, L. Goux, S. Clima, B. Govoreanu, A. Belmonte, D. Linten, M. Jurczak, “Causes and consequences of the stochastic aspect of filamentary RRAM”, Microelectronic Eng., 147, pp. 171-175, 2015.

[11] G. González-Cordero, F. Jiménez-Molinos, J.B. Roldán, M.B. González, F. Campabadal, “In-depth study of the physics behind resistive switching in TiN/Ti/HfO2/W structures”, J. Vac. Sci. Technol. B 35, 01A110, 2017.

[12] P. Huang, X. Y. Liu, B. Chen, H.T. Li, Y. J. Wang, Y.X. Deng, K.L. Wei, L. Zeng, B. Gao, G. Du, X. Zhang, J.F. Kang, "A Physics-Based Compact Model of Metal-Oxide-Based RRAM DC and AC Operations," Electron Devices, IEEE Transactions on, vol.60, no.12, pp. 4090-4097, 2013.

[13] G. González-Cordero, M.B. González, H. García, F. Campabadal, S. Dueñas, H. Castán, F. Jiménez-Molinos, J.B. Roldán, “A physically based model for resistive memories including a detailed temperature and variability description”, Microelectronic Engineering, Vol. 178, pp. 26-29, 2017.

[14] M. Bocquet, D. Deleruyelle, H. Aziza, C. Muller, J. Portal, T. Cabout, E. Jalaguier, “Robust compact model for bipolar oxide-based resistive switching memories”, IEEE Transactions on Electron Devices, 61, pp. 674-681, 2014.

[15] G. González-Cordero, J. B. Roldán, F. Jiménez-Molinos, J. Suñé, S. Long, M. Liu, “A new compact model for bipolar RRAMs based on truncated cone conductive filaments, a Verilog-A approach”, Semicond. Sci. Technol., vol. 31, no. 11, pp. 1–13, 2016.

[16] F. Jiménez-Molinos, M.A. Villena, J.B. Roldán, A.M. Roldán, “A Spice Compact Model For Unipolar RRAM Reset Process Analysis”, IEEE Trans. Elec. Dev., vol 62, pp. 955-962, 2015.

[17] M.A. Villena, J.B. Roldán, F. Jiménez-Molinos, J. Suñé, S. Long, E. Miranda, M. Liu, "A comprehensive analysis on progressive reset transitions in RRAMs", Journal of Physics D: applied physics, 7, 205102, 2014.

[18] S. Poblador, M.B. Gonzalez, F. Campabadal, Investigation of the multilevel capability of TiN/Ti/HfO2/W resistive switching devices by sweep and pulse programming, Microelectron. Eng. 187–188 (2018) 148–153. doi:10.1016/j.mee.2017.11.007.

[19] J. Guo, X. Kang, Y. Gao, W. Chen, X. Zhao, “Enhanced magnetic modulation in HfO_2-based resistive memory with an Hf top electrode”, Appl. Phys. Letters, 113, 043502, 2018.

[20] G. Chen, C. Song, C. Chen, S. Gao, F. Zeng, F. Pan, “Resistive Switching and Magnetic Modulation in Cobalt- Doped ZnO”, Adv. Mater., 24, 3515–3520, 2012.

[21] D.P. Sahu, S.N. Jammalamadaka, “Remote control of resistive switching in TiO2 based resistive random access memory device”, Scientific Reports, 7, 17224, 335103, 2017.

[22] J. Wang et al., “Magnetic field controllable nonvolatile resistive switching effect in silicon device”, Appl. Phys. Let., 104, 243511, 2014.

[23] B. Sun, Y. Liu, W. Zhao, P. Chen, “Magnetic-field and white-light controlled resistive switching behaviors in Ag/[BiFeO3/g-Fe2O3]/FTO device”, RSC Advances, 5, 13513, 2015.

[24] S. Das, S. Majumdar, S. Giri, “Magnetic Field, Temperature, and Time Controlled Manipulation of Switching Mechanism in NiO Film: Evidence of Large Magnetoconductance”, J. Phys. Chem., 114, 6671–6675, 2010.

[25] M. Pedro, J. Martin-Martinez, R. Rodriguez, M.B González, F. Campabadal, M. Nafría, “A flexible characterization methodology of RRAM: Application to the modeling of the conductivity changes as synaptic weight updates”, Solid-State Electronics, 2019.

2.2. Statistical procedures to analyze resistive switching

In this section we have studied different types of measurements performed in several MIS devices in order to obtain the energy that is linked to the reset process. Particularly, instead of working on the usual current versus voltage domain, charge and flux have been calculated to study this special operation domain. Thereby, diverse numerical mechanisms such as Phase type Distributions (PHD) along Weibull distributions (WD) and Erlang distributions (ED) have been employed as theoretical tools to reproduce the experimental variability of the energy needed to complete a single reset process for the devices under consideration.

In particular, PHD is a probability distribution based on a convolution of exponential distributions that outcomes from an entity of one or several inter-related Poisson processes while ED is the distribution of sum of k independent exponential variables with mean $\frac{1}{\lambda}$ each. Likewise, it is the distribution of the time before the k_{th} case of a Poisson process with a ratio of λ. If k=1, this is reduced to the exponential distribution. On the other hand, WD is commonly used in the dielectric breakdown situations to study the hazard and failure rate of the devices, which is linked to a number of other probability distributions. It is a distribution that describes properties of system that fail because the rupture of the weakest-link.

Nonetheless, it is probed that WD and ED fail to reproduce the variability of the data whereas PHD makes that feasible as intermediary cases of degradation on a reset process which may be defined and related to probabilistic states (k) that evolve as the resistive switching process goes on.

The following section is an already published work [Maldonado2019b].

D. Maldonado et al.

Insulating Films on Semiconductors (2019)

D. Maldonado, C. Acal, M.B. González, J.E. Ruiz-Castro, A.M. Aguilera, R. Picos, F. Jiménez-Molinos, F. Campabadal, J.B. Roldán. An in-depth statistical study of resistive switching energies in unipolar RRAMs. 21th Conference on "Insulating Films on Semiconductors", Cambridge (UK), 2019.

International conference

An in-depth statistical study of resistive switching energies in unipolar RRAMs

D. Maldonado[1], C. Acal[2], M.B. González[3], J.E. Ruiz-Castro[2], A.M. Aguilera[2], R. Picos[4], F. Jiménez-Molinos[1], F. Campabadal[3], J.B. Roldán[1]

[1]*Departamento de Electrónica y Tecnología de Computadores. Universidad de Granada (Spain)*

[2]*Departamento de Estadística e Investigación Operativa. Universidad de Granada (Spain)*

[3]*Institut de Microelectrònica de Barcelona, IMB-CNM (CSIC), Campus UAB, 08193 Bellaterra (Spain)*
[4]*Departamento Física, Universitat de les Illes Balears (Spain)*
E-mail address of corresponding author: jroldan@ugr.es

1. Introduction

Resistive Random Access Memories (RRAMs) have shown an outstanding potential for storage class non-volatile memory applications [1]. Some of the advantages of RRAMs over FLASH devices, the current technology in massive non-volatile circuits, are a lower read latency, faster write performance and lower power consumption. RRAMs are also gaining momentum as memristive artificial synaptic interconnections, the key components in hardware neural networks and other neuromorphic circuits. The potential of these devices is fostering research in all the fronts, from materials to compact modeling and simulation [1].

In this work we have characterized the energy linked to reset processes in different types of unipolar metal-insulator-semiconductor devices [2]. We have chosen an approach followed by L. Chua [3]; instead of using an I-V domain, we work in a charge (Q) and flux (ϕ) domain [3], being these variables defined as follows,

$$Q(t) = \int_0^t i(t')\,dt' \qquad \phi(t) = \int_0^t v(t')\,dt'$$

Finally, we also calculate the energy needed in a reset process, given by:

$$E(t) = \int_0^t i(t')v(t')\,dt'$$

We have applied different numerical procedures to extract the statistical features of the experimental E_{reset} (energy consumed till a reset event takes place), for the different devices considered. To do so, we made use of a previously developed technique based on Phase type Distributions (PHD), whose theoretical development took place at the end of 20th century [4]. We will show that neither the Weibull distribution (WD), widely employed in the context of dielectric breakdown studies, nor the Erlang distribution (ED), that come up in previous RRAM analysis [4], fulfill the needed requirements to reproduce the experimental data variability. This new PHD analysis allows the characterization of possible intermediate states of degradation along a reset process. These states are linked to the different probabilistic states (k)

that can be extracted from the sample of E_{reset} data.

2. Device fabrication and measurement

The Ni/HfO_2/Si-n^+ devices with dielectric thicknesses of 10nm and 20nm and Cu/HfO_2(20nm)/Si-n^+ devices have been fabricated. The fabrication details are given in [2]. The device stacks schemes are shown in Fig. 1. Long series of I-V curves under negative voltage ramps have been measured by means of an HP-4155B semiconductor parameter analyzer controlled using Matlab via GPIB. The Si substrate was grounded.

3. Results and discussion

Typical I-V curves for the three technologies are shown in Fig. 2 for both set and reset processes. The corresponding Q versus ϕ curves are plotted in Fig 3a. At the reset point, the charge, flux and energy obtained are named as Q_{reset}, ϕ_{reset} and E_{reset}. The Q_{reset} versus ϕ_{reset} experimental distributions are shown in Fig 3. In Fig. 4, the E_{reset} versus ϕ_{reset} distributions are also given. The cumulative distribution functions (CDF) for the voltage, charge and energy at the reset point are shown in Fig. 5. It can be seen that we get approximately the same E_{reset} CDFs for the different technologies. This fact suggests that they are thermally activated since the energy consumed till the reset event shows a similar statistical pattern and that the physical mechanisms behind the reset are similar.

We have investigated this issue by applying different voltage ramp rates in the resistive switching cycles of the Ni 20nm-based technology. It can be seen that the differences in terms of E_{reset} CDFs are not significant in the studied ramp rate range.

Finally, PHDs have been employed to fit the E_{reset} distributions (Fig. 6). The WD and ED failed to reproduce the data. A canonical PHD (cPHD) works better, although with different number of intermediate states for each stack. The cPHD presents a forward movement between the intermediate states till the reset point is reached, with transitions characterized by the different probabilities between the states. This means that the transitions between the k intermediate states go from the first to the final state in a forward manner, there are no backward transitions.

4. Acknowledgements

The authors thank the support of the Spanish Ministry of Science and Universities and the FEDER program through projects TEC2017-84321-C4-1-R, TEC2017-84321-C4-3-R, MTM2017-88708-P, TEC2014-54906-JIN. This work has made use of the Spanish ICTS Network MICRONANOFABS.

References

[1] M. Lanza et al., Advanced Elec. Mat. (2018), 1800143
[2] M. Gonzalez et al., IEEE Trans. Dev. Mat. Rel. 14 (2014), 769–771
[3] L. Chua, Applied Physics A 102 (2011), 765–783
[4] C. Acal et al., J. of Comp. App. Math. 345 (2018), 23

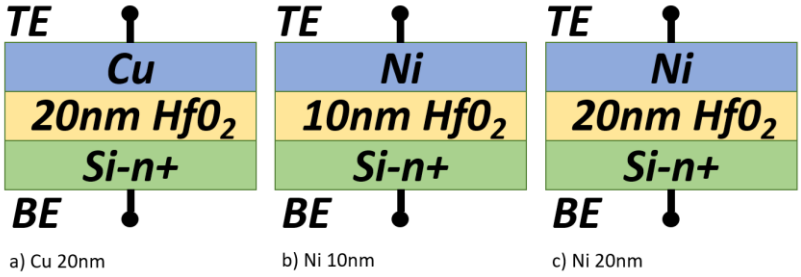

Fig. 1. Schematic of the unipolar RRAMs considered in this study. For the sake of brevity we name them using the top electrode metal and the thickness of the dielectric.

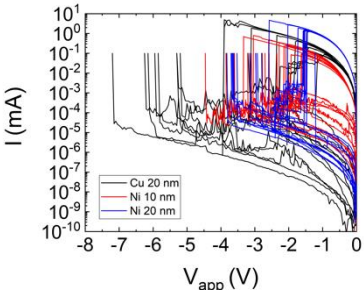

Fig. 2. Set and reset experimental I-V curves for the three devices considered and measured under unipolar regime. For the set process a current compliance of 100μA was employed.

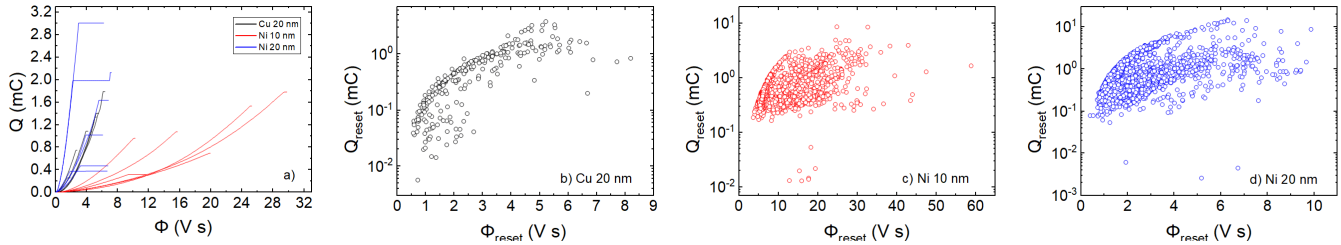

Fig. 3. Charge versus flux data for the three technologies considered (a). Extracted charge and flux data at the reset point for the devices with Cu electrode (b), Ni electrode and a 10nm thick oxide (c), and Ni electrode and a 20nm thick. oxide (d).

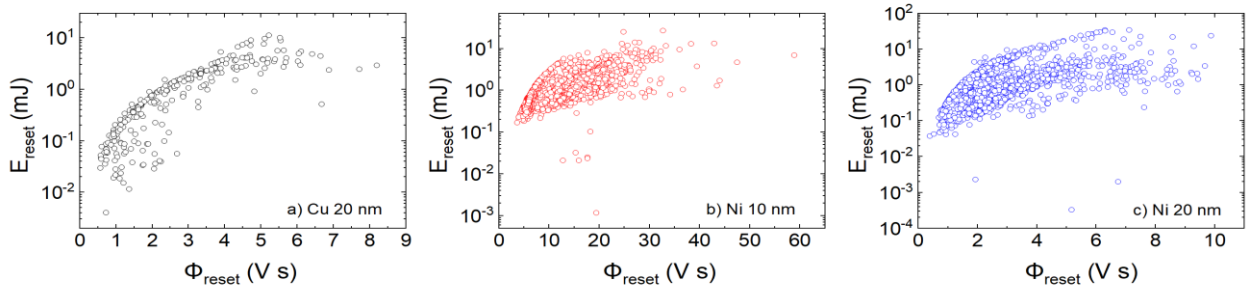

Fig. 4. Energy versus flux experimental data at the reset point for the devices with Cu electrode (a), Ni electrode and a 10nm thick oxide (b), and Ni electrode and a 20nm thick oxide (c).

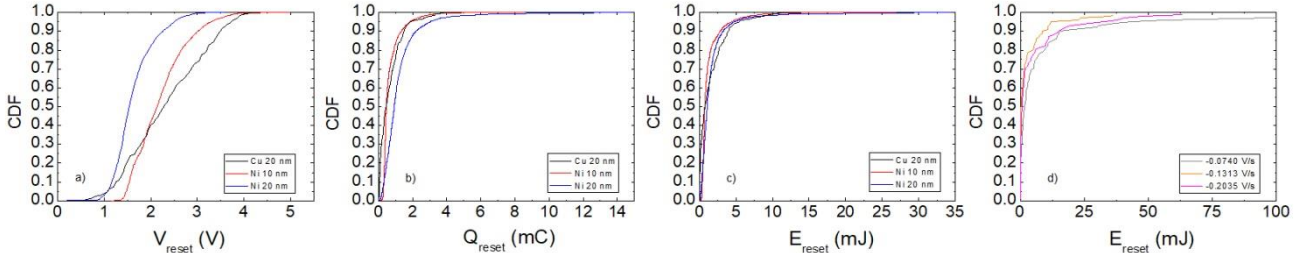

Fig. 5. For the technologies under study, Cumulative Distribution Functions (CDF), of V_{reset} (a) Q_{reset} (b), and E_{reset} (c). For the Ni 20nm devices, CDF for E_{reset} measured for three different voltage ramps (d).

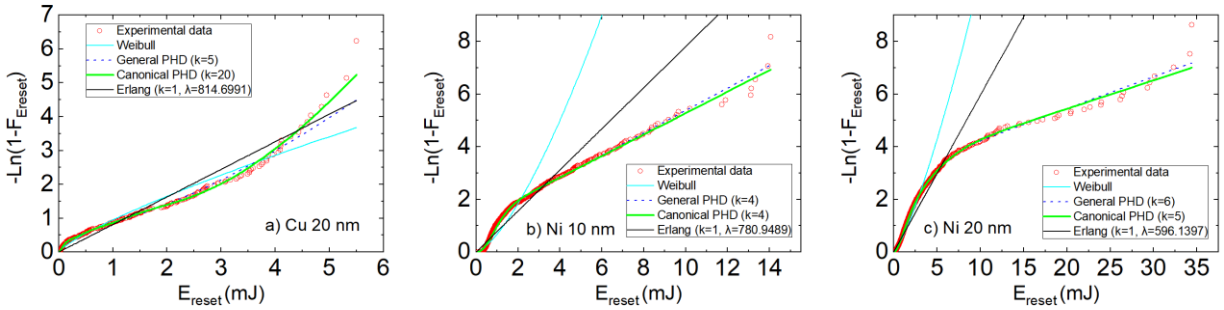

Fig. 6. Cumulative hazard rate calculated as $-\ln(1-F_{Ereset})$ versus energy at the reset point. Different distribution functions have been employed to fit the experimental data (shown in symbols). The WD is shown in light blue, it is seen that it is far from being a good fit, neither the Erlang distribution (used in [4]) worked out. PHDs were employed to improve the fitting. The PHD was the better fit in all cases, although using different number of probabilistic states (phases, whose number is described by k) for each stack.

Chapter 3.

3. Time series analysis for the study of variability in resistive memories

3.1. Introduction and application of the technique

Time series are a series of data listed in the time order they happened, commonly plotted in a temporal line chart. This is widely used in fields like statistics, weather forecasting, communications engineering or any situation related to temporal evaluations. Time series analysis evaluates the data in the series by means of different methods to take out the statistics. Different models can be implemented making use of this theory in order to predict future values of the series depending on previous observed ones.

Time series statistical analyses (TSSA) have been utilized in this chapter to assess and model the variability of RRAMs. In particular, set and reset voltages in a long RS series of different measured devices such as Ni/HfO_2/Si-n^+, Cu/HfO_2/Si-n^+ and Au/Ti/TiO_2/SiO_x/Si-n^+ have been obtained with the aim of forecasting future values as previous ones are established. Thus, several analytical models for this purpose are calculated. The autocorrelation (ACF) and partial autocorrelation (PACF) functions are obtained to develop the models and also to calculate the "inertia or memory" between the cycles, as they are mathematical tools for finding repeating statistical patterns.

The following section is an already published work [Roldán2019].

J. Roldán et al.

Journal of Applied Physics

(2019)

Roldán, J. B., Alonso, F. J., Aguilera, A. M., Maldonado, D., & Lanza, M. (2019). Time series statistical analysis: A powerful tool to evaluate the variability of resistive switching memories. Journal of Applied Physics, 125(17), 174504. DOI: 10.1063/1.5079409

Quality metrics

Data base	Rating	Quartile
Web of Science	Impact factor: 2.55	Q2
Scimago	Scientific journal ranking: 0.7	Q2

Publication citations (23-03-2022)

Google Scholar	Web of Science
24	**19**

Time series statistical analysis: a powerful tool to evaluate the variability of resistive switching memories

J.B. Roldán[1*], F. J. Alonso[2], A. M. Aguilera[2], D. Maldonado[1], M. Lanza[3]

[1]*Departamento de Electrónica y Tecnología de Computadores. Universidad de Granada. Facultad de Ciencias. Avd. Fuentenueva s/n, 18071 GRANADA, Spain.*

**Corresponding author Email: jroldan@ugr.es*

[2]*Departamento de Estadística e Investigación Operativa. Universidad de Granada. Facultad de Ciencias. Avd. Fuentenueva s/n, 18071 GRANADA, Spain.*

[3]*Institute of Functional Nano and Soft Materials (FUNSOM), Collaborative Innovation Center of Suzhou Nanoscience & Technology, Soochow University, 199 Ren-Ai Road, Suzhou, 215123, China.*

Abstract

Time series statistical analyses (TSSA) have been employed to evaluate the variability of resistive switching memories, and to model the set and reset voltages for modeling purposes. The conventional procedures behind time series theory have been used to obtain autocorrelation and partial autocorrelation functions and determine the simplest analytical models to forecast the set and reset voltages in long series of resistive switching processes. To do so, and for the sake of generality in our study, a wide range of devices have been fabricated and measured. Different oxides and electrodes have been employed, including bilayer dielectrics in devices such as: Ni/HfO_2/Si-n^+, Cu/HfO_2/Si-n^+ and Au/Ti/TiO_2/SiO_x/Si-n^+. The TSSA models obtained allowed to forecast the reset and set voltages in a series if previous values were known. The study of autocorrelation data between different cycles in the series allows estimating the inertia between cycles in long resistive switching series.

Overall, TSSA seems to be a very promising method to evaluate the intrinsic variability of resistive switching memories.

Index Terms—Resistive switching memory, RRAM, Conductive filaments, Variability, Time series modelling, Autocovariance, Stationary time series.

1 - INTRODUCTION

Resistive random access memories (RRAM) have shown an outstanding potential for information storage, especially for internet of things (IoT) and related applications, due to their excellent scalability, low power operation, fast switching speed, easy fabrication and good compatibility with the well-established complementary metal-oxide-semiconductor (CMOS) technology [1, 2, 3, 4, 5, 6, 7]. The most promising RRAM unit cells consist of matrixes of two-terminal metal/insulator/metal (MIM) nanocells, in which the electrical resistance of the insulating film can be switched between a high resistive state (HRS) and a low resistive state (LRS) depending on the electrical impulses applied between the two metallic electrodes. However, after more than one decade of intense research, RRAM devices still have not been mass produced by the industry, nor entered in the market of non-volatile memories (NVM), mainly due to variability problems [1, 2, 5, 8, 9, 10]. In RRAM devices the resistive switching (RS) is related to the formation and rupture of defect-rich conductive filaments (CFs) within the dielectric layer, which leads to a HRS-to-LRS (set) and a LRS-to-HRS (reset) transition (respectively). Set and reset transitions are related to diffusion, redox and nucleation of different chemical species within the MIM nanocells [1, 2, 5, 7, 10], which take place with a very high degree of randomness from one cycle to another, leading to an intrinsic high variability. Consequently, the electrical characteristics measured in a RRAM device reflects the stochasticity of these physical processes, and produces the so-called cycle-to-cycle variability.

In the past few years, the variability of RRAM devices has been statistically analysed in most cases using the Weibull distribution (WD) [1, 11, 12]. The WD comes out in the field of reliability physics [13] and its use makes sense for RRAMs under filamentary conduction since it is a weakest-link type distribution, i.e. the failure of the whole is dominated by the degradation rate for the weakest element. However, this method does not describe all the inherent statistical particularities of RRAM devices: and although it has been previously employed to deepen on the experimental data characteristic obtained for different technologies [1, 11, 12], it does not entirely capture the essence of the RS process. In fact, classical reliability analyses with the Weibull distribution assume that times to failure, in our case set voltage (V_{SET}) and/or reset voltage (V_{RESET}), are independent within a RS series. This assumption may not be valid in the case of stochastic processes associated with RRAMs because successive observations could be highly dependent (in fact, a CF is formed making use of broken parts of previous ones). It is worth highlighting that other mathematical approaches have been proposed to tackle different facets of the statistical study of variability in RRAMs and, in a more general scope, thin dielectrics. Among them, the use of a clustering statistical approach complementing the use of the WD [14] can be counted; in line with this, convolution-based modelling is also interesting being noticed [15]. Strategies making use of completely different distribution functions have also been reported; for example, the employment of phase-type distribution functions for certain devices led to interesting results [16]. Markov models have also been employed in the analysis of these devices [17, 18]. Kinetic Monte Carlo (KMC) and related simulations can also be considered as statistical tools to analyse RRAM variability, as they allow modifying very specific physical parameters of the devices (i.e. concentration of atomic

vacancies/dopants, insulator thickness fluctuations) within a reasonable range and analyse the deviation of the electrical characteristics. A broad number of contributions have been presented in this respect [10, 19-25]. The only drawback of KMC simulations is the longer computational time, which obligates researchers to make assumptions that simplify the calculations, leading in some cases to a loss of accuracy.

It is clear that variability is still an unresolved problem in RRAM devices both from the technological and the modelling viewpoint, and developing new analytical methods to shed light into this problem is highly necessary. Times series statistical analyses (TSSA) are powerful numerical methods that have been successfully applied for decades in the fields of economics and sociology, and more recently they have been also sporadically used in the field of engineering and reliability of electronic devices [26-27]. TSSA may be useful to analyse the variability of RRAM devices because: i) the data (V_{SET} and V_{RESET}) are collected in a continuous manner over the time (cycle-to-cycle) for a long RS series [28-29]; ii) TSSA is appropriate for physical processes that exhibit any kind of inertia in some of their particular features [30, 31]. In this respect, in RS cycling, the CF is formed (set process) making use of the remnants of the CFs ruptured in the previous cycle (reset process). Therefore, from a statistical point of view it is relevant to analyse any numerical relations between neighbouring cycles and assess the system "memory" in a long RS series (to put it in formal words, the parameters that characterize consecutive cycles in a RS series can be correlated and, therefore, the term autocorrelation comes up naturally). And iii) under certain mathematical conditions (i.e. time series stationarity, an assumption that our data distributions fulfil) a comprehensive analysis can be performed through a time series analysis approach [30, 31]. However, despite this strong parallelism, to the best of our knowledge, TSSA have never been employed to evaluate the variability of RRAM devices. In this work we present the first variability study of three different types of RRAM devices using the TSSA, and observe that in all cases essential RS parameters, such as V_{SET} and V_{RESET}, can be reasonably forecasted making use of mathematical models and the information of these parameters in previous cycles. In addition, in long RS series the dependence of forthcoming cycles on previous ones can be correctly studied by means of correlation and autocorrelation analyses, characterizing in this manner the inertia of RS operation in RRAMs for different technologies.

The manuscript is organized as follows: in Section II the new model is described in depth, in Section III the fabricated devices and measurement process details are given, in Section IV the new statistical analysis is explained, and in Section V the main results and discussion are presented. Finally, the main conclusions are drawn in Section VI.

2 – MODEL DESCRIPTION

Back in 1927, G.U. Yule introduced modern TSSA formulating a model for a pendulum dynamic movement time dependency [32]. After rearrangements in the corresponding equation describing the pendulum movement he came out with a second order autoregressive time series model where the pendulum displacement (z_t) from the equilibrium position was regressed on the two previous observations (z_{t-1}) and (z_{t-2}) —the physics governing the pendulum is linked to a second order differential equation—. In our study, we model the values of V_{SET} and V_{RESET}

of different RRAM devices over long series of RS cycles by considering the values of previous cycles using TSSA [30, 31, 33]. One of the main difficulties is to find the order of the model, i.e. how many V_{SET} or V_{RESET} values from previous cycles we need to forecast the current cycle (for a general model previous cycles are usually considered, see Equation 1). In addition, it is also necessary to find the weights ($\Phi_1 \ldots \Phi_p$) of the autoregressive model we are seeking (see Equation 1).

$$V_{reset_t} = \Phi_1 V_{reset_{t-1}} + \Phi_2 V_{reset_{t-2}} + \cdots + \Phi_p V_{reset_{t-p}} + \varepsilon_t \quad \text{(Eq. 1)}$$

The order of the model (p) depends on the physics governing RS, but we will not assume any knowledge of it and we will only make use of the information within the experimental data because the underlying physics and the technological details of the fabrication process are "hidden" in the RS data collected. Therefore, the models obtained with this approach are empirical and the TSSA output will consist of the order of the model (p) and the weights set ($\Phi_1, \ldots, \Phi_p$). Sometimes a model such as the one described in Equation 1 works better for the centred variables; e.g., $V_{RESET} - \mu$, where μ stands for V_{RESET} mean in the RS series (this formulation is equivalent to include a constant term Φ_0 in the model). The term ε_t, as usually employed in time series studies, stands for a residual that accounts for the model error (the difference between the measured value and the modelled value). This term is obtained in TSSA theory by generating random numbers with a normal distribution whose variance corresponds to the one calculated from the measured data. Nevertheless, for the sake of simplicity, this term will not be included in the models developed here, following the conventional notation in the engineering context. In this approach, the algebraic equations are employed in the form usually seen in compact modelling, i.e., the current value of reset or set voltages are given as a function of variables already known, such as reset and set voltages of previous cycles. The existence of a difference between the measured and modelled values is assumed. Equation 1 shows what is called an autoregressive (AR) model [30]; however, not always such an easy model can be obtained. Occasionally more complex models are needed; if this is the case, an autoregressive moving average (ARMA) model that includes AR and moving average (MA) parts are considered [30]. MA models are a linear combination of past residuals [30-32]. The general expression of an ARMA model is described in the Supplementary Information (see Equation A1).

We have employed TSSA to study and model the data obtained from RRAMs made of different materials. Three types of devices were considered, two of them including HfO_2 as the dielectric, sandwiched by different electrode materials (Ni and Cu), and another one based on a bilayer (TiO_2/SiO_X) insulating stack.

3 – DEVICE FABRICATION AND MEASUREMENT

The HfO_2-based RRAM devices consisted of $Ni/HfO_2/Si\text{-}n^+$ and $Cu/HfO_2/Si\text{-}n^+$ (20nm thick dielectric layers were used) stacks [28]. The active area of the MIM cells was 5 μm×5 μm, and the devices were patterned by photolithography. A HP-4155B semiconductor parameter analyser was used in the measurement process, which consisted of collecting long sequences (series) of current vs. voltage (I-V) curves by applying ramped voltage stress (RVS). The $Si\text{-}n^+$ substrate (bottom) electrode was grounded and a negative voltage

was applied to the Ni (0.3V/s ramps) or Cu (0.5V/s ramps) (top) electrode, although for simplicity we have assumed the absolute value of the applied voltage henceforth [28]. The RS phenomenon observed for both type of devices was unipolar, as displayed by the I-V curves (see Figures 1a, 1b) [5].

A RS series of 2800 cycles was obtained for the Ni/HfO_2/Si-n^+ RRAMs, and a series of 280 cycles for the Cu/HfO_2/Si-n^+ RRAMs. The values of V_{SET} and V_{RESET} were extracted from the I-V curves as reported in [1, 28, 34], and plotted in Figures 1b-1f. The variability of V_{SET} and V_{RESET} from one cycle to another can be clearly observed.

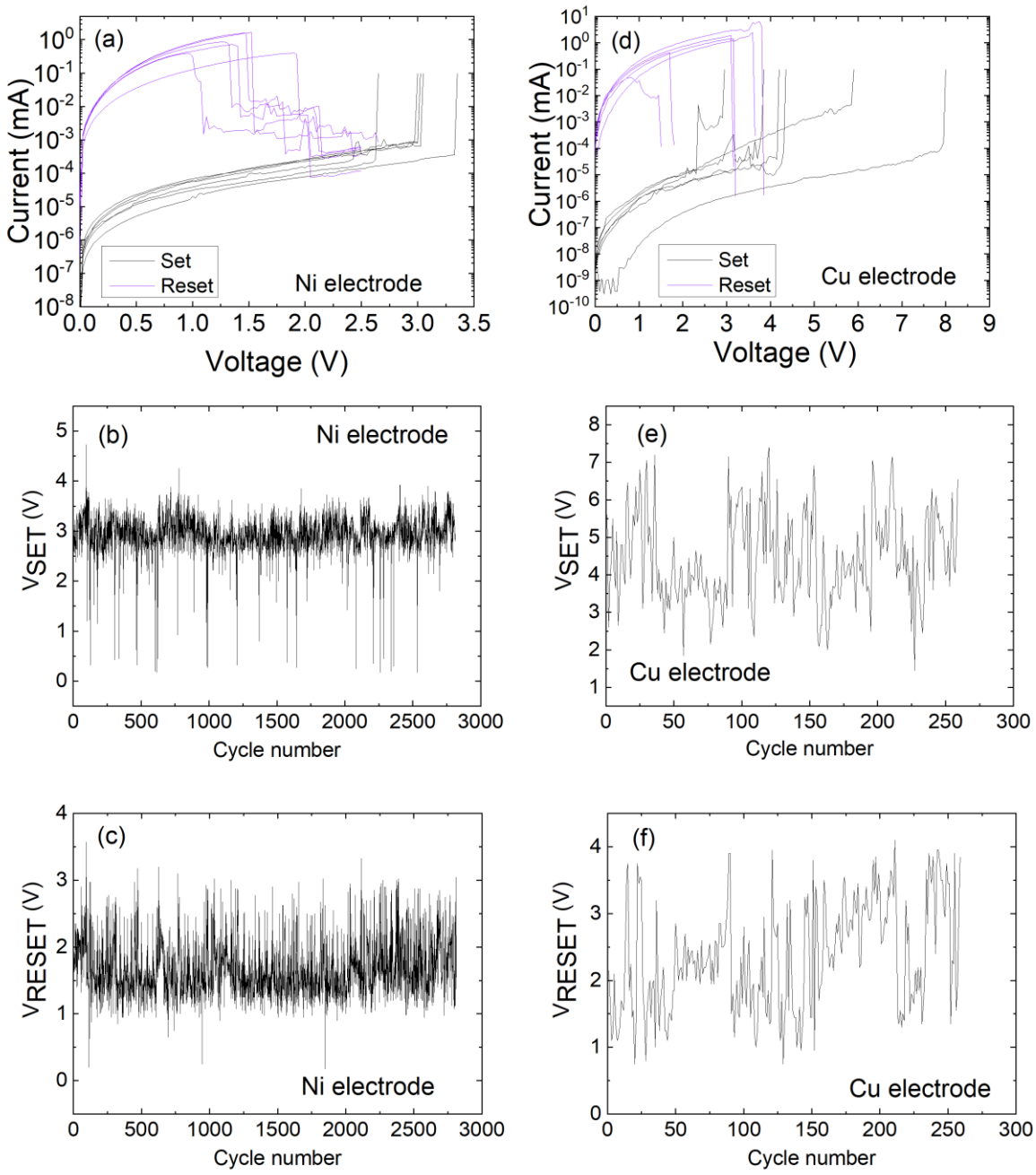

Figure 1. Typical I-V curves observed in (a) Ni/HfO_2/Si-n^+ and (d) Cu/HfO_2/Si-n^+ RRAMs. Experimental values of

V_{SET} (b, e) and V_{RESET} (c, f) versus cycle number for a series of continuous RS cycles under RVS for RRAMs based on Ni/HfO_2/Si-n^+ and Cu/HfO_2/Si-n^+ stacks.

The third type of RRAM devices was fabricated using an Au/Ti/TiO_2/SiO_X/Si-n^+ structure. A 2nm TiO_2 film was grown by atomic layer deposition (ALD), on Si-n^+ wafer with a ~1.5 nm thick native SiO_X layer. The device area was 5 µm x 5 µm and the thicknesses of other layers were Au (60nm) and Ti (20nm). The Ti interfacial top electrode was employed as a gathering layer for oxygen accumulation. More details about the fabrication process of these structures are given in Ref. [29]. 0.5V/s ramps were employed for the series measured in this case.

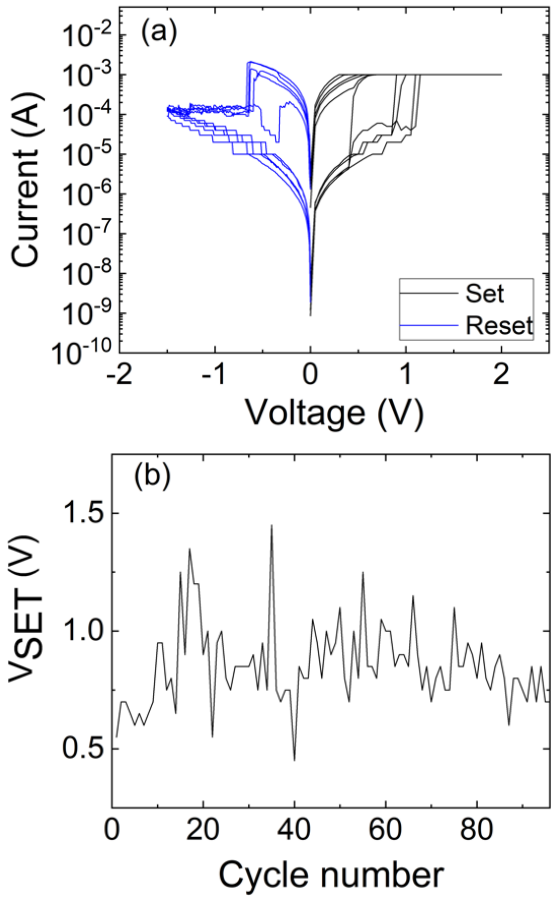

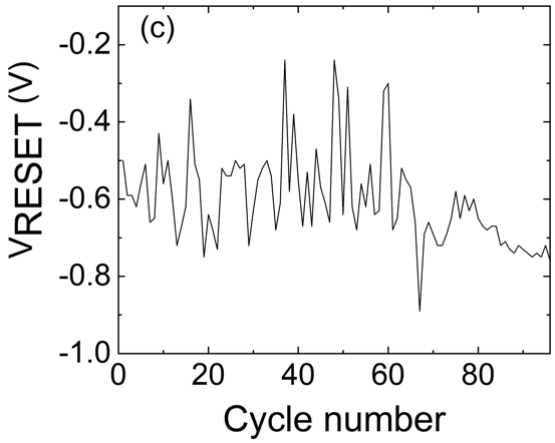

Figure 2. (a) Typical I-V curves observed in Au/Ti/TiO_2/SiO_X/Si-n^+ RRAMs. Experimental values of V_{SET} (b) and V_{RESET} (c) versus cycle number for a series of continuous resistive switching cycles under RVS.

Some of the I-V curves for the Au/Ti/TiO_2/SiO_X/Si-n^+ devices are plotted in Figure 2, which shows clear bipolar RS behaviour, and the extracted values of the set and reset voltages for a RS series of 100 cycles. As it can be seen, the different type of RS (bipolar) compared to Figure 1 (unipolar) also leads to different patterns in the V_{SET} and V_{RESET} plots. For the devices based on HfO_2 dielectrics the set (reset) voltage were determined by detecting a 70% current increase (decrease) with respect to the previous current point. For the devices with the TiO_2 dielectric the current maximum was selected to determine the reset voltage and the maximum change in the derivative was the choice for the determination of the set voltage. More details on these methods are given in Ref. [34].

4 – NEW STATISTICAL METHODOLOGY

We have employed TSSA to analyze the experimental V_{SET} and V_{RESET} plotted in Figure

1 and Figure 2 for the technologies under consideration. A detailed description of this statistical methodology is given in the Supplementary Information. This new statistical approach for RRAM variability modeling was implemented with the packages TSA and forecast in R language [35].

The first step of our methodology is to prove that our data constitute a stationary series [30, 31, 33]. This implies that the mean and variance are constant in time (RS cycle). Figure 1 indicates that the values are distributed around the mean value and no pattern in the data fluctuation can be found. This fact suggests that both the data mean and variance are constant all along the series, i.e. for all the cycle intervals considered —a numerical check of these issues has been also performed—. Therefore, according to the explanation given in the Supplementary Information, all the data series under consideration for the devices Ni/HfO_2/Si-n^+ and Cu/HfO_2/Si-n^+ are stationary. For the Au/Ti/TiO_2/SiO_x/Si-n^+ devices we obtain similar results in what is related to the stationarity of the series, i.e. the data are distributed around the mean value and no data fluctuation patterns are seen.

The second step is to select the most parsimonious ARMA model to forecast the voltage to reset/set in one cycle in terms of the voltages to reset/set in previous cycles. A parsimonious model is the simplest model (algebraically speaking) that can be used to correctly model a certain phenomenon [31].

4.1 – Modeling V_{SET}

For the V_{SET} distributions considered in this investigation, the mean values are $\hat{\mu}_{VSET}$=2.934 V (Ni/HfO_2/Si-n^+ devices) and $\hat{\mu}_{VSET}$=4.433 V (Cu/HfO_2/Si-n^+ devices). The autocorrelation functions (ACFs) and partial autocorrelation functions (PACFs) of the data samples are shown in Figure 3. The ACF is a function of the number of cycles k and measures the influence/connection between V_{SET}/ V_{RESET} separated by k cycles (k distant lags). On the other hand, the PACF measures the same correlation but eliminating the dependency due to the intermediated lags (1, 2, ..., k-1). That is, in the PACF the dependencies of each two cycles are evaluated making sure that statistical crossed dependencies by means of cycles in between are eliminated. A simple example to illustrate this concept can be built with a 3 elements series. For this series, the calculation of PACF between the first and third elements would need the elimination of the dependencies provided by the second on the first and the second on the third elements; in this way, the direct dependencies of the first on the third could be calculated.

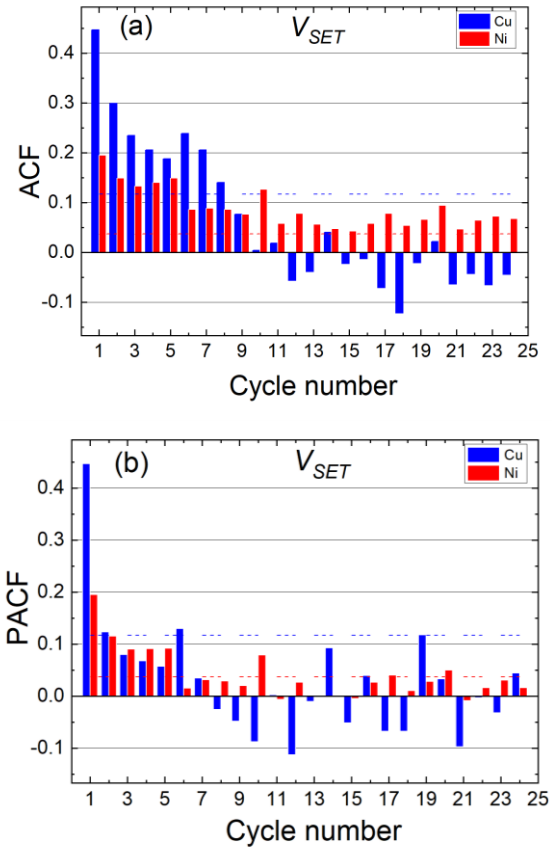

Figure 3. (a) ACF and (b) PACF versus cycle lag (distance apart in cycles within a RS series; for a cycle lag 1 the ACF and PACF of consecutive cycles are measured and so on) for the V_{SET} series described in Figure 1, corresponding to Ni/HfO_2/Si-n^+ and Cu/HfO_2/Si-n^+ devices. The ACF and PACF minimum threshold bounds for the Cu/HfO_2/Si-n^+ and Ni/HfO_2/Si-n^+ devices are 0.117 and 0.037 respectively, shown with dashed lines.

As Figure 3a shows, the ACF for Cu/HfO_2/Si-n^+ devices is higher than for Ni/HfO_2/Si-n^+ devices for the first two lag cycles (see that the blue columns are higher). In fact, we have just one component, the corresponding to the previous cycle, that dominates over the rest. These values have to be compared with the threshold bounds (Equation A10 in the Supplementary Information for ACF, which depends on the number of cycles of the series). In the PACF plot shown in Figure 3b (see also Equation A9 in the Supplementary Information), only the first value is above the threshold bound. Consequently, following the procedure to select the simplest model depicted in the Supplementary Information (Model identification section), an AR (1) model is proposed for the Cu/HfO_2/Si-n^+ devices (ACF decreases and PACF has only one significant value). This can be translated to Equation 2, that reflects that the V_{SET} model of a current cycle just depends on the value of the previous cycle:

$$V_{SET_t}(V) = 2.4263 + 0.4527V_{SET_{t-1}}. \quad \text{(Eq. 2)}$$

The numbers included in Equation 2 can be obtained as described in the Supplementary Information (Parameter estimation section). In this case and henceforth, as explained in the introduction, we will not include the residual for the current cycle (ε_t), as usually done in a mathematician context. For Ni/HfO_2/Si-n^+ devices, the ACF and PACF have several values outside the corresponding thresholds (the minimum threshold bounds for the Cu/HfO_2/Si-n^+ and Ni/HfO_2/Si-n^+ devices are 0.117 and 0.037 respectively) and both functions decrease. The model selection procedure suggests an ARMA (1,1) model. Thus, V_{SET} for the Ni/HfO_2/Si-n^+ RRAMs can be described by means of Equation 3:

$$V_{SET_t}(V) = 0.2380 + 0.9189V_{SET_{t-1}} + 0.8049\varepsilon_{t-1}. \quad \text{(Eq. 3)}$$

As it can be seen, the structure of the autocorrelation relations between cycles for the set voltage series lead to a more complex model for the Ni/HfO_2/Si-n^+ devices. Finally, the residuals (i.e. the difference between the measured and modeled values for each cycle) of both models (Equations 2 and 3) were computed and the white noise behavior (uncorrelated errors) was satisfactorily checked, as it is usually done.

For the Au/Ti/TiO_2/SiO_x/Si-n^+ devices the ACF and PACF have several values outside the corresponding thresholds and both functions decrease.

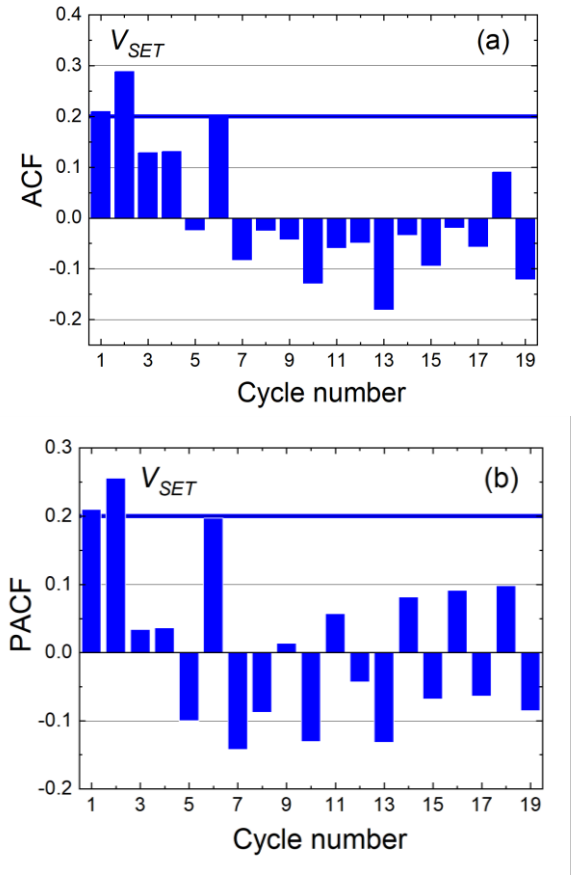

Figure 4. (a) ACF and (b) PACF versus cycle lag (distance apart in cycles within a RS series; for a cycle lag 1 the ACF and PACF of consecutive cycles are measured and so on) for the V_{SET} series described in Figure 2, corresponding to Au/Ti/TiO_2/SiO_x/Si-n^+ devices. The ACF and PACF minimum threshold bounds is 0.2, shown in solid line.

The model selection procedure suggests an AR (2) model with a null coefficient for the previous cycle component ($V_{SET(t-1)}$). Therefore, for this case V_{SET} is given in Equation 4:

$$V_{SET_t}(V) = 0.6051 + 0.2926\, V_{SET_{t-2}}(V \quad \text{(Eq. 4)}$$

4.2 – Modeling V_{RESET}

For the V_{RESET} model we have proceeded in a similar manner. The mean values are the following: $\hat{\mu}_{VRESET}$=2.358 V (Cu/HfO_2/Si-n^+) and $\hat{\mu}_{VRESET}$=1.665 V (Ni/HfO_2/Si-n^+). The sample ACF for the measured series of Figure 1 are given in Figure 5a, and the sample PACF is given in Figure 5b. The greater height of the blue bars in Figure 5, both in the ACF and PACF, indicate a higher autocorrelation function for Cu/HfO_2/Si-n^+ devices in comparison to Ni/HfO_2/Si-n^+ devices.

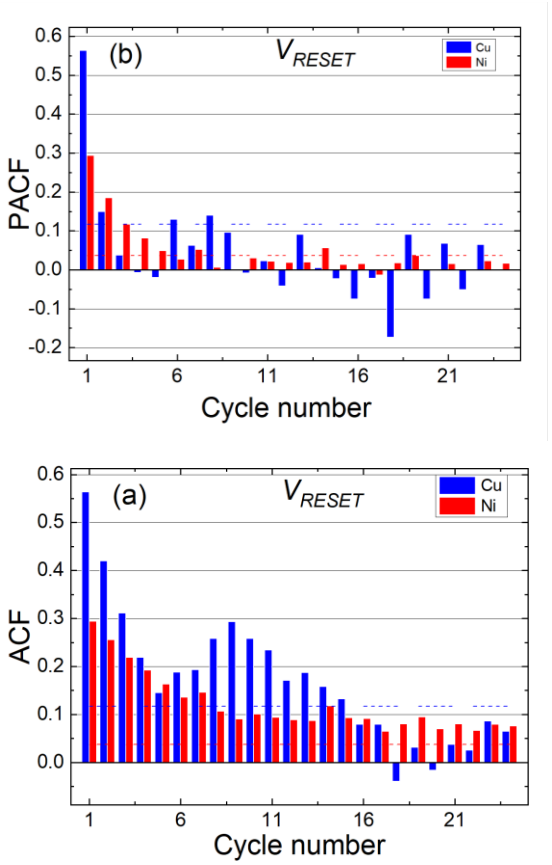

Figure 5. (a) ACF and (b) PACF versus cycle lag for the reset voltage of the Cu/HfO_2/Si-n^+ and Ni/HfO_2/Si-n^+ devices under study and the RS series described in section II. The ACF minimum threshold bounds for the Cu/HfO_2/Si-n^+ and Ni/HfO_2/Si-n^+ devices are 0.117 and 0.037 respectively, shown with dashed lines.

See that the sample PACF for Cu/HfO_2/Si-n^+ RRAMs has only two values (the first and second lagged cycles) above the threshold bound (Equation A9), so that an AR (2) model could be considered. However, taking into consideration that the second component is close to the threshold bound an AR (1) can be reasonable. After the AR (1) is adjusted all the validation considerations are satisfied. The

V_{RESET} model for these devices is given in Equation 5:

$$V_{RESET_t}(V) = 1.0117 + 0.5711\, V_{RESET_{t-1}}. \quad \text{(Eq. 5)}$$

For the Ni/HfO_2/Si-n^+ devices, the V_{RESET} model works similarly to what was determined for the set voltage modeling (ACF and PACF decrease). Then an ARMA (1,1) model (Equation 5) holds for the V_{RESET} time series for Ni/HfO_2/Si-n^+ devices:

$$V_{RESET_t}(V) = 0.237 + 0.8573 V_{RESET_{t-1}} + 0.6523 \varepsilon_{t-1}. \quad \text{(Eq. 6)}$$

The residuals of the V_{RESET} models depicted in Equations 5 and 6 have white noise behavior again, and confirm the appropriateness of the modeling procedure.

For the Au/Ti/TiO_2/SiO_x/Si-n^+ devices the ACF and PACF are given in Figure 6. In this case, the influence of other lagged cycles is more important than in previous cases; therefore, the reset voltage can be given by a linear combination of reset voltages obtained in the previous cycles. The model is a factorized AR (6) type.

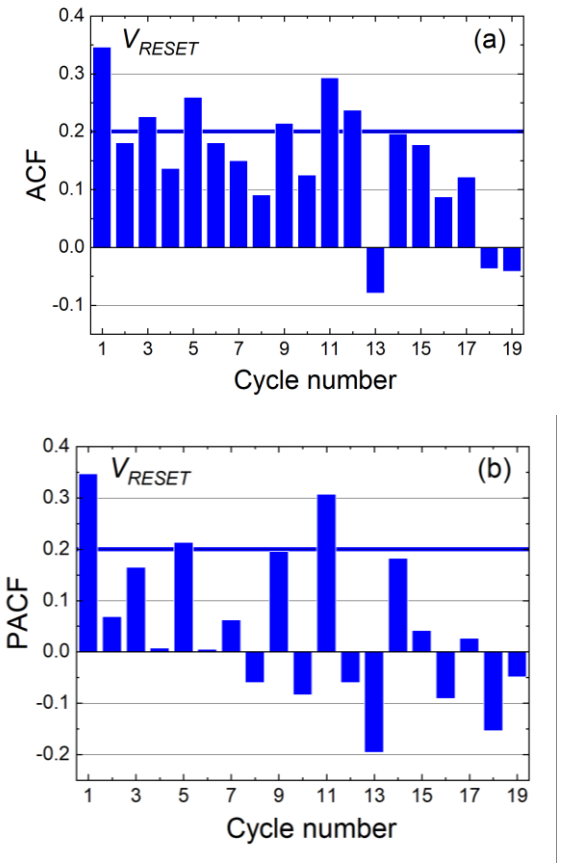

Figure 6. (a) ACF and (b) PACF versus cycle lag for the reset voltage of the Au/Ti/TiO_2/SiO_x/Si-n^+ devices under study and the RS series described in section II. The ACF and PACF minimum threshold bounds are 0.2 respectively, shown in blue lines.

The analytical expression for the TSSA description of the set voltage in Au/Ti/TiO_2/SiO_x/Si-n^+ devices is given by Equation 7.

$$V_{RESET_t}(V) = -0.3228 + 0.3198\, V_{RESET_{t-1}}(V) + 0.2197\, V_{RESET_{t-5}}(V) - 0.0703\, V_{RESET_{t-6}}(V) \quad \text{(Eq. 7)}$$

The residuals of the V_{RESET} models depicted in Equation 7 have white noise behavior again and consequently the modeling procedure is correct. Note that the coefficient of the (t-6) component is the product of the components (t-5) and (t-1)

because of the characteristics of the parameter calculation procedure.

The three technologies under study here show stationarity in the set and reset voltages series. Nevertheless, for other technologies a drift in the mean and variance shows up. In these cases, stationarity does not hold; therefore stationarity is not a general rule. If we are faced with a nonstationary data series, the methodology described in the supplementary material would not be appropriate and no models can be extracted. In these situations, there can be other options since the TSSA theory proposes changes of variables that lead the newly derived series to fulfill the stationary requirements that are needed prior to the modeling process. Autoregressive integrated moving average (ARIMA) approaches can be employed instead of the AR or ARMA modeling schemes explained above, Ref [30, 31].

5 - RESULTS AND DISCUSSION

In order to test the accuracy of the models previously developed we superposed in the same graphic the measured V_{SET} and V_{RESET} with the modeled ones for the devices under consideration in this manuscript. The modeling is a forecast of the actual value considering previous measured values, as it is conventionally done in TSSA. These results for V_{SET} (Figure 7) and V_{RESET} (Figure 8) are plotted taking into consideration Ni/HfO_2/Si-n^+ and Cu/HfO_2/Si-n^+ devices. As can be seen, the V_{SET} mean general trend is described reasonably well by Equations 2 and 3. The main dependencies have been correctly analyzed and incorporated with our procedure; hence, within the time series context, the model works well. We have validated this point by studying the residuals correlation, and we did not obtain any significant correlation between the residuals of the current cycle and those of the lagged ones (this constitutes the validation step, as explained in the Supplementary Information). Consequently, no more dependencies have to be incorporated to the models, since no information is statistically "hidden".

Although the scales and the modeling strategies are different for V_{SET}, i.e. AR (1) for Cu/HfO_2/Si-n^+ devices and ARMA (1,1) for Ni/HfO_2/Si-n^+ devices, the accuracy is similarly reasonable, as Figure 7 shows. The model error (ε_t), as highlighted before, presents a white noise structure. We have also checked that the model accuracy is maintained if the number interval is changed.

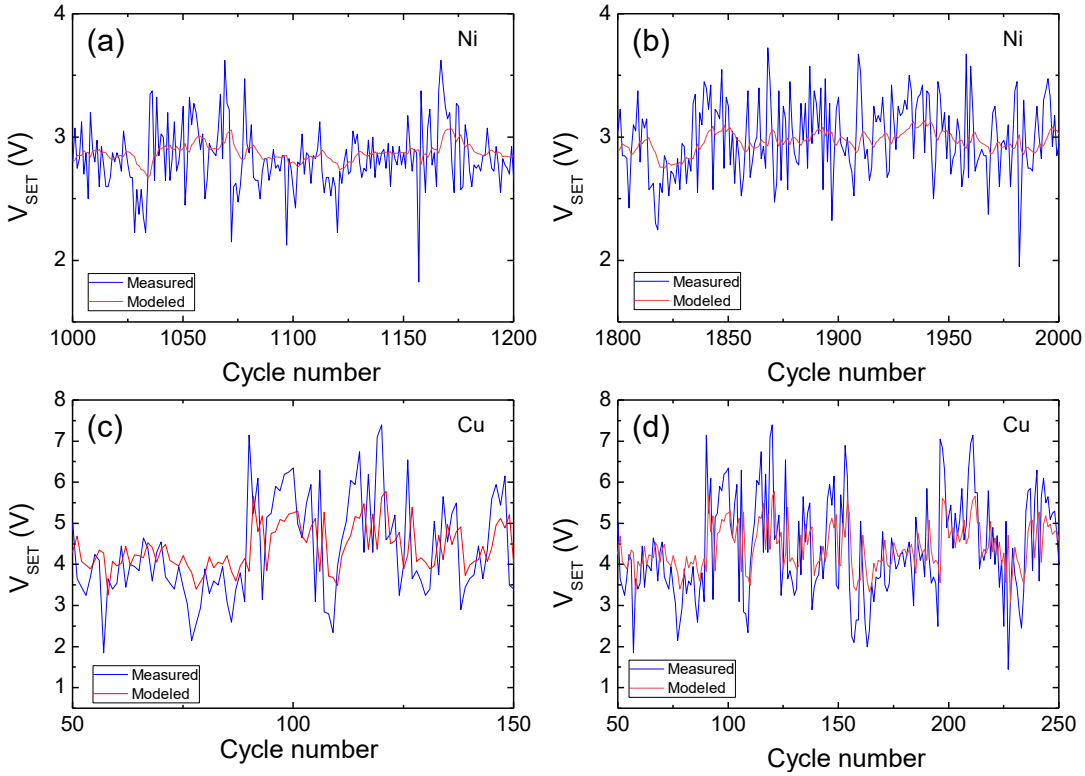

Figure 7. V_{SET} versus cycle number for the RS series under consideration. The measured values are shown in blue lines and the modelled ones in red. (a) Ni/HfO_2/Si-n^+ RRAMs, cycles 1000-1200, (b) Ni/HfO_2/Si-n^+ RRAMs, cycles 1800-2000 (c) Cu/HfO_2/Si-n^+ RRAMs, cycles 50-150, (d) Cu/HfO_2/Si-n^+ RRAMs, cycles 50-250.

The results for V_{RESET} are in line with those of V_{SET}. In this case, an AR (1) model is used for the Cu/HfO_2/Si-n^+ devices and ARMA(1,1) for Ni/HfO_2/Si-n^+ devices. Again, the model reproduces accurately the V_{RESET} mean evolution for all the cycle number intervals considered, as displayed in Figure 8.

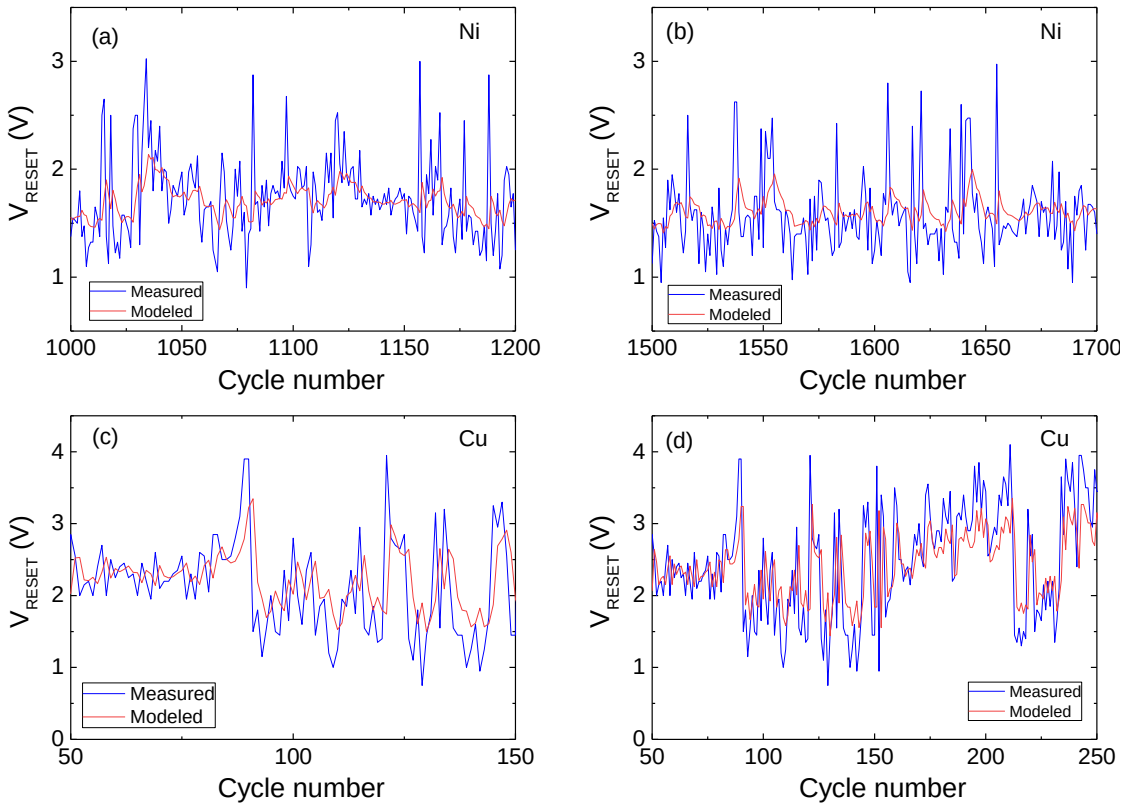

Figure 8. V_{RESET} versus cycle number for the RS series under consideration. The measured values are shown in blue lines and the modeled ones in red. (a) Ni/HfO_2/Si-n^+ RRAMs, cycles 1000-1200, (b) Ni/HfO_2/Si-n^+ RRAMs, cycles 1500-1700 (c) Cu/HfO_2/Si-n^+ RRAMs, cycles 50-150, (d) Cu/HfO_2/Si-n^+ RRAMs, cycles 50-250.

For the Au/Ti/TiO_2/SiO_x/Si-n^+ devices the comparison between measured and modelled data is shown in Figure 9. The prediction is also reasonable although more values of set (Equation 4) and reset (Equation 7) voltages of previous cycles are considered.

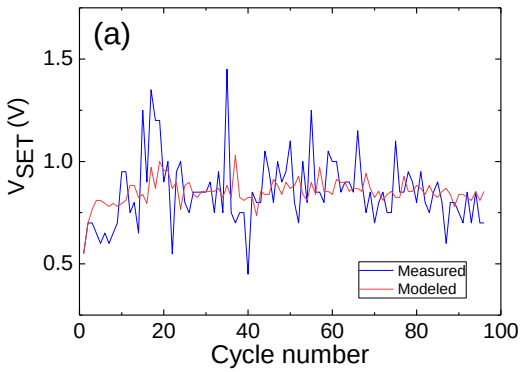

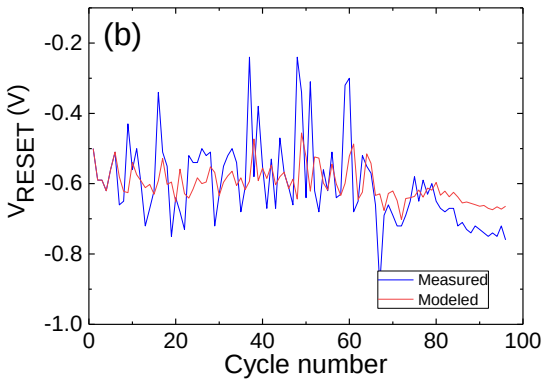

Figure 9. (a) Set (b) Reset voltage versus cycle number for the RS series under consideration. The measured values are shown in blue lines and the modeled ones in red. Au/Ti/TiO_2/SiO_x/Si-n^+ devices are considered here.

It can be observed in the figures above that in certain cases the fit is smaller than current values. This effect is seen when values much different than the mean show up. However, we

would like to highlight that the modeling methodology we are presenting deals well with the prediction of the set and reset voltage mean. The current voltage values are also predicted well in most cases by using the statistical information of previous cycles. Therefore, taking into account that current models in the literature do not have this information, and that prediction of variability is interesting in devices (RRAMs) that show inherent stochasticity, we believe that, although it is not a modeling final solution, this technique is a step forward that can be worthwhile to characterize the device physics and help with variability modeling.

It is important to highlight that Figure 3 and Figure 5 (in addition to the data needed for model building) provide information about the RS processes of the HfO_2-based devices analysed. In Figure 3a, we can see that the correlation between cycles is higher for the Cu/HfO_2/Si-n^+ devices for the first lag cycles with respect to the set voltage. In Figure 5a, a similar trend can be observed for the reset voltage series. So, in general, the influence of previous cycles in Cu/HfO_2/Si-n^+ devices is higher; i.e., the CF remnants from resets processes influence more the following set cycles, and that is why a higher correlation comes out for the set voltage values when several lag cycles are considered.

The qualitative explanation for this behaviour could be in the nature of RS in these devices. It is known that devices with Cu and Ag electrodes are employed in conductive-bridge RAMs [2, 36, 37] because of the capacity of Cu and Ag cations to diffuse in the dielectric and form, after a reduction process, a metallic-like conductive filament. In these devices, the reduction and oxidation potential are described by a thermally activated process whose activation energy depends on the number of atoms surrounding the one which is taken into consideration [1, 23, 24]. In this manner, the formation of the percolation path introduces "inertia" as the reduced atom clusters grow denser in the dielectric since they tend to maintain their shape hindering the oxidation processes of their atoms. This behaviour could explain the higher RS "inertia" shown by Cu/HfO_2/Si-n^+ devices since they maintain better the CF form and size that determine V_{SET} and V_{RESET} values. These effects would be reflected in the ACF plot with higher autocorrelation values for cycles not distant away in the series.

The lower autocorrelation (Figures 3a and 5a) for the Ni/HfO_2/Si-n^+ devices reflect a lower RS "inertia", as highlighted above. That could also be linked to a mixture of RS phenomena, since oxygen vacancies could be also involved in their resistive switching operation, as suggested in Ref. [38]. In this respect, the effects linked to activation energy lowering for oxidation of clustered metal atoms from the electrode would be mitigated, producing less correlation between the set and reset values of consecutive cycles.

In both cases, Ni/HfO_2/Si-n^+ and Cu/HfO_2/Si-n^+ devices, the most significant dependency (correlation) is with the previous value (first lag). In line with these latter issues, the results of Au/Ti/TiO_2/SiO_x/Si-n^+ devices can be analysed. In Figures 4 and 6, the cycles correlated in the ACF and PACF (mostly for the reset voltage) is higher than for the technologies studied previously. In particular, for the reset voltage, the correlation of cycles 9, 11, 13 is high with respect to the previous cases. This fact shows again an important inertia in the RS features of this technology in comparison to the devices based on HfO_2. The nature of CFs in TiO_2 for the filamentary current component and the presence of a volume current component (this component is linked to the ion distribution

that is spread out in the dielectric and that can affect several consecutive cycles in a RS series, as it was shown in devices of this kind [29]), is key to explain the higher correlation highlighted above.

It is important to highlight that the autocorrelation and partial autocorrelation functions employed to in the analysis presented above (Figures 3-6) can be used separately from the TSSA modeling. They reflect the correlation of set and reset voltages between the different cycles, this means extracting the dependencies of the current cycle on the previous ones. This information is useful even if no TSSA modeling is performed since it shows that the values studied as independent data, are, in fact, dependent, and this fact has implications in the study of cycle-to-cycle variability. It is important to highlight that ACF and PACF analysis could be easily performed on RRAM measured data to assess the correlation between the characteristics of successive RS cycles.

From the modeling viewpoint, TSSA models could be implemented in circuit simulators with Verilog-A compilers. TSSA models could be embedded in previous models to account for the RRAM stochastic behavior and for the correlation of certain parameters such as set and reset voltages in long RS series, as explained above. We have done so making use of the RRAM Stanford model [40]. In our case, a log file of previous set and reset values for the RRAMs has been employed in a model built on the TSSA approach making use of regressed values. The file was written with the current values of set and reset voltages every time a set or reset was performed. Previously, in order to simulate the RVS case we described experimentally above, we implemented a modification of the local enhancement factor (γ) [41] to be able to obtain the corresponding set and reset voltages, since these latter parameters are not model parameters.

Finally, we would like to comment on the fact that the operation regime of these devices would be characterized by pulses if they are used as storage-class memory in different chips or spikes of a variety of shapes if employed to mimic synapses in neuromorphic circuits. The device conductance depends on the pulse number for each signal amplitude, because of the different thermal inertia that is produced in each operation regime [39]. In this respect, we have chosen RVS measurements to show a particular application of the TSSA in a well-known characterization approach. This approach could be considered as the DC facet of a classical compact model, further developments could be needed to deal with transient events in a more general model where thermal and capacitive effects would be needed.

VI.- CONCLUSIONS

Times series statistical analyses (TSSA) have been used to study long series of resistive switching processes. The experimental data analyzed here were measured in resistive random access memories with Ni/HfO_2/Si-n^+, Cu/HfO_2/Si-n^+, Au/Ti/TiO_2/SiO_x/Si-n^+ structures. The conventional time series techniques were applied to model the V_{SET} and V_{RESET} of these devices; to do so, autocorrelation functions and partial autocorrelation functions were obtained for all the types of RRAMs. Autoregressive models were obtained for Cu/HfO_2/Si-n^+ devices and the autocorrelation function between cycles was high, showing an important inertia between resistive switching cycles. The better diffusion of Cu ions in the dielectric is behind this behaviour. For Ni/HfO_2/Si-n^+ devices more complex models are needed and autocorrelation data show less

inertia between resistive switching cycles. Finally, for $Au/Ti/TiO_2/SiO_x/Si\text{-}n^+$ devices a significant correlation can be observed for more distant cycles in the reset voltage description. A physical explanation has been developed in connection with the correlation results found. The models obtained can be used to forecast the values of set and reset voltages in a resistive switching series if previous values are known. The information obtained in this context can be employed in modelling and in the characterization of RRAM variability.

References

[1] F. Pan, S. Gao, C. Chen, C. Song, F. Zeng, "Recent progress in resistive random access memories: materials, switching mechanisms and performance", Materials Science and Engineering, 83, pp. 1-59, 2014.

[2] D. Ielmini, R. Waser. "Resistive Switching: From Fundamentals of Nanoionic Redox Processes to Memristive Device Applications", Wiley-VCH, 2015.

[3] R. Waser and M. Aono, "Nanoionics-based resistive switching", Nature materials, 6, pp. 833–840, 2007.

[4] M. Lanza, G. Bersuker, M. Porti, E. Miranda, M. Nafría, X. Aymerich, "Resistive switching in hafnium dioxide layers: Local phenomenon at grain boundaries", Applied Physics Letters, vol. 101, 193502, 2012.

[5] M. Lanza, H.-S. P. Wong, E. Pop, D. Ielmini, D. Strukov, B.C. Regan, L. Larcher, M.A. Villena, J.J. Yang, L. Goux, A. Belmonte, Y. Yang, F. M. Puglisi, J. Kang, B. Magyari-Köpe, E. Yalon, A. Kenyon, M. Buckwell, A. Mehonic, A. Shluger, H. Li, T.-H. Hou, B. Hudec, D. Akinwande, R. Ge, S. Ambrogio, J.B. Roldan, E. Miranda, J. Suñe, K.L. Pey, X. Wu, N. Raghavan, E. Wu, W.D. Lu, G. Navarro, W. Zhang, H. Wu, R. Li, A. Holleitner, U. Wurstbauer, M. Lemme, M. Liu, S. Long, Q. Liu, H. Lv, A. Padovani, P. Pavan, I. Valov, X. Jing, T. Han, K. Zhu, S. Chen, F. Hui, Y. Shi, "Recommended methods to study resistive switching devices", Advanced Electronics Materials, 2018, 1800143 (DOI: 10.1002/aelm.201800143).

[6] R. Waser (ed.), "Nanoelectronics and Information Technology", 3rd edition, Wiley, 2012.

[7] M.A. Villena, J.B. Roldán, F. Jiménez-Molinos, E. Miranda, J. Suñé, M. Lanza, "*SIM*^{2}*RRAM*: A physical model for RRAM devices simulation", Journal of Computational Electronics, in press, 2017.

[8] R. Degraeve, A. Fantini, N. Raghavan, L. Goux, S. Clima, B. Govoreanu, A. Belmonte, D. Linten, M. Jurczak, "Causes and consequences of the stochastic aspect of filamentary RRAM", Microelectronic Engineering, 147, pp. 171-175, 2015.

[9] F.M. Puglisi, N. Zagni, L. Larcher, P. Pavan, "Random Telegraph Noise in Resistive Random Access Memories: Compact Modeling and Advanced Circuit Design", IEEE Transactions on Electron Devices, 65, pp. 2964 – 2972, 2018.

[10] S. Menzel, P. Kaupmann, R. Waser, "Understanding filamentary growth in electrochemical metallization memory cells using kinetic Monte Carlo simulations", Nanoscale, 7, 12673, 2015.

[11] S. Long, X. Lian, T. Ye, C. Cagli, L. Perniola, E. Miranda, M. Liu, and J. Suñé, "Cycle-to-cycle intrinsic

RESET statistics in HfO_2-based unipolar RRAM devices", IEEE Electron Device Lett. 34(5), 623–625, 2013.

[12] W.C, Luo, J.C. Liu, H.T. Feng, Y.C. Lin, J.J. Huang, K.L. Lin, T.H. Hou, "RRAM SET speed-disturb dilemma and rapid statistical prediction methodololy", International Electron Device Meeting, p. 9.5.1, 2012.

[13] J.W. McPherson, "Reliability Physics and Engineering. Time-to-Failure Modeling", second ed. Springer, 2013.

[14] E. Y. Wu, B. Li, J.H. Stathis, "Modeling of time-dependent non-uniform dielectric breakdown using a clustering statistical approach", Applied Physics Letters, 103, p. 152907, 2013.

[15] E. Y. Wu, E. J. Nowak, R. Vollertsen, and L. K. Han, "Weibull Breakdown Characteristics and Oxide Thickness Uniformity", IEEE Trans. Electron Device 47, 2301–2309, 2000.

[16] C. Acal, J.E. Ruiz-Castro, A. M. Aguilera, F. Jiménez-Molinos, J.B. Roldán, "Phase-type distributions for studying variability in resistive memories", Journal of Computational and Applied Mathematics, 345, pp. 23–32, 2019.

[17] H. Tian, X.-F. Wang, M. A. Mohammad, G.-Y. Gou, F. Wu, Y. Yang, T.-L. Ren, "A hardware Markov chain algorithm realized in a single device for machine learning", Nature communications, 9, 4305, 2018.

[18] F.M. Puglisi, P. Pavan, "RTN analysis with FHMM as a tool for multi-trap characterization in HfO_X RRAM", **2013** IEEE International Conference of Electron Devices and Solid-state Circuits, **DOI:** 10.1109/EDSSC.2013.6628059

[19] F. Pan, S. Yin, V. Subramanian, "A detailed study of the forming stage of an electrochemical resistive switching memory by KMC simulation," IEEE Electron Device Lett. 32, 949–951, 2011.

[20] X. Guan, *Member, IEEE*, S. Yu, H.S. Philip Wong, "On the switching parameter variation of metal-oxide RRAM—Part I: Physical modeling and simulation methodology", *IEEE Transactions on Electron Devices,* 59, pp. 1172-1182, 2012.

[21] L. Larcher, A. Padovani, O. Pirrotta, L. Vandelli, and G. Bersuker, "Microscopic understanding and modeling of HfO2 RRAM device physics," in Proc. IEEE Int. Electron Devices Meeting, pp. 20.1.1–20.1.4, 2012.

[22] J. Guy, G. Molas, P. Blaise, M. Bernard, A. Roule, G. Le Carval, V. Delaye, A. Toffoli, G. Ghibaudo, Fellow, IEEE, F. Clermidy, B. De Salvo, L. Perniola , "Investigation of Forming, SET, and Data Retention of Conductive-Bridge Random-Access Memory for

Stack Optimization", IEEE Transactions on Electron Devices, 62(11), pp. 3482-3489, 2015

[23] S. Aldana, P. García-Fernández, A. Rodríguez-Fernández, R. Romero-Zaliz, M.B. González, F. Jiménez-Molinos, F. Campabadal, F. Gómez-Campos, J.B. Roldán, "A 3D Kinetic Monte Carlo simulation study of Resistive Switching processes in Ni/HfO2/Si-n+-basedRRAMs", Journal of Physics D: Applied Physics, 50, 335103, 2017.

[24] S. Aldana, J.B. Roldán, P. García-Fernández, J. Suñe, R. Romero-Zaliz, F. Jiménez-Molinos, S. Long, F. Gómez-Campos, M. Liu, "An in-depth description of bipolar resistive switching in Cu/HfOx/Pt devices, a 3D Kinetic Monte Carlo simulation approach", Journal of Applied Physics, 123, 154501, 2018.

[25] M. Schie, S. Menzel, J. Robertson, R. Waser and R. A. De Souza, "Field-enhanced route to generating anti-Frenkel pairs in HfO2", Physical Review Materials, 2, 035002, 2018.

[26] M. Xie, S.L. Ho, "Analysis of repairable system failure data using time series models", Journal of Quality in Maintenance Engineering, Vol. 5 Issue: 1, pp.50-61, 1999.

[27] K. L. Lee & S. A. Billings, "Time series prediction using support vector machines, the orthogonal and the regularized orthogonal least-squares algorithms", International Journal of Systems Science, 33:10, 811-821, DOI: 10.1080/00207720210000017317, 2002.

[28] M. B. González, J. M. Rafí, O. Beldarrain, M. Zabala, and F. Campabadal, "Analysis of the switching variability in Ni/HfO2-based RRAM devices," IEEE Trans. Device Mater. Reliab., vol. 14, no. 2, pp. 769–771, 2014.

[29] N. Xiao, M.A. Villena, B. Yuan, S. Chen, B. Wang, M. Elias, Y. Shi, F. Hui, X. Jing, A. Sheuermann, K. Tang, P.C. McIntyre, M. Lanza, "Resistive Random Access Memory Cells with a Bilayer TiO_2/SiO_xInsulating Stack for Simultaneous Filamentary and Distributed Resistive Switching", Advanced Functional Materials, 27, p. 1700384, 2017.

[30] P. J. Brockwell, R. A. Davis, "Introduction to Time Series and Forecasting", Second Edition, Springer, 2002.

[31] S.Bisgaard, M.Kulahci, "Time series analysis and forecasting by example", Wiley, 2011.

[32] G.U. Yule, "On a method of investigating periodicities in disturbed series, withreference to Wolfer's Sunspot Numbers", Philosophical Transactions of the Royal Society of London, Series A, 226, pp. 267–298, 1927.

[33] D. C. Montgomery, C. L. Jennings, M. Kulahci, "Introduction to Time Series Analysis and

Forecasting", Wiley Series in Probability and Statistics, Wiley, 2015.

[34] M.A. Villena, J.B. Roldán, F. Jiménez-Molinos, J. Suñé, S. Long, E. Miranda, M. Liu, "A comprehensive analysis on progressive reset transitions in RRAMs", Journal of Physics D: applied physics, 7, 205102, 2014.

[35] A. Coghlan, "A little book of R for time series", Release 0.2. In: https://media.readthedocs.org/pdf/a-little-book-of-r-for-time-series/latest/a-little-book-of-r-for-time-series.pdf, 2018.

[36] Yang, Y. et al. Electrochemical dynamics of nanoscale metallic inclusions in dielectrics. Nat. Commun. 5, 4232, 2014.

[37] Yuanyuan Shi, Xianhu Liang, Bin Yuan, Victoria Chen, Haitong Li, Fei Hui, Zhouchangwan Yu, Fang Yuan, Eric Pop, H.-S. Philip Wong, Mario Lanza ,"Electronic synapses made of layered two-dimensional materials**",** Nature Electronics 1, 458–465, 2018.

[38] U. Celano, L.Goux, R. Degraeve, A.Fantini, O. Richard, H. Bender, M.Jurczak, W.Vandervorst, "Three-Dimensional Observation of the Conductive Filament in Nanoscaled Resistive Memory Devices", Nanoletters, 14, pp. 2401-2406, 2014.

[39] S. Kim, C. Du, P. Sheridan, W. Ma, S. Choi, W. D. Lu, "Experimental Demonstration of a Second-Order Memristor and Its Ability to Biorealistically Implement Synaptic Plasticity", *NanoLetters, 15*, 2203, 2015.

[40] https://nano.stanford.edu/stanford-rram-model

[41] X. Guan, S. Yu, and H-S.P Wong, "A SPICE Compact Model of Metal Oxide Resistive Switching Memory with Variations", IEEE Elec. Dev. Lett., vol. 33, pp. 1405-1407, 2012.

Supplementary Information

In this paper, Box-Jenkins methodology [Bisgaard11] is applied for modeling the time series of reset and set voltages in resistive RRAMs. For the sake of clarity, a brief summary of the theoretical background related with autoregressive moving average (ARMA) models is given below.

The formulation of an ARMA(p,q) model is given as follows (the considerations would be the same for the set voltage),

$$\begin{aligned} V_{RESET_t} = \Phi_0 + \Phi_1 V_{RESET_{t-1}} + \cdots \\ + \Phi_p V_{RESET_{t-p}} \\ - \theta_1 \varepsilon_{t-1} + \cdots \\ - \theta_q \varepsilon_{t-q} \end{aligned} \quad \text{(A1)}$$

where V_{RESET_t} is the modeled reset voltage in the current cycle of an RS series, and $V_{RESET_{t-k}}$ are the modelled reset voltages lagged k cycles (i.e., the k reset voltage values of the previous RS cycles), ε_{t-k} are the errors (residuals) made in the modeling process from earlier cycles, with Φ_i(i=1, …, p) and θ_j(j=1, …, q) being the unknown regression coefficients to be estimated in the modelling process. In time series methodology the term ε_t is also included in the model but, in our case, we assume it. A similar description holds for the set voltage.

The current value of the modeled reset voltage can be calculated by means of two linear polynomials, one for the autoregressive part (AR, in this case the reset voltage is modeled as a linear function of some of its past values), and the other for the moving average part (MA, a linear combination of the past model errors or residuals). The parameters p and q are the orders of the autoregressive part and the moving average part, respectively.

The ARMA approach assumes that the time series is stationary and the model error ε_t shows a white noise behaviour (uncorrelated random errors). Because of this, the first step, previous to model fitting, is to determine if the time series is stationary. This characteristic is achieved if the data structure has the same properties, generally second order properties, in all the observation period. Therefore, the mean and the variance should be constant in time and the value of the covariance between two periods depends only on the distance or lag between them. That is, they have the following mathematical properties:

Mean:

$$E(V_{RESET_t}) = E(V_{RESET_{t-k}}) = \mu \quad \text{(A2)}$$

Variance:

$$\begin{aligned} Var(V_{RESET_t}) &= E\left[\left(V_{RESET_t} - \mu\right)^2\right] \\ &= Var(V_{RESET_{t-k}}) \\ &= \sigma \end{aligned} \quad \text{(A3)}$$

Autocovariance:

$$\begin{aligned} \gamma(k) &= Cov(V_{RESET_{t-k}}, V_{RESET_t}) \\ &= E[(V_{RESET_{t-k}} \\ &\quad - \mu)(V_{RESET_t} - \mu)] \end{aligned} \quad \text{(A4)}$$

A useful measure of the degree of dependence among the data (reset voltages) of different cycles is the Autocorrelation Function (ACF). It can be calculated as follows, taking into account that $\gamma(0)$ is the variance:

$$\begin{aligned} \rho(k) &= Cor\left(V_{RESET_{t-k}}, V_{RESET_t}\right) \\ &= \frac{Cov(V_{RESET_{t-k}}, V_{RESET_t})}{\sqrt{Var(V_{RESET_t}) Var(V_{RESET_{t-k}})}} \\ &= \frac{\gamma(k)}{\gamma(0)} \end{aligned} \quad \text{(A5)}$$

Notice that the ACF measures the correlation between two variables separated by k periods. That is, the ACF summarizes how correlated are the data that are k lags distant.

The usual estimate of the autocorrelation function from the observed data $\{V_{RESET_1}, V_{RESET_2}, \dots, V_{RESET_n}\}$ is the sample autocorrelation function (correlogram) given by,

$$\hat{\rho}(k) = \frac{\hat{\gamma}(k)}{\hat{\gamma}(0)} \qquad (A6)$$

where $\hat{\gamma}(k)$is the sample autocovariance function (see Equation A7)

$$\hat{\gamma}(k) = \frac{1}{n}\sum_{t=1}^{n-k}(V_{RESET_{t-k}} - \hat{\mu})(V_{RESET_t} - \hat{\mu}) \qquad (A7)$$

with$\hat{\mu}$ being the reset voltage mean function $\hat{\mu} = \frac{1}{n}\sum_{t=1}^{n} V_{RESET_t}$. Note, that accordingly to the statistics jargon, the functions with a hat are computed from experimental data only. In this way, they are distinguished from the functions without hat that corresponds to the theoretical model.

The ARMA modeling process can be performed in five main steps: checking stationarity, model identification, parameter estimation, validation and prediction.

Checking stationarity

First of all we must be sure that the series is stationary. If the series is plotted and there is no evidence of a change in the mean and the variance over time, it is said that the series is stationary in the mean and in the variance. Stationarity can be visually checked from the plot of the time series observed values. These values have to be distributed around a value (the mean) and the fluctuations above and under this value have to be similar in all the series range (the series values have to be within a constant interval). Also, the sample ACF must tail off near zero after a few lags. Nevertheless, if the sample ACF is very persistent (it decays very slowly and exhibits sample autocorrelations that are still rather large even at long lags) the time series is nonstationary. If the series is not stationary, some appropriate transformation (logarithm, differentiation…) is needed to be converted to a stationary series, and the modeling process would follow for the transformed series. A final reverse transformation would allow to obtain the model for the original variable.

Model identification

In order to select a tentative ARMA model (identify the orders p and q of the AR and MA polynomials respectively), the autocorrelation function (ACF) and partial autocorrelation function (PACF) of the data must be computed and compared to the corresponding theoretical ACF and PACF for various ARMA models.

The Partial Autocorrelation Function measures the correlation between two variables separated by k periods when the dependency due to the intermediate lags is eliminated. That is,

$$\begin{aligned}\pi(k) &= \mathrm{Cor}\left(V_{RESET_{t-k}}, V_{RESET_t} / V_{RESET_{t-1}}, V_{RESET_{t-2}}, V_{RESET_{t-k+1}}\right) \\ &= \mathrm{Cor}(V_{RESET_{t-k}} - \widehat{V}_{RESET_{t-k}}, V_{RESET_t} - \widehat{V}_{RESET_t})\end{aligned} \qquad (A8)$$

where $\widehat{V}_{RESET_t}$ is the estimated value by the linear regression model of V_{RESET_t} on the lagged variables $V_{RESET_{t-1}}, V_{RESET_{t-2}}, \dots, V_{RESET_{t-k+1}}$. These $\pi(k)$ can be iteratively computed in terms of correlations $\rho(k)$ (Equation A5) using for example the Durbin-Levinston algorithm

[Brockwell02] (in practice, it uses the estimated values, Equation A6).

If the data PACF is zero after lag p, this means that the data structure is well modeled using the p previous observed values. Thus, an AR model can be accurate enough for modeling the data. The number of regression terms (p) is given by the last significant value with respect to the threshold bounds in the PACF.

If the sample PACF tails off to zero, the ACF is inspected. If the sample ACF is zero after lag q, a MA model is used for the data. The order is given by the last significant term in the ACF function. If both functions, the sample ACF and PACF, tail off to zero the model needs autoregressive and moving average terms.

The sample partial autocorrelation $\hat{\pi}(k)$ at certain lag k is considered to be zero if they do not exceed the significance bound (threshold) given by,

$$\pm\frac{1.96}{\sqrt{n}}, \qquad \text{(A9)}$$

where n is the number of observed data (the number of cycles in our case) [Brockwell02].

The autocorrelation $\hat{\rho}(k)$ at certain lag k is considered to be zero if it does not exceed the significance bound (threshold) given by [Brockwell02],

$$\pm\frac{1.96}{\sqrt{n}}\sqrt{1+2\widehat{\rho^2}(1)+\cdots+2\,\widehat{\rho^2}(k-1)} \qquad \text{(A10)}$$

If several models appear to fit well the data, the principle of parsimony [Bisgaard11] is used to decide which among these models is the best. That is, we assume that the model with the fewest number of parameters (the simplest model) is the best option.

Parameter estimation

Once an ARMA model is selected, its parameters must be estimated (i.e., Φ_i, θ_j). The non-linear least square method can be used to calculate the parameters by using an iterative procedure. Initial estimates are used as starting points so that in successive steps these estimates are systematically improved until optimal values are found using the minimum mean square error as the criterion. This procedure also allows to calculate the residuals,ε_t, for all t.

Validation

In order to evaluate the adequacy of the estimated model, we must check that the residuals are not correlated. For this aim, the residuals (ε_j) ACF and PACF have to be plotted. These data, when plotted, have to be within the threshold bounds (Equations A9 and A10). A diagnostic test to check that the autocorrelation (Equation A6) of the error terms (residuals) is not significantly different from zero must be carried out. In practice, Ljung-Box statistic is used [Brockwell02]. This test checks that the first "L" correlations are equal to 0 ($\rho(1)=\rho(2)=\cdots=\rho(L)=0$).

If the residuals are correlated, the model must be discarded and the diagnosis test repeated with another of the possible model candidates to identify the most appropriate model.

Prediction

Once the best candidate model is selected, probabilistic predictions of future values can be made. In our case, the V_{RESET} (or V_{SET}) in cycle t could be predicted making use of the reset voltages and the residuals of previous cycles.

References

[Bisgaard11] S.Bisgaard, M.Kulahci, "Time series analysis and forecasting by example", Wiley 2011

[Brockwell02] P. J. Brockwell, R. A. Davis, “Introduction to Time Series and Forecasting”, Second Edition, Springer, 2002.

ACKNOWLEDGMENTS

We would like to thank F. Campabadal and M. B. González from the IMB-CNM (CSIC) in Barcelona for fabricating and providing the experimental measurements of the devices employed here. The authors thank the support of the Spanish Ministry of Science, Innovation and Universities under projects TEC2017-84321-C4-3-R and MTM2017-88708-P (also supported by the FEDER program). This work has made use of the Spanish ICTS Network MICRONANOFABS.

3.2. TSSA in h-BN memristors

In the same manner as in the previous section, we have characterized h-BN devices in order to be analyzed under the TSSA by extracting the set and resets voltages and currents. The memristor dielectric is based on a novel 2D material such as the hexagonal boron nitride, accounting with a few layers in the Au/Ti/h-BN/Au/Ti stack. Hence, ACF and PACF have been calculated to get the analytical models presented in the realm of time series analysis. Additionally, the Stanford model has been modified to account for the variability by including the mentioned statistical procedure.

The following section is an already published work [Roldán2021b].

J. Roldán et al.

IEEE International Reliability Physics Symposium (2021)

Roldán, J. B., Maldonado, D., Alonso, F. J., Roldán, A. M., Hui, F., Shi, Y., ... & Lanza, M. (2021, March). Time series modeling of the cycle-to-cycle variability in h-BN based memristors. In 2021 IEEE International Reliability Physics Symposium (IRPS) (pp. 1-5). IEEE. DOI: 10.1109/irps46558.2021.940510

Quality metrics

Data base	Rating
Scimago	Scientific journal & country rank h-index: 52

Publication citations (23-03-2022)

Google Scholar	Web of Science
1	**1**

Time series modeling of the cycle-to-cycle variability in h-BN based memristors

J. B. Roldán[1], D. Maldonado[1], F.J. Alonso[2], A. M. Roldán[1], F. Hui[3], Y. Shi[4], F. Jiménez-Molinos[1], A.M. Aguilera[2] and M. Lanza[5]

[1] *Dep. Electrónica y Tecnología de Computadores. Universidad de Granada. Facultad de Ciencias, 18071, Granada, Spain*

[2] *Dep. Estadística e Investigación Operativa. Universidad de Granada. Facultad de Ciencias, 18071, Granada, Spain*

[3] *Faculty of Materials Science and Engineering, Technion – Israel Institute of Technology, Haifa 3200003, Israel*

[4] *IMEC, Kapeldreef 75, B-3001 Leuven, Belgium*

[5] *Physical Sciences and Engineering Division, King Abdullah University of Science and Technology (KAUST), Thuwal 23955-6900, Saudi Arabia*

* *Corresponding author Email: jroldan@ugr.es, mario.lanza@kaust.edu.sa*

Abstract— We have characterized and modeled memristor devices based on the Au/Ti/multilayer h-BN/Au/Ti stack. Resistive switching (RS) operation has been analysed by extracting the reset and set voltages and currents. The evolution of the set and reset parameters along a RS series was mathematically modeled in a cycle-to-cycle (CTC) basis by means of the Time Series Analysis (TSSA). To do so, the Autocorrelation Functions (ACF) and the Partial Autocorrelation Functions (PACF) have been calculated. These tools help to perform a comprehensive variability study and to obtain the corresponding analytical models within the TSA context. Finally, we have included this modeling procedure in a complete compact model such as the Stanford to be able to account for this variability at the circuit level. Experimental current versus voltage (*I-V*) curves have been correctly fitted with the model.

Index Terms-- Memristor, variability, compact modeling, reliability, time series analysis, dielectric, two-dimensional material, electrical characterization.

1. Introduction

Memristors, predicted by Chua in 1971 [1], can be applied to different technologies [2]. Nowadays, there are different types of devices that can be considered as memristors; among them, there are the ones relying on ferroelectric, phase change or magnetic material properties [2-4]. Transition metal oxides have been extensively studied in this context [2-4]. In particular, resistive switching (RS) devices with filamentary charge conduction, based on HfO_2, TiO_2, Al_2O_3 dielectrics, among others, have shown outstanding features such as high endurance, good retention, low power consumption, CMOS technology compatibility, scalability, and capacity for being fabricated in 3D stacked structures [4-6].

Nevertheless, other dielectric alternatives based on 2D materials are being considered due to the outstanding features of the electron devices that employ them [7-10]. Intense research efforts are being conducted to describe yield, variability, reliability and stability in the field of 2D materials based solid-state nano/micro-electronic devices [9, 10]. 2D dielectric memristor technology can lead to solutions to some of the issues that show up in memristors industrial applications linked to non-volatile memories [2, 9], entropy sources for cryptographic hardware (random number generation and implementation of physical unclonable functions [2, 9, 11]) and, most important, neuromorphic computing [2, 8, 10]. In the latter case, the fabrication of devices that mimic the behavior of biological synapses is essential [8, 12, 13]. The capacity to build circuits to perform matrix-vector multiplications will allow the implementation of efficient hardware neural networks (HNN) that can greatly accelerate neuromorphic computing, and above all, reduce power consumption of brain-inspired designs and native artificial intelligence systems. In addition, properties such as spike timing dependent plasticity, long/short term plasticity, etc., facilitate the development of spiking neural networks that process information closely to what is done in the human brain [14].

For the use of these emerging technologies out of certain niche applications, both variability and implementation of mature simulation tools have to be addressed. We deal with both subjects in this work. It is known that the inherent random nature of the physical mechanisms behind RS makes memristor operation different to other type of electron devices [2, 5, 6]. In this respect, the device stochasticity has been studied and modeled from different viewpoints. For instance, advanced statistical distribution functions, e.g., Phase-type distributions have been successfully applied to deal with variability [15, 16]; approaches founded on functional data analysis were also used [17-19]; from another perspective, simulations linked to kinetic Monte Carlo techniques proved their adequacy [20, 21]. Here, we address CTC variability in h-BN memristors from the time series analysis perspective [22-24]. TSA has been proved to be an efficient tool for a comprehensive CTC variability characterization and modeling [22-24]. This modeling technique accounts for the "inertia" connected to RS processes; i.e., the dependencies of present set and reset events on previous RS operation is taken into consideration. This idea means keeping "modeling memory" of the RS previous operation; e.g., CF remnants left in past reset processes are considered when a new reset event is to be described. As far as we know, this is the first time this methodology has been used in 2D materials based devices.

2. Device fabrication and measurement

The memristors we have fabricated consists of the following layers (40 nm Au/10 nm Ti/multilayer h-BN/40 nm Au/10nm Ti/300 nm SiO_2/Si). E-beam evaporation was employed for the electrode

We thank the Spanish Ministry of Science for project TEC2017-84321-C4-3-R, MTM2017-88708-P, PGC2018-098860-B-I00 and Junta de Andalucía for projects A-TIC-117-UGR18 and A-FQM-345-UGR18 all with the support of the European Regional Development Fund. We also thank NSFC (61874075), MOST (BRICS2018-211-2DNEURO) and the Ministry of Finance of China (SX21400213).

deposition. The h-BN multilayer films were grown by chemical vapor deposition (CVD) on Cu foil and inserted between the electrodes via wet transfer. The (*I-V*) curves were measured through a Karl Suss probe station connected to a semiconductor parameter analyzer under ramped voltage stress (RVS). Long RS series were obtained including complete and consecutive set and reset cycles. The voltage was applied to the top electrode, the bottom electrode was grounded.

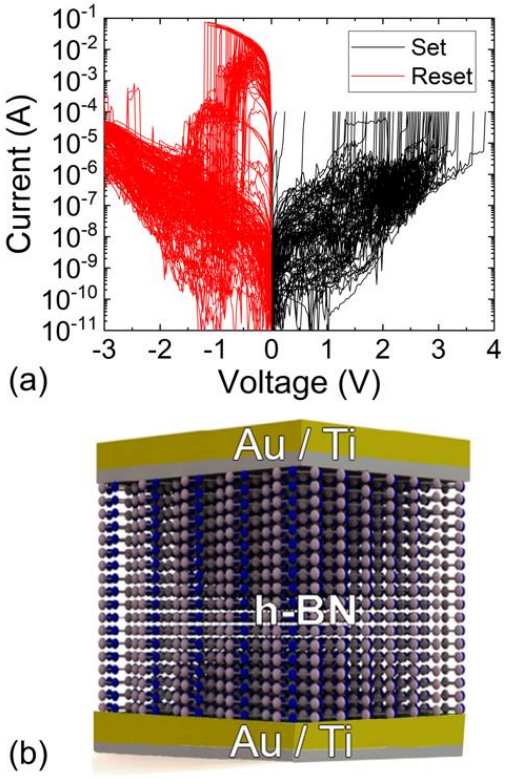

Figure 1. (a) Experimental current versus applied voltage for different RS cycles in a long series for the devices under study. 94 set (black curve) and reset (red curve) processes have been plotted. (b) Schematic of the fabricated devices, $I_{CC}=10^{-4}$ A.

The measured I-V curves are shown in Fig. 1 along with the device layer schema. The charge conduction is known to be filamentary, RS is produced by means of the rupture and creation of conductive filaments (CFs) that short the electrodes [2, 7]. The mechanisms involved in the CFs formation and rupture are random, this randomness is linked to the cycle-to-cycle (CTC) variability.

3. TSA Modeling, results and discussion

We have obtained the set and reset voltages and currents by identifying the higher I-V slope point and the maximum current point respectively (Fig. 2).

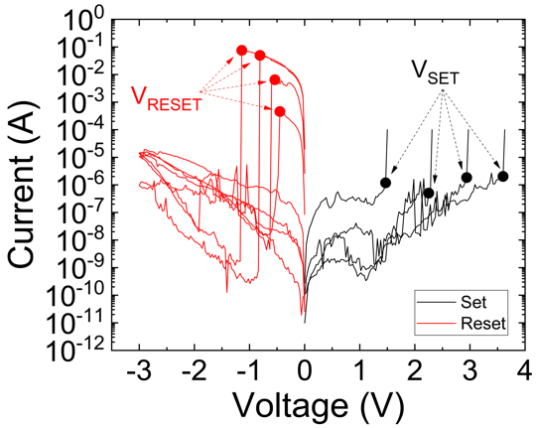

Figure 2. Experimental current versus applied voltage for different RS cycles. The points where V_{SET} and V_{RESET} are calculated have been marked. We have identified the higher I-V slope point for the set voltage determination and the maximum current point for the reset voltage.

The set and reset (absolute value) voltages cumulative distribution functions were plotted (Fig. 3) to describe the cycle-to-cycle variability for 94 RS cycles.

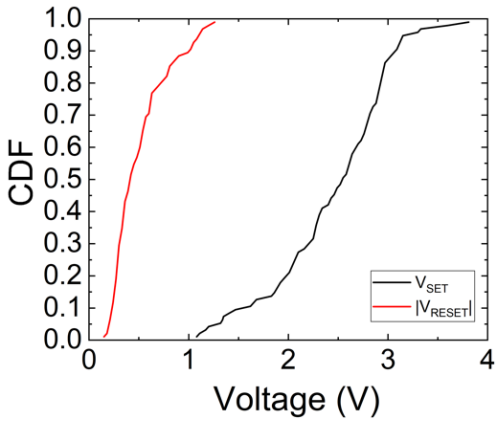

Figure 3. Cumulative Distribution Functions (CDF) for the calculated parameters V_{SET} and $|V_{RESET}|$.

The corresponding ACF (Fig. 4) and PACF (Fig. 5) plots have been calculated [22-23]. A useful measure of the degree of dependence among the data (reset and set voltages) of different cycles is the autocorrelation function. The ACF (Eq. 1), a function of the number of cycles, *k*, measures the influence/connection between V_{RESET} values separated

by k cycles (k distant lags in the RS series), this also works out for the other RS parameters, such as V_{SET} [22, 25-26]. For the V_{SET} (Fig. 4) we have several components, the corresponding to the previous cycle and two others that dominate over the reset. The values have to be compared with the threshold bounds, which depends on the number of cycles of the series [25, 26]. For the V_{RESET} we have just one component. The ACF, ρ, is given in Equation 1,

$$\rho(k) = Cor\left(V_{RESET_{t-k}}, V_{RESET_t}\right) = \frac{\mathrm{Cov}(V_{RESET_{t-k}}, V_{RESET_t})}{\sqrt{\mathrm{Var}(V_{RESET_t})\mathrm{Var}(V_{RESET_{t-k}})}} = \frac{\gamma(k)}{\gamma(0)} \quad (1)$$

where Cov is the covariance, Var is the variance, t is the actual V_{RESET} value and (t-k) the value of k cycles before [25].

To better understand the ACF, we stress that it accounts for the "inertia" produced in the RS parameter values by the CF remnants remaining in each RS cycle (these remnants characterize the influence of previous RS cycles on the current one). The PACF describes the same correlation than ACF eliminating the dependency due to the intermediate lags (1, 2..., k–1) [22, 23].

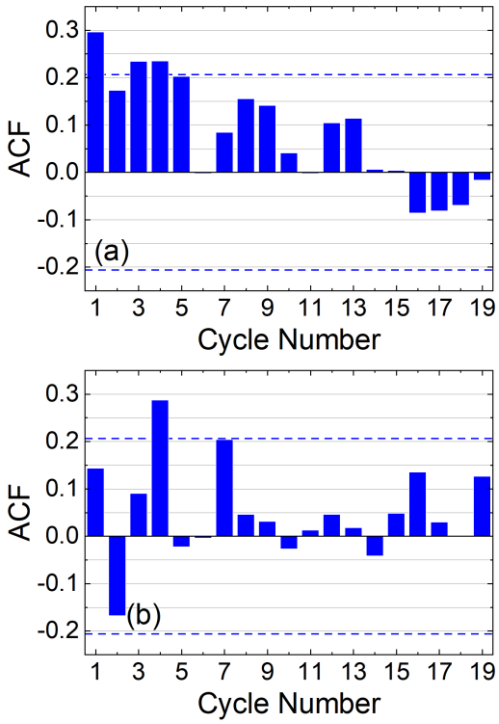

Figure 4. ACF vs cycle lag (distance apart in cycles within a RS series; for a cycle lag 1, the ACF of consecutive cycles is measured) for the (a) V_{SET} and (b) V_{RESET} series. The minimum and maximum threshold bounds are 0.20628 and -0.20628 respectively, shown by the dashed lines. These values depend on the number of data in the sample [22].

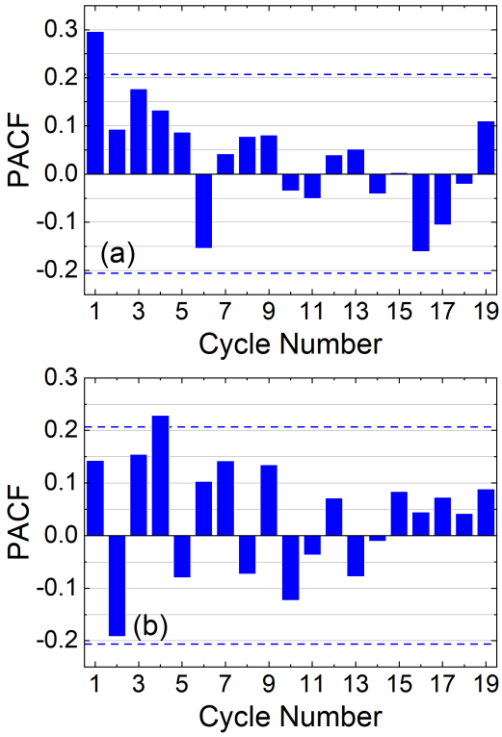

Figure 5. PACF vs cycle lag for the (a) V_{SET} and (b) V_{RESET} series described in Fig. 3. The minimum and maximum threshold bounds are 0.20628 and -0.20628 respectively, shown by the dashed lines.

The TSA techniques (along with the results of Figs. 4 and 5) allowed us to obtain the analytical expression of the time series for prediction of V_{SET} and V_{RESET}, see Table I. For the determination of the constants included in the equations and the number of terms and the type of models, see ref. [22, 25]. An Auto Regressive AR (1) model was employed for V_{SET} data, the V_{RESET} model proposed, in this case for the absolute value, is an AR (4) model with null coefficients in cycles t-1, t-2 and t-3:

TSA analytical expressions for prediction along a RS series for V_{SET} and V_{RESET}
$Vset_t = 1.68 + 0.3153\, Vset_{t-1}$
$Vreset_t = 0.3536 + 0.3217\, Vreset_{t-4}$

Table I. Time series analytical expressions based on a first order (V_{SET}) and fourth order (V_{RESET}) TSA autoregressive models.

See in Fig. 6 the measured and modeled values of the set and reset voltages, which were obtained by using the expressions of Table I. As can be seen, a reasonably good prediction can be performed for the cycle-to-cycle variability. This type of modeling, as far as we know, is the most accurate approach to deal with cycle-to-cycle variability because in addition to models where the V_{RESET} and V_{SET} variations are considered, the RS memory effects linked to resistive switching and past dependencies can be taken into account. It is also important to highlight that the time series is formulated accounting for the statistical features of the whole series; therefore, these characteristics are included in the corresponding analytical expression "on average". In this respect, the model reproduces the ups and downs (trend) of the experimental data; nevertheless, the sudden peaks in the data cannot be reproduced with a model that it's forged with the averaged features of the whole series. It is important to highlight that this sort of variability is important in the context of hardware neural networks, since although the training process could be affected by the variations in a conductance multilevel operation regime, variability could also compensate training weaknesses such as overfitting, when using memristors to implement synaptic devices.

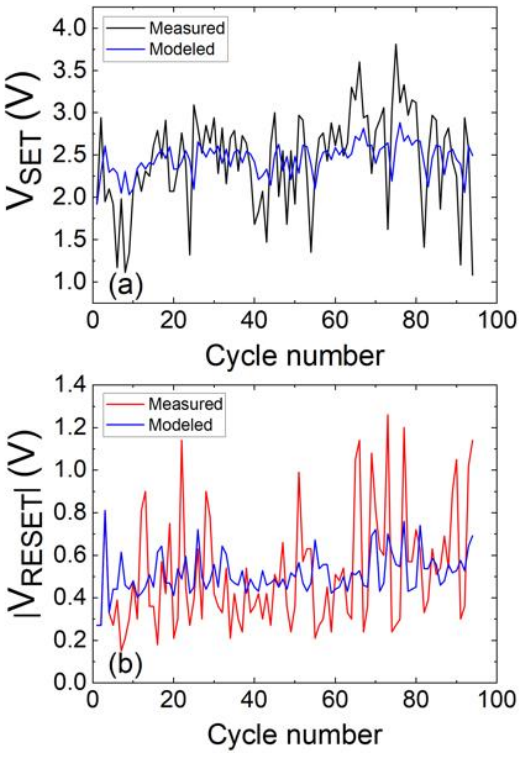

Figure 6. (a) V_{SET} (b) $|V_{RESET}|$ versus cycle number for the RS series under consideration.

Stanford model parameters			
Device Parameters	**Unit**	**Resistive Switching**	
		SET	**RESET**
V_o	V	0.75	0.45
I_0	mA	0.2	18
g_0	nm	0.2	0.143
ν_0	m/s	5×10^6	
α	-	3	
β	-	1	28
γ_0	-	16	44

Table II. Stanford model parameters employed for the experimental device under study.

Finally, a simulation based on the Stanford model [27-28] has been implemented (see the results in Fig. 7). A reasonably good fit of the experimental curves was obtained using different sets of parameters for the set and reset curves, as it was proposed in ref. [28], (see Fig. 7a). This fact shows the flexibility of the model, it works reasonably well although the nature of the dielectric could lead to complex charge transport mechanisms to explain the device operation. We have included the time series formula (Table I) and we were able to account for the experimental cycle-to-cycle variability we measured (Figs. 3, 6 and 7b) under the needed transformations to describe the resistive switching parameters variability in terms of the internal Stanford model parameters. This modeling was devoted to the reset and set voltages; nevertheless, other effects of the stochasticity inherent to resistive switching, such as different conductive filaments geometries, take place in each cycle. Therefore, other features (current levels, I-V curve shapes…) would have to be considered from the modeling viewpoint in the future.

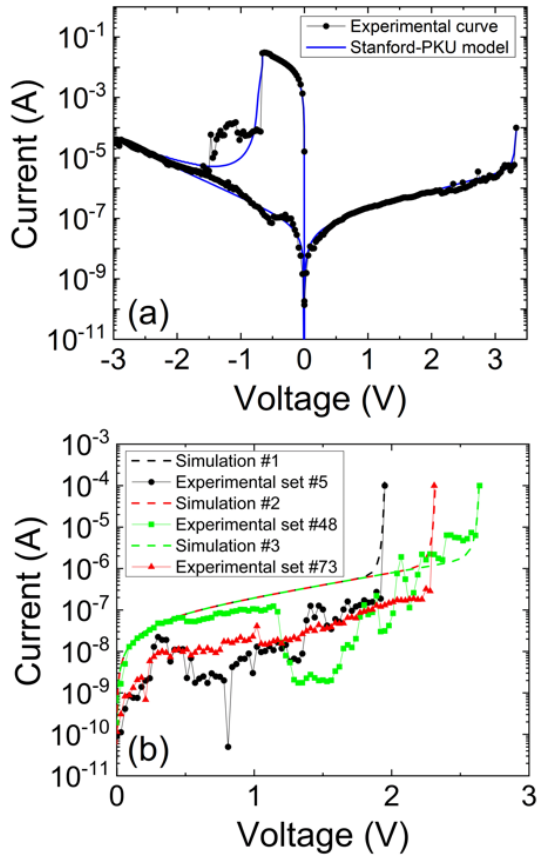

Figure 7. (a) Experimental cycle (black symbols) vs. voltage for the device measured. Modeled data employing the Stanford model (blue line). (b) Simulations as result of implementing the TSA expression of V_{SET} on the Stanford model (dashed lines) and experimental cycles (symbols).

4. Conclusions

We have measured and modeled memristors fabricated with the Au/Ti/h-BN/Au/Ti stack. Resistive switching (RS) operation has been analyzed; in particular, the evolution of the set and reset parameters along a RS series. Time series analysis techniques were employed to obtain analytical expressions to describe cycle-to-cycle variability. The equations obtained have been incorporated in the Stanford model to correctly reproduce the experimental measurements.

References

[1] L. Chua, "Memristor-The missing circuit element", in IEEE Transactions on Circuit Theory, vol. 18, no. 5, pp. 507-519, 1971.

[2] M. Lanza, et al., "Recommended methods to study resistive switching devices", Advanced Electronics Materials, 5, 1800143, 2019.

[3] M.A. Villena, J.B. Roldán, F. Jiménez-Molinos, E. Miranda, J. Suñé, M. Lanza, "SIM2RRAM: A physical model for RRAM devices simulation", Journal of Computational Electronics, 16, pp. 1095-1120, 2017.

[4] F. Pan, S. Gao, C. Chen, C. Song, F. Zeng, "Recent progress in resistive random access memories: materials, switching mechanisms and performance", Materials Science and Engineering, 83, pp. 1-59, 2014.

[5] D. Ielmini, "Modeling the universal set/reset characteristics of bipolar RRAM by field-and temperature-driven filament growth", IEEE Transactions on Electron Devices, 58(12), pp. 4309-4317, 2015.

[6] D. Ielmini, R. Waser. "Resistive Switching: From Fundamentals of Nanoionic Redox Processes to Memristive Device Applications", Wiley-VCH, 2015.

[7] F. Hui, M. A. Villena, W. Fang, A.-Y. Lu, J. Kong, Y. Shi, X. Jing, K. Zhu, M. Lanza, "Synthesis of large-area multilayer hexagonal boron nitride sheets on iron substrates and its use in resistive switching devices", 2D Materials, 5, 031011, 2018.

[8] Y. Shi, X. Liang, B. Yuan, V. Chen, H. Li, F. Hui, Z. Yu, F. Yuan, E. Pop, H.-S. P. Wong, M. Lanza "Electronic synapses made of layered two-dimensional materials", Nature Electronics 1, 458–465, 2018.

[9] Y. Illarionov, T. Knobloch, M. Lanza, D. Akinwande, M.I. Vexler, T. Mueller, M. Lemme, G. Fiori, F. Schwierz, and T. Grasser, "Insulators for 2D Nanoelectronics", Nature Communications, 11, 3385, 2020.

[10] M. Lanza, Q. Smets, C. Huyghebaert, L.-J. Li, "Yield, variability, reliability, and stability of two-dimensional materials based solid-state electronic devices", Nature Communications, 11, 5689, 2020.

[11] F.M. Puglisi, N. Zagni, L. Larcher, P. Pavan, "Random Telegraph Noise in Resistive Random Access Memories: Compact Modeling and Advanced Circuit Design", IEEE Transactions on Electron Devices, 65, pp. 2964 – 2972, 2018.

[12] M. Zidan, J.P. Strachan, W. Lu, "The future of electronics based on memristive systems", Nature Electronics, 1, 22-29, 2018.

[13] S. Yu, Y. Wu, R. Jeyasingh, D. Kuzum, H.-S. Wong, "An electronic synapse device based on metal oxide resistive switching memory for neuromorphic computation", IEEE Transactions on Electron Devices, 58 (8), pp. 2729–2737, 2011. doi: 10.1109/TED.2011.2147791.

[14] N. Zheng, P. Mazumder, "Learning in Energy-Efficient Neuromorphic Computing: Algorithm and Architecture Co-Design", Wiley, 2019.

[15] C. Acal, J.E. Ruiz-Castro, A. M. Aguilera, F. Jiménez-Molinos, J.B. Roldán, "Phase-type distributions for studying variability in resistive memories", Journal of Computational and Applied Mathematics, 345, pp. 23–32, 2019.

[16] E. Pérez, D. Maldonado, C. Acal, J.E. Ruiz-Castro, F.J. Alonso, A.M. Aguilera, F. Jiménez-Molinos, Ch. Wenger, J.B. Roldán, "Analysis of the statistics of device-to-device and cycle-to-cycle variability in TiN/Ti/Al:HfO_2/TiN RRAMs", Microelectronics Engineering, 214, pp. 104-109, 2019.

[17] M. C. Aguilera-Morillo, A. M. Aguilera, F. Jiménez-Molinos, J.B. Roldán, "Stochastic Modelling of Random Access Memories Reset Transitions", Mathematics and Computers in Simulation, 159 pp. 197-209, 2019.

[18] A.M. Aguilera, C. Acal, M.C. Aguilera-Morillo, F. Jiménez-Molinos, J.B. Roldán, "Homogeneity problem for basis expansion of functional data with applications to resistive memories", Mathematics and Computers in Simulation, in press, 2021.

[19] J.E. Ruiz-Castro, C. Acal, A.M. Aguilera, M.C. Aguilera-Morillo, J.B. Roldán, "Linear-Phase-Type probability modelling of functional PCA with applications to resistive memories", Mathematics and Computers in Simulation, in press, 2021.

[20] S. Aldana, P. García-Fernández, R. Romero-Zaliz, M.B. González, F. Jiménez-Molinos, F. Gómez-Campos, F. Campabadal, J.B. Roldán, "Resistive Switching in HfO2 based valence change memories, a comprehensive 3D kinetic Monte Carlo approach", Journal of Physics D: Applied Physics, 53, 225106, 2020.

[21] A. Padovani, L. Larcher, O. Pirrotta, L. Vandelli, G. Bersuker, “Microscopic Modeling of HfOx RRAM Operations: From Forming to Switching”, IEEE Transactions on Electron Devices, 62(6), pp. 1998-2006, 2015.

[22] J. B. Roldán, F. J. Alonso, A. M. Aguilera, D. Maldonado, M. Lanza, “Time series statistical analysis: a powerful tool to evaluate the variability of resistive switching memories”, Journal of Applied Physics, 125, 174504, 2019.

[23] F.J. Alonso, D. Maldonado, A.M. Aguilera, J. B. Roldan, "Memristor variability and stochastic physical properties modeling from a multivariate time series approach", Chaos, Solitons & Fractals, 143, 110461, 2021.

[24] N. Rodriguez, D. Maldonado, F.J. Romero, F.J. Alonso, A.M. Aguilera, A. Godoy, F. Jimenez-Molinos, F.G. Ruiz, J.B. Roldan, "Resistive switching and charge transport in laser-fabricated graphene oxide memristors: a Time Series and Quantum Point Contact modelling approach", Materials, 12, 3734, 2019.

[25] P. J. Brockwell, R. A. Davis, “Introduction to Time Series and Forecasting”, Second Edition, Springer, 2002.

[26] S.Bisgaard, M.Kulahci, “Time series analysis and forecasting by example”, Wiley, 2011.

[27] X. Guan, S. Yu, and H-S.P Wong, “A SPICE Compact Model of Metal Oxide Resistive Switching Memory with Variations”, IEEE Elec. Dev. Lett., vol. 33, pp. 1405-1407, 2012.

[28] Z. Jiang, Y. Wu, S. Yu, L. Yang, K. Song, Z. Karim, H.-S. P. Wong, "A Compact Model for Metal–Oxide Resistive Random Access Memory With Experiment Verification", IEEE Transactions on Electron Devices, vol. 63, no. 5, pp. 1884-1892, May 2016

3.3. TSSA in graphene oxide memristors

Novel laser fabricated graphene oxide devices are investigated in this section making use of the TSSA and the Quantum Point Contact model. It has been proved that RS phenomena takes place as a filament is created bridging the electrodes which makes the devices suitable memristor candidates. Thus, by employing this kind of material, some properties such as flexibility and conduction are offered in addition to the required non-volatility. The fabrication process is also an important issue here since these devices could be easily implemented in the industrial manufacturing context due to its simplicity. In this sense, no lithography masks are required and the electrodes could be chosen accounting with a great versatility.

The following section is an already published work [Rodríguez2019].

N. Rodríguez et al.

Materials (2019)

Rodriguez, N., Maldonado, D., Romero, F. J., Alonso, F. J., Aguilera, A. M., Godoy, A., ... & Roldan, J. B. (2019). Resistive Switching and Charge Transport in Laser-Fabricated Graphene Oxide Memristors: A Time Series and Quantum Point Contact Modeling Approach. Materials, 12(22), 3734. doi: 10.3390/ma12223734.

Quality metrics

Data base	Rating	Quartile
Web of Science	Impact factor: 3.62	Q2
Scimago	Scientific journal ranking: 0.7	Q2

Publication citations (23-03-2022)

Google Scholar	Web of Science
7	**5**

MATERIALS

Article

Resistive Switching and Charge Transport in Laser-Fabricated Graphene Oxide Memristors: A Time Series and Quantum Point Contact Modeling Approach

N. Rodriguez[1,2,*], D. Maldonado[1], F. J. Romero[1,2], F. J. Alonso[3], A.M. Aguilera[3], A. Godoy[1,2], F. Jimenez-Molinos[1], F.G. Ruiz[1,2] and J. B. Roldan[1]

[1] *Department of Electronics and Computer Technology, Science Faculty, University of Granada, Av. Fuentenueva s/n, 18071 Granada, Spain; davidmaldonado@correo.ugr.es (D.M.); franromero@ugr.es (F.J.R.); agodoy@ugr.es (A.G.); jmolinos@ugr.es (F.J.M.); franruiz@ugr.es (F.G.R.); jroldan@ugr.es (J.B.R.)*

[2] *Pervasive Electronics Advanced Research Laboratory, University of Granada, 18071 Granada, Spain*

[3] *Department of Statistics and Operations Research, Science Faculty, University of Granada, Av. Fuentenueva s/n, 18071 Granada, Spain; falonso@ugr.es (F.J.A.); aaguiler@ugr.es (A.M.A.)*

* *Correspondence: noel@ugr.es*

Received: 17 September 2019; Accepted: 10 November 2019; Published: 13 November 2019

Abstract: This work investigates the sources of resistive switching (RS) in recently reported laser-fabricated graphene oxide memristors by means of two numerical analysis tools linked to the Time Series Statistical Analysis and the use of the Quantum Point Contact Conduction model. The application of both numerical procedures points to the existence of a filament connecting the electrodes that may be interrupted at a precise point within the conductive path, resulting in resistive switching phenomena. These results support the existing model attributing the memristance of laser-fabricated graphene oxide memristors to the modification of a conductive path stoichiometry inside the graphene oxide.

Keywords: memristor; RRAM; variability; time series modeling; autocovariance; graphene oxide; laser

1. Introduction

Memristors have shown great potential in the context of neuromorphic circuits. Their operation, based on resistance modulation by means of ion transport and redox reactions, leads to the creation of regions of different conductivity mimicking neuronal synapses in a coherent and natural manner. Consequently, memristors are of most interest for the fabrication of optimized hardware that aims to design and implement artificial neural networks [1–3]. This potential, along with their intrinsic facet of non-volatility, poses the set of features needed by memristors to become the cornerstone for computation schemes beyond of the classical von Neumann paradigm, such as neuromorphic computing. This new focus will be essential to push forward the artificial intelligence challenges that the industry is facing currently [2,3].

From a more general perspective, the outstanding features of memristors make them also suitable for applications that run through non-volatile memories, Internet of Things (IoT) devices, 5G, etc. Among their promising characteristics, the following can be highlighted: fast read/write times for the set and reset processes, low power consumption, scalability and CMOS technology compatibility among others [3–7].

The physics behind memristors is strongly dependent on the materials employed and the details of their fabrication process. In this respect, there is a plethora of recent experimental, modeling and simulation studies on technologies that make use of transition metal oxides as the switching dielectric [4,5,8–15]. However, in the field of memristors based on 2D materials, the amount of studies and published manuscripts is much lower. In this context, the difficulties related to the creation of high quality metal contacts, the purity of the materials and the fabrication details pose extra difficulties for dealing with all of the facets of the study of these devices, and in particular, in regards to the physical simulation and modeling.

In the 2D material memristors landscape, there are h-BN based devices, memristors with a different number of graphene layers or other 2D materials that are employed for oxygen ion scavenging and other particular purposes [3,16,17]. Among all the 2D materials-based contenders, the laser fabrication of memristors based on graphene oxide (GO) was recently introduced [18]. GO is a highly functionalized form of polycrystalline nanographene that is decorated with oxygen-containing groups [19]. The use of GO as a memristive material takes advantage of its inherent 2D materials potential with respect to conduction and structural flexibility properties while simultaneously including its non-volatility and electrical plasticity [20], as expected in ideal memristors [21].

The implementation of a laser-assisted fabrication protocol provides the device with several attractive features for its potential industrial implementation: (i) the fabrication process is very simple, comprising a limited number of steps; (ii) there is no need for lithographic masks since the laser itself defines the geometry of the memristor; (iii) the devices do not require scarce or hazardous materials for their fabrication; (iv) the resistive switching behavior originates in the GO (and not in the electrodes) adding versatility from the contacting electrodes perspective and (v) the supporting substrate can be selected with versatility from a rigid surface to flexible polymers for conformal integration.

The novelty of the devices employed here results in a lack of studies linked to their resistive

switching features, both from the physical modeling and experimental viewpoint. Therefore, the physics lying behind their operation has only had its surface scratched [18]. In this work, we intend to tackle this issue making use of well-established numerical techniques previously developed for more "conventional" memristors that are developed with 3D stacks of transitions metal oxides [13,15,22,23]. Therefore, in this manuscript, we specifically deal with the characterization and analysis of resistive switching processes and charge conduction in laser-fabricated graphene oxide (GO) memristors [18] from a statistical perspective. We do not focus this study on the digital performance of the devices; we consider instead their conductance variation in an analogic manner, as it is the proper approach for neuromorphic applications.

The device variability has also been considered in this study, specifically by using Time Series Statistical Analysis (TSSA) [24–27]. From the statistical viewpoint, information can be extracted that is related to the correlation of successive RS cycles and the inherent stochasticity of RS memristors operation. The quantum properties of conduction along the conductive filaments that short the electrodes have been scrutinized by means of the Quantum Point Contact (QPC) model as described in [15,22].

Therefore, the outline of this work is as follows: the fabricated devices and measurement process are described in Section 2, and the numerical procedure, the main results and the discussion are explained in Section 3. Finally, the conclusions are given in Section 4.

2. Device Fabrication and Measurement

The memristors fabricated for this study are fully based on the process described in [18] and summarized in Figure 1. The raw precursor material is a graphene oxide colloid (4 mg/mL) prepared following a modified version of Hummers and Offerman's method [28]. The GO colloid is deposited by drop-casting onto a PET (Polyethylene terephthalate, 3 M) film (0.5 mL/cm2) and left on a 3D-shaker for 48 h until the water has completely evaporated (293 K, RH 50%). The CNC-driven laser is then applied in a rectangular pattern with the precise power that reduces the GO at the point where memristance is manifested (Plaser ~ 70 mW, λ = 405 nm) [18]. After the laser treatment, the volume of the reduced GO increases; the height difference between the GO film and the laser-treated GO is ~10 µm, determined using a DekTak XT profilometer from Bruker (Bruker Corporation, MA, USA). The devices were contacted using micro drops of conductive carbon-based paste (Bare Conductive Electric Paint, London, UK).

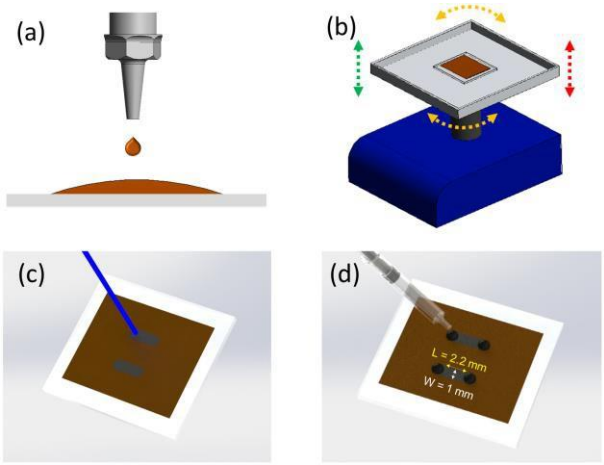

Figure 1. Schematic representation of the fabrication steps for graphene oxide memristors produced by laser. Graphene Oxide colloid is drop-casted on a PET substrate (**a**) and left 48 h on a 3D shaker for water evaporation (**b**). Then the laser diode is applied (70 mW) to partially reduce the GO resulting in the

memristive structures (**c**). Finally, electrical contacts are created by depositing microdrops of organic bare conductive paint (**d**).

The electrical measurement experiments were performed with the support of a two-channel Keysight® B2902A (Keysight Technologies, Inc., CA, USA) precision source-measurement unit controlled by Easy-Expert® software (version 6.2.1927.7790, CA, USA). Figure 2a presents measured current–voltage characteristics showing two consecutive voltage cycles extracted from an L = 2.2 mm, W = 1 mm laser-fabricated graphene oxide memristor. These curves reveal the characteristic fingerprint of a memristor device that is determined by a pinched hysteresis loop closed in the origin of the current–voltage axis [29]. Figure 2b depicts the time evolution of the current when a −3 to 3 V symmetric voltage ramp is applied, illustrating the fast and abrupt transitions of the resistance.

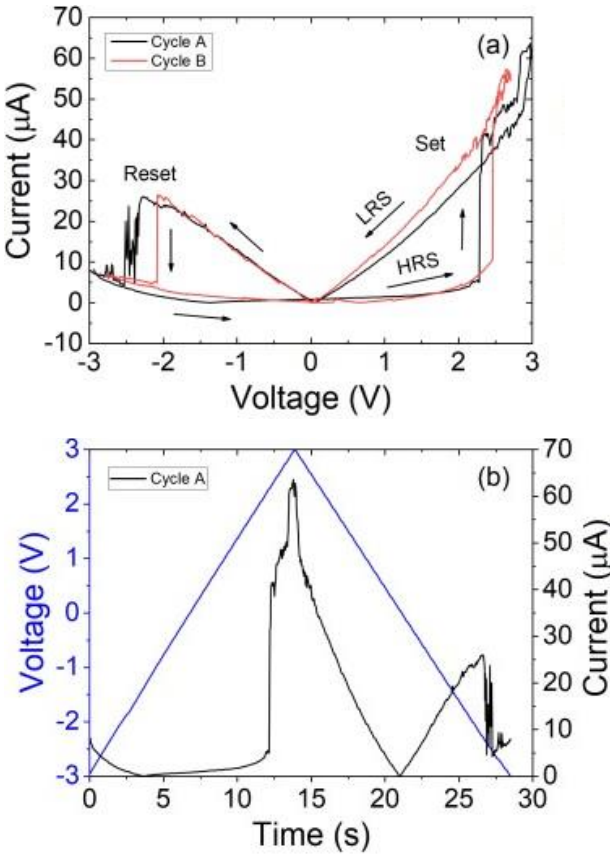

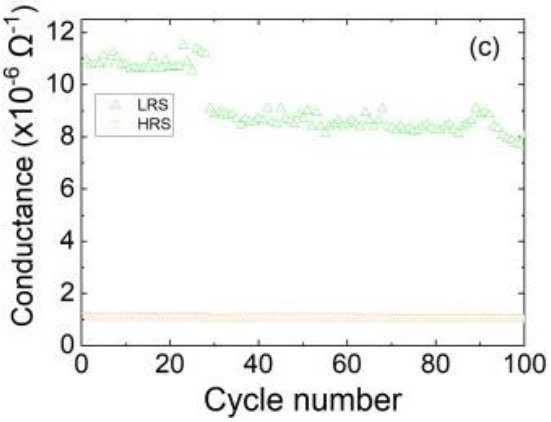

Figure 2. (**a**) Experimental current versus voltage for two different cycles within a resistive switching series. A ramped voltage with step of 10 mV was employed in the measurement process. (**b**) Voltage and current versus time for the cycle A shown previously. (**c**) Conductance values obtained during device cycling with limited compliance current [18]. The resistance was extracted in the range [−1,1] V of the current–voltage characteristics.

Figure 2c shows the device conductance extracted under successive device cycling from a laser-fabricated GO memristor. These measurements constitute the input of the Time Series Statistical Analysis discussed in Section 3. To avoid resistive switching degradation of the device, the current is limited to 20 μA [18]. As observed, the Low Resistance State (LRS) conductance presents a monotonic derivative, whereas the High Resistance State (HRS) conductance remains stable with cycling. The reader can notice the small conductance jump at cycle 28. This phenomenon is attributed to the defective nature of GO, which is heavily decorated with oxygen, hydroxyl and epoxy groups. Spontaneous movements of functional groups along the conductive path yields to local modification of the stoichiometry of the sample and, therefore, to the modification of its conductance [19]. Further structural and electrical details of Laser-Fabricated Graphene Oxide Memristors can be found in reference [18], including spectroscopic characterization, retention time and variability. The electrical

results (average HRS/LRS ratio, 6; retention time, 10^4 s; endurance, 10^2 cycles [18]) can be considered to be promising given the early stage of development of this technology, and they are expected to become more attractive once advanced laser lithography tools are employed for the development of GO laser-fabricated memristors.

3. Numerical Analysis of Charge Conduction and Resistive Switching Mechanisms, Results and Discussion

3.1. Time Series Statistical Analysis (TSSA)

The TSSA has been employed to characterize the statistical features of the device operation variables through a long RS series [24]. In particular, the resistances in the LRS and HRS have been studied. The Autocorrelation (ACF) and Partial Autocorrelation functions (PACFs) have been calculated and represented in Figure 3 (see also Supplementary Materials). As can be observed, the degree of correlation between the measurements of previous cycles is very high with respect to other technologies (see, for instance, Reference [24] for other technologies with transition metal oxides as a dielectric).

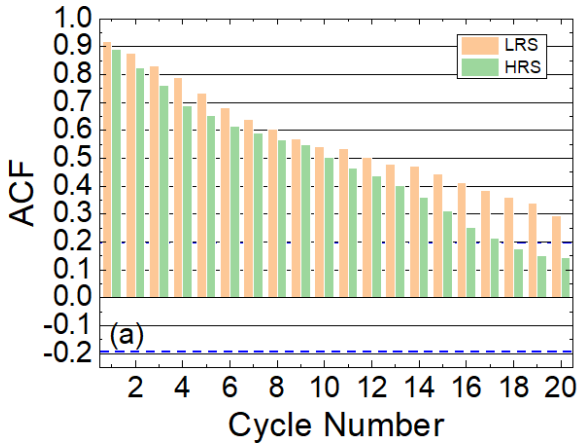

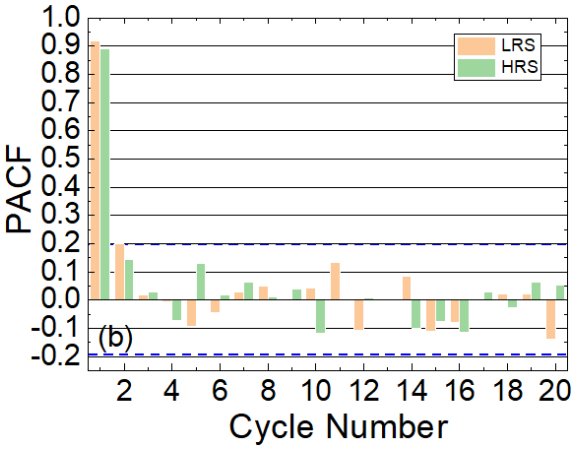

Figure 3. (**a**) ACF and (**b**) PACF versus cycle lag for the inverse of the values shown in Figure 2c. These functions show the ACF and PACFs versus cycle number that represent the distance apart in cycles within a RS series, see Reference [24]. The ACF and PACF minimum threshold bounds for the devices under study are ±0.195 for both plots (see the supplementary information for the information linked to the calculation of these threshold bounds), shown with dashed lines. We have considered 100 cycles in our series; this is a reasonable number to extract information on the correlation between the data and to extract a TSSA model.

It can be concluded that to obtain these results, the high conductivity region does not change much between different cycles; this feature is the main source of the correlation. This fact leads us to assume a filamentary-like conduction mechanism where a channel of high conductivity region is formed after a set process that shorts the electrodes. In addition, the high correlation suggests that the high conductivity path does not change much between cycles, keeping unaltered the main conduction properties. It is reasonable to assume that it is just a narrow region that changes in between two larger high conductivity regions that remain mostly unaltered. This narrowing is modified leading to the creation of a fully-formed high conduction path that shorts the electrodes or that isolates them in case the path is ruptured, leading to two large virtual

electrodes (filaments remnants connected to the electrodes [6]).

We have employed TSSA to analytically describe the dependencies of the LRS and HRS resistances on previous cycles throughout the complete RS series (see in the Supplementary Material a summary of the steps needed to develop a TSSA model). The general expression employed was based on an Autoregressive (AR) approach [24], as seen in Equation (1):

$$R_{LRS/HRS}(t) = \Phi_1 \times R_{LRS/HRS}(t\text{-}1) + \Phi_2 \times R_{LRS/HRS}(t\text{-}2) + \ldots + \Phi_p \times R_{LRS/HRS}(t\text{-}p) + \varepsilon_t \quad (1)$$

where t stands for the cycle number within a long resistive switching series. In this modeling technique, the order (p) is linked to the physics governing RS process in these devices. No previous knowledge is assumed to extract the information from experimental data because the underlying technology details and physics mechanisms are "hidden" in the RS data collected. The TSSA models are empirical and determine the weights set (Φ_1, ..., Φ_p), and the model order is determined by p. The term ε_t is a residual that accounts for the model error (the difference between the measured and the modeled value). In this respect, we focus here on the statistical information of the measured data without any previous assumption linked to the underlying physics.

The resistance at the LRS can be modeled with an AR(2) approach, as seen in Equation (2).

$$R_{LRS(t)} = 4936.018 + 0.7306 \times R_{LRS(t-1)} + 0.229 \times R_{LRS(t-2)} + \varepsilon_t. \quad (2)$$

The HRS resistance works well with an AR(1), as described in Equation (3).

$$R_{HRS(t)} = 69955.16 + 0.9236 \times R_{HRS(t-1)} + \varepsilon_t. \quad (3)$$

The time series residuals that are left after a comparison with the experimental data show a white noise behavior; therefore, we can conclude that all the statistical information is included in the models described in Equations (2) and (3). It is important to highlight at this point that TSSA is an ideal tool used to analyze data in a series (such as a RS series); in this respect, it works well for cycle-to-cycle variability analysis if we consider parameters such as the set and reset voltages or LRS/HRS device resistances.

3.2. *Quantum Point Contact Modeled Conduction*

An analysis of the I–V curves in terms of second derivative dependencies has been performed following [22]. In this respect, it is important to highlight that a screening procedure was developed in [22] to detect charge conduction features that can be modeled with the QPC model. The results are shown in Figure 4.

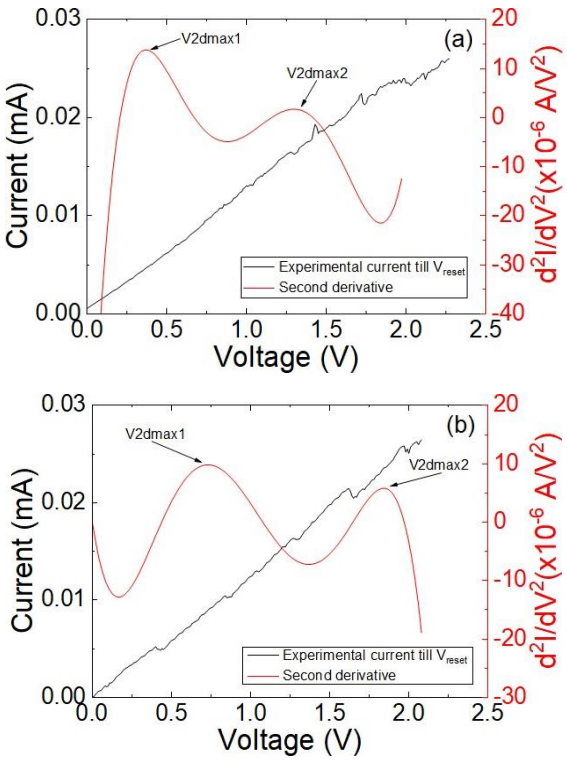

Figure 4. Experimental current versus applied voltage in the devices under study including the second derivative of the current versus voltage for cycle A (**a**) and cycle B (**b**) shown in Figure 2a. A pattern in agreement with the QPC model is seen in [22].

The characteristic one or two maxima in the current second derivative are seen in these devices. Following previous results [22], this behavior could be regarded as a footprint of the existence of QPC conduction. However, the fitting of the second derivative leads to an N parameter (number of channels in the QPC model [22]) lower than the unity, which is inconsistent with the QPC model. In this respect, a new representation is obtained assuming a series resistance of 5000 Ω (second numerical derivative of the corrected current, I, taking into account the series resistance is shown in Figure 5). This series resistance is reasonable considering the device resistance both at LRS and HRS, see Figure 2c. In this manner, the voltage on the constriction that leads to quantum effects can be obtained accurately.

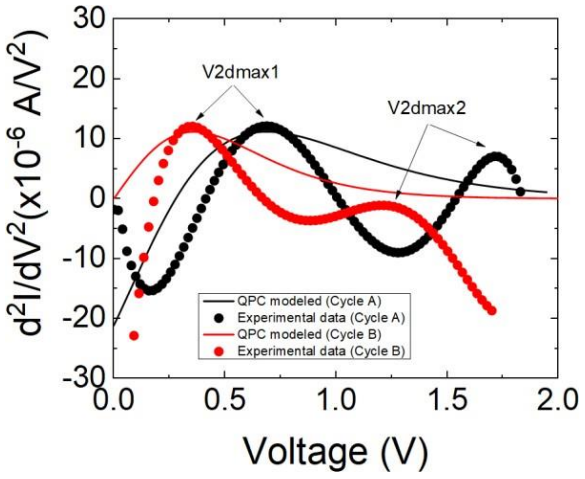

Figure 5. Second derivative of the experimental current (symbols) versus voltage in the device under study for the two reset curves shown in Figure 2. The analytically calculated QPC modeled current second derivative (solid lines) is also shown. The QPC model parameters employed for cycle A are the following: $\alpha = 6.5\ (\mathrm{eV})^{-1}$; $\beta = 0.4$; $\Phi = 0.13$ eV; $N = 1$; and for cycle B: $\alpha = 7.5(\mathrm{eV})^{-1}$; $\beta = 0.5$; $\Phi = 0.055$ eV; $N = 1$.

In both cases, there is only one channel for charge conduction, and this result corresponds to a low dimensional high conductivity region. Also, a low energy barrier is observed, suggesting an almost ohmic charge conduction regime, although in a low conductivity regime when compared with conventional memristors based on transition metal oxides.

The previous results support the existing model that attributes resistive switching in laser-reduced GO to the non-uniformity in the number and location of functional groups that create nanometric-size regions of different conductance [18]. The sp^2 regions present high-conductivity but they are interrupted by low-conductivity sp^3 domains at a nanoscale level that are responsible for a low current flow [30,31]. At certain locations within the structure, under the action of the voltage bias in the HRS, large electrostatic potential gradients are created in the nanometric-size low-conductivity regions, resulting in large localized electric fields. Assisted by Joule heating effects, these electric fields can trigger the drift of oxygen and oxygen-containing groups due to the low migration barrier in GO [32,33]. The group migration at a specific point within the structure establishes a continuity path of sp^2 domains, which was previously impeded by a nanometric sp^3 domain (quantum point contact as identified in this work) and leads to a LRS [18]. Finally, it is worth mentioning that the findings in this work, disclosing the filamentary nature of the conduction in laser fabricated GO memristors, open the path for scaling the devices down by using high precision laser scribing systems.

4. Conclusions

The origins of resistive switching in recently introduced laser-fabricated graphene oxide memristors have been studied by using statistical and numerical analysis tools. Time Series Statistical Analysis applied to the high and low resistance states of the devices has shown high correlation that supports the model of the formation of a conductive filament as the main

source of the device internal resistance switching. Furthermore, the quantum point contact conduction method has pointed to the existence of a quantized point of conduction, which is formed and destroyed, connecting the electrodes by means of a conductive path. These results underpin the existing theory that attributes the memristance in GO to the formation of a highly reduced path in which stoichiometry is modified at a precise point leading to the resistive switching.

Supplementary Materials: The following are available online at http://www.mdpi.com/19961944/12/22/3734/s1.

Author Contributions: Conceptualization, N.R., F.G.R., F.J.M. and J.B.R.; Experiments, F.J.R. and N.R.; Analytical and numerical tools, D.M., F.J.A., A.M.A., J.B.R.; Figures, D.M., F.J.R.; Writing-original draft, N.R. and J.B.R; Writing-review and discussion A.G., F.J.M. and F.G.R.

Funding: The authors thank the support of the Spanish Ministry of Science, Innovation and Universities under projects TEC2017-89955-P, TEC2017-84321-C4-3-R, MTM2017-88708-P and project PGC2018-098860-B-I00 (MCIU/AEI/FEDER, UE), and the predoctoral grant FPU16/01451.

Conflicts of Interest: The authors declare no conflict of interest.

References

1. Yu, S.; Wu, Y.; Jeyasingh, R.; Kuzum, D.; Wong, H.S. An electronic synapse device based on metal oxide resistive switching memory for neuromorphic computation. *IEEE Trans. Electron Devices* **2011**, *58*, 2729–2737. [CrossRef]
2. Yu, S. *Neuro-Inspired Computing Using Resistive Synaptic Devices*; Springer: NY, USA, 2017; ISBN 978-3-319-54312-3.
3. Lanza, M.; Wong, H.-P.P.; Pop, E.; Ielmini, D.; Strukov, D.; Regan, B.C.; Larcher, L.; VillenaJ, M.A.; Yang, J.J.; Goux, L.; et al. Recommended methods to study resistive switching devices. *Adv. Electron. Mater.* **2019**, *5*, 1800143. [CrossRef]
4. Pan, F.; Gao, S.; Chen, C.; Song, C.; Zeng, F. Recent progress in resistive random access memories: Materials, switching mechanisms and performance. *Mater. Sci. Eng.* **2014**, *83*, 1–59. [CrossRef]
5. Ielmini, D.; Waser, R. *Resistive Switching: From Fundamentals of Nanoionic Redox Processes to Memristive Device Applications*; Wiley-VCH: Weinheim, Germany, 2017; ISBN 978-3-527-33417-9.
6. Waser, R.; Aono, M. Nanoionics-based resistive switching. *Nat. Mater.* **2007**, *6*, 833–840. [CrossRef] [PubMed]
7. Villena, M.A.; Roldan, J.B.; Jimienez-Molinos, F.; Miranda, E.; Suñe, J.; Lanza, M. SIM2RRAM: A physical model for RRAM devices simulation. *J. Comput. Electron.* **2017**, *16*, 1095–1120. [CrossRef]
8. Long, S.; Cagli, C.; Ielmini, D.; Liu, M.; Suñe, J. Reset statistics of NiO-based resistive switching memories. *IEEE Electron Device Lett.* **2011**, *32*, 1570–1572. [CrossRef]
9. Long, S.; Lian, X.; Ye, T.; Cagli, C.; Perniola, L.; Miranda, E.; Liu, M.; Suñe, J. Cycle-to-cycle intrinsic RESET statistics in HfO2-based unipolar RRAM devices. *IEEE Electron Device Lett.* **2013**, *34*, 623–625. [CrossRef]
10. Gonzalez-Cordero, G.; Roldan, J.B.; Jimenez-Molinos, F.; Suñé, J.; Long, S.; Liu, M. A new model for bipolar RRAMs based on truncated cone conductive filaments, a Verilog-A approach. *Semicond. Sci. Technol.* **2016**, *31*, 115013. [CrossRef]
11. Tsuruoka, T.; Terabe, K.; Hasegawaand, T.; Aono, M. Forming and switching mechanisms of a cation-migration-based oxide resistive memory. *Nanotechnology* **2010**, *21*, 425205. [CrossRef]
12. Padovani, A.; Larcher, L.; Pirrotta, O.; Vandelli, L.; Bersuker, G. Microscopic Modeling of HfO x RRAM Operations: From

Forming to Switching. *IEEE Trans. Electron Device* **2015**, *62*, 1998–2006. [CrossRef]

13. Aldana, S.; Garcia-Fernandez, P.; Rodriguez-Fernandez, A.; Romero-Zaliz, R.; Gonzalez, M.B.; Jimenez-Molinos, F.; Campabadal, F.; Gomez-Campos, F.; Roldan, J.B. A 3D Kinetic Monte Carlo simulation study of Resistive Switching processes in Ni/HfO_2/Si-n^+-based RRAMs. *J. Phys. D Appl. Phys.* **2017**, *50*, 335103. [CrossRef]
14. Guy, J.; Molas, G.; Blaise, P.; Bernard, M.; Roule, A.; Carval, G.L.; Delaye, V.; Toffoli, A.; Ghibaudo, G.; Clermidy, F.; et al. Investigation of Forming, SET, and Data Retention of Conductive-Bridge Random-Access Memory for Stack Optimization. *IEEE Trans. Electron Devices* **2015**, *62*, 3482–3489. [CrossRef]
15. Villena, M.A.; Roldan, J.B.; Gonzalez, M.B.; Gonzalez-Rodalas, P.; Jimenez-Molinos, F.; Campabadal, F.; Barrera, D. A new parameter to characterize the charge transport regime in Ni/HfO_2/Si-n^+-based RRAMs. *Solid State Electron.* **2016**, *118*, 56–60. [CrossRef]
16. Hui, F.; Villena, M.A.; Fang, W.; Lu, A.-Y.; Kong, J.; Shi, Y.; Jing, X.; Zhu, K.; Lanza, M. Synthesis of large-area multilayer hexagonal boron nitride sheets on iron substrates and its use in resistive switching devices. *2D Mater.* **2018**, *5*, 031011. [CrossRef]
17. Shi, Y.; Liang, X.; Yuan, B.; Chen, V.; Li, H.; Hui, F.; Yu, Z.; Yuan, F.; Pop, E.; Wong, H.-S.P.; et al. Electronic synapses made of layered two-dimensional materials. *Nat. Electron.* **2018**, *1*, 458–465. [CrossRef]
18. Romero, F.J.; Toral-Lopez, A.; Ohata, A.; Morales, D.P.; Ruiz, F.G.; Godoy, A.; Rodriguez, N. Laser-Fabricated Reduced Graphene Oxide Memristors. *Nanomaterials* **2019**, *9*, 897. [CrossRef] [PubMed]
19. Dimiev, A.M.; Eigler, S. *Graphene Oxide: Fundamentals and Applications*; Wiley: NJ, USA, 2016; ISBN 978-1-119-06940-9.
20. Romero, F.J.; Toral-Lopez, A.; Ohata, A.; Morales, D.P.; Ruiz, F.G.; Godoy, A.; Rodriguez, N. Photothermically Lithographed Graphene-Oxide Memristors for Neuromorphic Applications. In Proceedings of the International Conference on Memristive Materials, Devices & Systems (MEMRISYS), Dresden, Germany, 8–11 July 2019.
21. Porro, S.; Accornero, E.; Pirri, C.F.; Ricciardi, C. Memristive devices based on Graphene oxide. *Carbon* **2015**, *85*, 383–395. [CrossRef]
22. Roldan, J.B.; Miranda, E.; Gonzalez-Cordero, G.; Garcia-Fernandez, P.; Romero-Zaliz, R.; Gonzalez-Rodelas, P.; Aguilera, A.M.; Gonzalez, M.B.; Jimenez-Molinos, F. Multivariate analysis and extraction of parameters in resistive RAMs using the Quantum Point Contact model. *J. Appl. Phys.* **2018**, *123*, 014501. [CrossRef]
23. Villena, M.A.; Gonzalez, M.B.; Roldan, J.B.; Campabadal, F.; Jimenez-Molinos, F.; Gomez-Campos, F.M.; Suñe, J. An in-depth study of thermal effects in reset transitions in HfO_2 based RRAMs. *Solid State Electron.* **2015**, *111*, 47–51. [CrossRef]
24. Roldan, J.B.; Alonso, F.J.; Aguilera, A.M.; Maldonado, D.; Lanza, M. Time series statistical analysis: A powerful tool to evaluate the variability of resistive switching memories. *J. Appl. Phys.* **2019**, *125*, 174504. [CrossRef]
25. Yule, G.U. On a method of investigating periodicities in disturbed series, with reference to Wolfer's Sunspot Numbers. *Philos. Trans. R. Soc. Lond.* **1927**, *226*, 267–298. [CrossRef]
26. Bisgaard, S.; Kulahci, M. *Time Series Analysis and Forecasting by Example*; Wiley: NJ, USA, 2011; ISBN 978-0-470-54064-0.
27. Brockwell, P.J.; Davis, R.A. *Introduction to Time Series and Forecasting*, 2nd ed.; Springer: NY, USA, 2002.
28. Romero, F.J.; Rivadeneyra, A.; Toral-Lopez, V.; Castillo, E.; Garcia-Ruiz, F.; Morales, D.P.; Rodriguez, N. Design guidelines of laser reduced graphene oxide conformal thermistor for IoT applications. *Sens. Actuators A Phys.* **2018**, *274*, 148–154. [CrossRef]
29. Chua, L. Resistance switching memories are memristors. *Appl. Phys. A* **2011**, *102*, 765–783. [CrossRef]

30. Qi, M.; Bai, L.; Xu, H.; Wang, Z.; Kang, Z.; Zhao, X.; Liu, W.; Ma, J.; Liu, Y. Oxidized carbon quantum dot–graphene oxide nanocomposites for improving data retention of resistive switching memory. *J. Mater. Chem. C* **2018**, *6*, 2026–2033. [CrossRef]
31. Abunahla, H.; Mohammad, B.; Homouz, D.; Okelly, C.J. Modeling Valence Change Memristor Device: Oxide Thickness, Material Type, and Temperature Effects. *IEEE Trans. Circuits Syst. I Regul. Pap.* **2016**, *63*, 2139–2148. [CrossRef]
32. Dai, Y.; Shuang, N.; Li, Z.; Yang, J. Diffusion and desorption of oxygen atoms on graphene. *J. Phys. Condens. Matter* **2013**, *25*, 405301. [CrossRef]
33. Zhou, S.; Bongiorno, A. Origin of the Chemical and Kinetic Stability of Graphene Oxide. *Sci. Rep.* **2013**, *3*, 2484. [CrossRef]

Chapter 4.

4. Enhanced compact modeling in resistive memories

4.1. Series resistance extraction and inclusion in the Stanford model

In this section the role of the series resistance in a RRAM device is thoroughly explored as it is an important parasitic element not considered so often in the literature. It can influence in a significant way the conduction characteristics. We have developed an algorithm to be able to process hundreds of experimental curves from different devices in order to extract the value of the resistance. Moreover, set and reset voltages have been determined to study its relevance and possible relation to the resistance value in HfO_2 VCM memories. Another important aspect like modeling, essential to study the behavior of the devices, has been addressed by modifying the Stanford model and including the series resistance in the Verilog-A code as another parameter to consider. The latter is of special interest specially when dealing with experimental data from devices that show snapback and snapforward effects, see **Figure 4.1.**

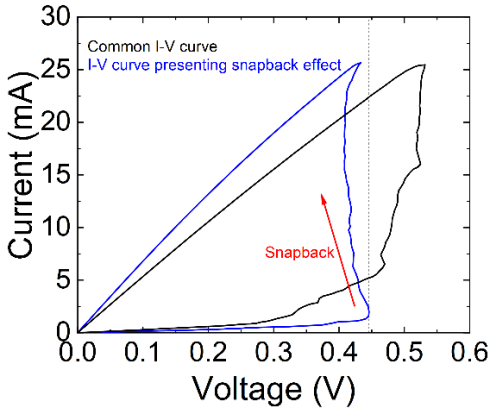

Figure 4.1. Example of a TiN/Ti/HfO_2/W experimental I-V curve (in blue) showing a rapid increase in the voltage compared to a typical one (in black). This is known as the snapback effect.

The following section is an already published work [Maldonado2021].

D. Maldonado et al.

Journal of Applied Physics (2021)

Maldonado, D., Aguirre, F., González-Cordero, G., Roldán, A. M., González, M. B., Jiménez-Molinos, F., ... & Roldán, J. B. (2021). Experimental study of the series resistance effect and its impact on the compact modeling of the conduction characteristics of HfO_2-based resistive switching memories. Journal of Applied Physics, 130(5), 054503, DOI: 10.1063/5.0055982

Quality metrics

Data base	Rating	Quartile
Web of Science	Impact factor: 2.55	Q2
Scimago	Scientific journal ranking: 0.7	Q2

Publication citations (23-03-2022)

Google Scholar	Web of Science
6	**4**

Experimental study of the series resistance effect and its impact on the compact modeling of the conduction characteristics of HfO_2-based resistive switching memories

D. Maldonado[1], F. Aguirre[2,3,4], G. González-Cordero[1], A.M. Roldán[1], M.B. González[5], F. Jiménez-Molinos[1], F. Campabadal[5], E. Miranda[3], J.B. Roldán[1]

[1]*Departamento de Electrónica y Tecnología de Computadores. Universidad de Granada. Facultad de Ciencias. Avd. Fuentenueva s/n, 18071 Granada, Spain. Email: jroldan@ugr.es*

[2]*Unidad de Investigación y Desarrollo de las Ingenierías (UIDI), Facultad Regional Buenos Aires, Universidad Tecnológica Nacional, Medrano 951 (C1179AAQ), Buenos Aires, Argentina*

[3]*Consejo Nacional de Investigaciones Científicas y Técnicas (CONICET), Godoy Cruz 2290 (C1425FQB), Buenos Aires, Argentina*

[4]*Dept. Enginyeria Electrònica. Universitat Autònoma de Barcelona, Edifici Q. 08193 Bellaterra, Spain*

[5]*Institut de Microelectrònica de Barcelona, IMB-CNM (CSIC), Carrer dels Til · lers, s/n. Campus UAB, 08193 Bellaterra, Spain*

Abstract

The relevance of the intrinsic series resistance effect in the context of RRAM compact modeling is investigated. This resistance notably affects the conduction characteristic of resistive switching memories so that it becomes an essential factor to consider when fitting experimental data, especially those coming from devices exhibiting the so-called snapback and snapforward effects. A thorough description of the resistance value extraction procedure and an analysis of the connection of this value with the set and reset transition voltages in HfO_2-based valence change memories is presented. Furthermore, in order to illustrate the importance of this feature in the shape of the I-V curve, the Stanford model for RRAM devices is enhanced by incorporating the series resistance as an additional parameter in the Verilog-A model script.

Index Terms — Resistive switching memory, RRAM, Snapback, Series resistance, Statistical analysis, Variability, Stanford model

I.-Introduction

Resistive Random Access Memories (RRAMs) are nowadays under study worldwide for their outstanding potential in the development of non-volatile memory-based applications [1, 2]. Because of their tunable conduction properties, resistive switching devices are also gaining momentum in the neuromorphic circuit landscape since they can mimic biological synapses [3, 4, 5, 6, 7]. Their use in a fully compatible CMOS technology context can unleash an overwhelming development of these applications to advance in neuromorphic computing and neural network hardware implementation [3, 4, 5, 6, 7]. Moreover, due to their inherent stochastic nature, these devices can be used as entropy sources for cryptographic circuits, such as physical unclonable functions and random number generators [8, 9, 10]. RRAMs features allow to stack cells in 3D and scale to very small process nodes. The cells typically employ a switching material (usually a transition metal oxide) sandwiched in between two metal electrodes [1, 2]. One of the most important physical mechanisms associated with resistive switching (RS) is the formation and rupture of nanofilaments across the dielectric film. From a technology point of view, there is substantial flexibility to optimize the performance through an appropriate selection of switching materials and memory cell organization. However, although RRAMs have demonstrated some advantages over flash devices and other emerging structures (phase change memories, ferroelectric memories) such as short read/write times, high endurance, low power operation, radiation hardness, CMOS compatibility, they are not exempt from serious drawbacks [2, 11]. It is worth mentioning that massive industrial production still faces several challenges such as a high variability and the lack of reliable Electronic Design Automation EDA tools. In this regard, compact models are essential tools to tackle these latter concerns.

RRAM compact modeling has been addressed in the last years at different levels. The Stanford model (STFM) [12-15] has been employed by many research groups. Other models have also been introduced [16-20]. In the general modeling context, both, analytical expressions to describe device operation and parameter extraction techniques need to be developed as a whole [21]. Even well-established models are unable to reproduce certain observable phenomena and, therefore, they must be continuously improved to account for new physical and technological features associated with particular materials or devices. This is precisely the focus of our work. In particular, we take the intrinsic series resistance effect in RRAM operation analysis into consideration and report a systematic approach to extract this series resistance from the experimental results. As it will be shown in the following sections, the role played by the series resistance is of utmost importance for understanding the RRAM electrical behavior, an issue which has been already recognized by several authors [22-25]. The study of the role played by the series resistance within RRAM models is particularly performed for the STFM, since its use is extended and its algebraic formulation is both compact as well as intuitive. The enhanced STFM flexibility to reproduce Valence Change Memories (VCM) experimental data is assessed in depth. For the sake of completeness, it is worth pointing out that in the last few years, VCM devices modeling has been addressed following a variety of approaches [12, 14, 16, 17, 18]; in particular, different types of filament shapes have been considered (cylindrical, truncated cone, hourglass [26]). In addition, from the analytical formulation viewpoint, the state variable has been assumed from a different perspective: the width of the gap between the conductive filament tip and the electrode [12, 13], the CF volume or radius [17, 18] and as a generalized memory variable [27]. The device current calculation has been performed also under different considerations including tunneling, Schottky, Poole-Frenkel, and ohmic conduction regimes [12, 14, 20, 26]. Some of the modeling implementations also account for variability [28] and noise; in the latter case, Random Telegraph Noise (RTN) has been found appropriate for

cryptographic purposes such as random number generation circuits [9, 29].

The paper is organized as follows, in section II we introduce the device fabrication and measurement details. Section III is devoted to the series resistance extraction procedures, while the modeling developments are tackled in section IV; finally, we wrap up with the main conclusions in section V.

II.-Device description and measurement

The RRAMs were fabricated using a highly doped N-type ($\rho = 4\ m\Omega \cdot cm$) silicon wafer. The top metal electrode consists of a 200 nm TiN/10 nm Ti bi-layer while the bottom metal, a 50 nm-thick W layer, was deposited on the silicon substrate with a 20 nm Ti adhesion layer, see Figure 1a. The back of the wafers was metalized with aluminum for electrically contacting the bottom electrode through the silicon substrate. The dielectric layer consists of a 10nm-thick HfO_2 film deposited by ALD. The area of the devices is $15\times15\ \mu m^2$. It is worth mentioning that the fabricated RRAMs are valence change mechanism-based devices.

The electrical characterization of the devices was performed applying a ramped voltage (0.08 V/s) to the TiN/Ti top electrode with a voltage step of 0.01 V and with the W bottom electrode grounded. A forming process was performed with current compliance I_{CC}=0.1 mA and subsequently a sequence of 1000 RS cycles was measured, see Figure 1b. These cycles consist of consecutive set and reset transitions. In particular, for positive voltages a set process leads to the formation of a conductive filament (CF) that shorts the electrodes [30] and the device switches to the low resistance state (LRS). The reset process occurs at negative voltages, in this case the CF is ruptured and the device switches back to the high resistance state (HRS) [30]. See the set and reset voltages indicated in the inset of Figure 1b.

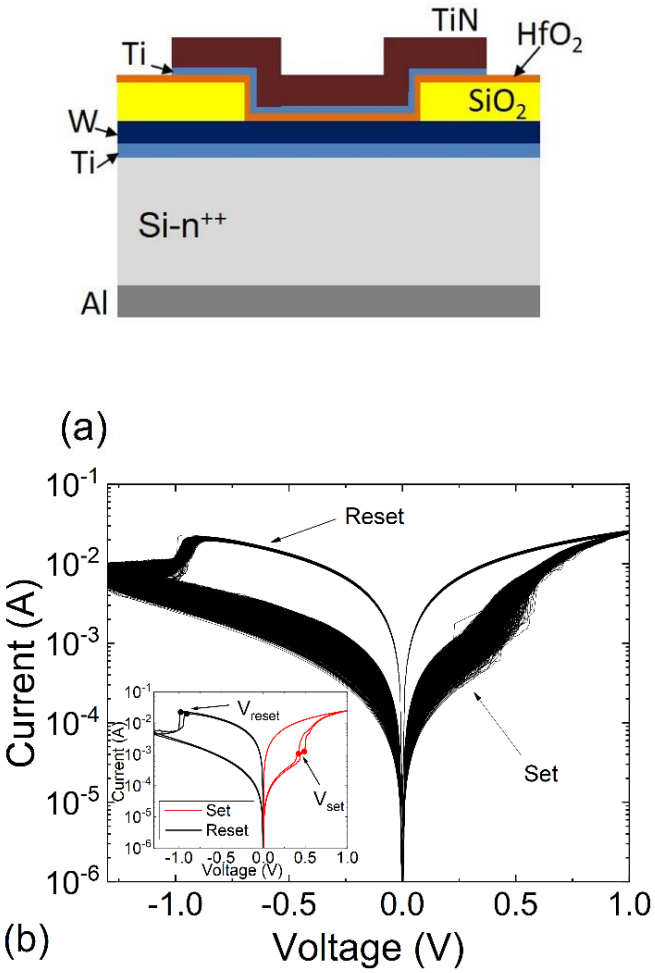

Figure 1. a) Layer stack scheme of the devices under study, b) experimental I-V curves for 1000 set/reset cycles. The inset in (b) shows the set and reset voltages for two of the curves measured.

III.- Series resistance and transition voltages extraction

In order to calculate the intrinsic series resistance, R_{series}, for compact modeling purposes, a numerical procedure similar to that used in previous publications [22-24] is considered here. The method consists in using a redefined voltage scale, $V_N=V_{Applied}-I_{Measured}xR_{series}$, where $V_{Applied}$ is the external applied voltage and $I_{Measured}$ the measured current. We replot the experimental I-V curves (as the ones shown in Figure 1) by changing the variable in the X-axis to V_N instead of the experimental $V_{Applied}$. By sweeping R_{series} we obtain different modified $I_{Measured}$ - V_N curves (see Figure 2). Among them, we select the one with the

steepest slope (close to a vertical line) in the region after the curve knee; in doing so, we make sure the set process is visualized properly as long as the current rises while the voltage is constant as shown in Figure 2. This behavior is a clear sign of a sustained conductive filament growth that leads to a current rise even if the device voltage is fixed. The slope of the curve is computed by a linear regression scheme along its straightest part.

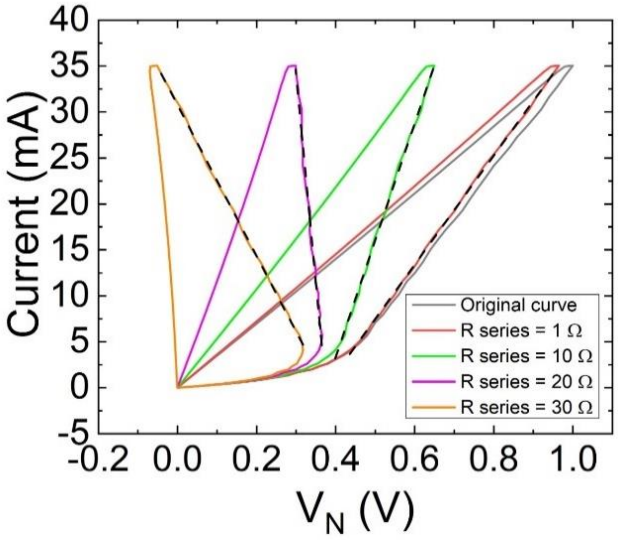

Figure 2. Modified I-V curves (measured current versus V_N) for a set process making use of different series resistances. For the sake of clarity, only 4 curves corresponding to different series resistances are included. The black-dashed lines are the result of the linear regression performed to choose the curve with the highest slope in the methodology proposed.

Based on the obtained R_{series} value, a comparison between V_{set} and the transition voltage for the set process (V_{TS}) is performed to assess the influence of R_{series} on the I-V curves. Notice that V_{set} is obtained from the original I-V curve (first point where the maximum current slope along the I-V curve is found) and V_{TS} from the modified one ($I_{Measured}$ - V_N) after the R_{series} calculation. In this latter case, the projection in the X axis of the vertical line obtained in the new curve ($I_{Measured}$ - V_N) is assumed as V_{TS} (see Figure 3).

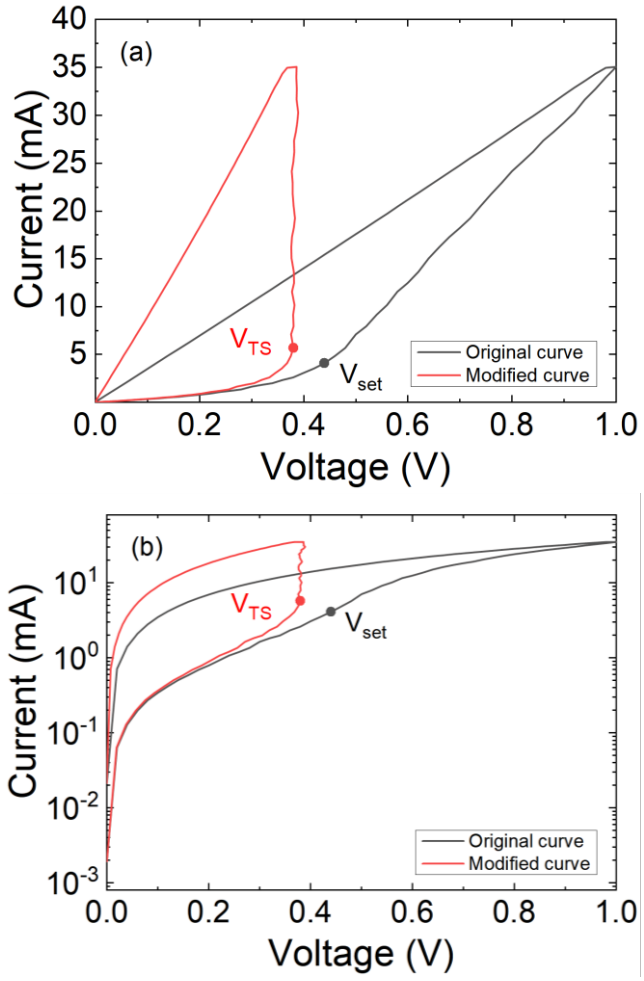

Figure 3. Experimental current versus applied voltage for one cycle in a long RS series for one of the devices under study. The new transition voltage V_{TS} is obtained from the I-V_N curve. (a) Linear and (b) logarithmic scale.

The above described methodology can lead to erroneous values for the series resistance in some particular I-V_N curves (because of the snapback effect). In order to improve the parameter extraction method, only a region of the vertical section of the modified I-V curve is fitted when searching for the steepest slope. As indicated in Figure 4a, the fitting region is selected to be in between a current value of $0.9xI_{max}$ and a current resulting from the average of the current (I_S) (obtained at the point where the set voltage is determined in the original experimental curve) and the maximum current I_{max}, as shown in Figure 4a. This methodology has been found to be more appropriate when snapback effects (Figure 4a) take place in the lower part of the "intrinsic" I-V curve [22, 23, 24]. By doing this, the snapback is avoided since this region

represents the starting phase of the conductive filament formation (the weight of the series resistance with respect to the overall resistance, device plus series resistance, changes fast here). The proper set process takes place in the vertical section of the I-V_N curve, as already stated. While the highest region of the curve cannot be considered because of a different reason. When the filament can no longer expand, the process slows down, which can be regarded as the appearance of an additional series resistance.

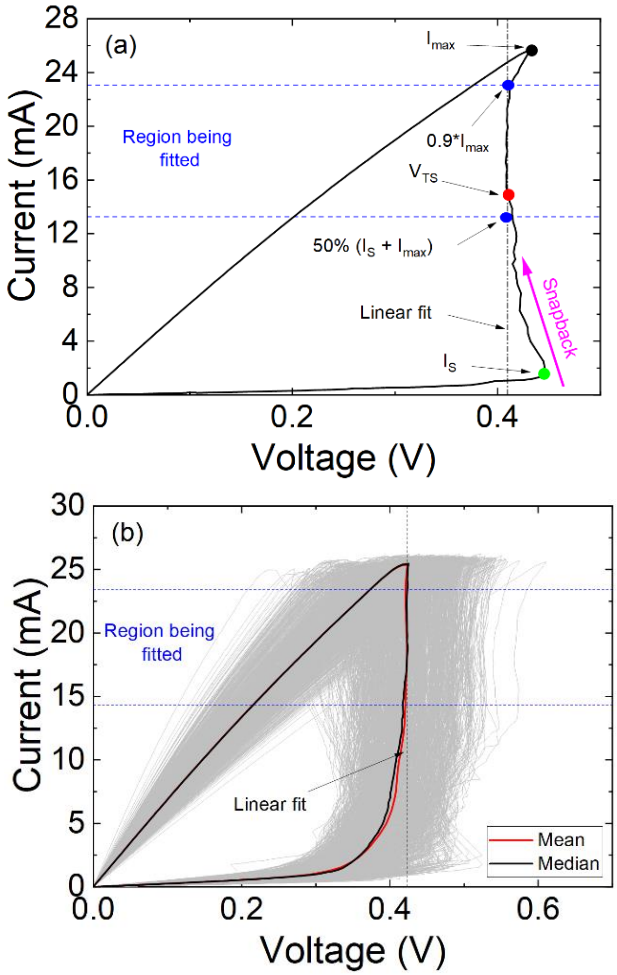

Figure 4. a) Modified I-V curve in a set process for a series resistance = 22.1 Ω. This value was obtained with the improved methodology. b) Application of this methodology to the 1000 RS set cycles measured (for each I-V curve one series resistance value is obtained). The red line indicates the average curve (calculated as the mean) of all the RS cycles, while the black curve corresponds to the median curve of all the RS cycles considered.

Figure 4b shows the proposed fitting methodology applied to the measured 1000 RS cycles as well as the median and average I-V curve. As it can be seen, the snapback effect is clear for some of the curves plotted. Once R_{series} is determined after obtaining the steepest slope, the reset curves are corrected accordingly as illustrated in Figure 5.

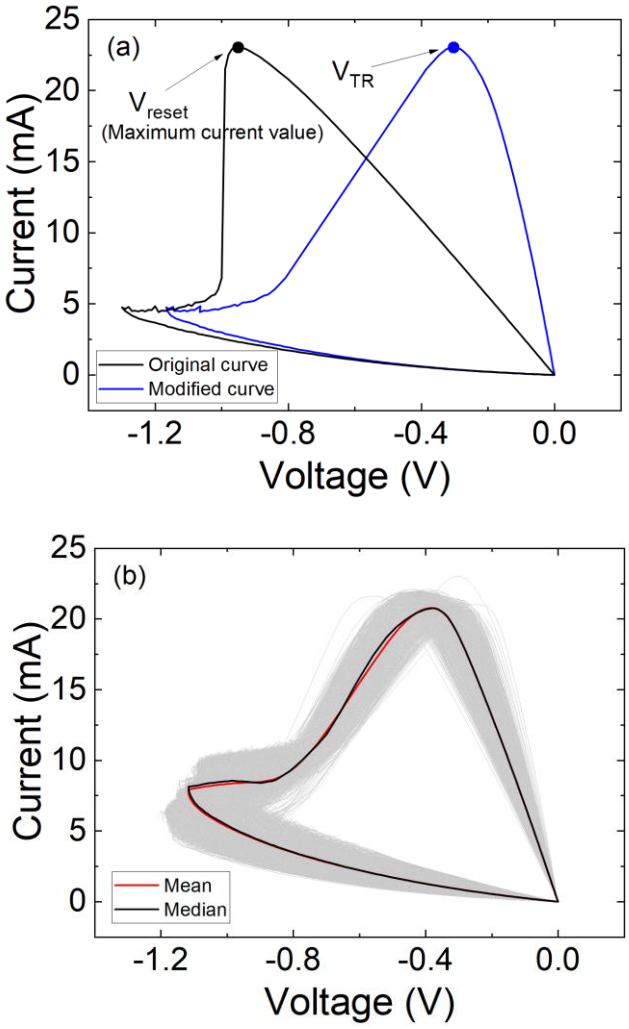

Figure 5. a) Experimental and modified reset I-V curves. b) Modified I-V reset curves for the 1000 cycles measured. The red line corresponds to the average curve (calculated as the mean) of all the RS cycles and the black curve corresponds to the median.

In addition, the reset and reset transition (V_{TR}) voltages are calculated from the measured and corrected reset curves, respectively. They are obtained as the voltages corresponding to the maximum current values, see Figure 5a. Notice that the values of the set and reset transition voltages are quite similar, suggesting a clear electric field dependence of the resistive switching mechanisms. They are the

minimum voltages required to induce the vacancy movements in opposite directions. Nevertheless, temperature effects are also known to be involved in resistive switching due to the thermally activated nature of the diffusive transport mechanism [12, 30-35]. It is interesting to notice the axes scale in Figure 6a, the transition voltages are located in relatively narrow intervals; i.e, cycle-to-cycle variability is low (within a few tenths of a volt). In addition, see that the higher the transition voltages absolute value, the lower the series resistance, Figure 6b.

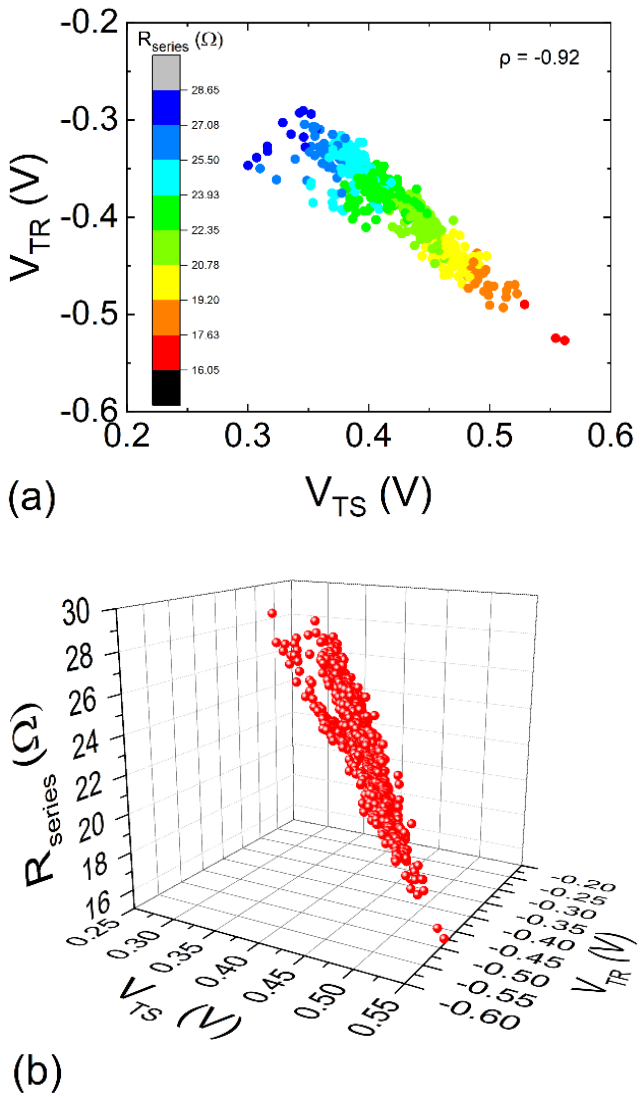

Figure 6. Transition voltage for reset versus transition voltage for set for the data under study (1000 cycles). a) The correlation of the variables plotted is shown and the corresponding series resistances are given in a color code, b) 3D plot of the series resistance versus set transition voltage and reset transition voltage for the whole RS series.

Figure 7a illustrates the cumulative distribution function (CDF) for the series resistances extracted from the 1000 cycles measured. The corresponding transition voltages CDFs are shown in Figure 7b. Notice that V_{TS} and V_{TR} are described by the same CDF except for the voltage sign (they are parallel).

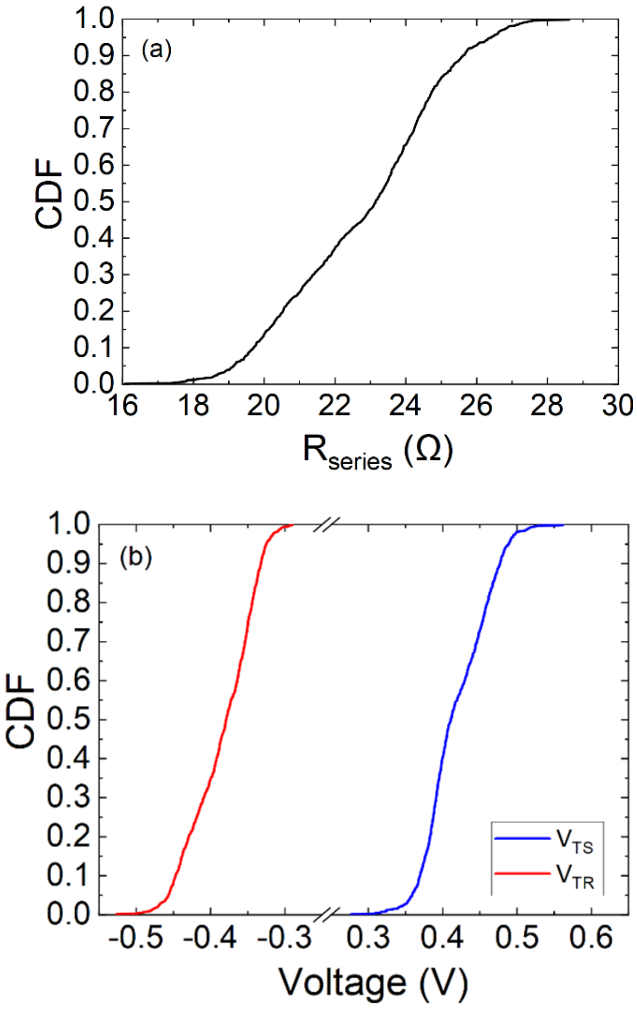

Figure 7. Cumulative distribution functions for the studied parameters in the whole RS series: a) series resistance, b) transition voltages for the set (V_{TS}) and for the reset processes (V_{TR}). The mean values for the series resistance, V_{TS} and V_{TR} are 22.80Ω, 0.418V and -0.384V, respectively. The standard deviation for the latter parameters is 2.26 Ω, 0.042V and 0.043V in each case.

The variability of the series resistance and the transition voltages as a function of the cycle number is illustrated in Figures 8a and 8b, respectively. A reasonable modeling of these numerical series can be performed by means of time series analysis for circuit simulation purposes [36]. Notice that cycle-to-cycle

(C2C) autocorrelation effects cannot be disregarded. In addition, the results seem to be consistent, at least in the medium term, with a mean-reverting stochastic process. In the case of V_{TR} and V_{TS}, the cross-correlation is more than evident: as V_{TS} increases, V_{TR} decreases in a symmetrical fashion. Again, this is a clear evidence that the same physical mechanism activates the switching process.

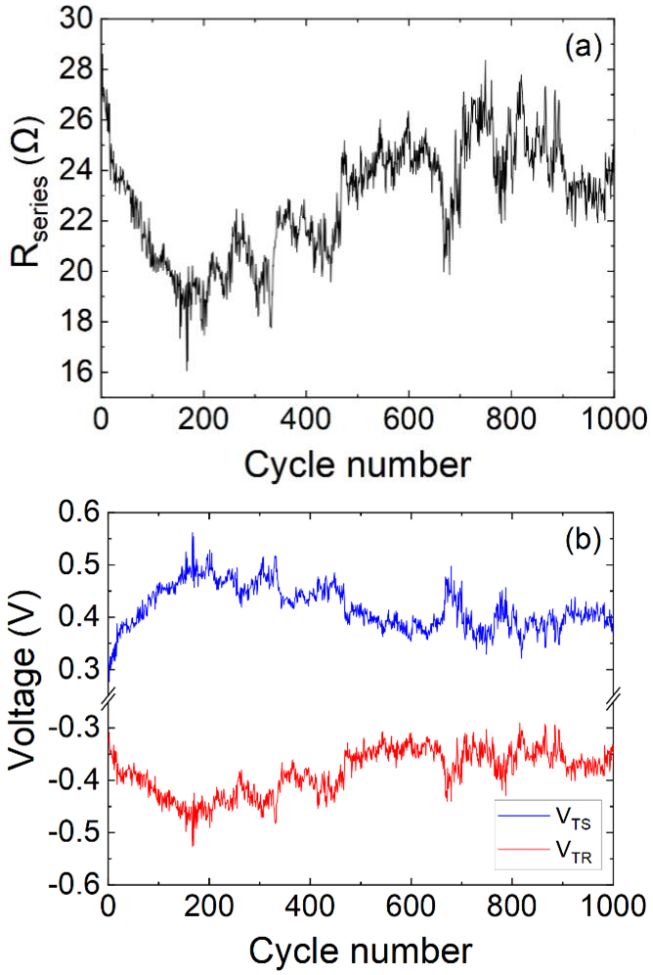

Figure 8. a) Calculated series resistance versus cycle number in the whole RS series for the data under study, b) set transition voltage (V_{TS}) and reset transition voltage (V_{TR}) versus cycle number in the whole RS series for the data under study.

Once the intrinsic series resistance parameter is extracted, the C2C variability and the statistical distribution of the results can be analysed and quantified; in the next section, we introduce the observed parameter variation in the compact modeling approach. It is important to highlight that the methodology introduced here, although presented for VCM devices could also be employed with other RRAM technologies.

IV.- Series resistance influence on RRAM compact modeling

In this section, the role played by the series resistance in the RRAM electrical behavior is investigated by means of the Stanford model [12-15], see Figure 9. The model consists in a differential equation that describes the gap between the conductive filament tip and the electrode (g), a current equation that shows exponential dependencies with the gap and the applied voltage and a thermal model that allows the calculation of the main filament temperature by means of the device thermal resistance and capacitance. The series resistance is introduced as a series component to the original model. Notice that by doing this we consider the case in which part of this series resistance can be external to the device.

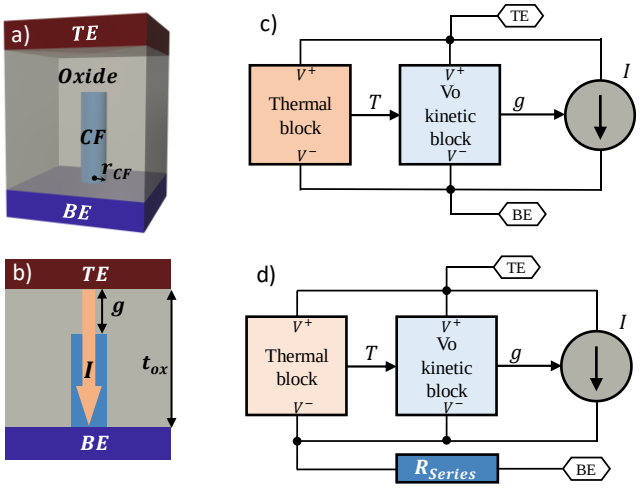

Figure 9. a) Three-dimensional view of the STFM modeling structure with an indication of different device regions (Top electrode (TE), Dielectric, Conductive Filament and Bottom electrode (BE)), b) schematic representation of the main model geometrical parameters. The gap (g) between the TE and the filament tip is one of the state variables, the other one is the temperature (T), c) subcircuit for the STFM implementation, d) proposed modification of STFM implementation with cylindrical CF including the series resistance.

Figure 10 illustrates a typical RS cycle simulation using the STFM. The model is coded in Verilog-A. The inclusion of the series resistance notably improves the

fitting of the original experimental results (see Table I for the model parameters).

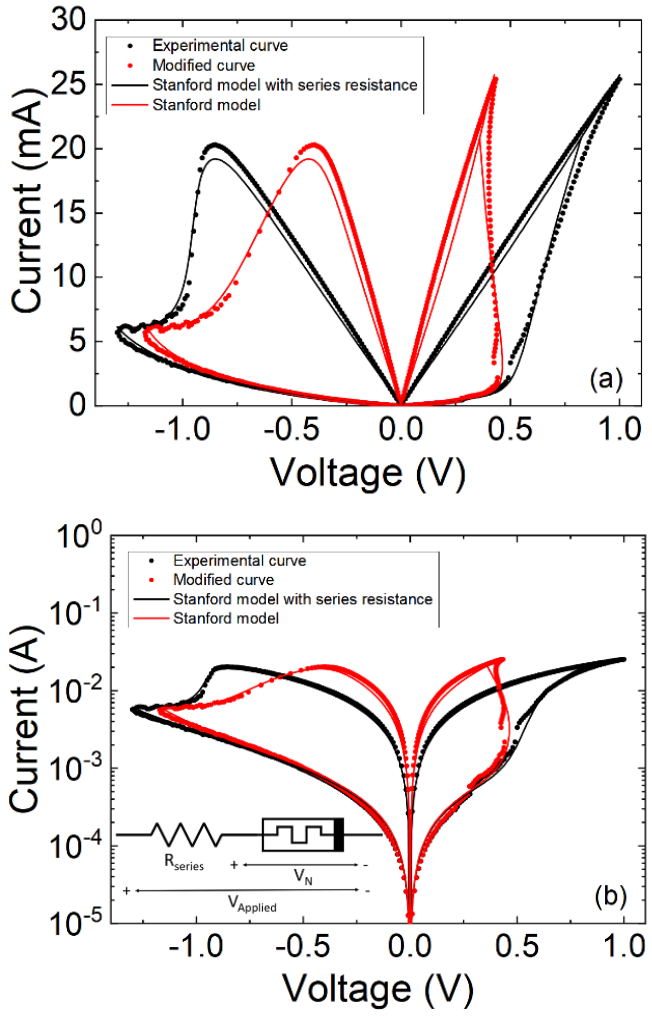

Figure 10. Experimental (black symbols) and modified current (red symbols) versus voltage. Modeled data employing the STFM are shown for the modified (red line) and original (black line, in this case it is included an external resistance to account for the role of the series resistance, see the schematic). a) Linear, b) logarithmic scale.

The fitting was performed with and without a series resistance (previously extracted, R_{series}=22.3 Ω) in the simulation, see Figure 9d. As can be seen, a good approximation was obtained in the experimental I-V curve. This versatile and simple model works well; however, for higher accuracy, other models (with even higher complexity) need to be considered [16, 17, 18, 19]. As expected, there is a trade-off between accuracy and complexity in the RRAM modeling approach. In particular, for the devices considered here, we assume some model parameters different for the set and reset processes, as suggested in [14], see Table I.

Stanford model parameters			
Device Parameters	**Unit**	**Resistive Switching**	
		SET	RESET
V_o	V	0.45	
I_0	mA	48	
g_0	nm	0.35	
ν_0	m/s	$5x10^6$	
α	-	1	1.1
β	-	1	15
γ_0	-	20	

Table I. Stanford model parameters employed for the fitting of the experimental devices under study, in particular for the cycle selected in Figure 10.

Importantly, the set of parameters employed to simulate the TiN/Ti/HfO_2/W structure is different from what was used for other type of devices [14]. In particular, device currents for our devices are higher than those reported in [14] and the abruptness of the I-V curves at the onset of the set and reset processes is different. To have a clear picture of the model behavior, we have analyzed the influence of some of the model parameters on the I-V curve shape, see Figure 11 (in this case no series resistance correction is included). By accounting for the parameter variation, we can reproduce the cycle-to-cycle variability observed in our devices. Although this is out of the scope of this paper, we will try to establish next the connection between the resistance variation and the CF physical aspect.

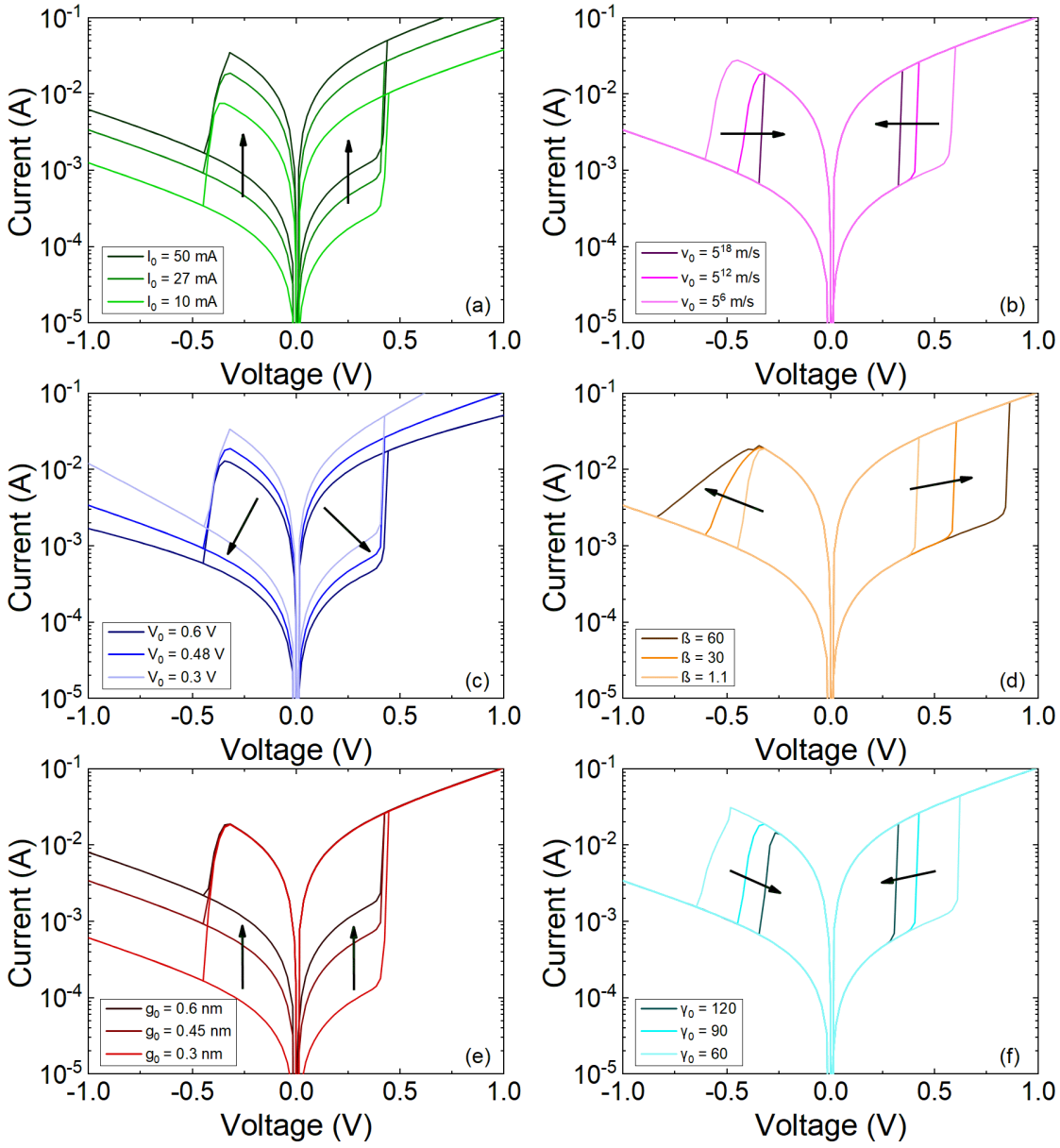

Figure 11. Current versus voltage for the modeled curves obtained with the Stanford model isolating some parameter variations. a) I_0, b) ν_0, c) V_0, d) β, e) g_0, f) γ_0

In order to complete the picture, the series resistance effect can be incorporated into the STFM assuming approximately a cylinder-like structure for the CF. This could be linked to the filament remnants after the reset process. In this case, as shown in the schematics included in Fig. 9, due to the particularities of these devices, we can compute the cylinder radius under this approximation using Equation 1 (see Figure 12).

$$R_{series} = \frac{t_{ox} - g}{\pi \, \sigma_{CF} \, r_{CF}^2} \qquad (1)$$

The following values for the gap and electrical conductivity are considered in Figures 12a and 12b (g=2nm and $\sigma_{CF}=5\times10^5$ S/m, this latter value is in line with those previous reported in Refs. [17]), and in Figures 12c and 12d, g=2nm and $\sigma_{CF}=5\times10^6$ S/m (a conductivity value in line with Ref. [37]) were employed.

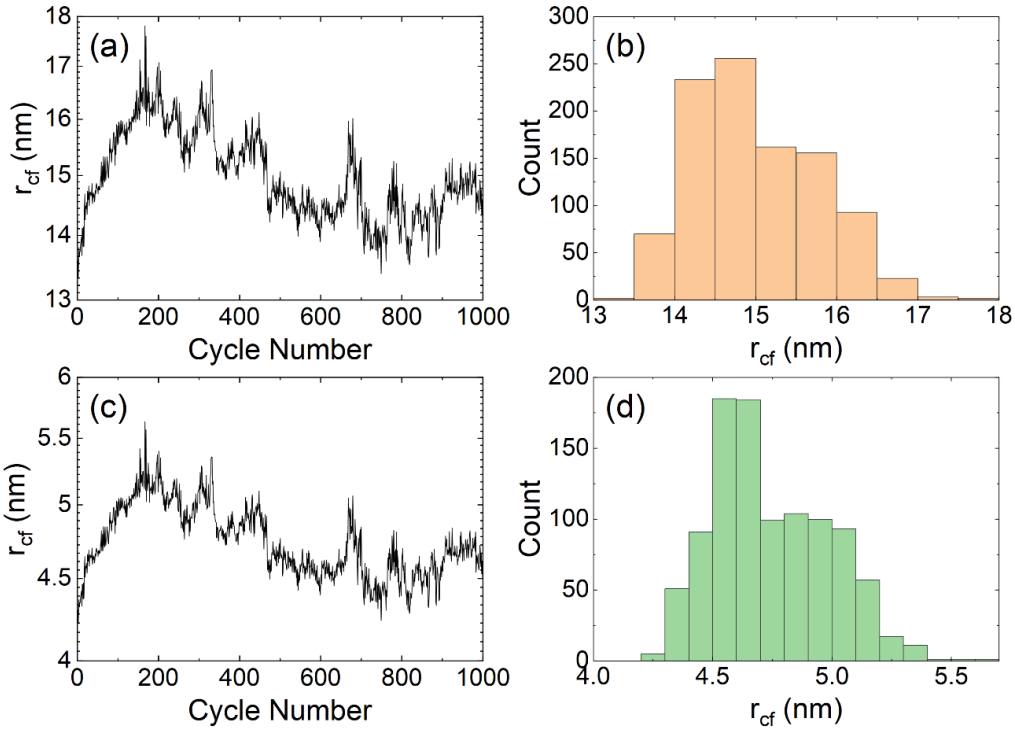

Figure 12. Calculated radii of a cylindrical CF employed to model series resistance versus cycle number in the whole RS series obtained considering g=2nm and $\sigma_{CF}=5\times10^{5}$ S/m (a), or g=2nm and $\sigma_{CF}=5\times10^{6}$ S/m (c). (b), (d) Corresponding cylinder radii histogram for g=2nm and $\sigma_{CF}=5\times10^{5}$ S/m, ($\sigma_{CF} = 5\times10^{6}$ S/m)

See that the estimated radii are in the order of several nanometers (Figure 12a, 12b) but recall that this could depend on the electrical conductivity considered (Figure 12c, 12d); in this respect, a kind of "effective" radii should be understood here since, in real devices, conductive filaments are not strictly cylindrical; in fact, the wider parts seem to be located close to the electrodes [30].

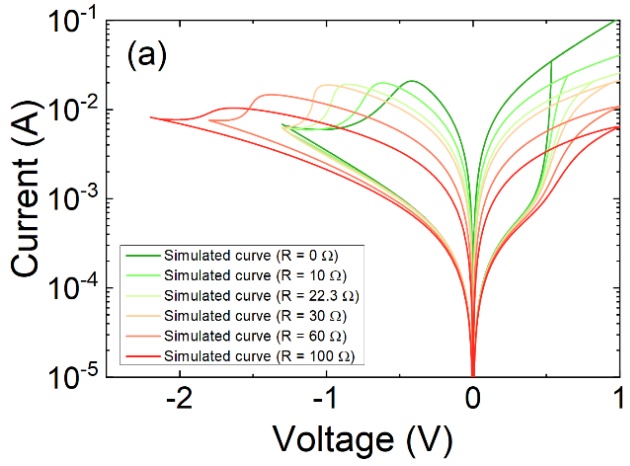

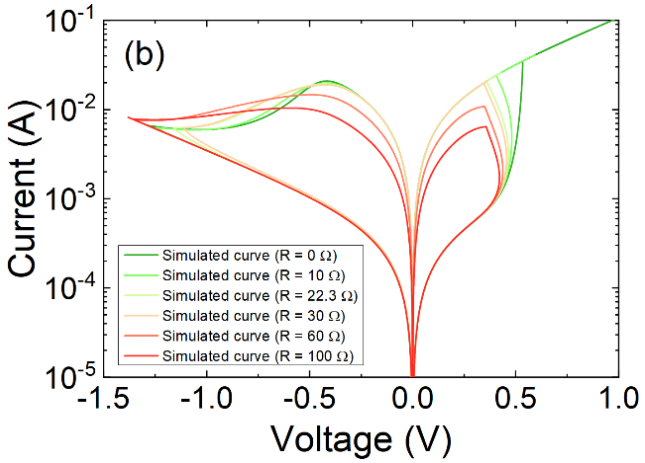

Figure 13. Modeled current versus voltage curves for different series resistances. (a) Current versus RRAM applied voltage (I-$V_{Applied}$). (b) Current versus modified voltage (I-V_N) using the series resistances.

Finally, Figure 13 shows the original fitting (see red line in Figure 10) and simulations including a series resistance ranging from 0 to 100 Ω. The role played by the series resistance is clearly recognized from these plots. The experimental I-V curve shapes in this type of devices (Figure 1) are more closely reproduced when series resistances are included (Figure 13). In

particular, as the series resistance increases the set curve slope drops off. Notice that this is not related to the progressiveness of the set transition but only a consequence of the additional potential drop. Similarly, a more progressive current reduction in the reset region is seen as the series resistance increases.

V.-CONCLUSIONS

The role played by the intrinsic series resistance in RRAM devices has been analyzed from a compact modeling viewpoint. The extraction procedure of the series resistance parameter has been evaluated using experimental data from HfO_2-based VCM devices. The use of the series resistance to redefine the measured I-V curves allows to extract device transition voltages. These transition voltages are shown to be correlated. It has been found that the lower the series resistance is, the higher the transition voltage absolute values are. We have also employed the series resistance to enhance the accuracy of the RRAM Stanford model. The use of this parameter to enhance the Stanford model allows to improve experimental data fitting.

VI. - ACKNOWLEDGMENTS

The authors thank the support of the Spanish Ministry of Science, Innovation and Universities and the FEDER program through projects TEC2017-84321-C4-1-R, TEC2017-84321-C4-3-R and TEC2017-84321-C4-4-R, and project A.TIC.117.UGR18 and IE2017-5414 funded by the Consejería de Conocimiento, Investigación y Universidad, Junta de Andalucía (Spain) and the FEDER program.

Data available on request from the authors. The data that support the fundings of this study are available from the corresponding author upon reasonable request.

References

[1] M. Lanza, H.-S. P. Wong, E. Pop, D. Ielmini, D. Strukov, B.C. Regan, L. Larcher, M.A. Villena, J.J. Yang, L. Goux, A. Belmonte, Y. Yang, F. M. Puglisi, J. Kang, B. Magyari-Köpe, E. Yalon, A. Kenyon, M. Buckwell, A. Mehonic, A. Shluger, H. Li, T.-H. Hou, B. Hudec, D. Akinwande, R. Ge, S. Ambrogio, J.B. Roldan, E. Miranda, J. Suñe, K.L. Pey, X. Wu, N. Raghavan, E. Wu, W.D. Lu, G. Navarro, W. Zhang, H. Wu, R. Li, A. Holleitner, U. Wurstbauer, M. Lemme, M. Liu, S. Long, Q. Liu, H. Lv, A. Padovani, P. Pavan, I. Valov, X. Jing, T. Han, K. Zhu, S. Chen, F. Hui, Y. Shi, "Recommended methods to study resistive switching devices", Advanced Electronics Materials, 5, 1800143, 2019.

[2] F. Pan, S. Gao, C. Chen, C. Song, F. Zeng, "Recent progress in resistive random access memories: materials, switching mechanisms and performance", Materials Science and Engineering, 83, pp. 1-59, 2014.

[3] Z. Wang, C. Li, W. Song, M. Rao, D. Belkin, Y. Li, P. Yan, H. Jiang, P. Lin, M. Hu, J. P. Strachan, N. Ge, M. Barnell, Q. Wu, A. G. Barto, Q. Qiu, R. S. Williams, Q. Xia, J. J. Yang, "Reinforcement learning with analogue memristor arrays", Nature Electronics, 2, pp. 115-124, (2019).

[4] P. Yao, H. Wu, B. Gao, J. Tang, Q. Zhang, W. Zhang, J. J. Yang, H. Qian, "Fully hardware-implemented memristor convolutional neural network", Nature, 577, PP. 641-646, (2020).

[5] P. A. Merolla, J. V. Arthur, R. Alvarez-Icaza, A. S. Cassidy, J. Sawada, F. Akopyan, B.L. Jackson, N. Imam, C. Guo, Y. Nakamura, B. Brezzo, I. Vo, S.K. Esser, R. Appuswamy, B. Taba, A Amir, M.D. Flickner, W.P. Risk, R. Manohar, D. S. Modha, "A million spiking-neuron integrated circuit with a scalable communication network and interface", Science 345, pp. 668-673, 2014.

[6] F. Alibart, E. Zamanidoost, D.B. Strukov, "Pattern classification by memristive crossbar circuits using ex situ and in situ training", Nature Communications, 4, p. 2072 (2013).

[7] M. Prezioso, F. Merrikh-Bayat, B. D. Hoskins, G. C. Adam, K. K. Likharev, D. B. Strukov "Training and operation of an integrated neuromorphic network based on metal-oxide memristors", Nature, 521, pp. 61-64 (2015).

[8] R. Carboni, D. Ielmini, "Stochastic Memory Devices for Security and Computing", Advanced Electronic Materials, 5, p. 1900198, 2019.

[9] M. Lanza, C. Wen, X. Li, T. Zanotti, F. M. Puglisi, Y. Shi, F. Saiz, A. Antidormi, S. Roche, W. Zheng, X. Liang, J. Hu, S. Duhm, K. Zhu, F. Hui, J. B. Roldan, B. Garrido, T. Wu, V. Chen, E. Pop, "Advanced data encryption using two-dimensional materials", Advanced Materials, 2100185, 1-12, 2021.

[10] D. Arumí, S. Manich, R. Rodríguez-Montañés and M. Pehl, "RRAM based random bit generation for hardware security applications," 2016 Conference on Design of Circuits and Integrated Systems (DCIS), Granada, 2016, pp. 1-6. doi: 10.1109/DCIS.2016.7845382

[11] M. A. Zidan, J. P. Strachan and W. D. Lu, "The future of electronics based on memristive systems", Nature Electronics, 1, 22-29, 2018.

[12] X. Guan, S. Yu, and H.-S. Philip Wong, "A SPICE Compact Model of Metal Oxide Resistive Switching Memory With Variations," Electron Device Letters, IEEE, vol.33, no.10, pp.1405,1407, Oct. 2012.

[13] Z. Jiang; S. Yu; Y. Wu; J.H. Engel; X. Guan; H.S. P. Wong, "Verilog-A Compact Model for Oxide-based Resistive Random Access Memory," Simulation of Semiconductor Processes and Devices (SISPAD), 2014 International Conference on, vol., no., pp.41,44, 9-11 Sept, 2014.

[14] Z. Jiang, Y. Wu, S. Yu, Member, L. Yang, K. Song, Z. Karim, H.-S. P. Wong, "A Compact Model for Metal–Oxide Resistive Random Access Memory With Experiment Verification", IEEE Transactions on Electron Devices, vol. 63, no. 5, pp. 1884-1892, May 2016.

[15] P. Chen and S. Yu, "Compact Modeling of RRAM Devices and Its Applications in 1T1R and 1S1R Array Design" IEEE Transactions on Electron Devices, vol. 62, no. 12, pp. 4022-4028, Dec. 2015.

[16] Huang, P., Liu, X. Y., Chen, B., Li, H. T., Wang, Y. J., Deng, Y. X., … Kang, J. F., "A Physics-Based Compact Model of Metal-Oxide-Based RRAM DC and AC Operations", IEEE Transactions on Electron Devices, 60(12), 4090–4097, 2013.

[17] G. González-Cordero, F. Jiménez-Molinos, J.B. Roldán, M.B. González, F. Campabadal, "An in-depth study of the physics behind resistive switching in TiN/Ti/HfO2/W structures", Journal of Vacuum Science and Technology B, 35, 01A110, 2017.

[18] G. González-Cordero, M.B. González, H. García, F. Campabadal, S. Dueñas,, H. Castán, F. Jiménez-Molinos, J.B. Roldán, "A physically based model for resistive memories including a detailed temperature and variability description", Microelectronic Engineering, 178, pp. 26-29, 2017.

[19] Huang, P., Zhu, D., Chen, S., Zhou, Z., Chen, Z., Gao, B., … Kang, J., "Compact Model of HfOx-Based Electronic Synaptic Devices for Neuromorphic Computing", IEEE Transactions on Electron Devices, 64(2), 614–621, 2017.

[20] M.A. Villena, J.B. Roldán, F. Jiménez-Molinos, E. Miranda, J. Suñé, M. Lanza," SIM2RRAM: a physical model for RRAM devices simulation", Journal of Computational Electronics, 16, p. 1095, 2017. https://doi.org/10.1007/s10825-017-1074-8

[21] R. Woltjer, L. Tiemeijer, D. Klaassen, "An industrial view on compact modeling", Solid State Electronics, 51, pp. 1572–1580, (2007).

[22] V. Karpov, D. Niraula, I. Karpov," Thermodynamic analysis of conductive filaments", Applied Physics Letters, 109, 093501, 2016.

[23] D. J. Wouters, S. Menzel, J. A. J. Rupp, T. Hennen, R. Waser, "On the universality of the I–V switching characteristics in non-volatile and volatile resistive switching oxides", Faraday Discussions, The Royal Society of Chemistry, pp. 1359-6640, 2019.

[24] A. Fantini, D.J. Wouters, R. Degraeve, L. Goux, L. Pantisano, G. Kar, Y.-Y. Chen, B. Govoreanu, J.A. Kittl, L. Altimime, M. Jurczak, "Intrinsic switching behavior in HfO2 RRAM by fast electrical measurements on novel 2R test structures", *4th IEEE International Memory Workshop*, Milan, pp. 1-4., 2012.

[25] M.B. González, M. Maestro, F. Jiménez-Molinos, J.B. Roldán, F. Campabadal, "Current Transient Response and Role of the Internal Resistance in HfOx-based Memristors", Applied Physics Letters, 117, 262902, 2020.

[26] R. Degraeve, A. Fantini, N. Raghavan, L. Goux, S. Clima, Y.Y. Chen, A. Belmonte, S. Cosemans, B. Goroveanu, D.J. Wouters, Ph. Roussel, G.S. Kar, G. Groeseneken, M. Jurczak, "Hourglass concept for RRAM: A dynamic and statistical device model," Proceedings of the 21th International Symposium on the Physical and Failure Analysis of Integrated Circuits (IPFA), 2014, pp. 245-249, doi: 10.1109/IPFA.2014.6898205.

[27] E. Miranda and J. Suñé, "Memristive State Equation for Bipolar Resistive Switching Devices Based on a Dynamic Balance Model and Its Equivalent Circuit Representation," in IEEE Transactions on Nanotechnology, vol. 19, pp. 837-840, 2020, doi: 10.1109/TNANO.2020.3039391.

[28] E. Salvador, M.B. Gonzalez, F. Campabadal, J. Martin-Martinez, R. Rodriguez, E. Miranda, "SPICE Modeling of Cycle-to-Cycle Variability in RRAM Devices", Solid-State Electronics, 108040, 2021

[29] G. González-Cordero, M. B. González, F. Campabadal, F. Jiménez-Molinos and J. B. Roldán, "A physically based SPICE model for RRAMs including RTN," 2020 XXXV Conference on

Design of Circuits and Integrated Systems (DCIS), 2020, pp. 1-6, doi: 10.1109/DCIS51330.2020.9268665.

[30] S. Aldana, P. García-Fernández, R. Romero-Zaliz, M.B. González, F. Jiménez-Molinos, F. Gómez-Campos, F. Campabadal, J.B. Roldán, "Resistive Switching in HfO2 based valence change memories, a comprehensive 3D kinetic Monte Carlo approach", Journal of Physics D: Applied Physics, 53, 225106, 2020.

[31] S. Aldana, P. García-Fernández, A. Rodríguez-Fernández, R. Romero-Zaliz, M.B. González, F. Jiménez-Molinos, F. Campabadal, F. Gómez-Campos, J.B. Roldán, "A 3D Kinetic Monte Carlo simulation study of Resistive Switching processes in Ni/HfO_2/Si-n+-based RRAMs", Journal of Physics D: Applied Physics, 50, 335103, 2017.

[32] S. Menzel, P. Kaupmann, R. Waser, "Understanding filamentary growth in electrochemical metallization memory cells using kinetic Monte Carlo simulations", Nanoscale, 7, 12673, 2015.

[33] A. Padovani, L. Larcher, O. Pirrotta, L. Vandelli, G. Bersuker, "Microscopic Modeling of HfO x RRAM Operations: From Forming to Switching", IEEE Transactions on Electron Devices, 62(6), pp. 1998-2006, 2015.

[34] S. Dirkmann, J. Kaiser, C. Wenger, T. Mussenbrock, "Filament Growth and Resistive Switching in Hafnium Oxide Memristive Devices", ACS applied materials & interfaces, 10(17), 14857-14868, 2018.

[35] M. Maestro, M.B. González, F. Jiménez-Molinos, E. Moreno, J.B. Roldán, F. Campabadal, "Unipolar resistive switching behavior in Al_2O_3/HfO_2 multilayer dielectric stacks: fabrication, characterization and simulation", Nanotechnology, 31, 135202, 2020.

[36] J.B. Roldán, F.J. Alonso, A.M. Aguilera, D. Maldonado, M. Lanza, "Time series statistical analysis: a powerful tool to evaluate the variability of resistive switching memories", Journal of Applied Physics, 125, 174504, 2019.

[37] Bocquet M, Deleruyelle D, Aziza H, Muller C, Portal J-M, Cabout T and Jalaguier E, "Robust compact model for bipolar oxide-based resistive switching memories", IEEE Trans. Electron Devices, 61, pp. 674–81, 20.

4.2. Inclusion of thermal effects on the quantum point contact model

The quantum point contact model is based on the fact that the CF acts as a quantum wire capable to detail the conduction both in the LRS and HRS. These two states exhibit linear and non-linear I-V properties, presenting ohmic conduction and conductance quantization only in the former case. Thus, in the HRS the conduction is linear only at high enough voltages, exhibiting a tough non-linearity at low ones. The model considers that during the reset process the conduction depends on an extremely narrow CF that quantizes the energy perpendicularly to the electron transport, which gives rise to a pseudo 1D arrangement, see **Figure 4.2** [Lian2012].

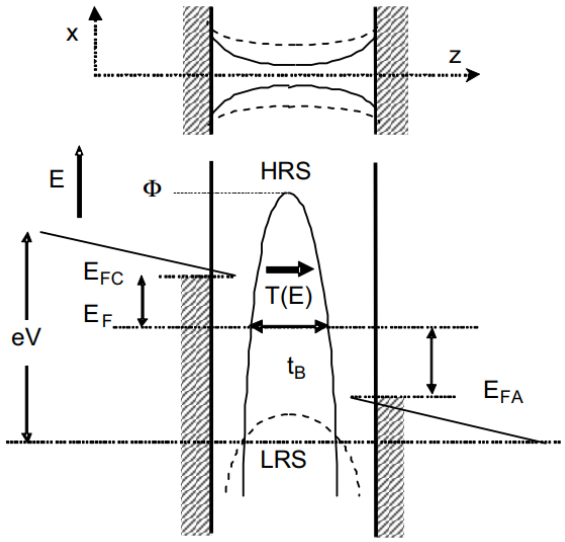

Figure 4.2. Diagram of a variable width CF including the energy band description. See that as the potential barrier height increases, the constriction width of the CF decreases and vice versa [Lian2012].

In this section we have presented an analytic expression for the non-linear I-V behavior of filamentary memories based on different approximations of the tunneling coefficient in the structure of Landauer's theory. In particular, the effect of the charge reservoirs temperature on the current has been included and assessed based on experimental measurements in Ni/HfO_2/Si devices.

M. Calixto et al.

Journal of Physics D: Applied Physics (2020)

Calixto, M., Maldonado, D., Miranda, E., & Roldán, J. B. (2020). Modeling of the temperature effects in filamentary-type resistive switching memories using quantum point-contact theory. Journal of Physics D: Applied Physics, 53(29), 295106, DOI: 10.1088/1361-6463/ab85e5

Quality metrics

Data base	Rating	Quartile
Web of Science	Impact factor: 3.2	Q2
Scimago	Scientific journal ranking: 0.86	Q1

Publication citations (23-03-2022)

Google Scholar	Web of Science
4	**3**

Modeling of the temperature effects in filamentary-type resistive switching memories using quantum point-contact theory

M. Calixto[1*], D. Maldonado[2†], E. Miranda[3‡] and J.B. Roldán[2§]

[1] *Departamento de Matemática Aplicada e Instituto "Carlos I" de Física Teórica y Computacional (iC1). Universidad de Granada. Facultad de Ciencias. Avd. Fuentenueva s/n, 18071 GRANADA, Spain.*

[2] *Departamento de Electrónica y Tecnología de Computadores. Universidad de Granada. Facultad de Ciencias. Avd. Fuentenueva s/n, 18071 GRANADA, Spain.*

[3] *Dept. Enginyeria Electrònica. Universitat Autònoma de Barcelona, Edifici Q. 08193 Bellaterra, Spain.*

Abstract

Electron transport in filamentary-type resistive switching memories is modeled using quantum point-contact theory. The filament is represented by a parabolic-shaped tube-like constriction in which the first quantized subband behaves as a one-dimensional tunneling barrier. Computation of the current flowing through the atomic-sized structure is carried out by means of the finite-bias Landauer approach. Different approximations for the barrier transmission coefficient are assessed with the aim of determining the role played by the temperature of the charge reservoirs. In order to corroborate the proposed model, current-voltage measurements in electroformed Ni/HfO_2/Si devices operating in the non-linear transport regime were performed in the temperature range from -40C to 200C. Obtained results using inverse modeling indicate that a temperature-induced barrier lowering effect explains the experimental observations. Finally, the model proposed to calculate the device current including the temperature dependence is developed.

Index Terms: Resistive switching memory, Resistive Random Access Memories, Conductive filaments, Variability, Quantum point contact, tunneling effects.

*calixto@ugr.es

†dmaldonado@ugr.es

‡enrique.miranda@uab.cat

§Corresponding author: jroldan@ugr.es

1. Introduction

Filamentary-type resistive switching memory is currently considered a suitable candidate for the next generation of non-volatile memory devices because of its high switching speed, low power consumption and scaling properties, among others [1]. Although variability as- sociated with the stochastic nature of the switching process is still a serious concern for this technology, the idea of storing one bit of information in the form of an opened or closed atomic chain embedded in a dielectric film sandwiched by two metal electrodes is very appealing not only for its simplicity but also for the low fabrication cost involved. In Resistive Random Access Memory (RRAM) devices, the atomic-sized conducting bridge consists of oxygen vacancies or metal ions depending on the metal-dielectric system combination. These species move under the application of an external electric field by hopping enabling or blocking the pass of electrons from one electrode to the opposite. These two extreme situations are referred to as the low (LRS) and high (HRS) resistance states of the device. Intermediate states and thus multibit storage is also a reality in these structures. While LRS is often regarded as a completely formed filament with a linear current-voltage (I-V) characteristic associated, HRS is represented as a filament with a kind of gap along its length. In this latter case, the I-V curve is no longer linear but exhibits an exponential dependence on the applied voltage. This behavior has been pointed out as indicative of the presence of a potential barrier as considered in many other mesoscopic systems [2]. As already proposed in the past for the soft-breakdown current in MOS devices [3, 4] and more recently for RRAMs [5, 6, 7], the electron transport in these structures can be envisaged as a one-dimensional tunneling problem in which the filament is represented by a parabolic-shaped potential barrier associated with the lateral confinement of the electron wave function when passing through the constriction's bottleneck, i.e. the gap or the filament remnants. Remarkably, the effect of the charge reservoirs temperature on this non-linear conduction regime has not received extensive attention in the literature. Most of the works concerning the temperature effects focus exclusively on the linear conduction regime [8, 9, 10] or on the ion/vacancy diffusive movement through numerically solving the standard heat equation in combination with the current continuity equation [11, 12, 13]. It is clear that this classical approach does not leave space for a quantum treatment of the phenomenon disregarding recent studies pointing out in that direction [14, 15, 16]. In this work, we explore by means of inverse modeling the role played by the temperature on the confinement barrier and proposed a simple analytic model for the I-V curves based on the Landauer formalism [2]. After a brief presentation of the theoretical framework and a review of past developments in the area, we derive a method for extracting the relevant parameters of the tunneling barrier from experiments and verify that the feature dimensions obtained for the filament are those expected for an atomic-sized constriction, giving support to the initial paradigms

2. The model

Because of symmetry considerations, the problem of quantum transport through a 3D tube-like constriction becomes a simple 1D tunneling problem, so that the expression for the current I is given by the Landauer formula, within the Landauer-Buttiker formalism

$$I = \frac{2q}{h}\int_{-\infty}^{\infty} D\,(E)[F(E-\mu_1) - F(E-\mu_2)]dE \quad (1)$$

where q is the electron charge, h the Planck constant, $\mu_1 = \mu + \beta qV$ and $\mu_2 = \mu - (1 -$

$\beta)qV$ are the cathode (top electrode) and anode (bottom electrode) quasi-Fermi levels at the two ends of the constriction[¶], respectively, V is the voltage drop across the constriction[II], β is the fraction of V that drops at the cathode side, E is the energy, $D(E)$ is the transmission coefficient of the system and $F(E)$ is the Fermi-Dirac distribution function

$$F(E) = 1/\left(1 + \exp\left(\frac{E}{k_B T}\right)\right) \quad (2)$$

with $k_B = 8.617\times10^{-5}$eV/K the Boltzmann constant and T the temperature. Since we are dealing with electrons, the Fermi-Dirac statistics must be used. It is employed to represent the carrier density at both sides of the constriction. For the sake of simplicity, we are assuming that there is no additional potential drop along the filament, therefore this statistics reflects what is happening at the electrodes.

In the zero temperature limit, $F(E)$ becomes the unit step function so that the I-V expression simplifies as:

$$I = \frac{2q}{h}\int_{\mu_1}^{\mu_2} D(E)dE \quad (3)$$

which only relies on the transmission coefficient $D(E)$. The constriction's bottleneck can be approximately described by an inverted parabolic potential barrier, for which an exact analytic expression for the corresponding tunneling probability (transmission coefficient) is known [17, 18],

$$D_P(E) = 1/\left(1 + e^{-\alpha(E-E_0)}\right), \quad (4)$$

where E_0 is related to the potential barrier height and α to its curvature (inverse width). In general, there are N 1D propagating channels connecting the electrodes, which can be considered identical for simplicity. The current for this case turns out to be straightforwardly integrated and analytically expressed as [19]:

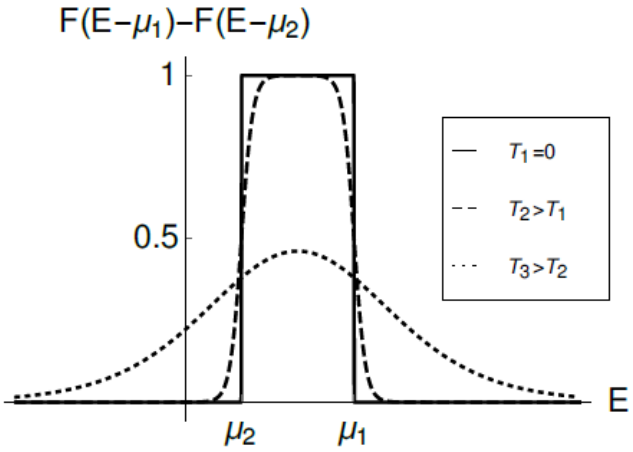

Figure 1: Effect of the temperature on the energy window associated with the injected carriers.

$$I(V) = \frac{2qN}{h}\left\{qV + \frac{1}{\alpha}\ln\left[\frac{1+e^{\alpha(\phi-\beta qV)}}{1+e^{\alpha(\phi+(1-\beta)qV)}}\right]\right\}, \quad (5)$$

where $\phi = E_0 - \mu$. For a non-zero temperature $T \neq 0$, no analytical expression for the current (1) with the transmission coefficient (4) is available. We see in Figure 1 that, for $T \neq 0$, the Fermi functions smear over an effective energy region larger than the interval $[\mu_2, \mu_1]$. This issue introduces a dependence of the current I on the

---

[¶] We understand the term constriction as the narrowest section along the filamentary structure. As always, the quasi-Fermi levels dictate the population of electrons under non-equilibrium conditions (corresponding to a biased device).

[II] In a resistive memory with a conductive filament formed, since the filament regions outside the constriction are low resistance regions, the voltage V can be assumed to be in some cases the externally applied voltage if the Maxwell and series resistance are low enough.

temperature T which will be analyzed in the following section.

In order to obtain analytic formulae for the current at $T \neq 0$, we replace the trans- mission coefficient (4) by a continuous piecewise linear approximation as follows:

$$D_L(E) = \begin{cases} 0 & E \leq E_0 - \delta \\ \frac{\delta + E - E_0}{2\delta} & E_0 - \delta < E < E_0 + \delta \\ 1 & E \geq E_0 + \delta \end{cases} \quad (6)$$

which is illustrated in Figure 2. The width of the barrier (4) is inversely proportional to α and we take $\delta \simeq \frac{\pi}{\alpha}$ for a fairly good matching of both transmission coefficients** (see Section 4 for a relationship between transmission coefficients and potential barriers).

Indeed, a comparison between the currents $I(V)$ at $T = 0$ obtained from the trans- mission coefficient (4) and its piecewise linear estimation (6) is given in Figure 3 for a particular choice of parameters E_0, φ, β, N, showing a good qualitative and quantitative agreement. Note that the current (3) obtained by integrating the continuous piecewise linear transmission coefficient (6) on the interval $[\mu_2, \mu_1]$ is a spline of order three [28] (a continuous and differentiable piecewise polynomial of degree two).

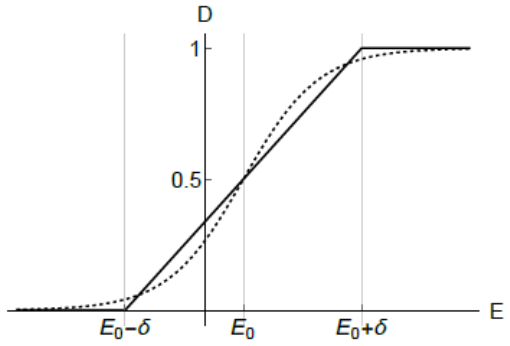

Figure 2: Comparison between the tunneling probability D_P for a parabolic barrier of height E_0 (dashed) and its piecewise linear approximation D_L (solid black) for a barrier width $2\delta \simeq \frac{2\pi}{\alpha}$.

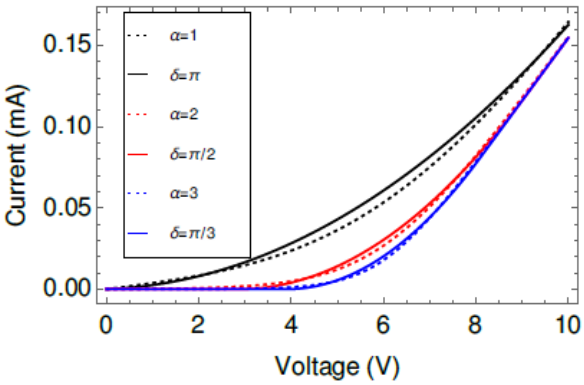

Figure 3: Comparison between the currents $I(V)$ at $T = 0$ obtained from the parabolic transmission coefficient (dashed curves) in (4) and its piecewise linear approximation (solid curves) in (6) for barrier thickness $\delta = \pi/\alpha$

3. Temperature effects on the I-V characteristics

As mentioned above, no analytical expression of the current (1) at $T \neq 0$ for the transmission coefficient (4) is available. Some approximations have been considered in the literature (see e.g., [4] and [20]), which consists in replacing (4) by $D(E) \approx \exp[\alpha(E - E_0)]$ for $E < E_0 - 3/\alpha$, which

**This relationship between δ and α arises when we make to coincide the average dispersion of the derivatives D'(E) (with a bell shape), which can be calculated as $\int_{-\infty}^{\infty} D'(E)(E - E_0)^2 dE$, for the parabolic (4) and for the piecewise linear (6) transmission coefficients, giving $\pi^2/(3\alpha^2)$ and $\delta^2/3$, respectively, that is $\pi^2/(3\alpha^2) = \delta^2/3 \Rightarrow \delta = \pi/\alpha$.

gives the current at low voltages (exclusively the tunneling regime)

$$I_P(V,T) = \frac{2qN}{h\alpha}\frac{\exp[-\alpha(\phi-\beta qV)]}{\mathrm{sinc}(\pi\alpha k_B T)}[1-\exp(-\alpha qV)], \quad (7)$$

valid for a Fermi level μ at least $3k_BT$ below the tip E_0 of the barrier and $k_BT\alpha < 1$. Note that when $\alpha \to 0$, we recover the ballistic case $D = 1$ and therefore the standard Landauer formula.

For the continuous piecewise linear transmission coefficient (6), the integral (1) can be performed and an explicit analytical formula for the current is obtained as

$$I_L(V,T) = \frac{2qN}{h}\left\{qV + \frac{(k_BT)^2}{2\delta}\left[\mathrm{Li}_2\left(-e^{-\frac{q\beta V+\delta-\phi}{k_BT}}\right) - \mathrm{Li}_2\left(-e^{-\frac{q\beta V-\delta-\phi}{k_BT}}\right) + \mathrm{Li}_2\left(-e^{-\frac{q(\beta-1)V-\delta-\phi}{k_BT}}\right) - \mathrm{Li}_2\left(-e^{-\frac{q(\beta-1)V+\delta-\phi}{k_BT}}\right)\right]\right\} \quad (8)$$

in terms of the dilogarithm or Spence's function Li_2 (see the appendix A for specific calculations and for more information about these special functions).

We can relate all energies to the Fermi level, so that $\phi = E_0$ is the barrier height for zero applied voltage. The model presented here works well at low voltages. In the quantum regime, Joule heating effects are assumed to occur both outside and inside the region of interest, i.e. the constriction's bottleneck. It is widely accepted in mesoscopic theory that for $D = 1$ dissipation takes place exclusively at the reservoirs. However, for $D < 1$, only part of the total power is dissipated in the filament. This part is what contributes to the thermal movement of the atoms that form the filament and which ultimately reduces the average barrier height. Since we don't have access to the internal temperature we link the thermal movement with the external temperature. These effects introduce a temperature dependence in the barrier height $\phi = \phi(T)$, which can be linearly approximated by

$$\varphi(T) \approx \varphi_0 - \theta T, \quad (9)$$

with θ a (positive) temperature coefficient. This effect has been previously introduced in Ref. [20]. We shall introduce this extra temperature dependence in the currents (7) and (8) coming from "parabolic" and piecewise linear transmission coefficients. In Figure 4 we see the effect of temperature on the current I_L for fixed values of δ, β, N, φ_0 and θ. We see that $I_L(V, T)$ is an increasing function of T. We have employed experimental data to try to assess the accuracy of our model (see Figure 5). In particular, we have used structures fabricated at the Institut of Microelectronics of Barcelona IMB-CNM (CSIC), they are based on a $Ni/HfO_2/Si - n^+$ [21].

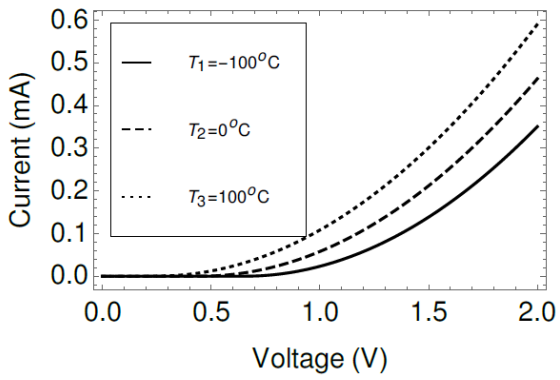

Figure 4: Current I_L in eq. (8) against voltage for three different temperatures. We have chosen $\delta = 1\text{eV}$, $\beta = 1$, $N = 10$, $\phi_0 = 2\text{eV}$ and $\theta = 0.002\text{eV/K}$ for the three cases.

In these devices the top 200 nm-thick Ni electrode was deposited by magnetron sputtering, then a lift-off process went on. The area of the cells was $5\times5\mu\text{m}^2$, defined by the field oxide patterning. The statistical features of variability in this technology have been analyzed previously [22, 23].

The ALD fabricated dielectric layer was 20nm thick. The conduction is filamentary in these devices; i.e., it takes place through conductive

filaments (CFs) that are formed and destroyed within the the Resistive Switching (RS) device operation. At low volt- ages these I-V curves are non-linear and, in previous publications [7, 24, 25], the QPC model was employed to analyze the conduction. These devices were measured at different temperatures, precisely, 50 cycles of set and reset processes for each temperature.

For these curves we first selected the reset curves at $T_1 = -40$ºC, $T_2 = 20$ºC, $T_3 = 140$ºC and $T_2 = 200$ºC (five cycles for each temperature). For these temperatures, the conductive filaments are destroyed arround the reset voltages $V = 1.5$ V, $V = 1.4$ V, $V = 1.1$ V and $V = 1$ V, respectively. The behaviour of these values is in line with the evolution of the barrier height $E_0 = \phi$ with temperature (see later in this section and Figure 9). It is interesting to highlight that the effects of variability in these type of devices have to be considered and assumed taking into account the stochastic nature of resistive switching. Studies on these variability issues have to account for hundreds of curves in long resistive switching series and they have to be performed under a statistical methodology [22, 23]. For the validation of the model presented here and for the sake of simplicity, we have limited the amount of experimental curves considered. A comparison between experimental values of the current $I(V, T)$ at these four temperatures and their fit to the "linear" current formula (8) is presented in Figure 5. The agreement of this formula with experimental data is good far from the reset point (that is, in the low voltage regime). All the curves in Figure 5 can be reasonably well fitted to I_L with common parameters: zero temperature barrier height $\varphi_0 =$ 2.2 eV and zero anode quasi-Fermi level $\beta = 1$. The barrier width δ is a decreasing function of temperature and θ varies in the interval [0.0025, 0.003] eV/K; the main difference between these currents comes from the number N of propagating channels (conductive filaments) formed within each RS device operation. When the number of filaments is higher than one, we consider an average of the existing channels. This is a reasonable and simplifying approach from the compact modeling viewpoint. In this case, the QPC parameters should be considered as effective parameters, since the individual filament details (barrier heights, widths, etc.) cannot be accessed individually. Also, the barrier height $E_0 = \varphi$ gets affected by temperature according to formula (9), giving $\phi(T_1) \simeq 1.5$eV, $\phi(T_2) \simeq 1.38$eV and $\phi(T_3) \simeq \phi(T_4) \simeq 1$eV. This is better appreciated in the potential barrier profiles calculated in the next section (see Figure 9).

The linear dependence of $I(V;T)$ on the number of propagating channels N masks the intrinsic dependence of $I(V;T)$ on temperature in Figure 5. This is linked to the conductive filament length and intrinsic variability of these devices in their resistive switching operation. However, we can still appreciate this temperature dependence when we take into consideration an average within a resistive switching series. To better see this, we compute the average current, measured considering all the curves at our disposal, for three different low voltages (0.1V, 0.2V and 0.3V) inside the temperature range T [233, 473] Kelvin. Figure 6 shows these averaged data of I versus temperature T , together with their fittings using formulas (8) (left) and (7) (right). We find a qualitative fitting for barrier width $\delta = 2$eV ($\alpha = \pi/2\text{eV}^{-1}$), zero anode quasi-Fermi level $\beta = 1$, $N = 6$ propagating channels, zero temperature barrier height $\varphi_0 = 2.4$eV and temperature factor $\Theta = 0.002$eV/K. We see that formula (8) captures the qualitative behavior (increase of I with T and V), although the

variability inherently linked to resistive switching makes the quantitative behavior less accurate. Other issues, such as the ohmic resistance of the conductive filament, the existence of tree-branched filaments, etc., should also be taken into account when comparing with experimental measurements, as it is the case here. For the temperature range considered, the threshold $k_B T\alpha < 1$ [imposed for the validity of (7)] is not exceeded, since $k_B T_{\max}\alpha = 0.064$ for the maximum temperature $T_{\max} = 473\text{K}$ and $\alpha = \pi/2$. However, we observe that the fitting with I_P in Figure 6 is less accurate at higher temperatures. The expression (8) for I_L is not affected by this constraint.

4. Transmission coefficients and potential barriers

As we stated in Section 2, the transmission coefficient $D_P(E)$ for an inverted parabolic barrier $U(x) = E_0 - kx^2/2$ (here k reminds a "spring constant") is given by (4) with $\alpha = 2\pi\sqrt{m/k}/\hbar$ where m is the effective mass of the particle in the constriction. In this article we have proposed continuous piecewise linear estimations of $D(E)$ like (6), and we wonder what is the corresponding barrier shape. For this purpose, we shall use the semiclassical (WKB) formula:

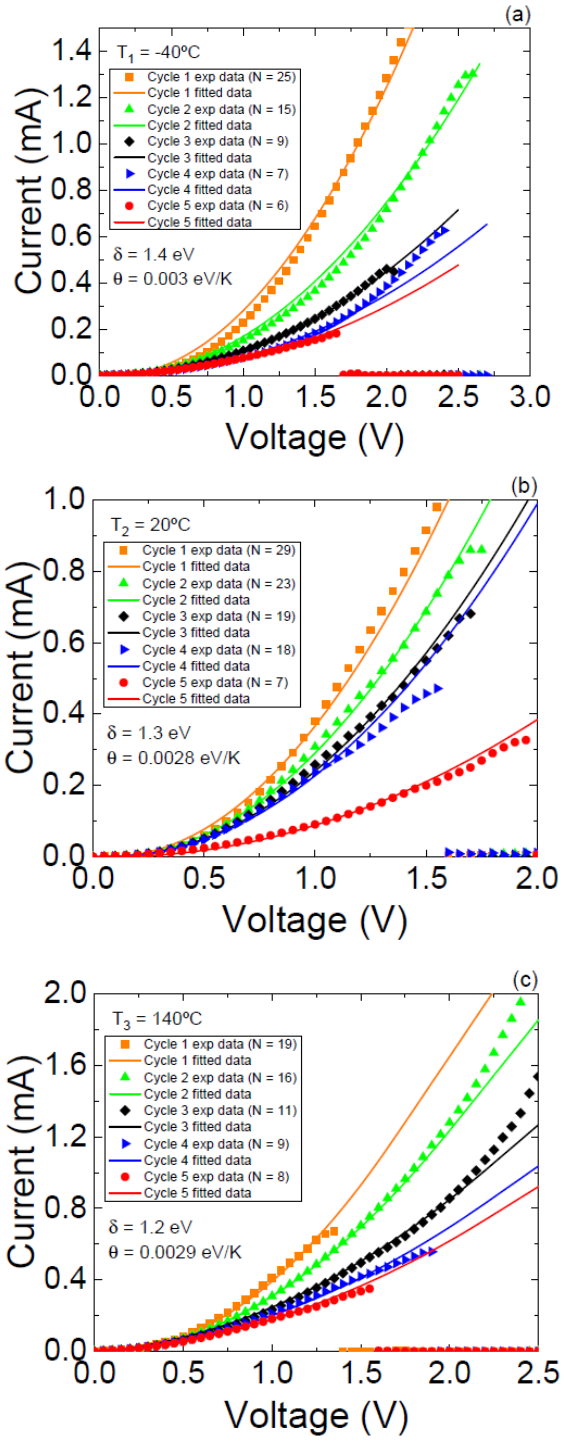

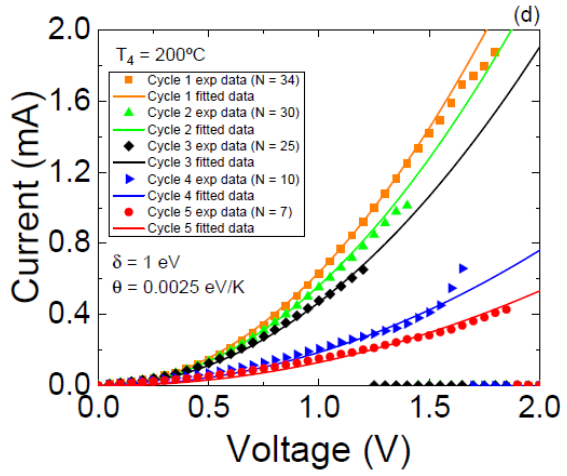

Figure 5: Comparison between experimental values of the current (for four temperatures and five cycles for each temperature) and their fit to the linear formula $I_L(V,T)$ in eq. (8), as a function of voltage V_{RRAM}. All the curves can be reasonably well fitted to the common parameters: zero temperature barrier height $\varphi_0 = 2.2$ eV and zero anode quasi- Fermi level $\beta = 1$. The barrier width δ is a decreasing function of temperature and $\theta \in [0.0025,\ 0.003]$. The main difference between cycles has to do with the number N of propagating channels (different filaments corresponding to different cycles).

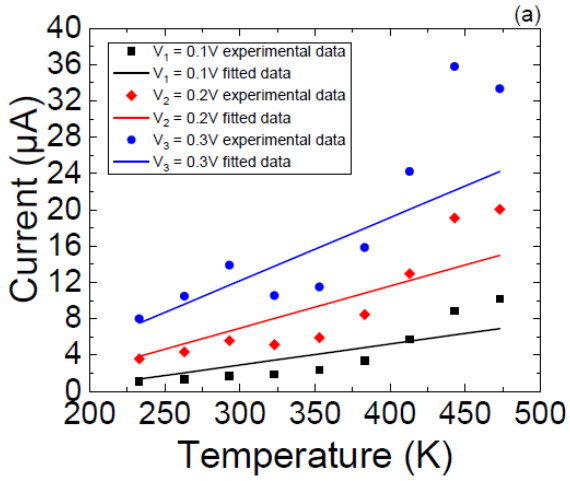

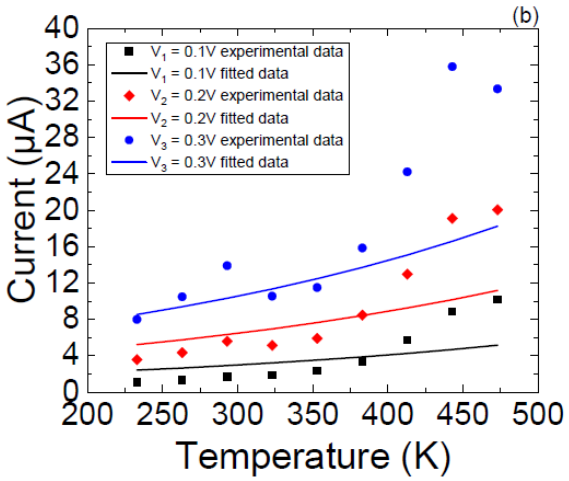

Figure 6: Experimental data, and fitting with formulas (8) (a) and (7) (b), of average currents values against temperature T for three different voltages: 0.1, 0.2 and 0.3V. The fitting parameters correspond to: $\delta = 2$ ($\alpha = \pi/2$), $\beta = 1$, $N = 6$, $\varphi_0 = 2.4$ and $\theta = 0.002$.

$$D(E) \simeq \exp\left[-2\int_{x_-(E)}^{x_+(E)} d\,x\sqrt{\frac{2m}{\hbar^2}(U(x)-E)}\right] \equiv Q(E), \quad (10)$$

where $U(x_-(E)) = U(x_+(E)) = E$. We shall assume a symmetric potential barrier so that the turning points are $x_-(E) = -x_+(E) = -x(E)$. This semiclassical formula is only valid for low energies $E \ll E_0$ compared to the barrier height E_0. This formula has been used in the past [26] to obtain, from experiments, the barrier profile of a soft breakdown filament in MOS capacitors.

In this manuscript we shall consider an extension of this formula as

$$D(E) = \frac{Q(E)}{1+Q(E)}, \quad (11)$$

which turns out to give good results even for $E \approx E_0$. Additionally, formula (11) repro- duces the value $D(E_0) = 0.5$ for the linear and parabolic transmissions (see Figure 2). Solving the previous expression (11) for $Q(E)$ gives

$$Q(E) = \frac{D(E)}{1-D(E)}. \quad (12)$$

In order to obtain the shape of the confinement potential barrier $U(x)$ for a given transmission $D(E)$, we shall discretize the values of the energy and take $E = E_n,\ n = 0, \ldots, M$ in decreasing order, with E_0 the potential barrier height. If we restrict ourselves to energy values between $[E_0 - \Delta,\ E_0]$, then we have $E_n = E_0 - n\Delta/M$. We shall also discretize the integral that defines the exponent of $Q(E)$ in (10). Denoting $x_m = x(E_m)$, $x_0 = 0$, the left Riemann sum (rectangle rule) states that, for an even function $f(x)$, a rough calculation of the integral is given by

$$\int_{-x_n}^{x_n} f(x)dx = 2\int_{x_0}^{x_n} f(x)dx = 2\sum_{m=0}^{n-1}\int_{x_m}^{x_{m+1}} f(x)dx \approx 2\sum_{m=0}^{n-1} f(x_m)(x_{m+1} - x_m). \quad (13)$$

Therefore, using that $U(x_m) = E_m$, we can approximate

$$\ln\big(Q(E_n)\big) \simeq a\sum_{m=0}^{n-1}\sqrt{n-m}\,(x_{m+1} - x_m),\ n = 1, \ldots M, \quad (14)$$

with $a = -4\frac{\sqrt{2mq\Delta}}{\hbar\sqrt{M}}$. Solving the linear system coming from (12)

$$\ln\big(Q(E_n)\big) = \ln\left[\frac{D(E_n)}{1-D(E_n)}\right], \quad (15)$$

we estimate the values for the points x_m at which $U(x_m) = E_m$. This linear system can be compactly written as $Ax = b$, with $= (x_1, \ldots, x_M)^t$ the column vector of unknowns. The coefficient matrix

$$A = a\begin{pmatrix} 1 & 0 & 0 & \ldots & 0 & 0 \\ \sqrt{2}-\sqrt{1} & 1 & 0 & \ldots & 0 & 0 \\ \sqrt{3}-\sqrt{2} & \sqrt{2}-\sqrt{1} & 1 & 0 & \ldots & 0 \\ \vdots & \vdots & \vdots & \vdots & \vdots & \vdots \\ \sqrt{M}-\sqrt{M-1} & \sqrt{M-1}-\sqrt{M-2} & \ldots & \ldots & \sqrt{2}-\sqrt{1} & 1 \end{pmatrix} \quad (16)$$

is lower triangular and $b_n = \ln\left[\frac{D(E_n)}{1-D(E_n)}\right]$ are the entries of the column vector b.

In figure 7 we represent the potential barriers obtained from the modified WKB formula (15) for the transmission coefficients (4) and (6), for two values of $\alpha\ (\delta = \pi/\alpha)$ and $\Delta = E_0$. Note that the parabolic transmission coefficient D_P in eq. (4) is never zero, whereas the linear transmission coefficient D_L in eq. (6) is zero for $E \le E_0 - \delta$, which means $x_\pm(E) = \pm\infty$. We avoid this divergence by taking $\Delta = E_0 < \delta$. We can appreciate in Figure 7 the different shape of the potential barriers coming from D_P and D_L. In order to test the validity of the modified WKB formula (11), we also plot in figure 7 the exact parabolic barrier $U(x) = E_0 - kx^2/2$ curves associated with D_P for $\alpha_1 = \pi/\delta_1$ (solid blue) and $\alpha_2 = \pi/\delta_2$ (dashed blue). Recall that the relationship between the "spring constant" k of the parabola and the parameter α is $k = 4\pi^2 m/(\hbar^2\alpha^2)$. We see that the formula (15) accurately recovers the original parabolic potential barrier (in blue). Therefore, we shall use this adapted semiclassical formula to obtain the shape of potential barriers associated with transmission coefficients coming from I-V curves.

In fact, starting from (1), with integration interval $[\beta qV, \infty)$, assuming the Boltzmann approximation $F(E) \simeq \exp(-E/k_BT)$ and neglecting the left-going current component

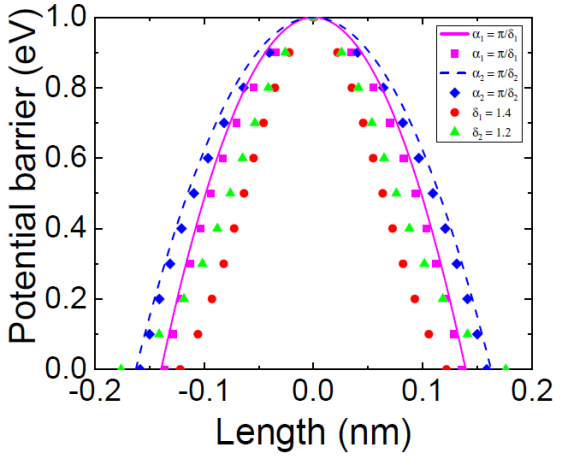

Figure 7: Potential barrier $U(x)$ (in eV), obtained from the modified WKB formula (15), against the longitudinal x-axis (in nanometers)

associated with the transmission coefficient $D(E) = 1/\left(1 + e^{-\alpha(E-E_0)}\right)$ (blue diamond and pink square) and the piecewise linear estimation (6) (green triangle and red dot), for inverse thickness $\alpha_1 = \pi/\delta_1$ ($\delta_1 = 1.4$eV) and $\alpha_2 = \pi/\delta_2$ ($\delta_2 = 1.2$eV), potential barrier height $E_0 = 1$eV and $M = 10$ points. We also plot the exact parabolic barrier $U(x) = E_0 - kx^2/2$ curves, with $k = 4\pi^2 m/(\hbar^2\alpha^2)$, associated with the transmission (4) for α_1 (solid pink) and α_2 (dashed blue).

flowing back from anode to cathode [second negative addend in (1)], one can arrive to the formula [26]

$$D(\beta qV) \simeq \frac{\frac{q}{k_B T} I + \frac{1}{\beta q}\frac{\partial I}{\partial V}}{N\frac{2q^2}{h}\exp\left(\frac{\mu}{k_B T}\right)}, \quad (17)$$

which allows a numerical reconstruction of transmission coefficients from experimental I-V data (inverse modeling). As already mentioned, this formula has been used in [26] to obtain the barrier profile for a soft-breakdown filament in electrically stressed MOS capacitors. In our case, we shall neglect $\frac{q}{k_B T} I$ compared to $\frac{1}{\beta q}\frac{\partial I}{\partial V}$ and we shall take Fermi level $\mu = 0$, which eventually seems to be a reasonable choice; note that formulas (7) and (8) depend on the relative value $\phi = E_0 - \mu$, but we do not have direct access to the absolute values of the potential barrier height E_0 nor to the Fermi energy μ. Therefore, we shall use the simple formula

$$D(E) \simeq \frac{h}{2q^2 N}\frac{\partial I(E)}{\partial E}. \quad (18)$$

This formula, when applied to I_L in (8), reproduces the piecewise linear transmission D_L in eq. (6) with a slight smoothing due to temperature effects. However, the parabolic trans- mission D_P in eq. (4) is not recovered from I_P in eq. (7) since, as we already noticed, this formula is only valid for low energies below E_0. In Figure 8 we compute the transmission coefficients D(E) from the I-V curves in Figure 5. The derivative is carried out numerically using the simple difference quotient $I'(E_n) \simeq \left(I(E_{n+1}) - I(E_n)\right)/\Delta$, with energy step size $\Delta/M = 0.05$eV, which gives $a = -4.5823\text{nm}^{-1}$, and $(2q^2/h)^{-1} = 12906.4$A/eV. The result is compared with $D_L(E) = \frac{h}{2q^2 N}\frac{\partial I_L(E)}{\partial E}$ (black solid curve) and $D_P(E) = 1/\left(1 + e^{-\alpha(E-E_0)}\right)$ (black dashed curve). We choose the interval $E \in [0, E_0]$, for which $D(E) \in [0, 0.5]$, approximately [remember Figure 2]. From Figure 8, we can conclude that, despite the variability associated with experimental current measurements and their numerical derivatives, formula (18) still captures the general behavior of the transmission coefficient, with a reasonable fitting to D_L.

Inserting (18) into (12) and solving

$$\ln[Q(E_n)] \simeq \ln\left[\frac{I\prime(E_n)}{\frac{2q^2 N}{h} - I\prime(E_n)}\right], \; n = 1, \ldots, M, \quad (19)$$

for x_n, we get in Figure 9 the potential barriers from the experimental values of the I-V curves of Figure 5. We see that the general effect of temperature is to lower the potential barrier height E_0, according to the formula (9) for $\phi = E_0$ for zero Fermi level $\mu = 0$. In particular, we have $\phi(T_1) \simeq 1.5$eV, $\phi(T_2) \simeq 1.38$eV and $\phi(T_3) \simeq \phi(T_4) \simeq 1$eV; this effect has also been reported in Ref. [20]. Finally, the barrier width along the conductive filament constriction can be estimated by the relation [19]

$$t_B = \frac{\hbar\alpha}{\pi}\sqrt{\frac{2\phi}{m}}, \quad (20)$$

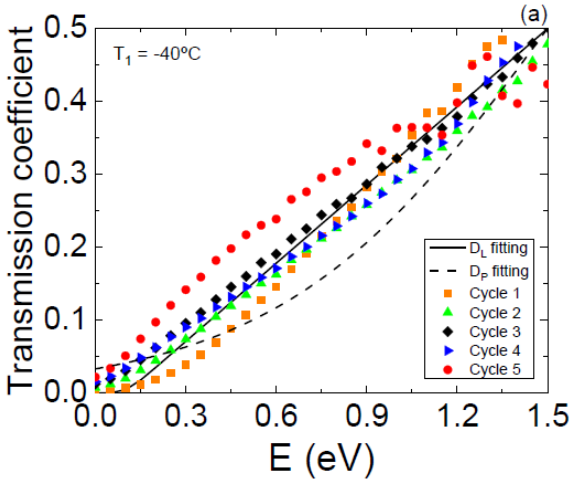

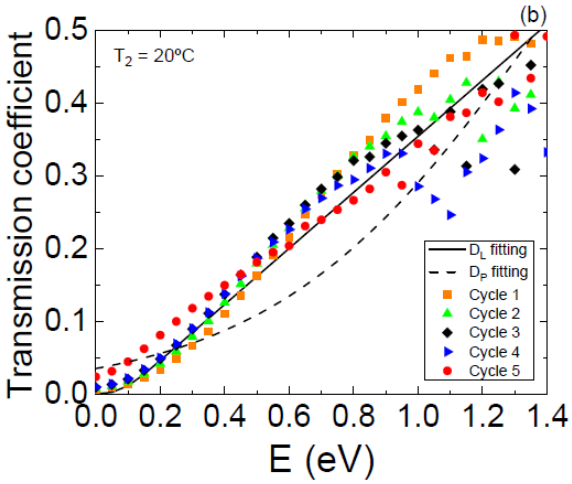

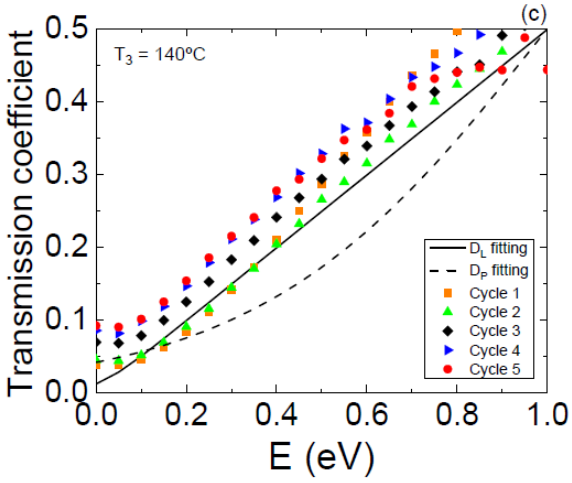

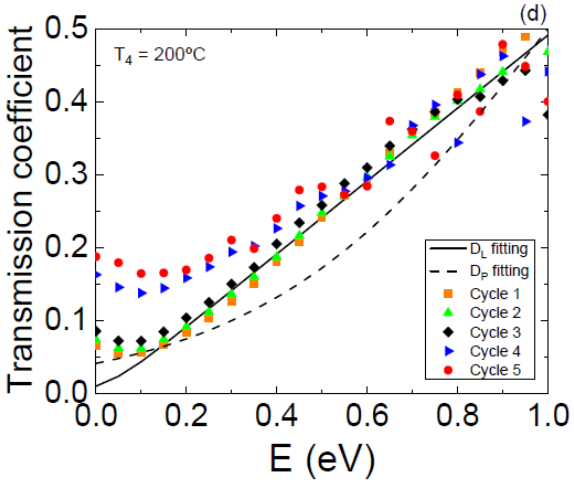

Figure 8: Transmission coefficient $D(E)$ from the experimental I-V curves in Figure 5, together with their fittings to $D_L(E) = \frac{h}{2q^2N}\frac{\partial I_L(E)}{\partial E}$ (black solid curve) and $D_P(E) = 1/\left(1+e^{-\alpha(E-E_0)}\right)$ (black dashed curve).

where m is the electron effective mass and we are taking $\alpha = \pi/\delta$. Assuming that $m(T_1) = 0.1m_e$, $m(T_2) = 0.2m_e$, $m(T_3) = 0.4m_e$, $m(T_4) = 0.5m_e$ (these are reasonable electron effective mass values for HfO_2 [5]), and taking the fitting values of δ from Figure 5, we get $t_B(T_1) \simeq 1.1$nm, $t_B(T_2) \simeq 0.79$nm, $t_B(T_3) \simeq 0.51$nm and $t_B(T_4) \simeq 0.55$nm, which are in concordance with the barrier widths in Figure 9. Another interesting representative parameter is the radius of the constriction, estimated by [5]

$$r_B = \frac{\hbar z_0}{\sqrt{2m\phi}} \quad (21)$$

where $z_0 = 2.404$ is the first zero of the Bessel function J_0, when considering the problem of a particle in an infinite circular well [27]. In our case, using the same electron effective masses as before, we get $r_B(T_1) \simeq 1.2$nm, $r_B(T_2) \simeq 0.89$nm, $r_B(T_3) \simeq 0.74$nm and $r_B(T_4) \simeq 0.66$nm, which are of the order of the values of the barrier widths previously calculated.

Note that the barrier profiles of Figure 9 at low temperatures are sharper than the barrier profiles at high temperatures, where quantum effects get blurred. This blurring of the potential is more apparent near the barrier top where filaments start being destroyed. Moreover, we observe a barrier narrowing at high temperatures for energies close to zero. This is due to the fact that the transmission coefficient $D(E)$ turns out to be higher than expected at low energies and high temperatures [see Figure 8(c) and especially 8(d)]. This narrowing of the potential barrier does not occur when $D(E)$ is an increasing function of E, like it happens in Figure 2 for the parabolic barrier (this is the usual case, but not the more general one).

In any case, the barrier profile coming from experimental I-V curves seems to slightly differ from the barrier profiles coming from lineal D_L and parabolic D_P transmissions. Perhaps the use of higher-degree continuous piecewise estimations of $D(E)$ provides a better fitting to the experiment. This is left for future work.

Conclusions

An analytic expression for the non-linear current-voltage characteristic of resistive memories based on filamentary conduction was presented. The model was developed within the framework of Landauer's theory for mesoscopic conductors. The role of the confinement effect on the electron wavefunction was highlighted through an in-depth investigation of different approximations for the tunneling coefficient. In addition, the role of the charge reservoirs temperature on the current magnitude was thoroughly analyzed. In agreement with previous reports, it was found that the smearing of the Fermi functions at the electrodes cannot explain by itself the current increase observed for increasing temperatures. Instead, a barrier-lowering effect can indeed explain the experimental results. This is directly obtained by inverse modeling of the tunneling current, without making any assumption about the barrier profile as done in the past. The proposed approach reveals that quantum effects cannot be ruled out when discussing the electron transport mechanisms in this kind of RRAM devices and that a classical simulation framework only describes specific situations. It is important to highlight that we have developed a current model including temperature and quantum effects that can be employed for circuit design and simulation.

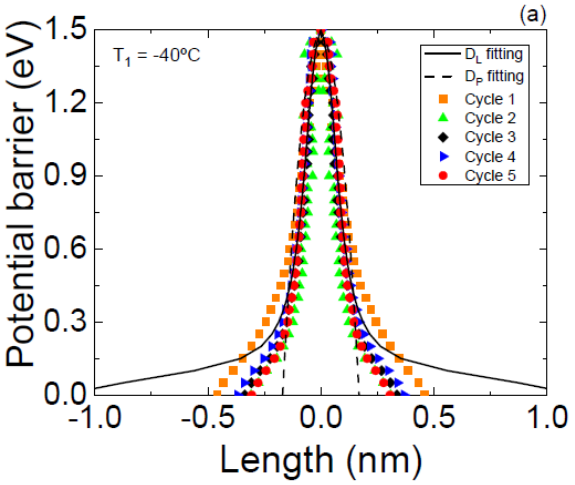

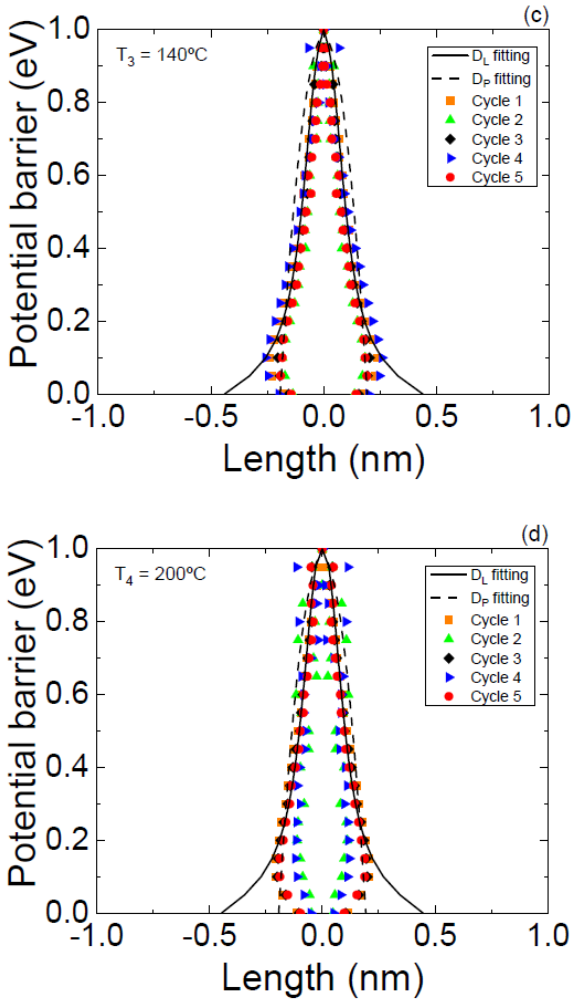

Figure 9: Potential barrier $U(x)$ (in eV), against the longitudinal x-axis (in nanometers), associated with the transmission coefficient (18) obtained from the experimental values of the I-V curves of Figure 8 for four temperatures. The potential barriers obtained from D_L and D_P are represented by solid and dashed black curves, respectively.

Acknowledgements

We would like to thank F. Campabadal and M. B. González from the IMB-CNM (CSIC) in Barcelona for fabricating and providing the experimental measurements of the de- vices employed here. The authors thank the support of the Spanish Ministry of Science and Universities and the FEDER program through projects TEC2017-84321-C4-3- R, TEC2017-84321-C4-4-R and PGC2018-097831-B-I00. This study has been partially financed by the Consejería de Conocimiento, Investigación y Universidad, Junta de Andalucía and European Regional Development Fund (ERDF) under projects A-TIC-117- UGR18, SOMM17/6105/UGR, UHU-1262561 and the research group FQM-381. This work has made use of the Spanish ICTS Network MICRONANOFABS.

A. Polylogarithm functions

Replacing the piece-wise linear transmision coefficient (6) into the Landauer-Buttiker equation (1) for the current I, we arrive to

$$I = \frac{2q}{h}\int_{E_0-\delta}^{E_0+\delta}\frac{E-(E_0-\delta)}{2\delta}\big(F(E-\mu_1)-F(E-\mu_2)\big)dE + \frac{2q}{h}\int_{E_0+\delta}^{\infty}\big(F(E-\mu_1)-F(E-\mu_2)\big)\,dE \quad (22)$$

If we write the Fermi-Dirac distribution function (2) as

$$F(E-\mu) = \frac{1}{1+\exp\left(\frac{E-\mu}{k_BT}\right)} = \frac{1}{1+e^{\epsilon}/z},\ \epsilon \equiv \frac{E}{k_BT},\ z \equiv e^{\frac{\mu}{k_BT}},$$

And use that

$$\int_0^{\infty} F\,(E-\mu)dE = k_BT\ln(1+z)$$

and the definition of the dilogarithm or Spence's function [29]

$$\mathrm{Li}_2(-z) \equiv -\int_0^{\infty}\frac{\epsilon d\epsilon}{1+e^{\epsilon}/z} = \sum_{k=1}^{\infty}(-1)^k\frac{z^k}{k^2}, \quad (23)$$

we can easily compute

$$\int_{E_0-\delta}^{E_0+\delta}(E-E_0)\,F(E-\mu)dE = -k_BT\delta\big(\ln(1+z_+)+\ln(1+z_-)\big) + k_B^2T^2\big(\mathrm{Li}_2(-z_-)-\mathrm{Li}_2(-z_+)\big),$$

with $z_{\pm} \equiv \exp\left(\frac{-\mu+E_0\pm\delta}{k_BT}\right)$, together with

$$\int_{E_0-\delta}^{E_0+\delta} F\,(E-\mu)dE = 2\delta + k_BT\big(\log(1+z_-) - \log(1+z_+)\big)$$

and

$$\int_{E_0+\delta}^{\infty} F\,(E-\mu)dE = -(E_0+\delta) + k_BT\log\left(e^{\frac{E_0+\delta}{k_BT}}+z\right).$$

Putting together all the previous partial calculations into (22) and using the definition of the cathode $\mu_1 = \mu + \beta qV$ and anode $\mu_2 = \mu - (1-\beta)qV$ quasi-Fermi levels in terms of the voltage V, we finally arrive to the expression (8).

The dilogarithm or Spence's function is also defined as [29]

$$\mathrm{Li}_2(z) = -\int_0^z \frac{\ln(1-t)}{t}dt = -\int_0^1 \frac{\ln(1-zt)}{t}dt \quad (24)$$

and it turns out to be a particular case ($n = 2$) of the polylogarithm (Jonquière's) function [30]

$$\mathrm{Li}_n(-z) = -\frac{1}{(n-1)!}\int_0^\infty \frac{\epsilon^{n-1}d\epsilon}{1+e^{\epsilon}/z} = \sum_{k=1}^{\infty}(-1)^k\frac{z^k}{k^n}, \quad (25)$$

which can be extended to non-integer n values. These functions are common in quantum statistics, where they are also called Fermi-Dirac or Bose-Einstein integrals. Moreover, in quantum electrodynamics, they arise in the calculation of processes represented by higher-order Feynman diagrams. In our context, the trilogarithm Li_3 function would arise when considering piecewise parabolic (quadratic spline) approximations to the transmission coefficient $D(E)$. In general, a piecewise polynomial transmission coefficient $D(E)$ of degree m would give rise to a current $I(V, T)$ (1) written in terms of Li_{m+1}.

References

[1] S. Slesazeck, T. Mikolajick, Nanoscale resistive switching memory devices: a review, Nanotechnology 30, 2019. DOI: 10.1088/1361-6528/ab2084

[2] Supriyo Datta, Electronic transport in mesoscopic systems, Cambridge University Press, 1995

[3] E. Miranda, J. Suñé, Electron transport through broken down ultra-thin SiO2 layers in MOS devices, Microelectronics Reliability 44, 1-23, 2004

[4] A. Avellán, E. Miranda, D. Schroeder and W. Krautschneider, Model for the voltage and temperature dependence of the soft breakdown current in ultrathin gate oxides, Journal of Applied Physics 97, 014104, 2005

[5] E. Miranda, C. Walczyk, C. Wenger, T. Schroeder, Model for the resistive switch- ing effect in HfO2 MIM structures based on the transmission properties of narrow constrictions, IEEE Electron Device Letters, 31, 609-611, 2010

[6] C. Walczyk, D. Walczyk, T. Schroeder, T. Bertaud, M. Sowinska, M. Lukosius, M. Fraschke, D. Wolansky, B. Tillack, E. Miranda, C. Wenger, Impact of Temperature on the Resistive Switching Behavior of Embedded HfO2-Based RRAM Devices, IEEE Transactions on Electron Devices 58, 2011.

[7] M.A. Villena, M.B. González, F. Jiménez-Molinos, F. Campabadal, J.B. Roldán, J. Suñé, E. Romera y E. Miranda, Simulation of thermal reset transitions in resistive switching memories including quantum effects, Journal of Applied Physics, 115, 214504, 2014

[8] E. Yalon, A. Sharma, M. Skowronski, J. Bain, D. Ritter, I. Karpov, Thermometry of filamentary RRAM devices, IEEE Trans Electron Dev 62, 2972, 2015

[9] D. Niraula, V. Karpov, Heat transfer in filamentary RRAM devices, IEEE Trans Electron Dev 64, 4106-4113, 2017. DOI: 10.1109/TED.2017.2741782

[10] A. Lohn, P. Mickel, M. Marinella, Analytical estimations for thermal crosstalk re- tention, and scaling limits in filamentary resistive memory, J Appl Phys 115, 234507, 2014

[11] S. Larentis, F. Nardi, S. Balatti, D. Gilmer, D. Ielmini, Resistive switching by voltage-driven ion migration in bipolar RRAM-Part II: Modeling, IEEE Trans Elec- tron Dev 59, 2468, 2012

[12] S. Kim, S. Choi, W. Lu, Comprehensive physical model of dynamic resistive switch- ing in an oxide memristor, ACS Nano 8, 2369-2376, 2014

[13] M. von Witzleben, K. Fleck, C. Funck, B. Baumkotter, M. Zuric, A. Idt, T. Breuer, R. Waser, U. Bottger, S. Menzel, Investigation of the impact of high temperatures on the switching kinetics of redox-based resistive switching cells using a high-speed nanoheater, Adv Electron Mater 3, 1700294, 2017

[14] Y. Li, S. Long, Y. Liu, C. Hu, J. Teng, Q. Liu, H. Lv, J. Suñé, M. Liu, Conductance quantization in resistive random access memory, Nanoscale Research Letters 10, 420, 2015

[15] W. Yi, S. Savelev, G. Medeiros-Ribeiro, F. Miao, M. Zhang, J. Yang, A. Bratkovsky, R. Stanley Williams, Quantized conductance coincides with state instability and excess noise in tantalum oxide memristors, Nature Communications 7, 11142, 2016

[16] E. Wu, A. Kim, B. Li, J. Stathis, Elapsed-time statistics of successive breakdown in the presence of variability for dielectric breakdown in BEOL/MOL/FEOL ap- plications, 2018 IEEE International Reliability Physics Symposium (IRPS). DOI: 10.1109/IRPS.2018.8353553

[17] L.D. Landau and E.M. Lifshitz, Quantum Mechanics, Non-relativistic theory, Perg-amon Press 1977, page 184

[18] H.A. Fertig and B.I. Halperin, Transmission coefficient of an electron through a saddle-point potential in a magnetic field, Phys. Rev. B36 (1987) 7969-7976

[19] E. Miranda and J. Suñe, Analytic Modeling of Leakage Current Through Multiple Breakdown Paths in SiO_2 Films, in Proceedings of the 39th Annual 2001 IEEE International Reliability Physics Symposium (2001), pp. 367-379.

[20] Christian Walczyk et al., Impact of Temperature on the Resistive Switching Be-havior of Embedded HfO_2-Based RRAM Devices, IEEE Transactions on Electron Devices 58, No. 9, (2011)

[21] M.B. Gonzalez, J.M. Rafí, O. Beldarrain, M. Zabala and F. Campabadal Analysis of the switching variability in Ni/HfO2-based RRAM devices, IEEE Trans. Dev. Mat. Reliab. 14(2), 769-771, 2014.

[22] C. Acal, J.E. Ruiz-Castro, A. M. Aguilera, F. Jiménez-Molinos, J.B. Roldán, Phase- type distributions for studying variability in resistive memories, Journal of Compu-tational and Applied Mathematics, 345, pp. 23-32, 2019.

[23] J.B. Roldán, F.J. Alonso, A.M. Aguilera, D. Maldonado, M. Lanza, Time series statistical analysis: a powerful tool to evaluate the variability of resistive switching memories, Journal of Applied Physics, 125, 174504, 2019.

[24] M.A. Villena, M.B. González, J.B. Roldán, F. Campabadal, F. Jiménez-Molinos, F.M. Gómez-Campos y J. Suñé, An in-depth study of thermal effects in reset tran- sitions in HfO2 based RRAMs, Solid State Electronics, 111, pp. 47-51, 2015.

[25] S. Aldana, P. García-Fernández, R. Romero-Zaliz, F. Jiménez-Molinos, F. Gómez-Campos, J.B. Roldán, Analysis of conductive filament density in resistive RAMs, a 3D Kinetic Monte Carlo approach, Journal of Vacuum Science and Technology B, 36, p. 62201, 2018

[26] A. Cester et al., A Novel Approach to Quantum Point Contact for post Soft Break-down Conduction, International Electron Device Meeting (2001) 305

[27] R. Robinett, Visualizing the solutions for the circular infinite well in quantum and classical mechanics, Amer. J. Phys., 64, 440-446, 1996.

[28] Larry Schumaker, Spline functions: basic theory, Cambridge University Press (2007), third edition.

[29] Abramowitz, M.; Stegun, I.A. (1972). Handbook of Mathematical Functions with Formulas, Graphs, and Mathematical Tables. New York: Dover Publications. ISBN 978-0-486-61272-0.

[30] A. Jonquière, Note sur la serie $\sum_{n=1}^{\infty} x^N/n^s$, Bull. Soc. Math. France 17 (1889) 142- 152. C.

Truesdell (1945) On a function which occurs in the theory of the structure of polymers. Ann. of Math. (2) 46, pp. 144-157.

Chapter 5.

5. Use of dynamic route maps to understand resistive memories operation

5.1. Introduction

A Dynamic Route Map (DRM) consists of a tool devoted to examining the temporal evolution of resistive memories in the more general context of dynamical systems. In that sense, the DRM supplies valuable information of the state variable that controls the device to reach a better understanding of the RS process. Thereby, a unique surface in a phase diagram for stability of the state variable that describes the device is created where multiple trajectories are included depending on several conditions such as the frequency of the input signal applied or the voltage signal shape. Two different models have been included in the study, the first one is based on a physical description considering filamentary conduction and the second one is based on the mathematical definition of a memristor through a nonlinear analytical association between charge and flux.

To check these analytical models, a set of measurements has been carried out employing different slopes and waveforms which implies different ramped voltages. Thus, the CF average radius is extracted assuming a truncated-cone shape to show that all the points belong to the DRM surface no matter what the input voltage signal waveform is.

The following section is an already published work [Maldonado2020].

D. Maldonado et al.

Chaos, Solitons & Fractals (2020)

Maldonado, D., González, M. B., Campabadal, F., Jiménez-Molinos, F., Al Chawa, M. M., Stavrinides, S. G., ... & Chua, L. O. (2020). Experimental evaluation of the dynamic route map in the reset transition of memristive ReRAMs. Chaos, Solitons & Fractals, 139, 110288, DOI: 10.1016/j.chaos.2020.110288

Quality metrics

Data base	Rating	Quartile
Web of Science	Impact factor: 5.94	Q1
Scimago	Scientific journal ranking: 1.04	Q1

Publication citations (23-03-2022)

Google Scholar	Web of Science
10	**7**

Experimental Evaluation of the Dynamic Route Map in the Reset Transition of Memristive ReRAMs

David Maldonado[a], Mireia B. Gonzalez[b], Francesca Campabadal[b], Francisco Jiménez-Molinos[a], M. Moner Al Chawa[c], Stavros G. Stavrinides[d], Juan B. Roldan[a], Ronald Tetzlaff[c], Rodrigo Picos[e], Leon O. Chua[f]

[a]*Dept. de Electrónica y Tecnología de Computadores, Universidad de Granada, Spain*

[b]*Institut de Microelectrònica de Barcelona, IMB-CNM, CSIC, Barcelona, Spain*

[c]*Institute of Circuits and Systems, Technische Universität Dresden, Dresden, Germany*

[d]*School of Science and Technology, International Hellenic University, Thessaloniki, Greece.*

[e]*Physics Department, University of Balearic Islands, Balearic Islands, Spain.*

[f]*Electrical Engineering and Computer Science Department, University of California, Berkeley, CA, USA*

Abstract

In this paper, we analyze the reset transition in bipolar TiN/Ti/HfO_2 (10 nm)/Al_2O_3(2 nm)/W ReRAM devices using a tool that allows studying the temporal behaviour of these devices. This tool, the Dynamic Route Map (DRM), provides information about the temporal evolution of the state variable that governs the behaviour of the device, thus allowing an increased insight into resistive switching processes.

Here, we show that this DRM is a powerful tool, that may help explaining some non-intuitive behaviours of memristors, like the difference in the reset voltage when the inputs are from different frequency or shape. Using this tool, this fact can be explained as a different trajectory on a unique surface defining the device.

As a first step, we have used two different models, one based on a physical description, and another one based on the mathematical definition of memristor as a non linear relation between charge and flux. We check that similar DRM can be obtained from both models.

Additionally, several series of set-reset transitions have been measured using voltage ramps of different slopes. From the measured transitions, the corresponding resistance has been extracted and,

assuming conductive filaments (CF) as the switching mechanism, the corresponding CF radius has been calculated. Using these data, we show that explanations from the model are also supported when using experimental data, thus proving the validity of the approach.

Email addresses: s.stavrinides@ihu.edu.gr (Stavros G. Stavrinides),

rodrigo.picos@uib.es (Rodrigo Picos)

Preprint submitted to Elsevier July 27, 2021

1. Introduction

The apparent symmetry between the relations of the four fundamental electrical magnitudes, namely the current i, the voltage v, the charge q and the flux ϕ, was something that passed unnoticed for many years in circuit theory. It was this idea that led Leon O. Chua, during the early 70s, to present the axiomatic introduction and the related description of a fourth (missing at that moment) electrical element, named the Memristor [1]. Its name originated from the fact that such an element should behave as a resistor endowed with memory, these two properties (resistance and the feature memory) being unified in one element. In fact, memristors had been described many years ago [2], though they had never been in the mainstream of electrical or circuit theory. Besides, Chua's work led to the generalization of a class of devices as well as systems that are inherently nonlinear and governed by a state-dependent, algebraic relation accompanied by a set of differential equations, which are called memristive systems or devices [3].

As a result of the inherent memory feature embodied in memristors, these novel devices are expected to be one of the key enablers of a technological breakthrough in integrated circuit (IC) performance-growth, beyond and more than Moore [4]. Among others, they are expected to provide a solution to the classical problem of the bottleneck in data transmission between memories and processors. The Internet-of-Things (IoT) and other edge computing applications are expected to be areas where the introduction of memristors and memristive devices would be beneficial, or even a radical changer of the related technological landscape. Thus, an increasing number of memristor-based applications has already been proposed: new kind of memories (ReRAMs, MRAM, etc.) [5, 6, 7], innovative new sensor devices [8, 9], or fundamental elements in bio-inspired systems (artificial neural networks (ANNs) and other) [10], among many others.

On the other hand, memristive devices can be nowadays implemented in a wide range of technologies, from spintronics [11] to organic materials [12, 13] and many different oxides [14, 15, 16, 17], or even emulators [18, 19, 20, 21]. However, and up to the best of our knowledge, very few foundries are including memristors in their design repertoire, as it customarily happens with other passive elements, like resistors or capacitors. This is due to the inadequate level of maturity of all the up-to-date proposed memristive technologies, which is a drawback that is expected to be solved in the near future.

Simulating a new design incorporating memristors is not a straightforward task; many good models have been proposed, both using the classical approach that utilizes current and voltage [22, 23, 24, 25, 26], or the more recent charge and flux approach [27, 28, 29, 30], which historically had been also used in oxide breakdown. However, most of these models appear to have drawbacks that make the simulation of large circuits rather difficult or even impractical [31]. Besides, some of the main problems of current memristor device technologies are: the variability they exhibit, from cycle to cycle [32, 33]; and the short number of cycles they can withstand (between 10^6 and 10^8 cycles).

A very good test to show the goodness of a model is the so-called Dynamic Route Map (DRM), that plots the evolution of the governing variable of a system in front of its rate of change (i.e., its temporal derivative). As will be explained later, this representation is a powerful tool that may provide significant insight into the

inner workings of the device. In this work, we aim to show experimentally that the DRM tool actually makes sense in memristive ReRAMs, and can be used as a unifying tool to describe the different behaviour of the devices under various stimuli. We will show that this behaviour can be described as a different trajectory on the same surface. Specifically, we will focus on the Low Resistance to High Resistance State (LRS to HRS, or RESET) transition, since it is considered to be more complex than the SET transition and, thus, a more appropriate example to highlight the merits of the DRM technique.

The paper is structured following this idea: after this introduction, Section 2 introduces the basic principles of formal memristor modelling, where the DRM naturally appears. Then, Section 3 is devoted to introduce the concept of the Dynamic Route Map and its applications, as well as two different models showing two different approaches to DRM. The first model directly introduces an equation for the variable of concern (the radius of a conductive filament), while the second model derives the effective radius from the calculation of the conductance. Section 4 presents the results obtained by applying different waveforms to a single device, showing that we can obtain experimentally its DRM. Finally, Section 5 ends the paper summarizing the main points and results.

2. Memristor Modelling Framework

A fundamental theoretical framework for studying memristors and circuits presenting memristive behaviour in the flux–charge (ϕ-q) domain, was developed by Corinto *et al.* in [34]. In that paper, the authors explain the advantages of using the flux–charge (ϕ-q) domain in studying memristor elements, compared to the current–voltage (i-v) domain.

On the other hand, utilizing the taxonomy proposed in [35], memristors are classified according to their proximity to the original definition of the memristor. Thus, three main categories of memristor devices emerge, namely the ideal, the generic, and the extended memristor. In the same work [34], the essential mathematical framework describing their behaviour was also developed. This extended categorization emerged as a necessity in order to include theoretically the description of pinched, hysteretic behaviours demonstrated by various elements, not only in circuit theory and electronics but also in nature.

Among the different categories presented above, the class of extended memristors is the most general one and it refers to memristors that have extra state variables (next to ϕ and q). For the specific case of flux-controlled memristors, they are described by Eqs. (1) to (3):

$$i = G(\varphi, v, x) \cdot v \qquad (1)$$

$$\dot{x} = g_{\varphi}(\varphi, v, x) \qquad (2)$$

$$\dot{\varphi} = v \qquad (3)$$

The nonlinear memconductance G in Eq. (1) represents the inverse memristance M of an extended memristor, while v is the voltage applied to the memristor, and $\boldsymbol{\varphi}$ is the flux or voltage first momentum. The vector $\mathbf{x}$ stands for a *set* of extra state variables, which includes physical magnitudes according to the memristive system; indicatively they could be the internal temperature, the radius of a conducting filament, or any other non-electrical variable describing the state of the memristor. In addition, the dynamics of the state variables $\mathbf{x}$ are governed by g_{ϕ} and Eq. 2. It is noted that all the real-world memristor devices that have appeared until now, are indeed extended memristors.

Taking into account the Lagrangian L and the Jacobian **J**, these are defined in Eqs. (4) and (5), respectively.

$$L(\varphi, v, x) = \frac{\partial g_{\varphi}(\varphi,v,x)}{\partial v} \quad (4)$$

$$J(\varphi, v, x) = \left(\frac{\partial g_{\varphi}(\varphi,v,x)}{\partial x_1}, \ldots, \frac{\partial g_{\varphi}(\varphi,v,x)}{\partial x_n}\right) \quad (5)$$

If no parasitic effects are present, then extended memristors can be simplified to generic memristors (or, simply, memristors). That is because function g_{ϕ} is only dependent on flux ϕ and the state variables **x**, thus $L = 0$. Finally, ideal memristors (those corresponding to the original definition described by [1]) are generic memristors that demonstrate no other state variable dependence, thus, $J = 0$.

A special case of Eq. (2) is often referred to as the power–off plot (POP) equation and determines the memory capability of the system under no excitation; in this case for $v = 0$ or ϕ = *constant*. It is apparent that if the POP equation is zero, the system presents a long–term memory since the state variable will not change with time, while if it is different than zero, the system is capable of exhibiting only short–term memory.

It is noted that the above framework has been already used in successfully modelling different kinds of memristive systems, further improving the generalized framework for compact modelling in the flux-charge space [36]. Other relevant works using this approach could also be found, like in the case of [37] where a charge-dependent mobility model was used to describe a memristor, [28] or [30] which presented semi-empirical models for ReRAMs as memristors, [38] that described a Monte Carlo model for ReRAMs, [39] which derives a delay model for memristor–based memories utilizing a flux-charge description, or [27] where a model for phase change memories is presented. Finally, two examples of experimental characterization of a memristive system utilizing the flux-charge notation, are presented in [40], where a light bulb is determined to be a generic memristor and in [41, 42], where the influence of waveform frequency and shape are discussed.

3. The Dynamic Route Map

3.1. The Dynamic Route Map Technique

Phase space, initially introduced by J. Liouville [43], is a space proposed by Poincaré [44] for studying nonlinear systems. The study of nonlinear systems in phase (or state) space is an established approach in nonlinear dynamics, since important attributes of the systems clearly emerge within. The case of a two dimensional phase space, that of the phase plane, i.e. the space of X vs. dX/dt (where X is a state variable of the studied system), was introduced and utilized by the Ehrenfests in the early 1900s [45].

As already mentioned above, memristors are described, in general, by Eqs. (1) - (3). These equations refer to the case of extended, flux-controlled memristors; while a duality principle holds for the case of charge-controlled ones. Considering their hysteretic behaviour (fingerprint) and furthermore their switching properties, memristors clearly emerge as nonlinear elements [46]. Thus, it is expected that studying their properties within a phase space, would provide useful information about the devices and their dynamical properties.

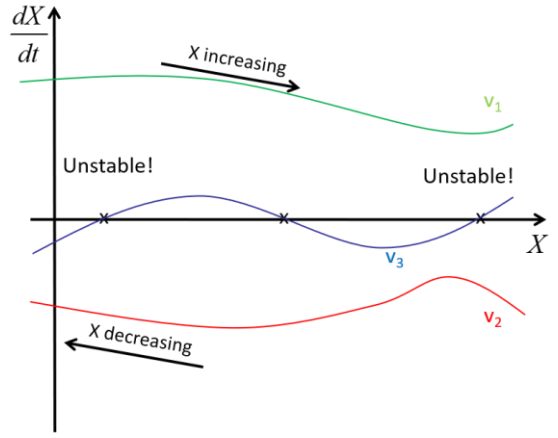

Figure 1: A typical DRM for an arbitrary system, having as a parameter the voltage applied. It includes three distinct cases; the case in middle provides an example of identifying the equilibrium points of a system - two unstable (labeled x) and a stable one (unlabelled x), in this case.

To this direction, the Dynamic Route Map technique, a method mounted within the phase plane, was proposed to be applied in the case of memristors; thus providing information on specific features they demonstrate, such as their switching properties [47].

Beginning from the definition in the case of memristors, the Dynamic Route defines the course of a non-zero state variable, within its phase plane, when memristor's voltage (for flux-controlled) or current (for charged-controlled) gets a specific value. Notice that this is equivalent to plot Eq. 2. Consequently, the DRM is a parametric collection of a theoretically infinite number of Dynamic Routes [47]. In Fig. 1, a typical example of a DRM is presented. In this figure three distinct cases appear; the most characteristic is the case in middle, which includes a stable and two unstable equilibrium points (where $dX/dt = 0$).

Important features of DRM and consequences coming out of it, include the following (for a comprehensive and detailed presentation, see [47]):

- DRM is infinitely dense.
- For visualizing DRM, only some of the Dynamic Routes (a finite number) are displayed.
- Any point of a dynamic route, belonging to the upper half plane, moves to the right (increasing the value of the variable).
- For a dynamic route belonging to the upper half plane, the higher it stands, the faster its points move along their tracks (to the right).
- Any point of a dynamic route, belonging to the lower half plane, moves to the left (decreasing the value of the variable).

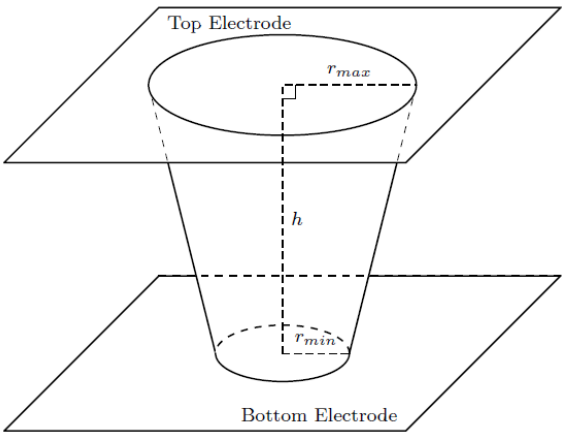

Figure 2: Parameters of a conductive filament when considered as a truncated cone.

- For a dynamic route belonging to the lower half plane, the lower it stands, the faster its points move along their tracks (to the left).
- Points laying on the horizontal axis, are equilibrium points (since their possess null velocity $dX/dt = 0$).
- An equilibrium point in 2D may be stable (the trajectories are such that the

points converge towards it) or unstable (the points diverge from it).

The dynamic route for a zero parameter value – in the case of memristor for zero voltage v=0 (or current i=0) – reduces to the Power-Off Plot (POP). The POP has been proposed as a tool for identifying memristor volatility in simple visual way. According to [47], any memristor demonstrating one stable and two unstable equilibrium points appears to be a volatile device; on the contrary, non-volatile memristors demonstrate one unstable and two stable equilibrium points.

Finally, it is worth commenting on one important issue that could be easily identified by utilizing the DRM: the dynamics demanded in order to achieve switching in a memristor device (i.e. setting and resetting it) can be visualized on the DRM. This way it becomes clear that these two operations could be achieved by obliging the operation point to change the dynamic route for a specific period of time. This operation is usually achieved by the application of suitable positive or negative pulses that compel switching between two equilibrium points.

3.2 Example of DRM: Toy Model

For the shake of clarity, a simple toy model, that can be easily conceived, is presented in this section. Let's consider that the memristive behaviour is mediated by a conductive filament, defined as in Fig. 2. To provide a physical basis, we can consider a model described by [48], but strongly simplified to retain only some features. We can describe this model using the formalism presented in the previous section as the following set of equations:

$$i = G(\varphi, v, r) \cdot v \quad (6)$$

$$\dot{r} = g_{\varphi}(\varphi, v, r) = A \cdot v \cdot exp\left(-\frac{B \cdot r^2}{a+v}\right) \quad (7)$$

$$G(\varphi, v, r) = K\frac{r^2}{h} \quad (8)$$

$$L(\varphi, v, x) = \frac{\partial g_{\varphi}(\varphi, v, x)}{\partial v} = A \cdot e^{-\frac{Br^2}{a+x}} \frac{a^2+2av+v(Br^2+v)}{(a+v)^2} \quad (9)$$

$$J(\varphi, v, x) = \frac{\partial g_{\varphi}(\varphi, v, x)}{\partial r} = -2\,A\,B\frac{v\,r}{a+v} \cdot exp\left(-\frac{B \cdot r^2}{a+v}\right) \quad (10)$$

In the equations above A, B, and K are constants related to the technology, and h is the device dielectric thickness. The radius r is defined as an effective average between r_{max} and r_{min} in Fig. 2. This model corresponds to an extended memristor device, since neither the Laplacian (Eq. 9) nor the Jacobian (Eq. 10) are nil. In addition, we can see that the POP equation (Eq. 7 for $v = 0$: $\dot{r}(v = 0) = 0$) is nil. Thus, the model corresponds to an extended memristor with long-term memory.

This very simple model already leads to a behaviour showing some of the most intriguing dynamics of real resistive memristor devices, namely a high dependence on initial conditions (i.e., the initial radius of the CF), and a reset voltage (i.e., the voltage where the radius gets to zero) depending on both the initial conditions and on the shape and frequency of the used waveform, as has been shown experimentally [41, 49].

The dependence on the input signal shape and frequency of this model is shown in Fig. 3, where four different signals are plotted

versus time until the filament breaks at $r = 0$, all starting from the same initial point. Notice that this is equivalent to the reset point. The same waveforms are plotted in Fig 4, but plotting the current versus the voltage. In the case of the sinusoidal waveforms (blue and black lines), the memory effect is clearly shown in the apparition of lobes. Thus, this demonstrates that a repetitive signal can be used to set the desired resistance of the device.

On a separate thread, we have then used Eq. 7 to plot the evolution of the radius versus the radius (the Dynamic Route Map, DRM), in Fig. 5. In this plot, it is clearly seen that the radius decreases faster for higher voltages and smaller radius, as expected.

Finally, we have used the same Eq. 2 to plot a 3D surface in Fig. 6, where we have also plotted the evolution of the waveforms in Fig. 3. Notice that when using this representation, the evolution of the system means that all the waveforms simply move over the surface defined by Eq. 7, thus providing a valuable insight into the dynamics that govern the device.

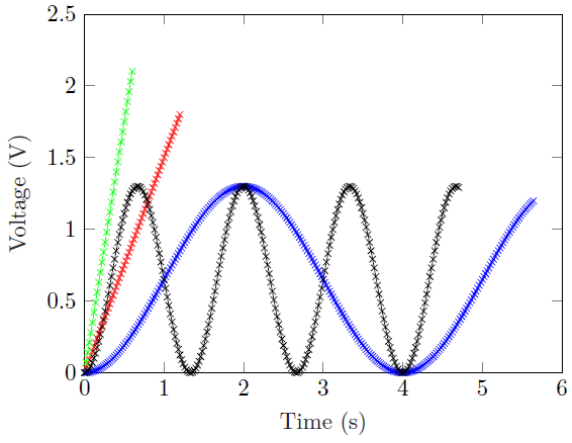

Figure 3: Temporal evolution of the curve of the applied signal until the reset point for different waveforms. Notice that the curves stop when the reset point is reached (the CF radius gets to zero) and, thus, have different lengths.

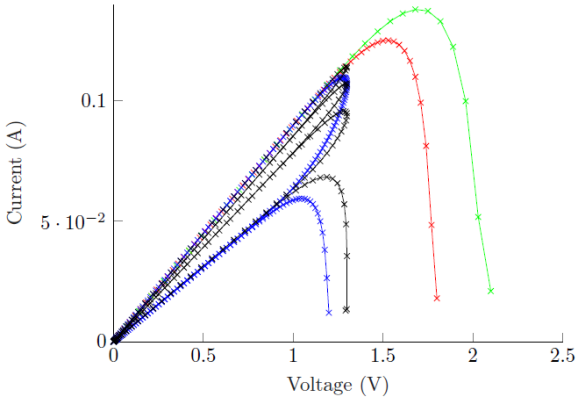

Figure 4: Current vs Voltage evolution of the curve of the applied signal until the reset point for different input waveforms, as shown in Fig. 3. Notice that the curves stop when the reset point is reached (the CF radius gets to zero).

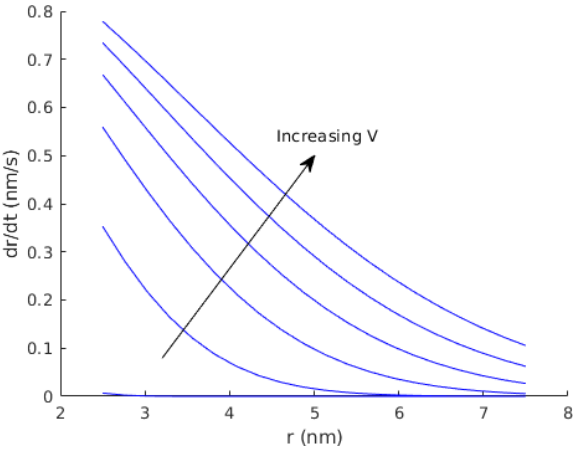

Figure 5: DRM of the CF radius, as in Eq. 7, for various constant voltages. The arrow shows the direction of increasing voltage between 0 and 2V, with 0.4V increment.

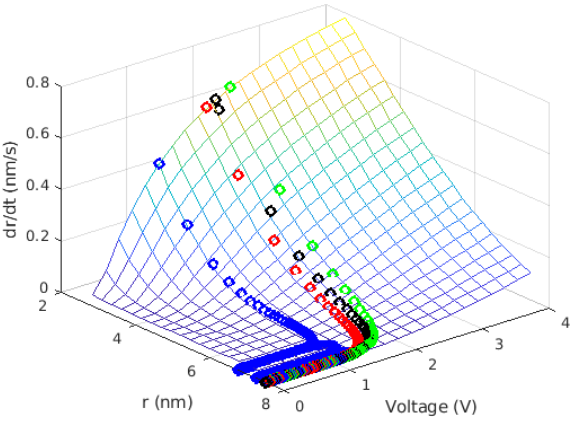

Figure 6: Evolution of the curve of the applied signal in the DRM space. The curves are extracted from those in Figures 4 and 5, as calculated with Eqs. 6-10. Notice that the curves stop when the reset point is reached, which is when the CF radius gets to zero. The surface corresponds to the 3D representation of Fig. 5.

3.3 DRM in a Flux-Charge model

As another example, we will consider an already existing model [50, 51, 52, 53], derived from that presented in [28]. This model starts by defining a relation between charge and flux, as in Eq. 11.

$$Q = Q_0 \cdot \left(\frac{\phi}{\phi_0}\right)^n \quad (11)$$

The memconductance G is then described by:

$$G = \frac{dQ}{d\phi} = n \cdot \frac{Q}{\phi} \quad (12)$$

Its rate of change can be written by taking the derivative of the memconductance (12) as following:

$$\frac{dG}{dt} = G \cdot v \cdot \frac{n-1}{\phi} \quad (13)$$

Notice that this is already the DRM equation for the conductance. However, it can be written in a more compact way assuming that n is nearly a constant:

$$\frac{dG}{dt} = G\,(n-1)\,\frac{d}{dt}ln(\phi) = G\,\frac{d}{dt}ln(\phi^{n-1}) \quad (14)$$

The effective radius r_{eff} of the conductive filament can also be calculated easily, assuming a cylinder [30, 38]:

$$G = \frac{\sigma\,\pi\,r_{eff}^2}{h} \quad (15)$$

where σ is the conductance of the conductive filament, assumed to be nearly constant.

Then, the radius and its rate of change can be expressed as:

$$r_{eff} = r_0\sqrt{G} \quad (16)$$

where $r_0 = \sqrt{h/\sigma\pi}$.

$$\frac{dr_{eff}}{dt} = \frac{r_0}{2\sqrt{G}}\frac{dG}{dt} = \frac{1}{2}r_{eff}\,\frac{d}{dt}ln(\phi^{n-1}) \quad (17)$$

For instance, let us consider the case of a simple ramp for the input voltage with slope α:

$$V = \alpha t \quad (18)$$

Then the flux is:

$$\phi = \frac{1}{2}\alpha t^2 + \phi_0 \quad (19)$$

Then, the DRM can be expressed as:

$$\frac{dG}{dt} = (n-1)\,G\,\frac{d}{dt}ln\left[\left(\frac{1}{2}\alpha t^2 + \phi_0\right)\right] = \frac{(n-1)\,G\,\alpha t}{\frac{1}{2}\alpha t^2+\phi_0} \quad (20)$$

or using the effective radius:

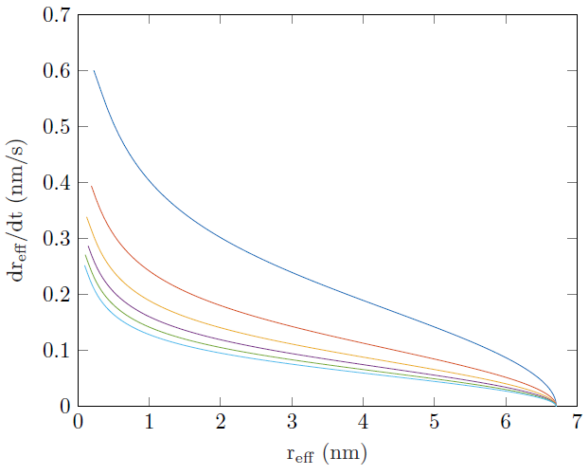

Figure 7: DRM for the effective radius and its temporal derivative for different voltage ramp slopes (α), using memristor model described by Eq. 21. Notice that dr_{eff}/dt is plotted in absolute value.

$$\frac{dr_{eff}}{dt} = \frac{(n-1)\,r_{eff}\,\alpha t}{\alpha t^2+2\phi_0} \quad (21)$$

Figure 7 plots Eq. 21 for different values of the slope α to obtain the DRM in the case of the effective radius. It can be seen that the rate of change of the radius r_{eff} increases when the radius decreases, which is coherent with a

thermal model where the relation between the volume where the power is generated and the surface where the power is dissipated goes as $1/r_{eff}$. This behaviour implies a higher power dissipation efficiency for smaller radius, thus causing higher radius decreasing rates due to higher temperatures.

4. Experimental Measurements and Results

After introducing the DRM technique, we have presented two different examples on how to calculate it in the case of two models. These two examples have shown how to interpret the evolution of the system under different input waveforms. This method has then been utilized to interpret data obtained from real devices.

We have measured TiN/Ti/HfO_2(10 nm)/Al_2O_3(2 nm)/W devices, where the dielectric layers were grown by Atomic Layer Deposition. For all our measurements, the W layer was grounded and the different input voltage signals were applied to the TiN/Ti top electrode. To estimate the DRM, we considered the effects of different ramp speeds and sine function voltage signals of different frequency, measuring 100 Resistive Switching (RS) cycles for each different waveform as in [49]. The ramp speeds were (0.08, 0.16, 0.24, 0.34, 0.43) V/s, while the sinusoidal signal frequency were (0.0131, 0.0340, 0.0540) HzThe measurements were performed by using a HP 4145B parameter analyzer and a probe station. The signals were generated by the 4145B, which was GPIB connected and controlled remotely. This same instrument was also measuring the currents through the devices under test. Figure 8 shows some examples of the I-V curves measured for a selected device under the different inputs waveforms, where a significant dependence on frequency and shape is observed, as expected [41, 49].

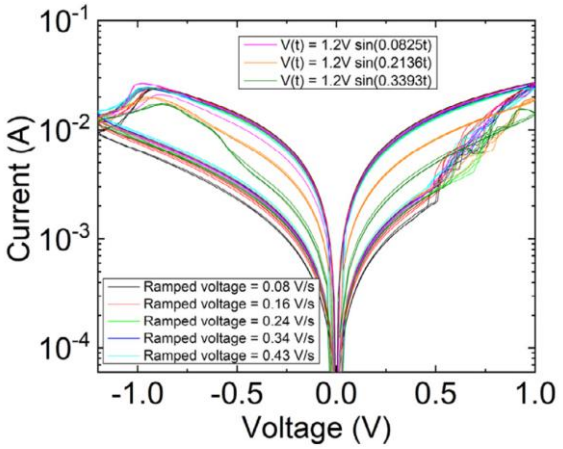

Figure 8: Examples of different I-V curves of the selected devices under different waveform excitation.

This work has focused on the low (LRS) to high resistance state (HRS) transition. In our case, for slow signals, and assuming that the conductive filament (CF) has a truncated-cone shape, we could consider the minor radius r of the CF as the sole estate variable, as in Fig. 2 (in the most common case of filamentary conduction ReRAMs).

For this region, the resistance R of the conductive filament (CF) was estimated by using Eq. 22 and the values in Table 1. The CF shape was assumed to correspond to a truncated-cone with small radius r, high radius $4 * r$, and thickness h. Using these assumptions, we have estimated the radius evolution for each measured curve during the LRS to HRS. This process is depicted in Fig. 9, and can be divided into three parts:

1. **IV curves**. The I-V curves were measured for each LRS to HRS transition, and the reset point was determined.

2. **Resistance Determination.** From the previous experimental curves, the resistance up to the reset point was calculated using Ohm's Law.

3. **Radius calculation.** Using the resistance calculated in the previous step, and the value of the conductance in Table 1, the value of the radius was estimated as:

4.

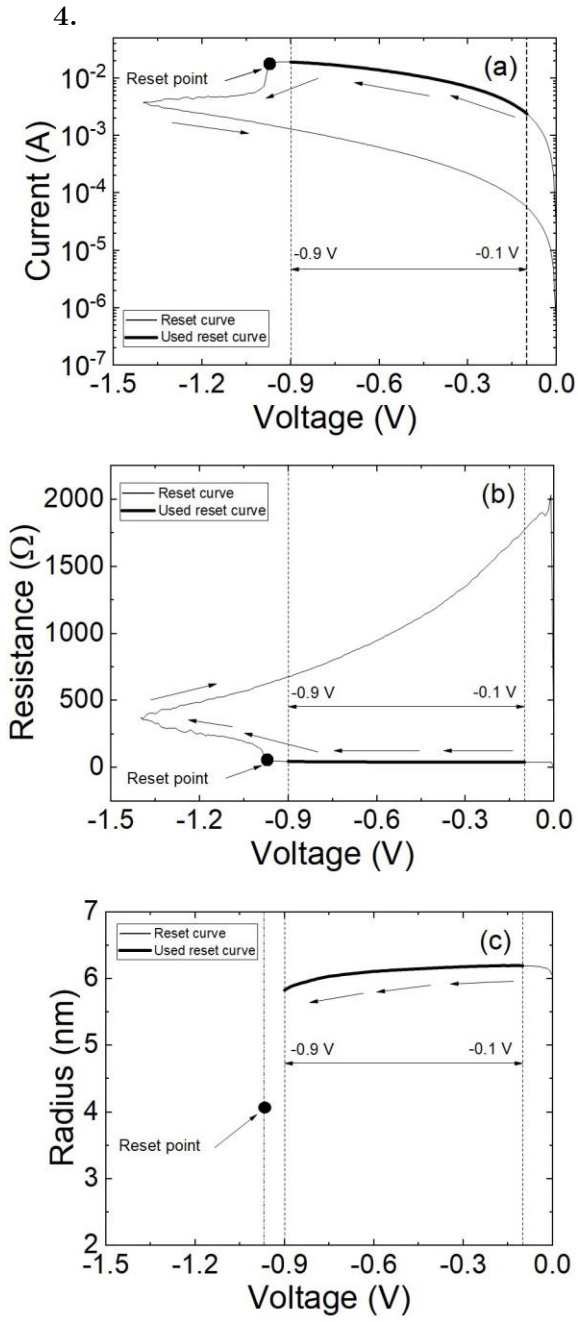

Figure 9: a) Current versus applied voltage (the reset curve section employed in the calculation is shown in bold) obtained making use of an input voltage with a ramp of -0.08 V/s; b) The resistance is extracted and shown versus the applied voltage; c) The conductive filament radius versus applied voltage is estimated.

Table 1: Technological parameters and fitting constants used for the TiN/Ti/HfO_2/Al_2O_3/W stack used to fabricate the ReRAM memristive device. (* The value of h is calculated by adding the thicknesses of the HfO_2 layer (10 nm) and the Al_2O_3 (2 nm)).

Parameter	Value	Units
$h\ (*)$	12	nm
σ	$5 \cdot 10^5$	S/m

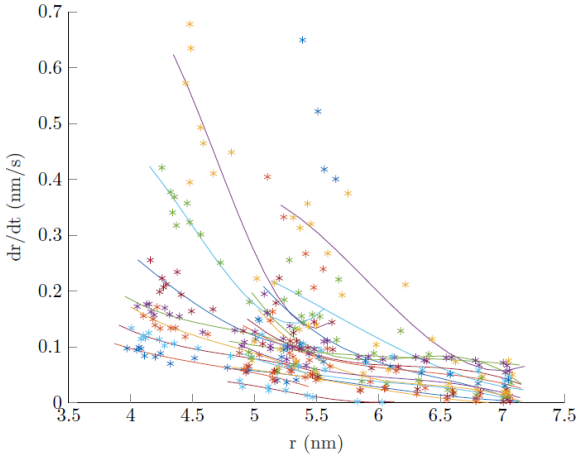

Figure 10: Radius of the conductive filament versus dr/dt (in absolute value), extracted from experimental measurements as described in the text. The points correspond to the evolution of the CF, as estimated, and the lines show their moving average.

$$r = \sqrt{\frac{h}{4\pi R\sigma}} \quad (22)$$

Since the thermal inertia can be neglected in the low frequency operation regime considered for our calculations, a first order memristor can be assumed. Plotting the values of radii extracted, using Eq. 22, for several reset curves, applying both ramp input voltage signals

and sinusoidal input waveforms $v(t)$, results in Figure 10. To create this figure, we first have plotted all the [r, dr, v(t)] points. Then, to obtain a drawing similar to Figure 5, we plot in Fig. 10 the points corresponding to constant V values. In this same Figure, the lines correspond to a moving average. It has to be pointed out that each full I-V cycle causes different initial CF r values. Notice that the moving averages strongly resemble those in Figures 6 and 7, as expected.

As a second step, we have plotted in a 3D graph the $[v,\ r,\ abs(dr/dt)]$ triplets, corresponding to the experimental measurements (see Figure 11) to further emphasize that their dynamic behaviour is located on a surface. These points define the DRM surface, where all the trajectories of the system must lay on. It is apparent in this Figure that the DRM behaviour seems to hold true for all the curves considered. The deviations from this surface are attributed to random fluctuations in the initial size and shape of the conductive filaments, which are created anew in the set part of the cycle. Additionally, another source of error is the propagation of the measurement error and noise, which directly translates into deviations of the estimated CF radius.

It is worth pointing out the existence of two secondary bumps in Fig. 11, probably due to multiple CF. These bumps are clearly exposed in Fig. 12, which is simply a rotation of Fig. 11.

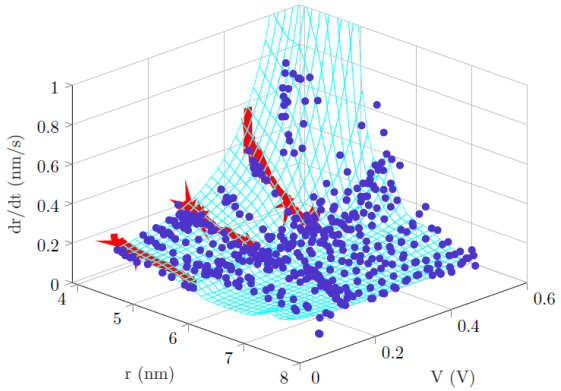

Figure 11: 3D plot of the experimental DRM, showing also an empirical surface fit. The points correspond to a random selection of extracted [V, r, dr/dt] triplets. For the sake of clarity, three specific indicative trajectories are marked as red lines.

It has to be noted that results from both the toy model (Eq. 7) and the charge and flux model (Eq. 21), closely resemble experimental data; thus showing that the model reproduces the physics behind the reset mechanism, in a reliable way. Specifically, all of them show very similar behaviour in the evolution of the radius time derivative, which accelerates as the radius tends to zero; further reflecting the positive feedback process between conductance and temperature, which is behind reset events in resistive switching devices.

Moreover, it has to be noted that the evolution of the experimental curves dr/dt vs. r and $v(t)$ fall on a surface in the 3D plot, as predicted by the models, and as shown in Figure 11. This last result hints for the fact that the response of the device under an arbitrary input is being mainly governed by the initial conditions (aka the initial CF radius) and the shape of the DRM.

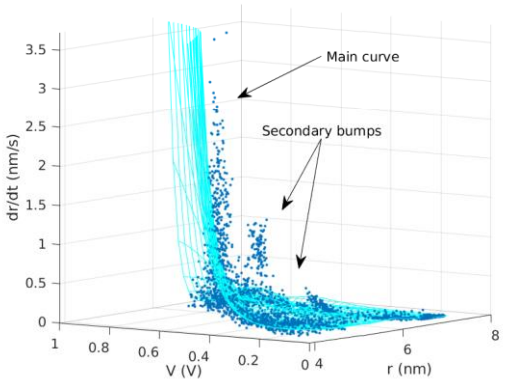

Figure 12: Rotation of the 3D plot of the experimental DRM, showing the presence of two secondary bumps on the main surface, caused probably by the existence of different CF. The points correspond to the whole range of extracted [V, r, dr/dt] triplets, and the grid corresponds to an empirical fit of those points.

5. Conclusions

In this paper we have made a presentation of the Dynamic Route Map (DRM) concept and its great potential in the modelling and analysis of memristive devices. To do so, we have tackled with the DRM analysis from the modelling side on a first step. In particular, we have addressed the issue by means of two memristor models based on different paradigms. The first of those models is based on a physical description of the memristor, assuming filamentary conduction. It is described by an explicit equation for the radius variation, that, under the convenient formulation, leads to the calculation of the system DRM. We have plotted this DRM, and we have shown that different effects (reset voltage dependence on the waveform, variation of the device behaviour caused by different waveforms, etc.) are easily explained using this framework. We followed the same approach using a second model, which is based on a memristor definition through a nonlinear analytical link between the device charge and flux. We have also derived an expression for the CF radius, and plotted the DRM for this second model, obtaining a shape that resembles the one of the previous case.

As a second complementary step, we have extracted experimentally the DRM of a ReRAM device. This is an interesting task, involving many modelling assumptions and measurement noise. We considered a truncated-cone shape for the conductive filament, and extracted the CF average radius in much the same way than for the charge-flux model. The results show that all the points move very close to the surface generated by the DRM, independently of the input voltage signal waveform, or the actual considered cycle. Consequently, we have shown that, actually, the memristors are not behaving differently under different stimuli. It is simply that the observed device response is the projection on the I-V variables of a trajectory on a different phase space determined by a governing state variable, its rate of change, and the input stimulus. The relation between these magnitudes is what really defines the device behaviour, and, as shown, this relation can be experimentally determined.

Acknowledgments

We thank the Spanish Ministry of Science for Projects DPI2017-86610-P, TEC2017-84877-R, TEC2017-84321-C4-1-R, and TEC2017-84321-C4-3-R (also supported by the FEDER program). This work has made use of the Spanish ICTS Network MICRONANOFABS.

References

[1] L. O. Chua, "Memristor-the missing circuit element," *Circuit Theory, IEEE Transactions on*, vol. 18, no. 5, pp. 507–519, 1971.

[2] T. Prodromakis, C. Toumazou, and L. Chua, "Two centuries of memristors," *Nature materials*, vol. 11, no. 6, pp. 478–481, 2012.

[3] L. Chua and S. M. Kang, "Memristive devices and systems", *Proceedings of the IEEE*, vol. 64, no. 2, pp. 209–223, Feb 1976.

[4] R. Tetzlaff, *Memristors and memristive systems*. Springer, 2013.

[5] H. Kim, M. P. Sah, C. Yang, and L. O. Chua, "Memristor-based multilevel memory," in *Cellular nanoscale networks and their applications (CNNA), 2010 12th international workshop on*. IEEE, 2010, pp. 1–6.

[6] S. Stathopoulos, A. Khiat, M. Trapatseli, S. Cortese, A. Serb, I. Valov, and T. Prodromakis, "Multibit memory operation of metal-oxide bi-layer memristors," *Scientific reports*, vol. 7, no. 1, pp. 1–7, 2017.

[7] K. Eshraghian, K.-R. Cho, O. Kavehei, S.-K. Kang, D. Abbott, and S.-
M. S. Kang, "Memristor mos content addressable memory (mcam): Hybrid architecture for future high performance search engines," *IEEE Transactions on Very Large Scale Integration (VLSI) Systems*, vol. 19, no. 8, pp. 1407–1417, 2011.

[8] S. Carrara, D. Sacchetto, M.-A. Doucey, C. Baj-Rossi, G. De Micheli, and
Y. Leblebici, "Memristive-biosensors: A new detection method by using nanofabricated memristors," *Sensors and Actuators B: Chemical*, vol. 171, pp. 449–457, 2012.

[9] I. Gupta, A. Serb, A. Khiat, R. Zeitler, S. Vassanelli, and T. Prodromakis, "Memristive integrative sensors for neuronal activity," *arXiv preprint arXiv:1507.06832*, 2015.

[10] Y. V. Pershin and M. Di Ventra, "Experimental demonstration of associative memory with memristive neural networks," *Neural Networks*, vol. 23, no. 7, pp. 881–886, 2010.

[11] J. Grollier, D. Querlioz, and M. D. Stiles, "Spintronic nanodevices for bioinspired computing," *Proceedings of the IEEE*, vol. 104, no. 10, pp. 2024–2039, 2016.

[12] B. Sun, X. Zhang, G. Zhou, P. Li, Y. Zhang, H. Wang, Y. Xia, and Y. Zhao, "An organic nonvolatile resistive switching memory device fabricated with natural pectin from fruit peel," *Organic Electronics*, vol. 42, pp. 181–186, 2017.

[13] S. Battistoni, A. Dimonte, and V. Erokhin, "Organic memristor based elements for bio-inspired computing," in *Advances in Unconventional Computing*. Springer, 2017, pp. 469–496.

[14] D. B. Strukov, G. S. Snider, D. R. Stewart, and R. S. Williams, "The missing memristor found," *nature*, vol. 453, no. 7191, pp. 80–83, 2008.

[15] C. Dias, H. Lv, R. Picos, P. Aguiar, S. Cardoso, P. Freitas, and J. Ventura, "Bipolar resistive switching in Si/Ag nanostructures," *Applied Surface Science*, 2017.

[16] S. Brivio, G. Tallarida, E. Cianci, and S. Spiga, "Formation and disruption of conductive filaments in a HfO_2/tin structure," *Nanotechnology*, vol. 25, no. 38, p. 385705, 2014.

[17] B. Mohammad, M. A. Jaoude, V. Kumar, D. M. Al Homouz, H. A. Nahla,M. Al-Qutayri, and N. Christoforou, "State of the art of metal oxide mem- ristor devices," *Nanotechnology Reviews*, vol. 5, no. 3, pp. 311–329, 2016.

[18] J. Kalomiros, S. G. Stavrinides, and F. Corinto, "A two-transistor non-ideal memristor emulator," in *Modern Circuits and Systems Technologies (MOCAST), 5th International Conference on*. IEEE, 2016, pp. 1–4.

[19] O. Camps, M. M. Al Chawa, C. de Benito, M. Roca, S. G. Stavrinides,
R. Picos, and L. O. Chua, "A purely digital memristor emulator based on a flux-charge model," in *2018 25th IEEE International Conference on Electronics, Circuits and Systems (ICECS)*. IEEE, 2018, pp.565–568.

[20] M. M. Al Chawa, C. de Benito, M. Roca, R. Picos, and S. Stavrinides, "Design and implementation of passive memristor emulators using a charge- flux approach," in *2018 IEEE International Symposium on Circuits and Systems (ISCAS)*. IEEE, 2018, pp. 1–5.

[21] O. Camps, R. Picos, C. de Benito, M. M. Al Chawa, and S. G. Stavrinides, "Emulating memristors in a digital environment using stochastic logic," in *2018 7th International Conference on Modern Circuits and Systems Technologies (MOCAST)*. IEEE, 2018, pp. 1–4.

[22] I. Messaris, A. Serb, A. Khiat, S. Nikolaidis, and T. Prodromakis, "A compact verilog-a ReRAM switching model," *arXiv preprint arXiv:1703.01167*, 2017.

[23] P. S. Georgiou, S. N. Yaliraki, E. M. Drakakis, and M. Barahona, "Window functions and sigmoidal behaviour of memristive systems," *International Journal of Circuit Theory and Applications*, 2016.

[24] A. Ascoli, R. Tetzlaff, and L. Chua, "Continuous and differentiable approximation of a TaO memristor model for robust numerical simulations," in *Emergent Complexity from Nonlinearity, in Physics, Engineering and the Life Sciences*. Springer, 2017, pp. 61–69.

[25] F. Jimenez-Molinos, M. Villena, J. Roldan, and A. Roldan, "A spice com- pact model for unipolar RRAM reset process analysis," *IEEE Transactions*

on Electron Devices, 2015.

[26] Q. Li, A. Serb, T. Prodromakis, and H. Xu, "A memristor spice model accounting for synaptic activity dependence," *PloS one*, vol. 10, no. 3, p. e0120506, 2015.

[27] J. Secco, F. Corinto, and A. Sebastian, "Flux-charge memristor model for phase change memory," *IEEE Transactions on Circuits and Systems II: Express Briefs*, 2017, in press.

[28] R. Picos, J. B. Roldan, M. M. Al Chawa, P. Garcia-Fernandez, F. Jimenez- Molinos, and E. Garcia-Moreno, "Semiempirical modeling of reset tran- sitions in unipolar resistive-switching based memristors," *RADIOENGI- NEERING*, vol. 24, no. 2, p. 421, 2015.

[29] E. Garcia-Moreno, R. Picos, and M. M. Al-Chawa, "Spice model for unipolar RRAM based on a flux-controlled memristor," in *Power, Electronics and Computing (ROPEC), 2015 IEEE International Autumn Meeting on*. IEEE, 2015, pp. 1–4.

[30] M. M. Al Chawa, R. Picos, J. B. Roldan, F. Jimenez-Molinos, M. A. Villena, and C. de Benito, "Exploring resistive switching-based memristors in the charge–flux domain: a modeling approach," *International Journal of Circuit Theory and Applications*, pp. n/a–n/a, 2018, cta.2397. [Online].Available: http://dx.doi.org/10.1002/cta.2397

[31] Z. Kolka, D. Biolek, V. Biolkova, and Z. Biolek, "Evaluation of memristor models for large crossbar structures," in *Radioelektronika (RADIOELEK- TRONIKA), 2016 26th International Conference*. IEEE, 2016, pp. 91–94.

[32] R. Picos, J. Roldan, M. Al Chawa, F. Jimenez-Molinos, and E. Garcia- Moreno, "A physically based circuit model to account for variability in memristors with resistive switching operation," in *Design of Circuits and Integrated Systems (DCIS), Conference on*. IEEE, 2016, pp. 1–6.

[33] R. Naous, M. Al-Shedivat, and K. N. Salama, "Stochasticity modeling in memristors," *IEEE Transactions on Nanotechnology*, vol. 15, no. 1, pp. 15–28, 2016.

[34] F. Corinto, P. P. Civalleri, and L. O. Chua, "A theoretical approach to memristor devices," *IEEE Journal on Emerging and Selected Topics in Circuits and Systems*, vol. 5, no. 2, pp. 123–132, 2015.

[35] L. O. Chua, "Everything you wish to know about memristors but are afraid to ask," *Radioengineering*, vol. 24, no. 2, p. 319, 2015.

[36] S. Shin, K. Kim, and S.-M. Kang, "Compact models for memristors based on charge-flux constitutive relationships," *Computer-Aided Design of Integrated Circuits and Systems, IEEE Transactions on*, vol. 29, no. 4, pp. 590–598, 2010.

[37] R. Picos, M. M. Al Chawa, M. Roca, and E. Garcia-Moreno, "A charge- dependent mobility memristor model," in *Proceedings of the 10th Spanish Conference on Electron Devices, CDE'2015*. IEEE, 2015.

[38] R. Picos, J. B. Roldan, M. M. Al Chawa, F. Jimenez-Molinos, M. Villena, and E. Garcia-Moreno, "Exploring ReRAM-based memristors in the charge-flux domain, a modeling approach," in *Proceedings of International Conference on Memristive Systems, MEMRISYS'2015*, 2015.

[39] C. de Benito, M. M. Al Chawa, R. Picos, and E. Garcia-Moreno, "A procedure to calculate a delay model for memristive switches," in *Workshop on Memristor Technology, Design, Automation and Computing*, 2017.

[40] A. Theodorakakos, S. G. Stavrinides, E. Hatzikraniotis, and R. Picos, "A non-ideal memristor device," in *Memristive Systems (MEMRISYS) 2015 International Conference on*. IEEE, 2015, pp. 1–2.

[41] M. M. Al Chawa, A. Rodriguez-Fernandez, M. Bargallo, F. Campabadal,C. de Benito, S. Stavrinides, E. Garcia-Moreno, and R. Picos, "Waveform and frequency effects on reset transition in bipolar ReRAM in flux-charge space," in *Memristive Systems (MEMRISYS) 2017 International Confer- ence on*. IEEE, 2017.

[42] M. M. Al Chawa, R. Picos, E. Covi, S. Brivio, E. Garcia-Moreno, andS. Spiga, "Flux-charge characterizing of reset transition in bipolar resistive- switching memristive devices," in *11th Spanish Conference on Electron De- vices*, 2017.

[43] J. Liouville, "Sur la théorie de la variation des constantes arbitraires,"*Journal des Mathématiques Pures et Applications*, vol. 3, pp. 342–349, 1838.

[44] H. Poincaré, "Les méthodes nouvelles de la mécanique céleste," vol. 3, 1892-99.

[45] P. Ehrenfest and T. Ehrenfest, "Encyklopadie der mathematischen wissenschaften," vol. 4, 1911.

[46] L. O. Chua, "If it's pinched it's a memristor," *Semiconductor Science and Technology*, vol. 29, no. 10, p. 104001, 2014.

[47] ——, "Five non-volatile memristor enigmas solved," *Applied Physics A*, vol. 124, no. 8, p. 563, 2018.

[48] D. Ielmini, F. Nardi, and C. Cagli, "Physical models of size-dependent nanofilament formation and rupture in NiO resistive switching memories,"

Nanotechnology, vol. 22, no. 25, p. 254022, 2011.

[49] A. Rodriguez-Fernandez, J. Suñé, E. Miranda, M. B. Gonzalez, F. Campabadal, M. M. Al Chawa, and R. Picos, "Spice model for the ramp rate effect in the reset characteristic of memristive devices," in *2017 32nd Conference on Design of Circuits and Integrated Systems (DCIS)*, 2017, pp. 1–4.

[50] M. M. Al Chawa, C. de Benito, and R. Picos, "A simple piecewise model of reset/set transitions in bipolar ReRAM memristive devices," *IEEE Trans- actions on Circuits and Systems I: Regular Papers*, vol. 65, no. 10, pp. 3469–3480, Oct 2018.

[51] M. M. Al Chawa and R. Picos, "A simple quasi-static compact model of bipolar ReRAM memristive devices," *IEEE Transactions on Circuits and Systems II: Express Briefs*, vol. 67, no. 2, pp. 390–394, 2020.

[52] M. M. Al Chawa, R. Picos, and R. Tetzlaff, "A simple memristor model for neuromorphic ReRAM devices," in *Circuits and Systems (ISCAS), 2020 IEEE International Symposium on."Accepted"*. IEEE, 2020.

[53] M. M. Al Chawa, S. G. Stavrinides, C. de Benito, M. Bargallo, and R. Picos, "A non-quasi static model for reset voltage variation in memristive devices," in *2019 26th IEEE International Conference on Electronics, Circuits and Systems (ICECS)*, 2019, pp. 1–4.

Chapter 6.

6. A resistive memory simulator based on circuit breakers

6.1. Introduction

As commented in section 1.4.4, there are still some hurdles in the RRAM realm to be addressed for its correct operation as non-volatile memories and the device implementation in neuromorphic circuits. As a consequence, industrial mass fabrication is limited at the moment as some impediments such as cycle-to-cycle and device-to-device variability, reliability or retention must be overcome. In this respect, variability emerges as one of the most critical aspects since it is directly related to the dispersion of electrical characteristics of the device. The variability of the device itself (also known as intrinsic variability on the contrary to extrinsic variability which is linked to the fabrication process), appears from the stochastic nature of the formation and rupture of the conductive filament which is dominated by the temperature, the electric field and the materials features. Thus, the CF shape must be properly studied as it plays an important role in the electrical features of the device. The typical variables and switching parameters affected as a result of the intrinsic variability are V_{set}, V_{reset}, I_{set}, I_{reset}, R_{HRS} and R_{LRS}. This chapter focuses on the study of all of these events involved in order to understand the physics behind RS so the need of a robust well performing simulator is needed. In this manner, we will design and build a new simulator tool based on resistive circuit breakers of different features; so forming, set and reset processes would be described in terms of the stochastic formation and rupture of conductive filaments of several branches in the dielectric. The simulation approach allows to connect in a natural manner to compact modeling solutions

because of both the electric field and temperature dependencies are incorporated in addition to other effects.

6.2. Description

This tool based on circuit breakers has been developed in order to analyze variability in RRAM devices due to the possibility to reproduce the typical current versus voltage experimental curves. In this manner, the device is modeled in a grid composed of $m \times n$ resistors as shown in **Figure 6**. The voltage is applied in all the top nodes at the same time while the bottom line is grounded to emulate the device electrical behavior. These resistances could have two, three or even four resistive levels. In addition, additional features like series resistance correction, dielectrics accounting with several layers, or quantum effects in the charge conduction by means of the QPC model among others are included. The breaker switching process is determined by evaluating the voltage drop in each circuit breaker by means of Kirchhoff's laws and comparing to the threshold voltages. In the same way, another rule to control switching requires to check the local temperature in the breaker, this is the thermal-driven switching. If this temperature reaches T_{set} then the switching from R_{off} to R_{on} takes place and conversely, if the temperature in the breaker reaches T_{reset} then the switching from R_{on} to R_{off} takes place. Simulation finishes when the compliance current is reached in a forming or set process and when a dramatic current drop is detected in a reset process.

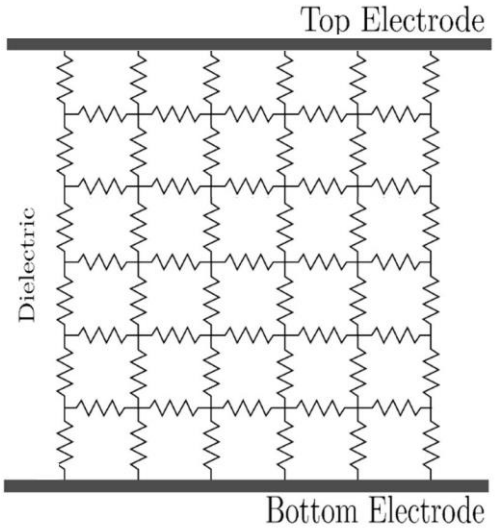

Figure 6.1. Sketch of the network composed of circuit breakers. An external voltage is applied to the nodes in the top electrode while the nodes in the bottom electrode are grounded.

We have coded and implemented this simulator tool in MATLAB by means of a graphical user interface in order to provide the final user a clear and intuitive interface without the need of understanding its internal operation, see **Figure 6** along its detailed main aspects described below.

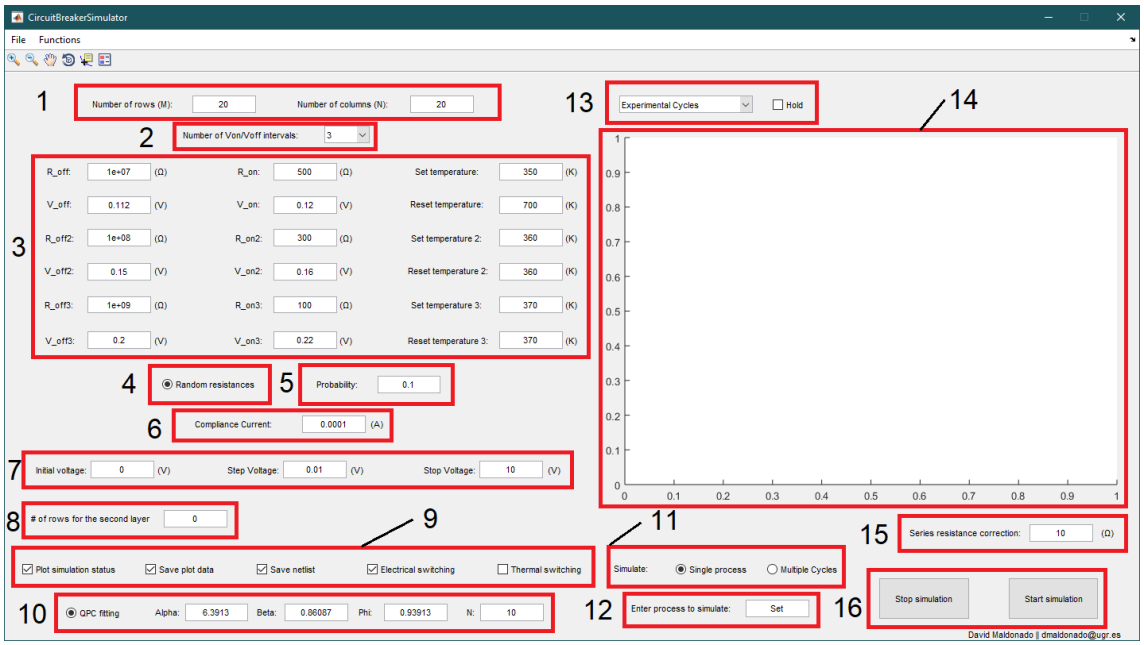

Figure 6.2. Graphical user interface of the simulator as it is initialized.

1. **Grid size:** number of rows (M) and columns (N) of breaker matrix included in the simulation.
2. **Breaker levels:** number of breaker resistance intervals. Two, three or even four levels could be selected in the pop-up menu.
3. **Parameter configuration:** depending on the number of intervals selected in (2), the corresponding menu boxes will appear to be determined. Resistance and voltage values are introduced here along with thermal-drive temperatures.
4. **Random resistances:** activate or deactivate the possibility to account with some resistances randomly chosen to be in the low resistance state at the beginning of the simulation.
5. **Probability of random resistances:** number of resistances (%) in the low resistance state when (4) is selected.
6. **Compliance current:** maximum current that can be reached during the simulation.
7. **Simulation range:** establishes the points where the simulation starts and finish as well as the step voltage to be increased between two consecutive simulation points.
8. **Second layer:** number of rows to account for a second oxide layer starting from the top electrode and downwards.
9. **Simulation options:** *plot simulation status* enables to plot the grid situation step by step in a new window. *Save plot data* saves the Matlab files of the simulation to account with the possibility to be plotted in the future by another function of the simulator. *Save netlist* saves the netlist files including voltages and resistances in a spice format for all the simulation points. *Electrical* and *thermal switching* determine the switching rules, note that both of them may be activated at the same time.
10. QPC **configuration:** allows to activate or deactivate the QPC module to describe charge transport. If activated, the *alpha*, *beta*, *phi* and *N* parameters should be introduced.

11. **Type of simulation:** simulate a single or multiple RS cycles. Only one could be selected at the same time.
12. **Process to simulate:** when a single cycle is selected in (11), the type of process should be introduced manually: forming, set or reset. If multiple cycles are chosen in (11), the box description changes to 'Number of cycles to simulate'.
13. **Experimental cycles selection:** allows selecting a certain experimental curve to be plotted when loaded. If the hold button is selected, the new plots are added to the axes without deleting previous ones.
14. **Graphic representation area:** space devoted to plot the simulation results.
15. **Series resistance correction:** value of the parasitic series resistance to be corrected in every run.
16. **Simulation start and stop:** buttons to start and stop the simulation.

6.3. Operation

As the simulations are launched, if the plot option is activated, a new window will show up to display the status of the network step by step, see an example in **Figure 6** for and external voltage applied of 0.8V.

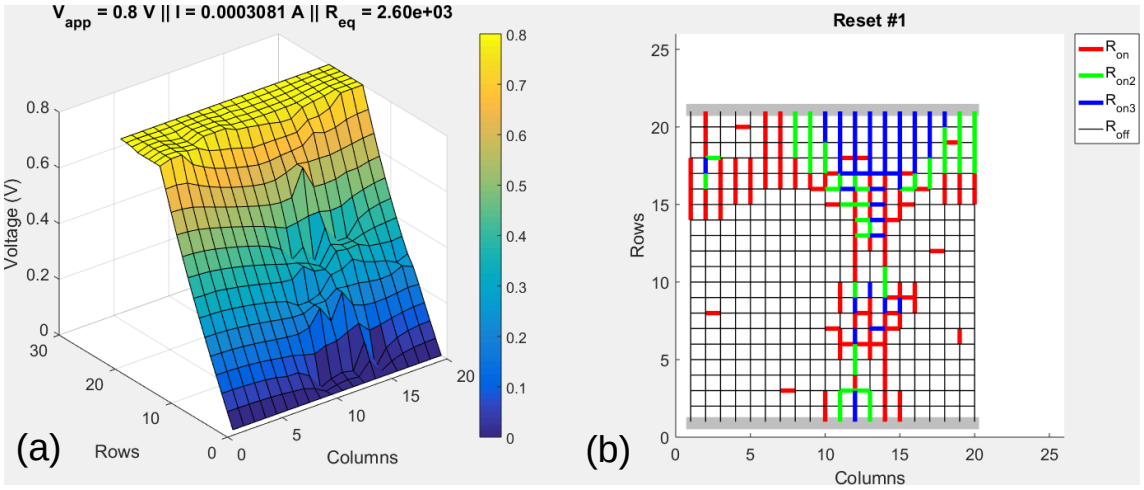

Figure 6.3. a) Voltage level in each node of the grid for an external applied voltage of 0.8 V. At this point, the total current flowing through the network is 0.3081 mA and the equivalent resistance 2.6 kΩ. b) Level of the resistances as a function of the voltage across the nodes, see the color code to describe the resistance state of each circuit breaker.

When the simulation is over, the obtained curve is plotted in the graphics representation area and the current versus voltage data is saved in a text file in the corresponding folder, see **Figure 6** for a set case.

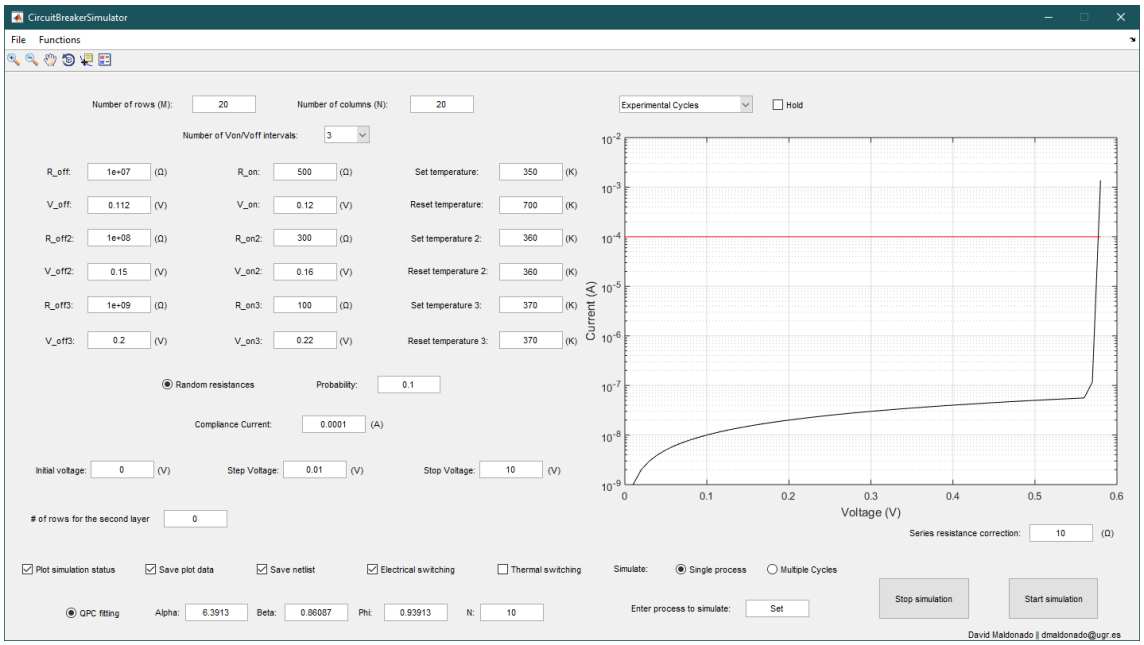

Figure 6.4. Graphical interface of the simulator when simulations are completed.

Additionally, a video was created in order to explain in a didactic way the operation of the simulator by showing its internal principles and how the circuit breakers form different branches of the percolation path in the dielectric, see **Video 1.1** [videoSimulator].

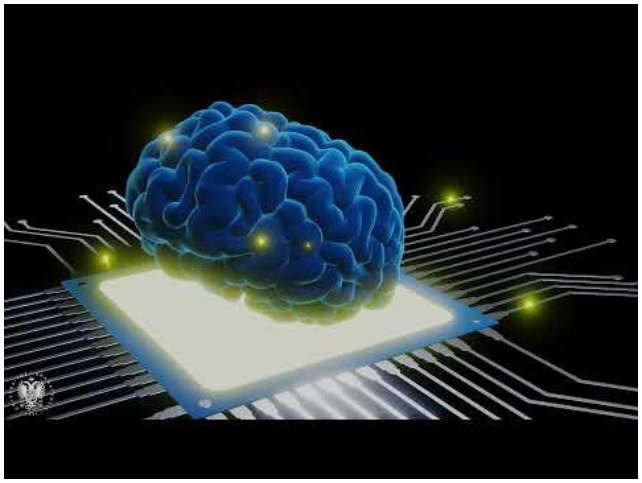

Video 1.1 Video detailing the principles of the presented simulator [videoSimulator].

6.4. Functionalities

In addition to the aspects detailed in previous sections, this tool accounts for several features to provide the user an optimal fitting and operation experience. One of these consists of loading experimental cycles along with simulated ones to compare the curves and improve the parameter election. This function is called *Load Cycles* and could be found in the *File* tab located in the toolbar menu, see **Figure 6.5**. As it is clicked, a new window appears to ask the user to provide the experimental curves location as shown in **Figure 6.6.**.

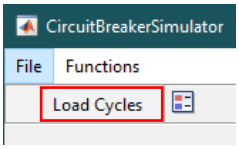

Figure 6.5. Loading cycles tab location.

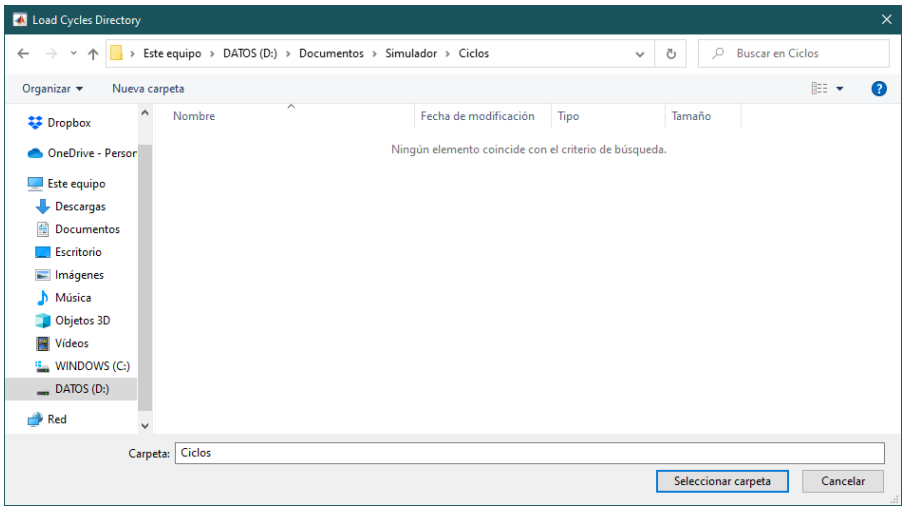

Figure 6.6. Selection of experimental measurements folder window.

Finally, the type of cycles to be loaded must be indicated choosing between sets or resets as shown in **Figure 67**.

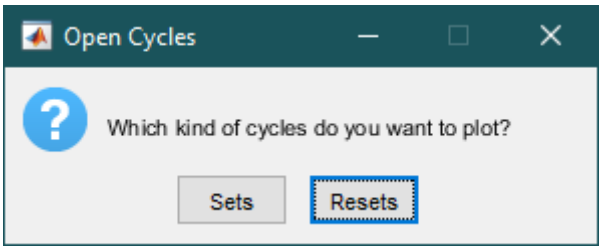

Figure 6.7. Experimental curves selection window

Experimental cycles will be plotted together in the representation area as they are loaded. It is possible to visualize just one cycle at the same time by selecting the cycle number in the drop-down menu, see **Figure 68**

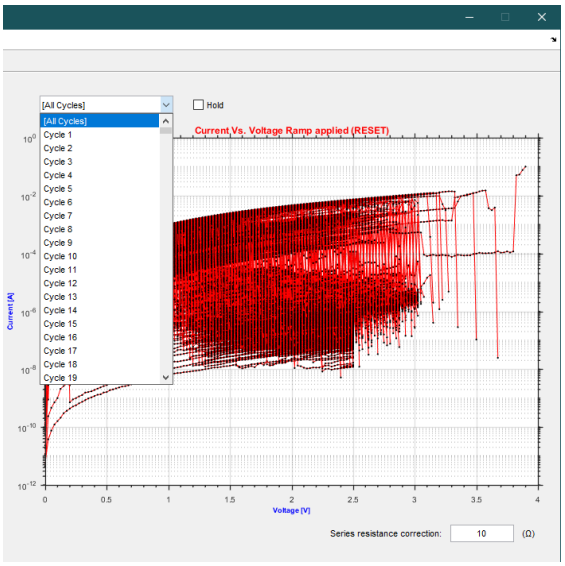

Figure 6.8. Graphical interface aspect when experimental cycles are loaded.

By selecting one or several cycles, the user is able to represent as many cycles as desired. A lot of combinations are possible due to the hold button, see **Figure 69**.

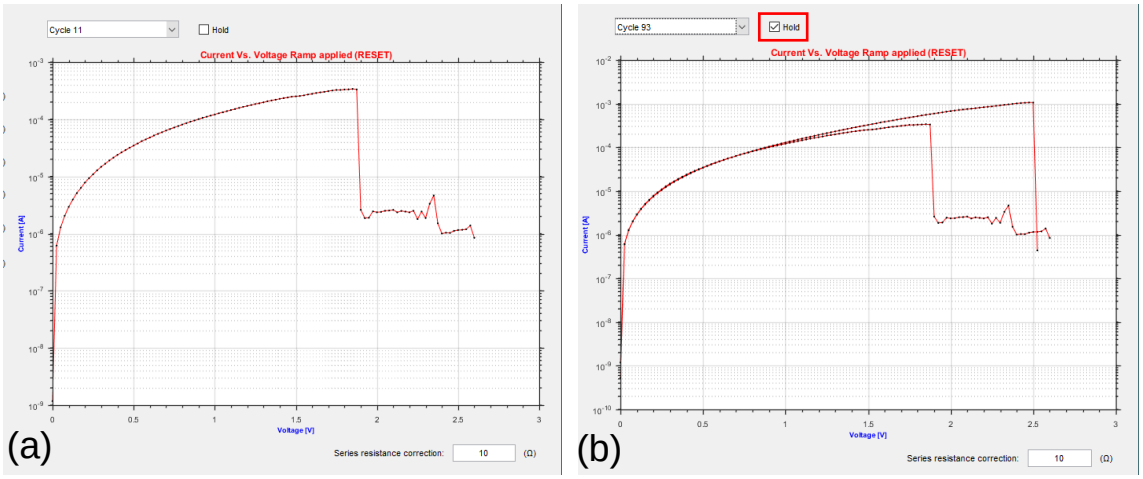

Figure 6.9. Graphical interface with a) one cycle loaded, b) two cycles loaded by means of hold button.

Another available option in the functions tab called *plot step-by-step*, see **Figure 610a**, consists of plotting the obtained results in a previous run just in case the plot data was saved in that moment.

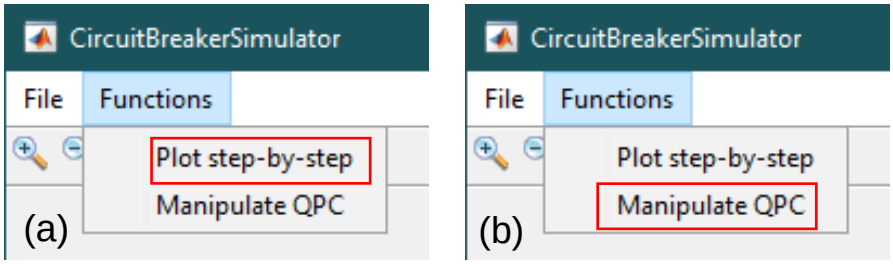

Figure 6.10. a) Plot step-by-step tab, b) manipulate tab location.

Thus, a new window will appear to ask the user to provide the location of the data to plot and the process will be carried out automatically resulting in what is shown in **Figure 6**. The last

functionality included in the simulator consists of a manipulate menu designed to provide a fast and comfortable way to select the most accurate QPC parameters to fit an experimental curve. That could be found on *Functions* tab as shown in **Figure 610b**. The menu relies on 4 sliders to adjust *alpha*, *beta*, *phi* and *N* in a certain range also configurable by the user. The most remarkable fact here is that at the same time the bar is moving, the plot is updated. In this manner, the user is seeing how the value of a particular variable affects the curve overall. In **Figure 611**, two sets of QPC parameters are chosen to see the difference in comparison to the same experimental curve.

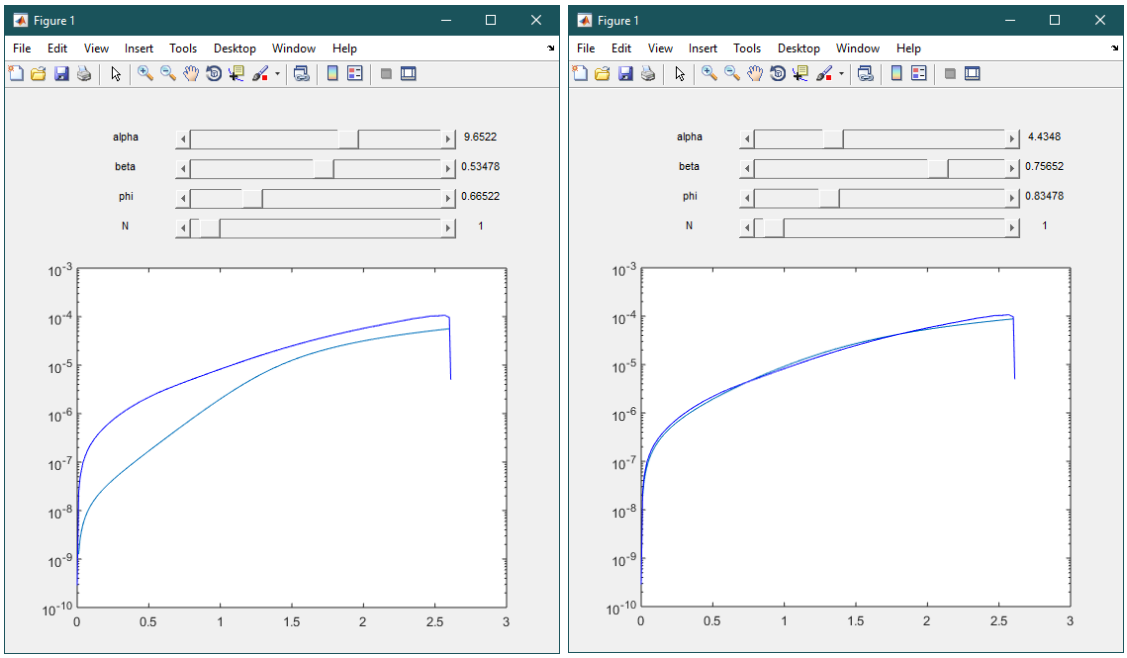

Figure 6.11. Manipulate menu with two different sets of parameters, a) alpha = 9.66, beta = 0.53, phi = 0.67, N = 1, b) alpha = 4.43, beta = 0.76, phi = 0.83, N = 1. In both cases, the experimental curve is fixed (dark blue), while the modified curve varies depending on the sliders position (light blue).

The following section is an already published work [Maldonado2022].

D. Maldonado et al.

Journal of Physics D: Applied Physics (2022)

Maldonado, D., Gómez-Campos, F. M., González, M. B., Roldán, A. M., Jiménez-Molinos, F., Campabadal, F., & Roldán, J. B. (2022). Comprehensive study on unipolar RRAM charge conduction and stochastic features: a simulation approach. Journal of Physics D: Applied Physics, 55(15), 155104. DOI: https://doi.org/10.1088/1361-6463/ac472c

Quality metrics

Data base	Rating	Quartile
Web of Science	Impact factor: 3.2	Q2
Scimago	Scientific journal ranking: 0.86	Q1

Publication citations (23-03-2022)

Google Scholar	Web of Science
0	**0**

Comprehensive study on unipolar RRAM charge conduction and stochastic features, a simulation approach

D. Maldonado[1], F. Gómez-Campos[1], M.B. González[2], A.M. Roldán[1], F. Jiménez-Molinos[1], F. Campabadal[2], J.B. Roldán[1]

[1]*Departamento de Electrónica y Tecnología de Computadores, Universidad de Granada, Facultad de Ciencias, Avd. Fuentenueva s/n, 18071 Granada, Spain. Email: jroldan@ugr.es*

[2]*Institut de Microelectrònica de Barcelona, IMB-CNM (CSIC), Campus UAB, 08193 Bellaterra, Spain.*

Abstract

An in-depth analysis of resistive switching (RS) in unipolar devices is performed by means of a new simulator based on resistive circuit breakers of different features. The forming, set and reset processes are described in terms of the stochastic formation and rupture of conductive filaments of several branches in the dielectric. Both, the electric field and temperature dependencies are incorporated in the simulation. The simulation tool was tuned with experimental data of devices fabricated making use of the Ti/HfO_2/Si stack. The variability and the stochastic behavior are characterized and reproduced correctly by simulation to understand the physics behind RS. Reset curves with several current steps are explained considering the rupture of different branches of the conductive filament. The simulation approach allows to connect in a natural manner to compact modeling solutions for the devices under study.

Index Terms — Resistive switching memory, RRAM, Circuit breakers, Simulation, Variability, Modeling, Variability, Percolation path

I.- Introduction

RRAMs are one of the emerging technologies in the agenda of the great companies devoted to integrated circuit (IC) fabrication. Resistive memories are faster and need much less energy than current Flash memories used in solid state drives among other applications; hence, they are good candidates for storage class low-power memory. Apart from their non-volatility, this new technology presents good endurance, retention, full compatibility with the CMOS technology and capability of 3D stack fabrication [1-5]. Classical computing architectures lead to von Neumann's bottleneck due to the high costs (both in energy and speed) linked to constant data shuttle forward and backward between the memory and the processor. Resistive switching devices could provide a solution since ultrahigh-density memory layers can be directly integrated on the processor chip reducing the bottleneck and improving the computing system energy efficiency and speed [6].

In addition to non-volatile memory applications, other uses of these type of devices (which can be included in a broader set of electron devices called memristors [7, 8]) is related to neuromorphic computing [6, 9-20]. The implementation of matrix-vector multiplication by means of resistive switching devices crossbar arrays is an important step forward to the firstly conceived neuromorphic engineering approach introduced by C. Mead in the late eighties [21]. The employment of these structures is convenient when dealing with large-scale data processing, as it is the case of deep neural networks (DNN). In this perspective, these devices mimic biological synapses to allow the fabrication of hardware neural networks [9, 10, 11, 13, 15, 17, 19, 20, 22]. The essential role of resistive switching devices in neuromorphic computing can be focused on neural network accelerators for multilayer perceptron and convolutional DNN, and for spiking neural networks; the latter encoding the information by means of spikes in the time and frequency domain [5, 23].

Cycle-to-cycle (C2C) variability is inherent to RRAM operation due to the stochasticity linked to RS [1-4, 24-26]. This variability can impose hurdles for certain applications; however, it can also be of advantage in some cases, for instance in dealing with some machine learning DNN training issues, such as overfitting [16, 18, 23, 27]. Variability is also behind outstanding solutions in hardware cryptography (physical unclonable functions and random number generators) that are growing by leaps and bounds [28-31]. In devices with filamentary conduction, C2C variability is linked to CF morphological changes in each RS cycle, where the CF is created (set process) and ruptured (reset process) successively.

In order to understand variability, different simulation and modeling tools have been developed. Among the procedures followed, there can be found the kinetic Monte Carlo (KMC) simulation [32-35]; the advanced statistical modeling [24-26, 36] and the compact modeling approach for circuit simulation [8, 37-47]. The KMC approach describes the device operation in detail, the most relevant physical mechanisms are included at the microscopic level and the device stochasticity is considered consistently within the KMC algorithm; yet, the computing time is too long. In the compact modeling arena, the simplicity versus accuracy paradigm is different. Device description is easier and faster than in other simulation tools; nevertheless, considering the variety of materials employed in the different devices found in the literature, there is also a long way to go in the compact modeling context. In this

field, the device description has to be quick from the numerical viewpoint to be able to simulate circuits with a high number of components. The main physical mechanisms are considered although some complex aspects are usually left behind because their associated numerical complexity is not reasonable for the accuracy needed at this description level. Among the features that are simplified, or sometimes simply neglected from the models, there is variability [24]. An interesting approach that stands in between the numerical techniques reported above in terms of complexity (KMC simulation and compact modeling for circuit simulation) is related to RRAM simulation by means of circuit breakers (CB) [4, 48-52]. This procedure allows a reasonably accurate CF description on RS devices with a resistance mesh that permits a qualitative insight to the randomness linked to the percolation path formation. In this work we have used a simulation procedure based on circuit breakers to study the operation of unipolar resistive switching devices with HfO_2 dielectrics. In addition to the general features of this simulation scheme [4, 48-51], we have introduced several improvements such as the inclusion of quantum effects by means of the quantum point contact model, the use of circuit breakers of four conductivity levels and a device series resistance, and the consideration of several dielectric layers with different conduction characteristics. A much better quantitative description is achieved in this manner.

We have fabricated and measured unipolar RS devices. The measurement results of the fabricated unipolar RS devices have been correctly fitted with this new simulation tool and different operational particularities have been explained in full. In particular, in section II we introduce the fabrication and measurement details; section III is devoted to the simulator description while section IV presents and discuss the main results obtained. Finally, the main conclusions are drawn in section V.

II.- Device fabrication and measurement setup

The fabrication of Ni/HfO_2/Si devices was performed on (100) n-type CZ silicon wafers with resistivity (0.007-0.013) $\Omega \cdot$cm. The 10nm-thick HfO_2 layers were grown by atomic layer deposition (ALD) at 200ºC, making use of tetrakis (Dimethylamido)-hafnium (TDMAH) and H_2O as precursors and N_2 as carrier and purge gas. The top Ni electrode with a 200nm thickness was deposited by magnetron sputtering. The area of the cells is 5x5 μm^2. A schematic cross-section of the final device structure is shown in Fig. 1(a).

A HP4155B semiconductor parameter analyser was employed to measure the I-V curves. The voltage was applied to the top Ni electrode and the Si substrate was grounded. Successive I-V measurements were performed to dynamically detect the set and reset currents. The semiconductor parameter analyzer was connected to the computer via GPIB that was controlled by MATLAB. More than 1800 successive resistive switching cycles were obtained, some of them are shown in Fig. 1(b).

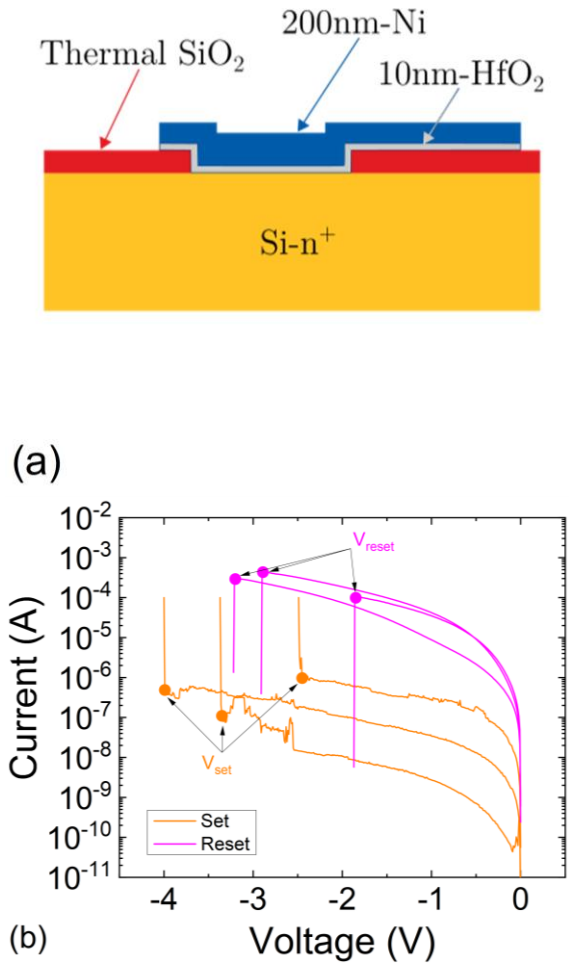

Figure 1. (a) Cross section scheme of the Ni/HfO_2/Si-n^+ devices, (b) current-voltage characteristics corresponding to set and reset cycles. A current compliance of 100 μA has been employed.

III.- Simulation description

We have developed a flexible and comprehensive simulator based on circuit breakers (CB) to analyze RRAM variability. It allows the step-by-step description of CF formation and rupture processes in a 2D approach. It can simulate both unipolar and bipolar memristor RS devices (including two or more dielectric layers with different electrical properties). This in-house tool is accurate enough to reproduce the typical I-V experimental curves as it will be shown below. The code has been implemented in MATLAB, and the simulations were carried out with a desktop Intel Core i5-7400 CPU @ 3GHz. For a conventional simulation cycle including set and reset transitions, for a CB matrix with N=20 and M=20, the simulation time is approximately 200s. This is obviously a much faster approach than kinetic Monte Carlo simulators [32-35], where a RS cycle takes several hours to simulate.

In our case, to improve the CB modeling (the basics of this approach have been already presented [4, 48-51]) and investigate the device RS characteristics and variability, we include CBs with up to four conductance levels, quantum effects in the charge conduction by means of the Quantum Point Contact (QPC) model, series resistance, dielectrics with several layers and other parameters.

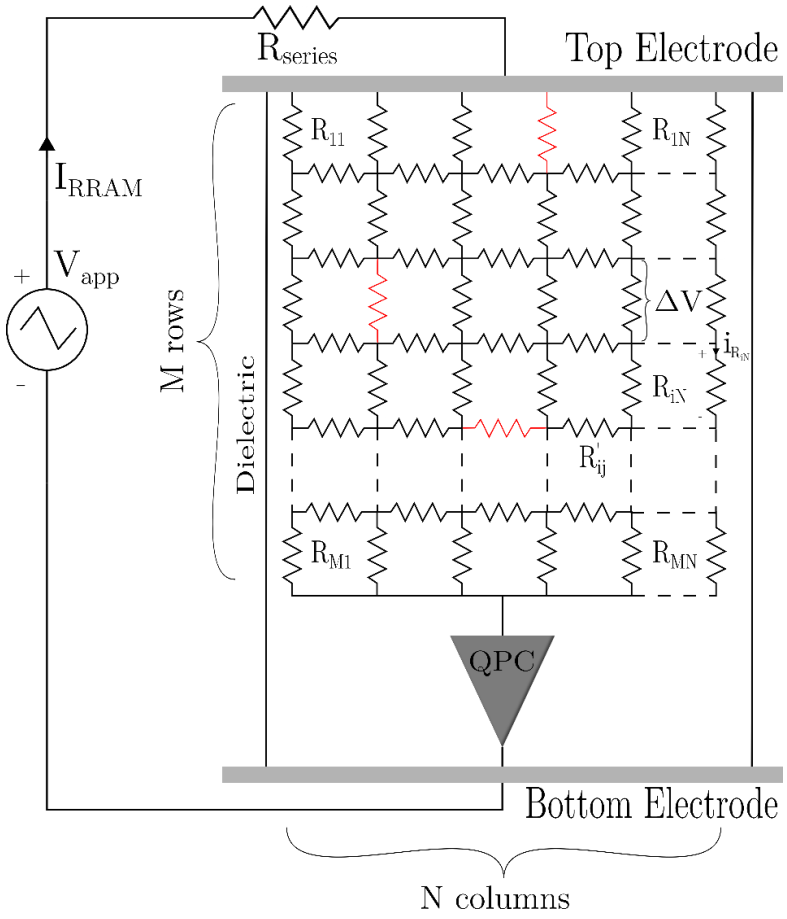

Figure 2. Diagram of the 2D CB network that models the device internal electric circuit. Each CB represents a cluster of ions embedded in the percolation path [32, 34, 53]. The black and red colors CBs represent clusters with different compactness, and therefore different resistance values (there could be more than two resistance levels). The horizontal grey bars stand for the electrodes that are connected to an external voltage source. The model also accounts for the device series resistance [54, 55]. Finally, quantum effects linked to any potential barriers along the charge conduction path are considered [54, 56, 57].

The CB 2D network is shown in Figure 2. It represents the conduction structure of the dielectric, permitting simulation of percolation paths formation that represent metallic-like CFs that short the electrodes after a successful set or forming process. The circuit breakers change their resistive state under the action of electric and thermal effects [58].

The simulator can include a series resistance and a module to account for the QPC model in series with the CB network. This latter module describes non-linear I-V relationship in the low resistive state among other effects (see Equation 10 in [54]). The QPC model describes charge transport due to a barrier under a mesoscopic approach in the different RS operation situations [56]. For the resistance network made of CBs with two resistive states shown in Figure 2, the CB resistance is either R_{on} (a low value linked to the low resistance state, LRS, plotted in red) or R_{off} (a high value linked to the high resistance state, HRS, plotted in black). In our simulator, CBs can be chosen to switch between two, three or even four different resistance values. These resistance values are linked to ion clusters of different compactness and size that could be part of a conductive filament (CF) that shorts the electrodes [32, 53]. The cluster (made of oxygen vacancies, reduced metallic ions from

the active electrode or both) compactness is directly linked to the conductance of the region that is modeled by the CB, as it was demonstrated by KMC simulations [32, 33, 53]. If electric field driven switching is assumed, the CB value is determined by evaluating ΔV (the voltage in the CB), that is obtained by means of Kirchhoff's circuit laws (see Figure 2) and later compared to the threshold voltages V_{off} and V_{on}, which are fitting parameters, see Figure 3.

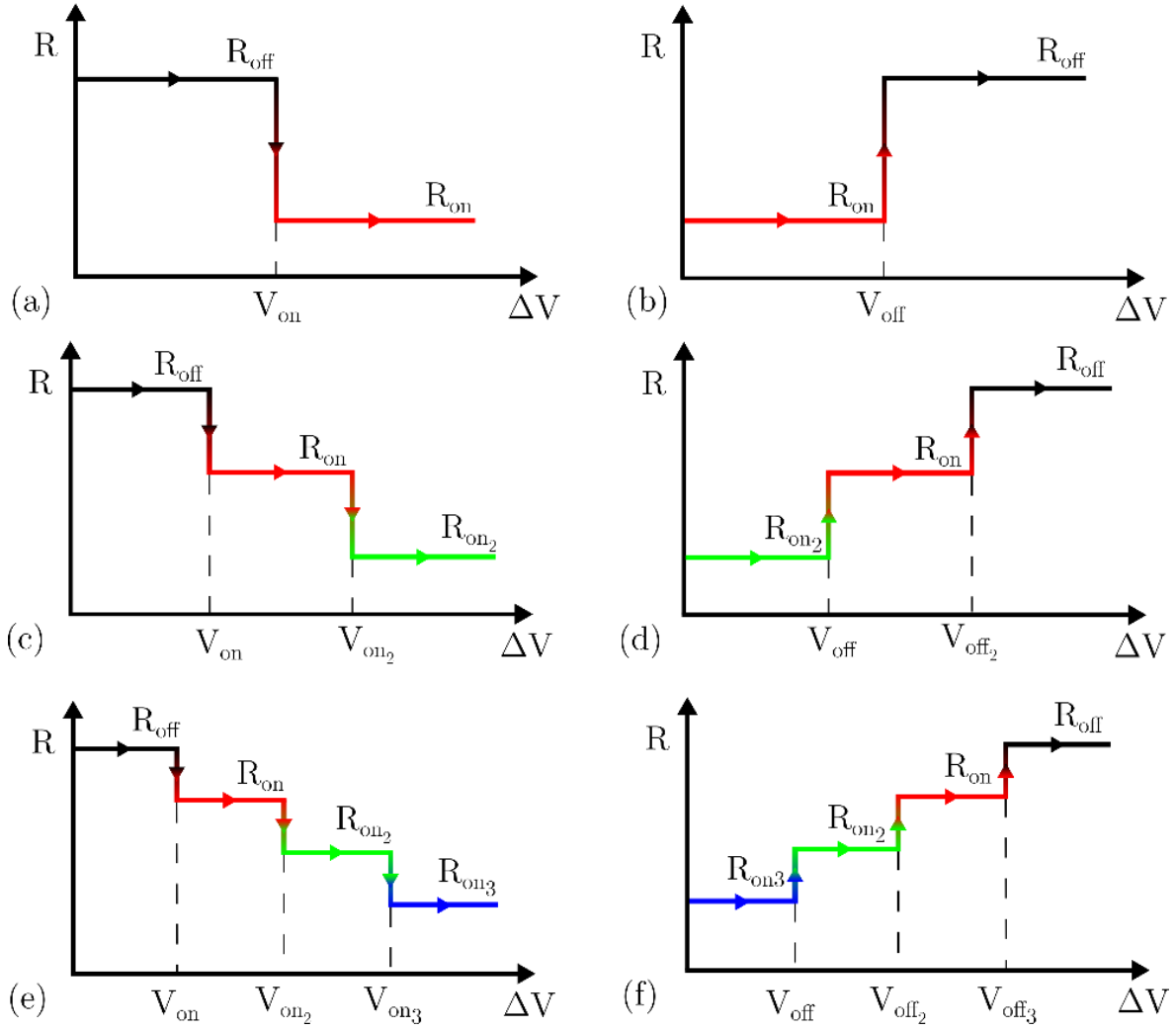

Figure 3. Circuit breaker internal resistance structure for the set (or forming) process (a) two levels, R_{off} and R_{on}; (c) three levels, R_{off}, R_{on} and R_{on2}; (e) four levels, R_{off}, R_{on}, R_{on2} and R_{on3}. For the reset process the CB internal resistance structure is described in (b) two levels, (d) three levels and (f) four levels.

A device with a pristine dielectric is assumed to start the simulation where some resistances are randomly chosen to be in the low state to better reproduce the stochastic behavior of a real device. If CBs with three or four levels are chosen, the different R_{on} values can be used for the random initialization of the dielectric.

Following the developments introduced in Refs. [50, 51], the Joule heating is considered and a thermal-driven switching rule is also implemented. It is explained in Figure 4a.

Thermal effects are known to be strongly linked to the devices under study since the physical mechanisms behind resistive switching are thermally activated [46, 59]; these effects also play a key role in other systems [5, 60-62].

If the CB local temperature, T_{CB}, reaches T_{set} (assuming a set and forming process), then the switching from R_{off} to R_{on} takes place. Conversely (Figure 4b, in a reset process), if T_{CB} reaches T_{reset}, then the switching from R_{on} to R_{off} takes place. This thermal switching rule can be extended to consider three or even four different resistance levels, as in the case depicted in Figure 3.

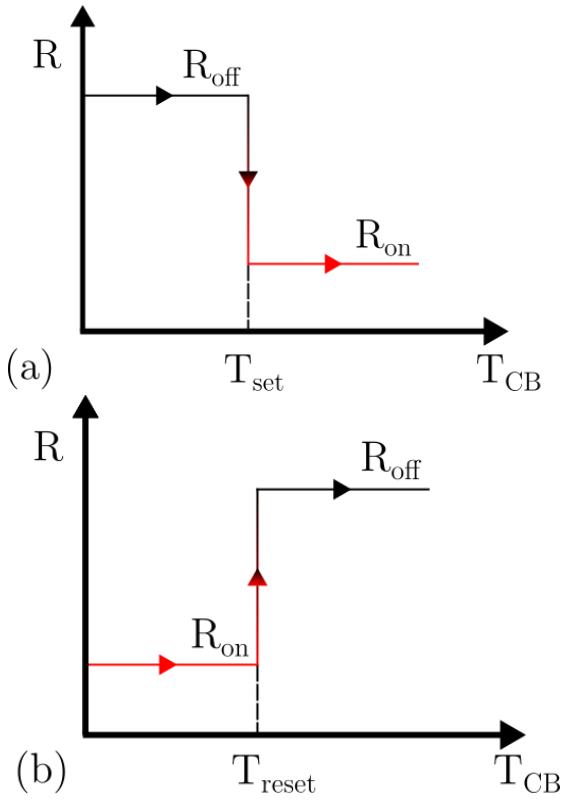

Figure 4. Thermal switching conditions of the circuit breaker, (a) from R_{off} to R_{on}, (b) from R_{on} to R_{off}. The thermal switching conditions of the circuit breaker are built upon the variation of T_{CB} in comparison with T_{set} and T_{reset}.

The calculation of T_{CB} is performed according to Equation 1, the heat equation.

$$C\frac{dT_{CB}}{dt} = Ri^2 - A(T_{CB} - T_0) \qquad (1)$$

where C stands for the heat capacitance, R is the electric resistance and A is the thermal conductance (the inverse of the thermal resistance, R_{th}) of every individual CB [46, 48, 51]. T_0 stands for reference temperature of the device, usually room temperature [46]. It is important to highlight that more complex thermal models could be taken into consideration, including a double thermal network with thermal resistances and capacitances in parallel, as explained in [46].

The CB switching is, therefore, implemented in this simulation tool both accounting for electric field and thermal effects, although these effects can be switched on and off in order to simulate devices with different RS activation processes (electrical or thermally driven) or analyze their sole influence on RS. In this manner, we make the model capable to describe filamentary RRAM operation, including the forming, set and reset processes, and also variability; both in the unipolar and bipolar cases [58].

Finally, we have considered the possibility of accounting for dielectrics made of different oxide layers [63]. In each layer, different values of CB resistances and switching voltages and temperatures would be considered. The layers width would be considered accounting for different rows in the CB network in relation to the network size as shown in Figure 5.

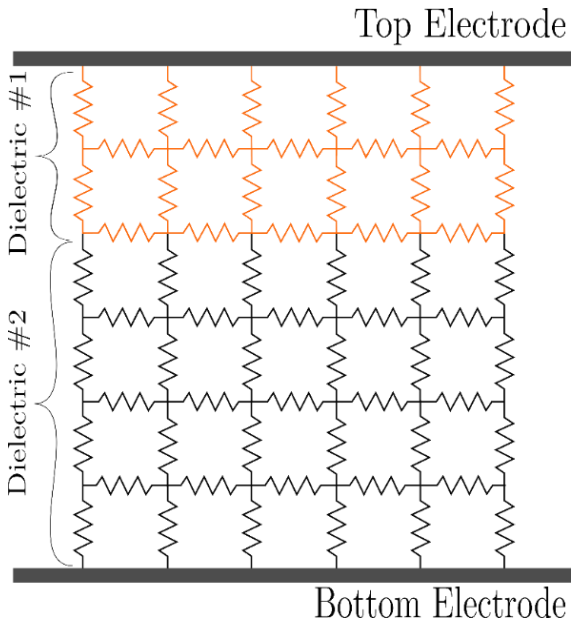

Figure 5. Schematic of the 2D CB network including two types of CBs to account for the bilayer oxide.

IV.- Results and discussion

We have used the simulator described in the previous section to reproduce the experimental measurements from the devices reported in section II. In particular, several cycles were accurately fitted as shown in Figure 6, both for the reset and set processes. The resistive switching process usually occurs as follows: when a percolation path (a CF) is fully formed by means of a chain of low resistances associated to CBs, ranging from the top to the bottom electrode, the device is in the LRS, showing a high current value (this state is achieved after a set or forming event). Later on, a reset process is launched within a resistive switching series; when the percolation path is ruptured, by switching one or more circuit breakers that where included in the CF to its high resistance value, the device turns back to the HRS. The fitting starts with the QPC model parameters and series resistance in the low voltage part of the I-V curve, then the CB matrix is established, and the CB configuration is chosen. The matrix size and the number of CB resistance states can be employed to improve the fitting of the experimental curve. As in every simulation tool, the accuracy and complexity trade-off has been considered in the fitting process.

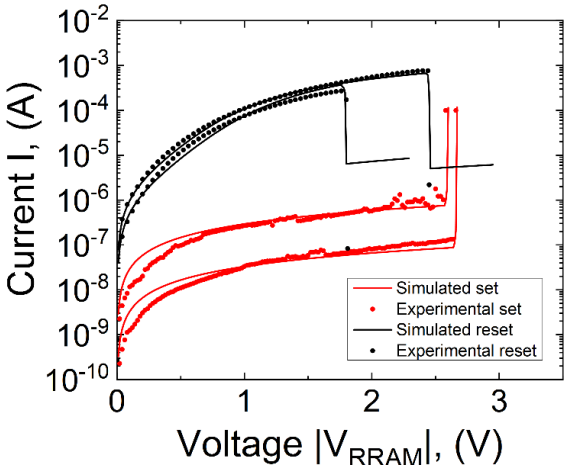

Figure 6. Current versus voltage curves of simulated data (solid lines) and experimental data (symbols) obtained from measured unipolar resistance switching (RS) devices described in section II. To obtain these simulations, a 50×20 network was employed using CBs with 4 resistance levels: $R_{off} = 1\times10^7\ \Omega$, $R_{on} = 500\ \Omega$, $R_{on2} = 300\ \Omega$ and $R_{on3} = 100\ \Omega$. The following parameters were employed: $V_{off} = 0.02V$, $V_{off2} = 0.05V$, $V_{off3} = 0.07V$, $V_{on} = 0.55V$, $V_{on2} = 0.6V$, $V_{on3} = 0.65V$. Since the CF narrowing that strangles the electron flux and creates a potential barrier for the charge transport [54, 56, 57] is different for each cycle, a set of QPC model parameters is needed for each curve. These are $\alpha_1 = 5.6$, $\beta_1 = 0.93$, $\varphi_1 = 0.94$, $N_1 = 10$ and $\alpha_2 = 5.6$, $\beta_2 = 0.93$, $\varphi_2 = 0.82$, $N_2 = 10$. An $R_{series}=10\ \Omega$ was employed in general in our simulations, a reasonable estimation according to [64].

Typical RS parameters such as V_{set}, V_{reset}, I_{set} and I_{reset} from the experimental curves are correctly reproduced, as shown in Figure 6. It is important to emphasize the fact that the experimental I-V curves have been fully fitted. In other approaches related to CB simulation tools, although the authors reproduced some RS features of their technology, no exact curve fitting is presented [50, 51]. In this respect, the switching parameters corresponding to Figure 3 and the QPC model parameters have been

fitted for the devices under study. In order to characterize the whole population of RS parameters (V_{set}, V_{reset}, I_{set} and I_{reset}) obtained in the complete series of I-V curves measured, a massive simulation study was performed, see Figures 7 and 8. Precisely, in Figure 7, 1800 experimental (I_{set}, V_{set}) points are plotted together with the results of 250 simulations for each area (red and blue circles). In Figure 8, in turn, the 1800 experimental (I_{reset}, V_{reset}) points are plotted together with the results of 150 simulations.

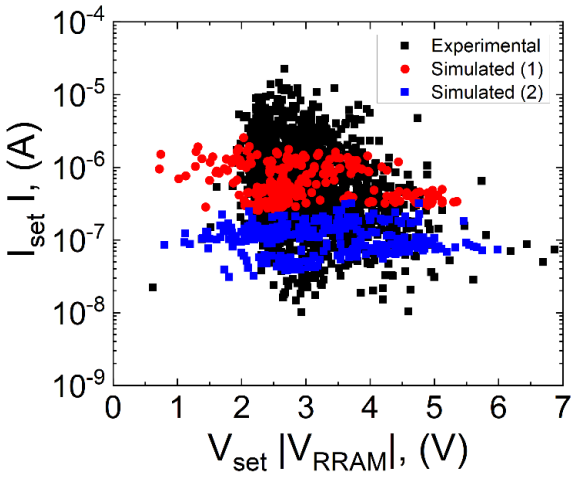

Figure 7. I_{set} versus V_{set} for simulated data (red circles and blue squares) compared with experimental data (black squares) from the devices described in section II. The first set of simulated values (red circles) were obtained choosing the following values, $R_{off} = 1\times10^{7}\ \Omega$, $R_{on} = 500\ \Omega$, $R_{on2} = 300\ \Omega$ and $R_{on3} = 100\ \Omega$ while the second set (blue squares) were obtained assuming $R_{off} = 1\times10^{8}\ \Omega$, $R_{on} = 1000\ \Omega$, $R_{on2} = 600\ \Omega$ and $R_{on3} = 200\ \Omega$. A 50×20 network was employed in all cases.

See that a great area of the experimental points in Figures 7 and 8 is covered by the simulation results obtained with the parameters employed in the I-V curve fitting shown in Figure 6. For these variability simulations we employed different random initial distributions according to our assumption of 0.5% of the CBs in the network. See that we can only cover part of the experimental cloud. In order to sweep a greater area in Figures 7 and 8 another set of parameters was employed, see the blue points. The use of different parameters is reasonable since the ion cluster formation that creates the CF varies, as observed in KMC simulations [53]; the presence of grain boundaries in different regions in the dielectric and their influence on ion clustering could also affect this issue. Changing the parameters accounts for the CF 3D formation differences that are modeled in the simplifying 2D approach pictured here; the different ion cluster density within the CF that could be formed [65] in each RS cycle is approximately described by a set of resistances and transition voltages for the CBs (Figure 3).

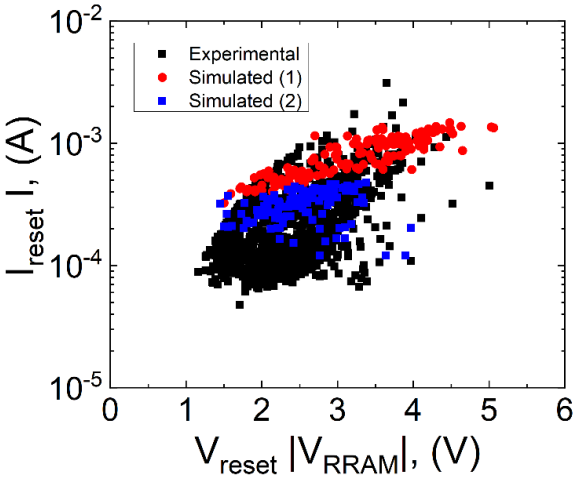

Figure 8. I_{reset} versus V_{reset} simulated data (red circles and blue squares) compared with experimental data (black squares) from the devices described in section II. The first set of simulated values (red circles) were obtained choosing the following values, $R_{off} = 1\times10^{7}\ \Omega$, $R_{on} = 500\ \Omega$, $R_{on2} = 300\ \Omega$ and $R_{on3} = 100\ \Omega$ while the second set of values (blue squares) were obtained by taking $R_{off} = 1\times10^{8}\ \Omega$, $R_{on} = 1000\ \Omega$, $R_{on2} = 600\ \Omega$ and $R_{on3} = 200\ \Omega$. A 50×20 network was employed in all cases.

Some facets of the RS stochasticity are captured by our simulator since we are able to reproduce experimental curves with several decreasing current steps taking place in the reset process. These steps are linked to the rupture of conductive branches which are part of a complete conductive filament, i.e., the

steps are linked to a partial filament destruction, see Figure 9 and 10.

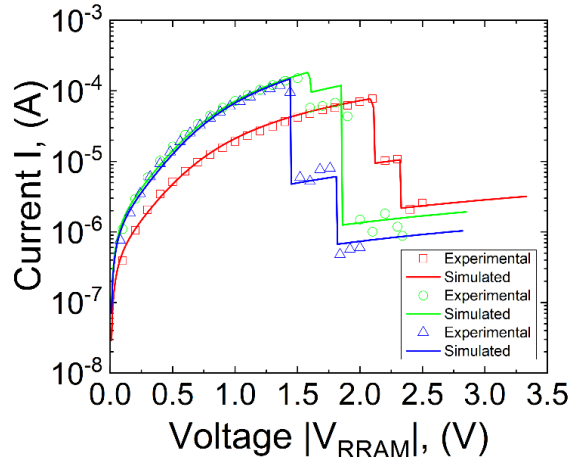

Figure 9. Current versus device voltage for simulated data (solid lines) and experimental data (symbols) measured from the devices described in section II. These simulation results were obtained by employing a 10x10 network using CBs with 2 resistance levels: R_{off} = 7.5×10^6 Ω and R_{on} = 2.5×10^3 Ω. The following parameters were employed: V_{off} = 0.19V and V_{on} = 0.15V.

In relation to the simulations of the previous figure and to better show the details of a CF partial rupture that leads to a decreasing step in an I-V reset curve, we show a simulation using a 20×20 network, see Figure 10.

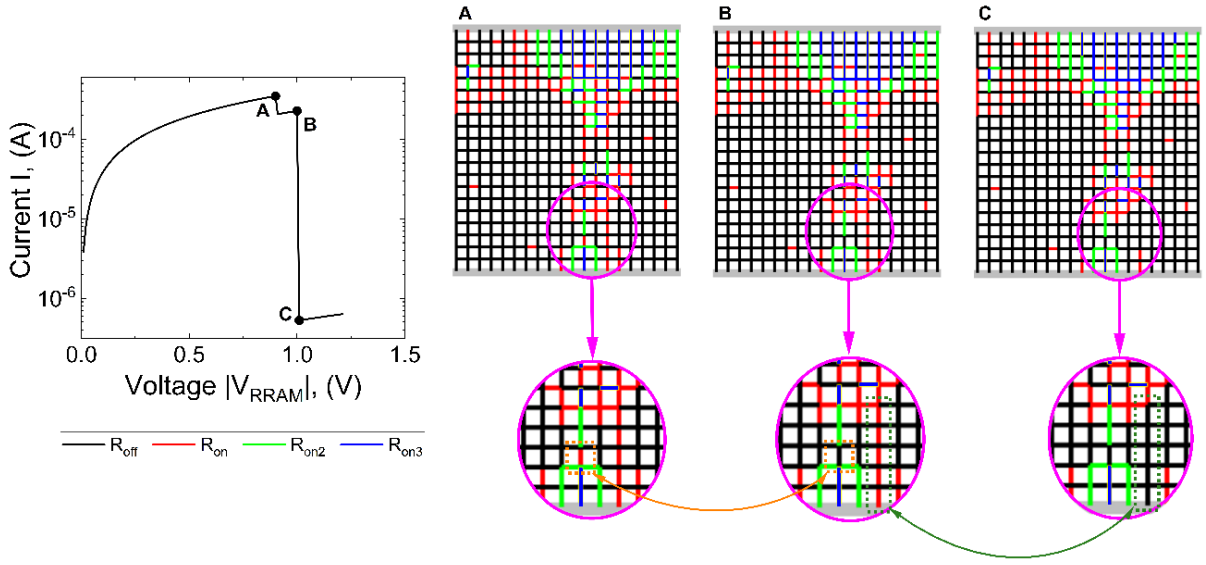

Figure 10. Simulated current versus voltage. CBs with four resistance values were employed. Points A, B and C in the I-V curve represent different CF evolution stages. A corresponds to a fully formed CF, see a continuous percolation path shorting the electrodes; B shows a CF partial rupture (that is why an abrupt current step is seen in the I-V curve), one of the two low resistive connecting paths between the CF main body and the bottom electrode is broken (it is shown in the zoomed in region); C shows a full CF rupture since the low resistance path next to the bottom electrode is gone at the CF narrowest region. These simulation results were obtained by employing a 10x10 network using CBs with 4 resistance levels: R_{off} = 1×10^7 Ω, R_{on} = 500 Ω, R_{on2} = 300 Ω and R_{on3} = 100 Ω. The following parameters were employed: V_{off} = 0.112V, V_{off2} = 0.15V, V_{off3} = 0.2V, V_{on} = 0.112V, V_{on2} = 0.15V, V_{on3} = 0.2V.

To illustrate the role of the temperature for resistive switching, we turned off the CB voltage driven switching. As explained above, Joule heating rises the CB local temperature. In figure 11, simulated forming, reset, and set processes were carried out by taking different R_{th} values in order to study their effects. As it is clearly seen, the higher the thermal resistance the lower the V_{reset} since the CF is heated faster, this also works for the set process. The CB associated thermal resistance values are higher than what is usually employed in modeling

complete resistive switching devices. In this respect it is important to point out that the power dissipated in each CBs can be one or two orders of magnitude lower than in the device since the current and, mostly, the voltage values are reduced in the resistance network nodes. Consequently, these corrections are translated to R_{th} in order to achieve temperatures in the order of what is found in simulation and modeling studies [46]. Since the T_{set} and T_{reset} are fitting parameters, a trade-off between these temperatures and R_{th} can be achieved; in our case, the parameters employed in Figure 11 worked well.

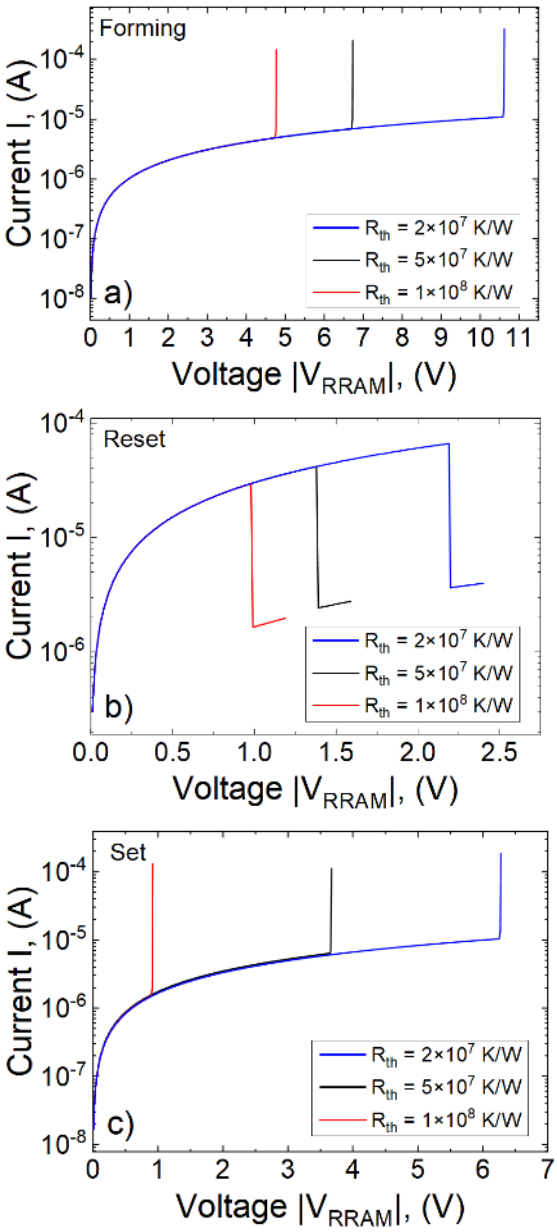

Figure 11. Simulated current versus device voltage for different a) forming, b) reset and c) set processes for different values of the thermal resistance. All the simulations were performed assuming the following values for the CB thermal model: $R_{off} = 1\times10^6\ \Omega$, $R_{on} = 5\ k\Omega$, $T_{set} = 350K$, $T_{reset} = 700K$. These simulations correspond to curves with ramped voltages that last several seconds; therefore, the time dependent term in Equation 1 was neglected and no thermal capacitances were considered.

V.- CONCLUSIONS

A simulator tool to study the formation and rupture processes of conductive filaments in

resistive switching (RS) has been developed and tested, including quantum effects and series resistance correction. Experimental measurements of RRAMs based on Ni/HfO_2/Si structures have been reproduced under several conditions to show the versatility of the simulator that accounts for the device electrical and thermal description. Both the ohmic and tunneling based conduction regimes are considered since their contribution depends on the device operation regime. I-V reset curves with decreasing steps are explained by means of partial conductive filament the ruptures of which are correctly reproduced. This tool, in terms of the computing time and device complexity, stands in a middle point between the physical simulation and compact modeling approaches.

VI. - ACKNOWLEDGMENTS

The authors thank the support of the Spanish Ministry of Science, Innovation and Universities and the FEDER program through projects TEC2017-84321-C4-1-R, TEC2017-84321-C4-3-R, and projects A.TIC.117.UGR18, B-TIC-624-UGR20 and IE2017-5414 funded by the Consejería de Conocimiento, Investigación y Universidad, Junta de Andalucía (Spain) and the FEDER program.

References

[1] Pan, F., Gao, S., Chen, C., Song, C., & Zeng, F. (2014). Recent progress in resistive random access memories: Materials, switching mechanisms, and performance. *Materials Science and Engineering: R: Reports*, *83*, 1-59.

[2] Lanza, M., et al. (2019). Recommended methods to study resistive switching devices. *Advanced Electronic Materials*, 5(1), 1800143.

[3] Ielmini, D., & Waser, R. (Eds.). (2015). *Resistive switching: from fundamentals of nanoionic redox processes to memristive device applications*. John Wiley & Sons.

[4] Lee, J. S., Lee, S., & Noh, T. W. (2015). Resistive switching phenomena: A review of statistical physics approaches. *Applied Physics Reviews*, *2*(3), 031303.

[5] Spiga, S., Sebastian, A., Querlioz, D., & Rajendran, B. (Eds.). (2020). *Memristive Devices for Brain-Inspired Computing: From Materials, Devices, and Circuits to Applications-Computational Memory, Deep Learning, and Spiking Neural Networks*. Woodhead Publishing.

[6] Hui, F., et al. (2021). In Situ Observation of Low-Power Nano-Synaptic Response in Graphene Oxide Using Conductive Atomic Force Microscopy. *Small*, 1-8, 2101100.

[7] Chua, L. O., & Kang, S. M. (1976). Memristive devices and systems. *Proceedings of the IEEE*, 64(2), 209-223.

[8] Corinto, F., Civalleri, P. P., & Chua, L. O. (2015). A theoretical approach to memristor devices. *IEEE Journal on Emerging and Selected Topics in Circuits and Systems*, 5(2), 123-132.

[9] Yu, S., Wu, Y., Jeyasingh, R., Kuzum, D., & Wong, H. S. P. (2011). An electronic synapse device based on metal oxide resistive switching memory for neuromorphic computation. *IEEE Transactions on Electron Devices*, 58(8), 2729-2737.

[10] Ambrogio, S., et al. (2018). Equivalent-accuracy accelerated neural-network training using analogue memory. *Nature*, 558(7708), 60-67.

[11] Merolla, P. A., et al. (2014). A million spiking-neuron integrated circuit with a scalable communication network and interface. *Science*, *345*(6197), 668-673.

[12] Nandakumar, S. R., & Rajendran, B. (2020). Bio-mimetic synaptic plasticity and learning in a sub-500 mV Cu/SiO2/W memristor. *Microelectronic Engineering*, 226, 111290.

[13] Alibart, F., Zamanidoost, E., & Strukov, D. B. (2013). Pattern classification by memristive crossbar circuits using ex situ and in situ training. *Nature communications*, 4(1), 1-7.

[14] González-Cordero, G., Pedro, M., Martin-Martinez, J., González, M. B., Jiménez-Molinos, F., Campabadal, F., N. Nafría & Roldán, J. B. (2019). Analysis of resistive switching processes in

TiN/Ti/HfO2/W devices to mimic electronic synapses in neuromorphic circuits. *Solid-State Electronics*, 157, 25-33.

[15] Prezioso, M., Merrikh-Bayat, F., Hoskins, B. D., Adam, G. C., Likharev, K. K., & Strukov, D. B. (2015). Training and operation of an integrated neuromorphic network based on metal-oxide memristors. *Nature*, 521(7550), 61-64.

[16] Pérez-Bosch Quesada, E., Romero-Zaliz, R., Pérez, E., Kalishettyhalli Mahadevaiah, M., Reuben, J., Schubert, M. A., F. Jiménez-Molinos, J.B. Roldán & Wenger, C. (2021). Toward Reliable Compact Modeling of Multilevel 1T-1R RRAM Devices for Neuromorphic Systems. *Electronics*, 10(6), 645.

[17] M Zidan, M. A., Strachan, J. P., & Lu, W. D. (2018). The future of electronics based on memristive systems. *Nature electronics*, 1(1), 22-29.

[18] Romero-Zaliz, R., Pérez, E., Jiménez-Molinos, F., Wenger, C., & Roldán, J. B. (2021). Study of Quantized Hardware Deep Neural Networks Based on Resistive Switching Devices, Conventional versus Convolutional Approaches. *Electronics*, 10(3), 346.

[19] Sakellaropoulos, D., Bousoulas, P., Nikas, G., Arvanitis, C., Bagakis, E., & Tsoukalas, D. (2020). Enhancing the synaptic properties of low-power and forming-free HfOx/TaOy/HfOx resistive switching devices. *Microelectronic Engineering*, 229, 111358.

[20] Pedro, M., Martin-Martinez, J., Rodriguez, R., Gonzalez, M. B., Campabadal, F., & Nafria, M. (2019). An unsupervised and probabilistic approach to Pavlov's dog experiment with OxRAM devices. *Microelectronic Engineering*, 215, 111024.

[21] Mead, C., & Ismail, M. (1989). Analog VLSI implementation of neural systems. *Springer Science & Business Media,* 80.

[22] Poblador, S., Gonzalez, M. B., & Campabadal, F. (2018). Investigation of the multilevel capability of TiN/Ti/HfO2/W resistive switching devices by sweep and pulse programming. *Microelectronic Engineering*, 187, 148-153.

[23] A Sebastian, A., Le Gallo, M., Khaddam-Aljameh, R., & Eleftheriou, E. (2020). Memory devices and applications for in-memory computing. *Nature nanotechnology*, 15(7), 529-544.

[24] Pérez, E., Maldonado, D., Acal, C., Ruiz-Castro, J. E., Alonso, F. J., Aguilera, A. M., Jiménez-Molinos, F. & Roldán, J. B. (2019). Analysis of the statistics of device-to-device and cycle-to-cycle variability in TiN/Ti/Al: HfO2/TiN RRAMs. *Microelectronic Engineering*, 214, 104-109.

[25] Mikhaylov, A. N., et tal. (2021). Stochastic resonance in a metal-oxide memristive device. *Chaos, Solitons & Fractals*, 144, 110723.

[26] Alonso, F. J., Maldonado, D., Aguilera, A. M., & Roldan, J. B. (2021). Memristor variability and stochastic physical properties modeling from a multivariate time series approach. *Chaos, Solitons & Fractals*, 143, 110461.

[27] Dalgaty, T., Castellani, N., Turck, C., Harabi, K. E., Querlioz, D., & Vianello, E. (2021). In situ learning using intrinsic memristor variability via Markov chain Monte Carlo sampling. *Nature Electronics*, 4(2), 151-161.

[28] Carboni, R., & Ielmini, D. (2019). Stochastic memory devices for security and computing. *Advanced Electronic Materials*, 5(9), 1900198.

[29] Wei, Z., Katoh, Y., Ogasahara, S., Yoshimoto, Y., Kawai, K., Ikeda, Y., Eriguchi, K., Ohmori, K., & Yoneda, S. (2016). True random number generator using current difference based on a fractional stochastic model in 40-nm embedded ReRAM. *IEEE International Electron Devices Meeting (IEDM)* (pp. 4-8). IEEE.

[30] Chen, A. (2014). Utilizing the variability of resistive random access memory to implement reconfigurable physical unclonable functions. *IEEE Electron Device Letters*, 36(2), 138-140.

[31] Lanza, M., et al. (2021). Advanced data encryption using two-dimensional materials. *Adv. Mater*, 33, 2100185.

[32] Aldana, S., García-Fernández, P., Romero-Zaliz, R., González, M. B., Jiménez-Molinos, F., Gómez-Campos, F., Campabadal, F. & Roldán, J. B. (2020). Resistive switching in HfO2 based valence change memories, a comprehensive 3D kinetic Monte Carlo approach. *Journal of Physics D: Applied Physics*, 53(22), 225106.

[33] Padovani, A., Larcher, L., Pirrotta, O., Vandelli, L., & Bersuker, G. (2015). Microscopic modeling of HfO x RRAM operations: From forming to switching. *IEEE Transactions on electron devices*, 62(6), 1998-2006.

[34] Dirkmann, S., Kaiser, J., Wenger, C., & Mussenbrock, T. (2018). Filament growth and resistive switching in hafnium oxide memristive devices. *ACS applied materials & interfaces*, 10(17), 14857-14868.

[35] Guy, J., et al. (2015). Investigation of forming, SET, and data retention of conductive-bridge random-access memory for stack optimization. *IEEE Transactions on Electron Devices*, 62(11), 3482-3489.

[36] Roldán, J. B., Alonso, F. J., Aguilera, A. M., Maldonado, D., & Lanza, M. (2019). Time series statistical analysis: A powerful tool to evaluate the variability of resistive switching memories. *Journal of Applied Physics*, 125(17), 174504.

[37] Huang, P., et al. (2013). A physics-based compact model of metal-oxide-based RRAM DC and AC operations. *IEEE transactions on electron devices*, 60(12), 4090-4097.

[38] González-Cordero, G., González, M. B., García, H., Campabadal, F., Dueñas, S., Castán, H., Jiménez-Molinos, F., & Roldán, J. B. (2017). A physically based model for resistive memories including a detailed temperature and variability description. *Microelectronic Engineering*, 178, 26-29.

[39] Chen, P. Y., & Yu, S. (2015). Compact modeling of RRAM devices and its applications in 1T1R and 1S1R array design. *IEEE Transactions on Electron Devices*, 62(12), 4022-4028.

[40] Bocquet, M., Deleruyelle, D., Aziza, H., Muller, C., Portal, J. M., Cabout, T., & Jalaguier, E. (2014). Robust compact model for bipolar oxide-based resistive switching memories. *IEEE transactions on electron devices*, 61(3), 674-681.

[41] Picos, R., Roldan, J. B., Chawa, M. M. A., Garcia-Fernandez, P., Jimenez-Molinos, F., & Garcia-Moreno, E. (2015). Semiempirical modeling of reset transitions in unipolar resistive-switching based memristors. *Radioengineering Journal*, 24, 420-424.

[42] Guan, X., Yu, S., & Wong, H. S. P. (2012). A SPICE compact model of metal oxide resistive switching memory with variations. *IEEE electron device letters*, 33(10), 1405-1407.

[43] Maldonado, D., Roldán, A. M., González, M. B., Jiménez-Molinos, F., Campabadal, F., & Roldán, J. B. (2019). Influence of magnetic field on the operation of TiN/Ti/HfO2/W resistive memories. *Microelectronic Engineering*, 215, 110983.

[44] Huang, P., Zhu, D., Chen, S., Zhou, Z., Chen, Z., Gao, B., Liu, L., Liu, X., & Kang, J. (2017). Compact model of HfO X-based electronic synaptic devices for neuromorphic computing. *IEEE Transactions on Electron Devices*, 64(2), 614-621.

[45] Jiang, Z., Wu, Y., Yu, S., Yang, L., Song, K., Karim, Z., & Wong, H. S. P. (2016). A compact model for metal–oxide resistive random access memory with experiment verification. *IEEE Transactions on Electron Devices*, 63(5), 1884-1892.

[46] Roldán, J. B., et al. (2021). On the Thermal Models for Resistive Random Access Memory Circuit Simulation. *Nanomaterials*, 11(5), 1261.

[47] González-Cordero, G., González, M. B., Campabadal, F., Jiménez-Molinos, F., & Roldán, J. B. (2019). A new technique to analyze RTN signals in resistive memories. *Microelectronic Engineering*, 215, 110994.

[48] Chang, S. H., Lee, J. S., Chae, S. C., Lee, S. B., Liu, C., Kahng, B., Kim D., & Noh, T. W. (2009). Occurrence of both unipolar memory and threshold resistance switching in a NiO film. *Physical review letters*, 102(2), 026801.

[49] Lee, S. B., Lee, J. S., Chang, S. H., Yoo, H. K., Kang, B. S., Kahng, B., Lee, M. J., Kim, C.J. & Noh, T. W. (2011). Interface-modified random circuit breaker network model applicable to both bipolar and unipolar resistance switching. *Applied Physics Letters*, 98(3), 033502.

[50] Chae, S. C., et al. (2008). Random circuit breaker network model for unipolar resistance switching. *Advanced Materials*, 20(6), 1154-1159.

[51] Brivio, S., & Spiga, S. (2017). Stochastic circuit breaker network model for bipolar resistance switching memories. *Journal of Computational Electronics*, 16(4), 1154-1166.

[52] Kim, K., Yoon, S. J., & Choi, W. Y. (2014). Dual random circuit breaker network model with equivalent thermal circuit network. *Applied Physics Express*, 7(2), 024203.

[53] Aldana, S., García-Fernández, P., Rodríguez-Fernández, A., Romero-Zaliz, R., González, M. B., Jiménez-Molinos, F., Campabadal, F., Gómez-Campos, F., & Roldán, J. B. (2017). A 3D kinetic Monte Carlo simulation study of resistive switching processes in Ni/HfO2/Si-n+-based RRAMs. *Journal of Physics D: Applied Physics*, 50(33), 335103.

[54] Villena, M. A., Roldán, J. B., Jiménez-Molinos, F., Miranda, E., Suñé, J., & Lanza, M. (2017). SIM2 RRAM: a physical model for RRAM devices simulation. *Journal of Computational Electronics*, 16(4), 1095-1120.

[55] Villena, M. A., Roldán, J. B., González, M. B., González-Rodelas, P., Jiménez-Molinos, F., Campabadal, F., & Barrera, D. (2016). A new parameter to characterize the charge transport regime in Ni/HfO2/Si-n+-based RRAMs. *Solid-State Electronics*, 118, 56-60.

[56] Miranda, E. A., Walczyk, C., Wenger, C., & Schroeder, T. (2010). Model for the Resistive Switching Effect in HfO2 MIM Structures Based on the Transmission Properties of Narrow Constrictions. *IEEE Electron Device Letters*, 31(6), 609-611.

[57] Roldán, J. B., Miranda, E., González-Cordero, G., García-Fernández, P., Romero-Zaliz, R., González-Rodelas, P., Aguilera, A. M., González, M.B., & Jiménez-Molinos, F. (2018). Multivariate analysis and extraction of parameters in resistive RAMs using the Quantum Point Contact model. *Journal of Applied Physics*, 123(1), 014501.

[58] Supplementary material: https://www.youtube.com/watch?v=-kq6-5k2-HY

[59] Villena, M. A., Roldán, J. B., Jimenez-Molinos, F., Suñé, J., Long, S., Miranda, E., & Liu, M. (2014). A comprehensive analysis on progressive reset transitions in RRAMs. *Journal of Physics D: Applied Physics*, 47(20), 205102.

[60] Menzel, S., Kaupmann, P., & Waser, R. (2015). Understanding filamentary growth in electrochemical metallization memory cells using kinetic Monte Carlo simulations. *Nanoscale*, 7(29), 12673-12681.

[61] Lanza, M., Palumbo, F., Shi, Y., Aguirre, F., Boyeras, S., Yuan, B., Yalon, E., Moreno, E., Wu, T., & Roldan, J. B. (2021). Temperature of Conductive Nanofilaments in Hexagonal Boron Nitride Based Memristors Showing Threshold Resistive Switching. *Advanced Electronic Materials*, 2100580.

[62] von Witzleben, M., Fleck, K., Funck, C., Baumkötter, B., Zuric, M., Idt, A., Breuer, T., Waser, R., Böttger, U., & Menzel, S. (2017). Investigation of the Impact of High Temperatures on the Switching Kinetics of Redox-Based Resistive Switching Cells using a High-Speed Nanoheater. *Advanced electronic materials*, 3(12), 1700294.

[63] Maestro-Izquierdo, M., Gonzalez, M. B., Jimenez-Molinos, F., Moreno, E., Roldan, J. B., & Campabadal, F. (2020). Unipolar resistive switching behavior in Al2O3/HfO2 multilayer dielectric stacks: fabrication, characterization and simulation. *Nanotechnology*, 31(13), 135202.

[64] Maldonado, D., Aguirre, F., González-Cordero, G., Roldán, A. M., González, M. B., Jiménez-Molinos, F., Campabadal, F., Miranda, E., & Roldán, J. B. (2021). Experimental study of the series resistance effect and its impact on the compact modeling of the conduction characteristics of HfO2-based resistive switching memories. *Journal of Applied Physics*, 130(5), 054503.

[65] Aldana, S., Pérez, E., Jiménez-Molinos, F., Wenger, C., & Roldán, J. B. (2020). Kinetic Monte Carlo analysis of data retention in Al: HfO2-based resistive random access memories. *Semiconductor Science and Technology*, 35(11), 115012.

Chapter 7.

7. Conclusions

Nowadays there is an increasing interest on data storing in the electronic device context either for volatile (temporary) and non-volatile (permanent) applications. This arises from several requirements related to 5G structures, advanced artificial intelligence implementations, internet of things (IoT) arrival, complex data mining, faster and smaller solid-state drives (SSD) and even common laptops and smartphones. Thus, RRAM devices appear as one of the best suitable candidates to be considered due to its outstanding characteristics such as extraordinary scalability accounting with the potentiality of 3D stacking, high endurance and speed and low latency and energy demand. In addition, the fabrication process is quite simple and cheap and the compatibility with CMOS technology in the Back-End-Of-Line (BEOL) is guaranteed, another key aspect to take into account.

This work has been focused on the characterization and measurement of RRAM devices including external effects such as temperature, electric field and magnetic field for the subsequent analysis and determination of results. Hence, modelling of these data adopting quantum effects and time series approach is addressed along the QPC model. Then, existing compact models are employed and modified to reproduce experimental data and simulate circuits to account for different issues like the series resistance correction. To conclude, a simulator tool based on resistive circuit breakers is designed and developed to study variability and the stochastic features of resistive memories. This thesis includes seven publications in scientific journals indexed in the Journal Citation Report of Science Citation Index, one proceeding published in IEEE Xplore digital library and one contribution to an International Conference and other publications outside this work where a book chapter is included and a video explaining the operation of the simulator among multiple congress contributions.

The most relevant results obtained can be compiled as follows:

1. Different RRAM technologies have been characterized and modeled. In particular, several devices based on Ni/HfO_2/Si-n^+, Cu/HfO_2/Si-n^+, Au/Ti/TiO_2/SiO_x/Si-n^+, Au/Ti/h-BN/Au/Ti, Au/h-BN/Au/Ti, TiN/Ti/HfO_2/W and TiN/Ti/HfO_2/Al_2O_3/W stacks, fabricated both in MIS and MIM structures, are tackled to extract the most representative RS parameters from the characterization viewpoint. The measured data have been elaborated using advanced statistical techniques. Among conventional measurements, diverse external effects (for instance a variable magnetic field) are included in order to study the impact they have on the operation of these devices.
2. We have studied the device-to-device and cycle-to-cycle variability by means of Weibull, Erlang and Phase type statistical distributions applicated on a great amount of experimental data. The latter distribution has shown a higher degree of reproducibility as the data gets fitted more consistently.
3. We have employed the time series analysis to evaluate variability in resistive memories. Different models have been obtained to assess current RS parameters as a function of the previous values in RS series. Devices based in h-BN and graphene oxide, along with different transition metal oxides, such as TiO_2, HfO_2, Al_2O_3 have been modeled by means of this technique; in doing so, ACF and PACF tools were calculated to achieve the proper analytical models and assess autocorrelation between the data. In general, the results show a correlation between set and reset voltages of different cycles in the series, this led us to obtain mathematical expressions based on Auto regressive modeling approaches in order to predict future values of the parameters studied along a RS series.
4. Modeling of quantum effects based on the quantum point contact model. Landauer's theory has been employed to get an analytical expression for the I-V characteristics in resistive memories based on filamentary conduction when non-linearity is present. The role of the temperature in the current calculation is also assessed. It is also proved that quantum effects must be taken into account when considering electron transport in these situations.
5. Dynamic route maps have been used in resistive memories reset transitions. This concept has been proved to have an outstanding potential in the modeling and analysis context of RRAM memories. By plotting the dynamic route map, it is shown that every variation provoked by external waveforms of different nature in the device in the measuring process belongs to the generated surface in the DRM. Thus, it is demonstrated that memristors do not respond in a different manner regarding different inputs. At the end, this is what actually determines the role of the device.
6. We have developed a methodology to extract the series resistance. The effects of this resistance have been included in compact models. Redefined I-V experimental curves are considered to extract the set and reset transition voltages, which exhibit correlation from the statistical viewpoint. In that sense, it has been demonstrated that the lower the series resistance, the higher the set and reset transition absolute voltages. The Stanford model has been modified to include this effect and enhance its accuracy to improve the fitting of experimental data of VCM devices.
7. We have developed a circuit breaker-based RRAM simulator tool implemented by resistances of different features to analyze RRAM variability. Typical RS processes such as forming, set and reset are reproduced progressively to detail the rupture and formation of the CF in a 2D resistance network. Experimental I-V measurements from unipolar and bipolar devices are reproduced as several dielectric layers with different characteristics could be included. To enhance the modeling process some functionalities are incorporated: quantum effects in a QPC module to describe non-linear curves, electrical and/or thermal

switching rules to change the resistive state of the circuit breakers, series resistance correction, a few layers to account for diverse dielectric stacks and resistances with up to four values.

In the last few years, an increase of the number of publications, congresses and workshops has been clearly observed. Many research groups worldwide are devoted to take RRAM applications to a new level. There are many fronts to advance in research and development in the future.

In the short-term, the improvement of the developed compact models and the creation of new ones is key for the proper evolution of this technology as detailed in section **1.5**. In addition, the simplification and the public release of the modeling tools could help to bring new developers to the community which implies more people pushing in the same direction. As a consequence of that, new layered structures could be properly investigated in order to get a better understanding of the resistive switching phenomena.

Moving up to the simulation level presented in Chapter **6**, there are some lines to pursue. For example, implementing a 3D circuit breaker network instead of the 2D would imply a more detailed step-by-step formation and rupture of the conductive filament. On the other hand, new conditions to trigger the resistive state of the breakers could be considered to achieve several conduction levels and reproduce different experimental curves.

References

[Acal2019] Acal, C., Ruiz-Castro, J. E., Aguilera, A. M., Jiménez-Molinos, F., & Roldán, J. B. (2019). Phase-type distributions for studying variability in resistive memories. Journal of Computational and Applied Mathematics, 345, 23–32. DOI: 10.1016/j.cam.2018.06.010

[Ahn2015] Ahn, C., Jiang, Z., Lee, C. S., Chen, H. Y., Liang, J., Liyanage, L. S., & Wong, H. S. P. (2015). 1D selection device using carbon nanotube FETs for high-density cross-point memory arrays. IEEE Transactions on Electron Devices, 62(7), 2197-2204.

[Aldana2017] Aldana, S., García-Fernández, P., Rodríguez-Fernández, A., Romero-Zaliz, R., González, M. B., Jiménez-Molinos, F., ... & Roldán, J. B. (2017). A 3D kinetic Monte Carlo simulation study of resistive switching processes in Ni/HfO2/Si-n+-based RRAMs. Journal of Physics D: Applied Physics, 50(33), 335103.

[Aldana2020] Aldana, S., García-Fernández, P., Romero-Zaliz, R., González, M. B., Jiménez-Molinos, F., Gómez-Campos, F., ... & Roldán, J. B. (2020). Resistive switching in HfO2 based valence change memories, a comprehensive 3D kinetic Monte Carlo approach. Journal of Physics D: Applied Physics, 53(22), 225106.

[Aldana2020b] Aldana, S. (2020). Resistive memories simulation based on the kinetic monte carlo algorithm.

[Alibart2013] Alibart, F., Zamanidoost, E., & Strukov, D. B. (2013). Pattern classification by memristive crossbar circuits using ex situ and in situ training. Nature communications, 4(1), 1-7.

[Alonso2021] Alonso, F. J., Maldonado, D., Aguilera, A. M., & Roldan, J. B. (2021). Memristor variability and stochastic physical properties modeling from a multivariate time series approach. Chaos, Solitons & Fractals, 143, 110461.

[Aritome1993] Aritome, S., Shirota, R., Hemink, G., Endoh, T., & Masuoka, F. (1993). Reliability issues of flash memory cells. Proceedings of the IEEE, 81(5), 776-788.

[Asamitsu1997] Asamitsu, A., Tomioka, Y., Kuwahara, H., & Tokura, Y. (1997). Current switching of resistive states in magnetoresistive manganites. Nature, 388(6637), 50-52.

[Atwood2004] Atwood, G. (2004). Future directions and challenges for ETox flash memory scaling. IEEE transactions on Device and Materials Reliability, 4(3), 301-305.

[Baek2004] Baek, I. G., Lee, M. S., Seo, S., Lee, M. J., Seo, D. H., Suh, D. S., ... & Chung, U. I. (2004, December). Highly scalable nonvolatile resistive memory using simple binary oxide driven by asymmetric unipolar voltage pulses. In IEDM Technical Digest. IEEE International Electron Devices Meeting, 2004. (pp. 587-590). IEEE

[Bai2013] Bai, W., Huang, R., Cai, Y., Tang, Y., Zhang, X., & Wang, Y. (2013). Record low-power organic RRAM with sub-20-nA reset current. IEEE electron device letters, 34(2), 223-225.

[Banerjee2020] Banerjee, W. Challenges and Applications of Emerging Nonvolatile Memory Devices. Electronics 2020, 9, 1029.

[Bersuker2010] Bersuker, G., Gilmer, D. C., Veksler, D., Yum, J., Park, H., Lian, S., ... & Shluger, A. (2010, December). Metal oxide RRAM switching mechanism based on conductive filament microscopic properties. In 2010 International Electron Devices Meeting (pp. 19-6). IEEE.

[Bez2003] Bez, R., Camerlenghi, E., Modelli, A., & Visconti, A. (2003). Introduction to flash memory. Proceedings of the IEEE, 91(4), 489-502.

[Bocquet2014] Bocquet, M., Deleruyelle, D., Aziza, H., Muller, C., Portal, J. M., Cabout, T., & Jalaguier, E. (2014). Robust compact model for bipolar oxide-based resistive switching memories. IEEE Transactions on Electron Devices, 61(3), 674-681.

[Bocquet2014b] Bocquet, M., Aziza, H., Zhao, W., Zhang, Y., Onkaraiah, S., Muller, C., ... & Portal, J. M. (2014). Compact modeling solutions for oxide-based resistive switching memories

[Calixto2020] Calixto, M., Maldonado, D., Miranda, E., & Roldan, J. B. (2020). Modeling of the temperature effects in filamentary-type resistive switching memories using quantum point-contact theory. Journal of Physics D: Applied Physics.

[Calka2013] Calka, P., Martinez, E., Delaye, V., Lafond, D., Audoit, G., Mariolle, D., ... & Guedj, C. (2013). Chemical and structural properties of conducting nanofilaments in TiN/HfO2-based resistive switching structures. Nanotechnology, 24(8), 085706.

[Carboni2019] Carboni, R., & Ielmini, D. (2019). Stochastic memory devices for security and computing. Advanced Electronic Materials, 5(9), 1900198.

[Cartoixa2012] Cartoixà, X., Rurali, R., & Suñé, J. (2012). Transport properties of oxygen vacancy filaments in metal/crystalline or amorphous HfO 2/metal structures. Physical Review B, 86(16), 165445.

[Celano2013] Celano, U., Yin Chen, Y., Wouters, D. J., Groeseneken, G., Jurczak, M., & Vandervorst, W. (2013). Filament observation in metal-oxide resistive switching devices. Applied Physics Letters, 102(12), 121602.

[Chand2015] Chand, U., Huang, C. Y., Jieng, J. H., Jang, W. Y., Lin, C. H., & Tseng, T. Y. (2015). Suppression of endurance degradation by utilizing oxygen plasma treatment in HfO2 resistive switching memory. Applied Physics Letters, 106(15), 153502.

[Chen2010] Chen, Y. S., Lee, H. Y., Chen, P. S., Wu, T. Y., Wang, C. C., Tzeng, P. J., ... & Lien, C. (2010). An Ultrathin Forming-Free $\hbox {HfO} _ {x} $ Resistance Memory With Excellent Electrical Performance. IEEE electron device letters, 31(12), 1473-1475.

[Chen2013] Chen, J. Y., Hsin, C. L., Huang, C. W., Chiu, C. H., Huang, Y. T., Lin, S. J., ... & Chen, L. J. (2013). Dynamic evolution of conducting nanofilament in resistive switching memories. Nano letters, 13(8), 3671-3677.

[Chen2015] Chen, P. Y., & Yu, S. (2015). Compact modeling of RRAM devices and its applications in 1T1R and 1S1R array design. IEEE Transactions on Electron Devices, 62(12), 4022-4028.

[Chen2016] Chen, A. (2016). A review of emerging non-volatile memory (NVM) technologies and applications. Solid-State Electronics, 125, 25-38.

[Chen2017] Chen, Y. C., Chang, Y. F., Wu, X., Zhou, F., Guo, M., Lin, C. Y., ... & Lee, J. C. (2017). Dynamic conductance characteristics in HfO x-based resistive random access memory. RSC advances, 7(21), 12984-12989.

[Chen2018] Chen, SX., Chang, SP., Hsieh, WK., Chang, SJ., Lin, CC. (2018) Highly stable ITO/Zn2TiO4/Pt resistive random access memory and its application in two-bit-per-cell. RSC Adv 8(32):17622–17628

[Chen2018b] Chen, X., Zhou, Y., Roy, V. A., & Han, S. T. (2018). Evolutionary metal oxide clusters for novel applications: toward high-density data storage in nonvolatile memories. Advanced Materials, 30(3), 1703950.

[Chiu2012] Chiu, F. C., Li, P. W., & Chang, W. Y. (2012). Reliability characteristics and conduction mechanisms in resistive switching memory devices using ZnO thin films. Nanoscale research letters, 7(1), 1-9.

[Chou2018] Chou, C., Lin, Z., Tseng, P., Li, C., Chang, C., Chen, W., Chih, Y.D., & Chang, T.J. (2018). An N40 256K×44 embedded RRAM macro with SL-precharge SA and low-voltage current limiter to improve read and write performance. 2018 IEEE International Solid - State Circuits Conference - (ISSCC), 478-480.

[Christensen2022] Christensen, D. V., Dittmann, R., Linares-Barranco, B., Sebastian, A., Le Gallo, M., Redaelli, A., ... & Pryds, N. (2022). 2022 roadmap on neuromorphic computing and engineering. Neuromorphic Computing and Engineering.

[Chua1971] Chua, L. (1971). Memristor-the missing circuit element. IEEE Transactions on circuit theory, 18(5), 507-519.

[Coll2019] Coll, M., Fontcuberta, J., Althammer, M., Bibes, M., Boschker, H., Calleja, A., ... & Granozio, F. M. (2019). Towards oxide electronics: a roadmap. Applied surface science, 482, 1-93.

[Crossbar2021] Crossbar Inc. RRAM fabrication company | Retrieved November 23, 2021, from https://www.crossbar-inc.com/company/about-crossbar/

[Dirkmann2018] Dirkmann, S., Kaiser, J., Wenger, C., & Mussenbrock, T. (2018). Filament growth and resistive switching in hafnium oxide memristive devices. ACS applied materials & interfaces, 10(17), 14857-14868.

[Duncan2016] Duncan, D., Magyari-Köpe, B., & Nishi, Y. (2016). Filament-induced anisotropic oxygen vacancy diffusion and charge trapping effects in hafnium oxide RRAM. IEEE Electron Device Letters, 37(4), 400-403.

[Duncan2017] Duncan, D., Magyari-Köpe, B., & Nishi, Y. (2017). Properties of Dopants in HfO x for Improving the Performance of Nonvolatile Memory. Physical Review Applied, 7(3), 034020.

[Frohman-Bentchkowsky1974] Frohman-Bentchkowsky, D. (1974). FAMOS—A new semiconductor charge storage device. Solid-State Electronics, 17(6), 517-529.

[Funck2021] Funck, C., & Menzel, S. (2021). Comprehensive Model of Electron Conduction in Oxide-Based Memristive Devices. ACS Applied Electronic Materials, 3 (9), 3674-3692.

[García2014] García, V., & Bibes, M. (2014). Ferroelectric tunnel junctions for information

[González-Cordero2016] G. Gonzalez-Cordero, J. B. Roldan, F. Jimenez-Molinos, J. Suñé, S. Long and M. Liu, "A new compact model for bipolar RRAMs based on truncated cone conductive filaments, a Verilog-A approach," Semiconductor Science and Technology, vol. 31, no. 11, pp. 1–13, 2016. DOI: 10.1088/0268-1242/31/11/115013

[González-Cordero2016b] G. González-Cordero, F. Jiménez-Molinos, J. B. Roldan, M. B. González and F. Campabadal, "Transient SPICE simulation of Ni/HfO2/Si-n+ resistive memories," in XXXI edition of the Design of Circuits and Integrated Systems Conference (DCIS), 2016 in Granada, Spain.

[González-Cordero2016c] G. González-Cordero, J. B. Roldan, and F. Jiménez-Molinos, "Simulation of RRAM memory circuits, a Verilog-A compact modeling approach," in XXXI edition of the Design of Circuits and Integrated Systems Conference (DCIS), 2016 in Granada, Spain. DOI: 10.1109/DCIS.2016.7845386

[González-Cordero2016d] G. González-Cordero, J. B. Roldan and F. Jiménez-Molinos (2016). A model for circuit simulation of bipolar RRAMs based on conductive filaments with truncated cone shapes. In Jornadas de Investigadores en Formación Fomentando la interdisciplinariedad (JIFFI). Granada, Spain.

[González-Cordero2017] G. González-Cordero, M. B. González, H. García, F. Campabadal, S. Dueñas, H. Castán, F. Jiménez-Molinos and J. B. Roldán, "A physically based model for resistive memories including a detailed temperature and variability description", Microelectronic Engineering, Volume 178, 25 June 2017, Pages 26-29. DOI: 10.1016/j.mee.2017.04.019

[González-Cordero2017c] G. González-Cordero, J. B. Roldán, F. Jiménez-Molinos, "SPICE simulation of RRAM circuits. A compact modeling perspective", in 11th edition of the Spanish Conference on Electron Devices (CDE), 2017 in Barcelona, Spain. DOI: 10.1109/CDE.2017.7905250

[González-Cordero2017d] G. González-Cordero, M. B. González, H. García, F. Jiménez-Molinos, F. Campabadal, S. Dueñas, H. Castán and J. B. Roldán, "A Physically Based Model to describe

Resistive Switching in different RRAM technologies", in 11th edition of the Spanish Conference on Electron Devices (CDE), 2017 in Barcelona, Spain. DOI: 10.1109/CDE.2017.7905223

[González-Cordero2019] Gonzalez-Cordero, G. (2019). Compact Modeling of Memristors Based on Resistive Switching Devices.

[González-Cordero2019a] Gerardo González-Cordero, Mireia B. González, Francisco Jiménez-Molinos, Francesca Campabadal, and Juan Bautista Roldán. "New method to analyze random telegraph signals in resistive random access memories" Journal of Vacuum Science and Technology B. 37, 012203 (2019). DOI: 10.1116/1.50593840

[Goux2012] Goux, L., Sankaran, K., Kar, G., Jossart, N., Opsomer, K., Degraeve, R., ... & Kittl, J. A. (2012, June). Field-driven ultrafast sub-ns programming in W\Al_2O_3\Ti\CuTe-based 1T1R CBRAM system. In 2012 Symposium on VLSI Technology (VLSIT) (pp. 69-70). IEEE.

[Goux2016] Goux, L., & Valov, I. (2016). Electrochemical processes and device improvement in conductive bridge RAM cells. physica status solidi (a), 213(2), 274-288.

[Govoreanu2011] Govoreanu, B., Kar, G. S., Chen, Y. Y., Paraschiv, V., Kubicek, S., Fantini, A., ... & Jossart, N. (2011, December). 10× 10nm 2 Hf/HfO x crossbar resistive RAM with excellent performance, reliability and low-energy operation. In 2011 International Electron Devices Meeting (pp. 31-6). IEEE.

[Gruverman2009] Gruverman, A., Wu, D., Lu, H., Wang, Y., Jang, H. W., Folkman, C. M., ... & Tsymbal, E. Y. (2009). Tunneling electroresistance effect in ferroelectric tunnel junctions at the nanoscale. Nano letters, 9(10), 3539-3543.

[Guan2008] Guan, W., Liu, M., Long, S., Liu, Q., & Wang, W. (2008). On the resistive switching mechanisms of Cu/ZrO 2: Cu/Pt. Applied Physics Letters, 93(22), 223506.

[Guan2012] Guan, X., Yu, S., & Wong, H. S. P. (2012). A SPICE compact model of metal oxide resistive switching memory with variations. IEEE electron device letters, 33(10), 1405-1407.

[Gupta2019] Gupta, V., Kapur, S., Saurabh, S., & Grover, A. (2019). Resistive Random Access Memory: A Review of Device Challenges. IETE Technical Review, 1-14.

[Guy2015] Guy, J., Molas, G., Blaise, P., Bernard, M., Roule, A., Le Carval, G., ... & De Salvo, B. (2015). Investigation of forming, SET, and data retention of conductive-bridge random-access memory for stack optimization. IEEE Transactions on Electron Devices, 62(11), 3482-3489.

[Horiuchi2008] Horiuchi, S., & Tokura, Y. (2008). Organic ferroelectrics. Nature materials, 7(5), 357-366.

[Hsu2013] Hsu, C. W., Wang, I. T., Lo, C. L., Chiang, M. C., Jang, W. Y., Lin, C. H., & Hou, T. H. (2013, June). Self-rectifying bipolar TaO x/TiO 2 RRAM with superior endurance over

10 12 cycles for 3D high-density storage-class memory. In 2013 Symposium on VLSI Technology (pp. T166-T167). IEEE.

[Huang2012] Huang, C. Y., Shen, W. C., Tseng, Y. H., King, Y. C., & Lin, C. J. (2012). A contact-resistive random-access-memory-based true random number generator. IEEE Electron Device Letters, 33(8), 1108-1110.

[Huang2013] Huang, P., Liu, X. Y., Chen, B., Li, H. T., Wang, Y. J., Deng, Y. X., ... & Zhang, X. (2013). A physics-based compact model of metal-oxide-based RRAM DC and AC operations. IEEE transactions on electron devices, 60(12), 4090-4097.

[Huang2013b] Huang, Y. C., Chou, C. H., Liao, C. Y., Tsai, W. L., & Cheng, H. C. (2013). High-performance resistive switching characteristics of programmable metallization cell with oxidized Cu-Ti electrodes. Applied Physics Letters, 103(14), 142905.

[Huang2016] Huang, Y., Shen, Z., Wu, Y., Wang, X., Zhang, S., Shi, X., & Zeng, H. (2016). Amorphous ZnO based resistive random access memory. RSC advances, 6(22), 17867-17872.

[Ielmini2009] Ielmini, D. (2009). Reliability issues and modeling of flash and post-flash memory. Microelectronic Engineering, 86(7-9), 1870-1875.

[Ielmini2015] Ielmini, D., & Waser, R. (Eds.). (2015). Resistive switching: from fundamentals of nanoionic redox processes to memristive device applications. John Wiley & Sons.

[Ielmini2016] Ielmini, D. (2016). Resistive switching memories based on metal oxides: mechanisms, reliability and scaling. Semiconductor Science and Technology, 31(6), 063002.

[Ielmini2017] Ielmini, D., & Milo, V. (2017). Physics-based modeling approaches of resistive switching devices for memory and in-memory computing applications. Journal of Computational Electronics, 16(4), 1121-1143.

[Jain2019] Jain, P., Arslan, U., Sekhar, M., Lin, B. C., Wei, L., Sahu, T., ... & Hamzaoglu, F. (2019, February). 13.2 A 3.6 Mb 10.1 Mb/mm 2 embedded non-volatile ReRAM macro in 22nm FinFET technology with adaptive forming/set/reset schemes yielding down to 0.5 V with sensing time of 5ns at 0.7 V. In 2019 IEEE International Solid-State Circuits Conference-(ISSCC) (pp. 212-214). IEEE.

[Jiang2016] Jiang, Z., Wu, Y., Yu, S., Yang, L., Song, K., Karim, Z., & Wong, H. S. P. (2016). A compact model for metal–oxide resistive random access memory with experiment verification. IEEE Transactions on Electron Devices, 63(5), 1884-1892.

[Jiménez-Molinos2017] Jiménez-Molinos, F., G. Gonzalez-Cordero, G., Cartujo-Cassinello, P., & Roldan, J. B. (2017). SPICE modelling of RRAM thermal reset transitions for circuit simulation purposes. In 2017 Spanish Conference on Electron Devices (CDE) (pp. 1–4). DOI: 10.1109/CDE.2017.7905227

[Jung2017] Jung, K., Magyari-Köpe, B., & Nishi, Y. (2017). Hydrogen-induced oxygen vacancy bistability and its impact on RRAM device operation. IEEE Electron Device Letters, 38(6), 728-731.

[Kamiya2012] Kamiya, K. (2012). MY yang, SG Park, BM Kope, Y. Nishi, M. Niwa, K. Shiraishi, ON-OFF switching mechanism of resistive-random-access-memories based on the formation and disruption of oxygen conducting channels. Appl. Phys. Lett, 100, 073502.

[Kang2015] Kang, J. F., Gao, B., Huang, P., Li, H. T., Zhao, Y. D., Chen, Z., ... & Liu, X. Y. (2015, December). Oxide-based RRAM: Requirements and challenges of modeling and simulation. In 2015 IEEE International Electron Devices Meeting (IEDM) (pp. 5-4). IEEE.

[Kim2012] Kim, H. D., An, H. M., Hong, S. M., & Kim, T. G. (2012). Unipolar resistive switching phenomena in fully transparent SiN-based memory cells. Semiconductor Science and Technology, 27(12), 125020.

[Kim2013] Kim, H. D., An, H. M., Hong, S. M., & Kim, T. G. (2013). Forming-free Si N-based resistive switching memory prepared by RF sputtering. physica status solidi (a), 210(9), 1822-1827.

[Kozicki2016] Kozicki, M. N., & Barnaby, H. J. (2016). Conductive bridging random access memory—materials, devices and applications. Semiconductor Science and Technology, 31(11), 113001.

[Kreupl2008] Kreupl, F., Bruchhaus, R., Majewski, P., Philipp, J. B., Symanczyk, R., Happ, T., ... & Graham, A. P. (2008, December). Carbon-based resistive memory. In 2008 IEEE International Electron Devices Meeting (pp. 1-4). IEEE.

[Kwon2010] Kwon, D. H., Kim, K. M., Jang, J. H., Jeon, J. M., Lee, M. H., Kim, G. H., ... & Hwang, C. S. (2010). Atomic structure of conducting nanofilaments in TiO 2 resistive switching memory. Nature nanotechnology, 5(2), 148-153.

[Lacaita2006] Lacaita, A. L. (2006). Phase change memories: State-of-the-art, challenges and perspectives. Solid-State Electronics, 50(1), 24-31.

[Lanza2019] Lanza, M., Wong, H. S. P., Pop, E., Ielmini, D., Strukov, D., Regan, B. C., ... & Belmonte, A. (2019). Recommended methods to study resistive switching devices. Advanced Electronic Materials, 5(1), 1800143.

[Lanza2021] Lanza, M., Waser, R., Ielmini, D., Yang, J. J., Goux, L., Suñe, J., ... & Pazos, S. (2021). Standards for the characterization of endurance in resistive switching devices. ACS nano.

[Lanza2021b] Wen, C., Li, X., Zanotti, T., Puglisi, F. M., Shi, Y., Saiz, F., ... & Lanza, M. (2021). Advanced Data Encryption using 2D Materials. Advanced Materials, 33(27), 2100185.

[Lee2002] Lee, J. D., Hur, S. H., & Choi, J. D. (2002). Effects of floating-gate interference on NAND flash memory cell operation. IEEE Electron Device Letters, 23(5), 264-266.

[Lee2008] Lee, H. Y., Chen, P. S., Wu, T. Y., Chen, Y. S., Wang, C. C., Tzeng, P. J., ... & Tsai, M. J. (2008, December). Low power and high speed bipolar switching with a thin reactive Ti buffer layer in robust HfO2 based RRAM. In 2008 IEEE International Electron Devices Meeting (pp. 1-4). IEEE.

[Lee2011] Lee, M. J., Lee, C. B., Lee, D., Lee, S. R., Chang, M., Hur, J. H., ... & Kim, K. (2011). A fast, high-endurance and scalable non-volatile memory device made from asymmetric Ta2O 5− x/TaO 2− x bilayer structures. Nature materials, 10(8), 625-630.

[Lee2015] Lee, J. S., Lee, S., & Noh, T. W. (2015). Resistive switching phenomena: A review of statistical physics approaches. Applied Physics Reviews, 2(3), 031303.

[Lian2012] Lian, X., Long, S., Cagli, C., Buckley, J., Miranda, E., Liu, M., & Suñe, J. (2012, March). Quantum point contact model of filamentary conduction in resistive switching memories. In 2012 13th International Conference on Ultimate Integration on Silicon (ULIS) (pp. 101-104). IEEE.

[Liao2011] Liao, Z., Gao, P., Meng, Y., Zhao, H., Bai, X., Zhang, J., & Chen, D. (2011). Electroforming and endurance behavior of Al/Pr0. 7Ca0. 3MnO3/Pt devices. Applied Physics Letters, 99(11), 113506.

[Lim2015] Lim, E. W., & Ismail, R. (2015). Conduction mechanism of valence change resistive switching memory: a survey. Electronics, 4(3), 586-613.

[Lim2016] Lim, S., Yoo, J., Song, J., Woo, J., Park, J., & Hwang, H. (2016, December). Excellent threshold switching device (I off∼ 1 pA) with atom-scale metal filament for steep slope (< 5 mV/dec), ultra low voltage (V dd= 0.25 V) FET applications. In 2016 IEEE International Electron Devices Meeting (IEDM) (pp. 34-7). IEEE.

[Lin2021] Lin, B., Pang, Y., Gao, B., Tang, J., Wu, D., Chang, T. W., ... & Wu, H. (2021). A highly reliable RRAM physically unclonable function utilizing post-process randomness source. IEEE Journal of Solid-State Circuits, 56(5), 1641-1650.

[Liu2012] Liu, S. H., Yang, W. L., Wu, C. C., Chao, T. S., Ye, M. R., Su, Y. Y., ... & Tsai, M. J. (2012). High-performance polyimide-based ReRAM for nonvolatile memory application. IEEE Electron Device Letters, 34(1), 123-125.

[Liu2013] Tz-Yi Liu, Tian Hong Yan, Scheuerlein, R., Yingchang Chen, Lee, J. K., Balakrishnan, G., … Quader, K. (2013). A 130.7mm2 2-layer 32Gb ReRAM memory device in 24nm technology. In 2013 IEEE International Solid-State Circuits Conference Digest of Technical Papers (pp. 210–211). IEEE.

[Liu2014] Liu, H., Lv, H., Yang, B., Xu, X., Liu, R., Liu, Q., ... & Liu, M. (2014). Uniformity improvement in 1T1R RRAM with gate voltage ramp programming. IEEE Electron Device Letters, 35(12), 1224-1226.

[Ma2000] Ma, T. P., & Han, J. P. (2000). U.S. Patent No. 6,067,244. Washington, DC: U.S. Patent and Trademark Office.

[Maldonado2017] Maldonado Correa, David (2017). Estudio de las memorias RRAM bajo la influencia de campos magnéticos.

[Maldonado2019] Maldonado, D., Roldán, A. M., González, M. B., Jiménez-Molinos, F., Campabadal, F., & Roldán, J. B. (2019). Influence of magnetic field on the operation of

TiN/Ti/HfO2/W resistive memories. Microelectronic Engineering, 215(April). DOI: 10.1016/j.mee.2019.110983.

[Maldonado2019b] Maldonado, D., Acal, C., González, M. B., Ruiz-Castro, J.E., Aguilera, A.M., Picos, R., Jiménez-Molinos, F., Campabadal, F., & Roldán, J.B. (2019). An in-depth statistical study of resistive switching energies in unipolar RRAMs. 21th Conference on "Insulating Films on Semiconductors", Cambridge (UK).

[Maldonado2019c] Maldonado Correa, David (2019). Caracterización y modelado de memorias RRAM basadas en estructuras metal-aislante-semiconductor y metal-aislante-metal.

[Maldonado2020] Maldonado, D., Gonzalez, M. B., Campabadal, F., Jimenez-Molinos, F., Al Chawa, M. M., Stavrinides, S. G., ... & Chua, L. O. (2020). Experimental evaluation of the dynamic route map in the reset transition of memristive ReRAMs. Chaos, Solitons & Fractals, 139, 110288., doi: 10.1016/j.chaos.2020.110288.

[Maldonado2020b] Maldonado, D., Roldán, J. B., Roldán, A. M., Jiménez-Molinos, F., Hui, F., Shi, Y., ... & Lanza, M. (2020, April). Influence of the magnetic field on dielectric breakdown in memristors based on h-BN stacks. In 2020 IEEE International Reliability Physics Symposium (IRPS) (pp. 1-5). IEEE.

[Maldonado2021] Maldonado, D., Aguirre, F., González-Cordero, G., Roldán, A. M., González, M. B., Jiménez-Molinos, F., ... & Roldán, J. B. (2021). Experimental study of the series resistance effect and its impact on the compact modeling of the conduction characteristics of HfO2-based resistive switching memories. Journal of Applied Physics, 130(5), 054503, doi: 10.1063/5.0055982.

[Maldonado2022] Maldonado, D., Gómez-Campos, F. M., González, M. B., Roldán, A. M., Jiménez-Molinos, F., Campabadal, F., & Roldán, J. B. (2022). Comprehensive study on unipolar RRAM charge conduction and stochastic features: a simulation approach. Journal of Physics D: Applied Physics, 55(15), 155104.

[Maldonado2022b] Maldonado, D., Aldana, S., Gonzalez, M. B., Jiménez-Molinos, F., Ibáñez, M. J., Barrera, D., ... & Roldán, J. B. (2022). Variability estimation in resistive switching devices, a numerical and kinetic Monte Carlo perspective. Microelectronic Engineering, 111736.

[Maestro-Izquierdo2020] Maestro-Izquierdo, M., Gonzalez, M. B., Jimenez-Molinos, F., Moreno, E., Roldan, J. B., & Campabadal, F. (2020). Unipolar resistive switching behavior in Al2O3/HfO2 multilayer dielectric stacks: fabrication, characterization and simulation. Nanotechnology, 31(13), 135202.

[Menzel2015] S. Menzel, P. Kaupmann, R. Waser, "Understanding filamentary growth in electrochemical metallization memory cells using kinetic Monte Carlo simulations", Nanoscale, 7, 12673, 2015.

[Merolla2014] Merolla, P. A., Arthur, J. V., Alvarez-Icaza, R., Cassidy, A. S., Sawada, J., Akopyan, F., ... & Brezzo, B. (2014). A million spiking-neuron integrated circuit with a scalable communication network and interface. Science, 345(6197), 668-673.

[Meyer2008] Meyer, R., Schloss, L., Brewer, J., Lambertson, R., Kinney, W., Sanchez, J., & Rinerson, D. (2008, November). Oxide dual-layer memory element for scalable non-volatile cross-point memory technology. In 2008 9th Annual Non-Volatile Memory Technology Symposium (NVMTS) (pp. 1-5). IEEE.

[Mikhaylov2021] Mikhaylov, A. N., Guseinov, D. V., Belov, A. I., Korolev, D. S., Shishmakova, V. A., Koryazhkina, M. N., ... & Spagnolo, B. (2021). Stochastic resonance in a metal-oxide memristive device. Chaos, Solitons & Fractals, 144, 110723.

[Mott2004] Mott, N. (2004). Metal-insulator transitions. CRC Press.

[Munjal2019] Munjal, S., & Khare, N. (2019). Advances in resistive switching based memory devices. Journal of Physics D: Applied Physics, 52(43), 433002.

[Nardi2011] Nardi, F., Balatti, S., Larentis, S., & Ielmini, D. (2011, December). Complementary switching in metal oxides: Toward diode-less crossbar RRAMs. In 2011 International Electron Devices Meeting (pp. 31-1). IEEE.

[Nili2018] Nili, H., Adam, G. C., Hoskins, B., Prezioso, M., Kim, J., Mahmoodi, M. R., ... & Strukov, D. B. (2018). Hardware-intrinsic security primitives enabled by analogue state and nonlinear conductance variations in integrated memristors. Nature Electronics, 1(3), 197-202.

[Onofrio2015] Onofrio, N., Guzman, D., & Strachan, A. (2015). Atomic origin of ultrafast resistance switching in nanoscale electrometallization cells. Nature materials, 14(4), 440-446.

[Padovani2015] Padovani, A., Larcher L., Pirrotta, O., Vandelli, L., & Bersuker, G. (2015). Microscopic Modeling of HfO x RRAM Operations: From Forming to Switching. IEEE Transactions on Electron Devices, 62(6), pp. 1998-2006, 2015.

[Pan2014] Pan, F., Gao, S., Chen, C., Song, C., & Zeng, F. (2014). Recent progress in resistive random access memories: materials, switching mechanisms, and performance. Materials Science and Engineering: R: Reports, 83, 1-59.

[Panda2018] Panda, D., Sahu, P. P., & Tseng, T. Y. (2018). A collective study on modeling and simulation of resistive random access memory. Nanoscale research letters, 13(1), 1-48.

[Pang2017] Pang, Y., Wu, H., Gao, B., Wu, D., Chen, A., & Qian, H. (2017, December). A novel PUF against machine learning attack: Implementation on a 16 Mb RRAM chip. In 2017 IEEE International Electron Devices Meeting (IEDM) (pp. 12-2). IEEE.

[Park2015] Park, M. R., Abbas, Y., Hu, Q., Yoon, T. S., Choi, Y. J., & Kang, C. J. (2015). Resistive switching characteristics of tantalum oxide thin film and titanium oxide nanoparticles hybrid structure. Journal of nanoscience and nanotechnology, 15(11), 8613-8616.

[Park2017] Park, T. H., Kim, H. J., Park, W. Y., Kim, S. G., Choi, B. J., & Hwang, C. S. (2017). Roles of conducting filament and non-filament regions in the Ta 2 O 5 and HfO 2 resistive switching memory for switching reliability. Nanoscale, 9(18), 6010-6019.

[Perez2019] Pérez, E., Maldonado, D., Acal, C., Ruiz-Castro, J. E., Alonso, F. J., Aguilera, A. M., … Roldán, J. B. (2019). Analysis of the statistics of device-to-device and cycle-to-cycle

variability in TiN/Ti/Al:HfO2/TiN RRAMs. Microelectronic Engineering, 214(April), 104–109. DOI: 10.1016/j.mee.2019.05.004

[Perez2019b] Perez, E., Mahadevaiah, M. K., Zambelli, C., Olivo, P., & Wenger, C. (2019). Data retention investigation in Al: HfO2-based resistive random access memory arrays by using high-temperature accelerated tests. Journal of Vacuum Science & Technology B, Nanotechnology and Microelectronics: Materials, Processing, Measurement, and Phenomena, 37(1), 012202.

[Pickett2012] Pickett, M. D., & Williams, R. S. (2012). Sub-100 fJ and sub-nanosecond thermally driven threshold switching in niobium oxide crosspoint nanodevices. Nanotechnology, 23(21), 215202.

[Picos2015] Picos, R., Roldan, J. B., Al Chawa, M. M., Garcia-Fernandez, P., Jimenez-Molinos, F., & Garcia-Moreno, E. (2015). Semiempirical Modeling of Reset Transitions in Unipolar Resistive-Switching based Memristors. Radioengineering, 24(2), 420–424. DOI: 10.13164/re.2015.0420

[Pietronero1988] Pietronero, L., & Wiesmann, H. J. (1988). From physical dielectric breakdown to the stochastic fractal model. Zeitschrift für Physik B Condensed Matter, 70(1), 87-93.

[Pirovano2004] Pirovano, A., Lacaita, A. L., Benvenuti, A., Pellizzer, F., & Bez, R. (2004). Electronic switching in phase-change memories. IEEE Transactions on Electron Devices, 51(3), 452-459.

[Poblador2020] Poblador, S., Maestro-Izquierdo, M., Zabala, M., González, M. B., & Campabadal, F. (2020). Methodology for the characterization and observation of filamentary spots in HfOx-based memristor devices. Microelectronic Engineering, 223, 111232.

[Prakash2014] Prakash, A., Park, J., Song, J., Woo, J., Cha, E. J., & Hwang, H. (2014). Demonstration of low power 3-bit multilevel cell characteristics in a TaO x-based RRAM by stack engineering. IEEE Electron Device Letters, 36(1), 32-34.

[Prezioso2015] Prezioso, M., Merrikh-Bayat, F., Hoskins, B. D., Adam, G. C., Likharev, K. K., & Strukov, D. B. (2015). Training and operation of an integrated neuromorphic network based on metal-oxide memristors. Nature, 521(7550), 61-64.

[Qin2012] Qin, S., Zhang, J., Fu, D., Xie, D., Wang, Y., Qian, H., ... & Yu, Z. (2012). A physics/circuit-based switching model for carbon-based resistive memory with sp 2/sp 3 cluster conversion. Nanoscale, 4(20), 6658-6663.

[Reed2001] Reed, M. A., Chen, J., Rawlett, A. M., Price, D. W., & Tour, J. M. (2001). Molecular random access memory cell. Applied physics letters, 78(23), 3735-3737.

[Rodríguez2019] N. Rodriguez, D. Maldonado, F.J. Romero, F.J. Alonso, A.M. Aguilera, A. Godoy, F. Jimenez-Molinos, F.G. Ruiz, J.B. Roldan, "Resistive switching and charge transport in laser-fabricated graphene oxide memristors: a Time Series and Quantum Point Contact modelling approach", Materials, 12, 3734, 2019.

[RodríguezMontañés2021] Rodríguez-Montañés, R., Arumí, D., Gómez-Pau, A., Manich, S., Gonzalez, M. B., & Campabadal, F. (2021). Enhanced serial RRAM cell for unpredictable bit generation. Solid-State Electronics, 183, 108059.

[RomeroZaliz2021] Romero-Zaliz, R., Pérez, E., Jiménez-Molinos, F., Wenger, C., & Roldán, J. B. (2021). Study of Quantized Hardware Deep Neural Networks Based on Resistive Switching Devices, Conventional versus Convolutional Approaches. Electronics, 10(3), 346.

[Roldán2019] Roldán, J. B., Alonso, F. J., Aguilera, A. M., Maldonado, D., & Lanza, M. (2019). Time series statistical analysis: A powerful tool to evaluate the variability of resistive switching memories. Journal of Applied Physics, 125(17), 174504. DOI: 10.1063/1.5079409.

[Roldán2021] Roldán, J. B., González-Cordero, G., Picos, R., Miranda, E., Palumbo, F., Jiménez-Molinos, F., ... & Chua, L. O. (2021). On the Thermal Models for Resistive Random Access Memory Circuit Simulation. Nanomaterials, 11(5), 1261.

[Roldán2021b] Roldán, J. B., Maldonado, D., Alonso, F. J., Roldán, A. M., Hui, F., Shi, Y., ... & Lanza, M. (2021, March). Time series modeling of the cycle-to-cycle variability in h-BN based memristors. In 2021 IEEE International Reliability Physics Symposium (IRPS) (pp. 1-5). IEEE.

[Sakellaropoulos2020] Sakellaropoulos, D., Bousoulas, P., Nikas, G., Arvanitis, C., Bagakis, E., & Tsoukalas, D. (2020). Enhancing the synaptic properties of low-power and forming-free HfOx/TaOy/HfOx resistive switching devices. Microelectronic Engineering, 229, 111358.

[Sebastian2020] Sebastian, A., Le Gallo, M., Khaddam-Aljameh, R., & Eleftheriou, E. (2020). Memory devices and applications for in-memory computing. Nature nanotechnology, 15(7), 529-544.

[Shi2017] Shi, Y., Pan, C., Chen, V., Raghavan, N., Pey, K. L., Puglisi, F. M., ... & Lanza, M. (2017, December). Coexistence of volatile and non-volatile resistive switching in 2D h-BN based electronic synapses. In 2017 IEEE International Electron Devices Meeting (IEDM) (pp. 5-4). IEEE.

[Son2010] Son, J. Y., Shin, Y. H., Kim, H., & Jang, H. M. (2010). NiO resistive random access memory nanocapacitor array on graphene. ACS nano, 4(5), 2655-2658.

[Song2011] Song, H., Reed, M. A., & Lee, T. (2011). Single molecule electronic devices. Advanced Materials, 23(14), 1583-1608.

[Spiga2020] Spiga, S., Sebastian, A., Querlioz, D., Rajendran, B. Memristive devices for brain-inspired computing. Elsevier, 2020.

[Strukov2008] Strukov, D. B., Snider, G. S., Stewart, D. R., & Williams, R. S. (2008). The missing memristor found. nature, 453(7191), 80-83.

[Sun2009] Sun, B., Liu, Y. X., Liu, L. F., Xu, N., Wang, Y., Liu, X. Y., … Kang, J. F. (2009). Highly uniform resistive switching characteristics of TiN/ZrO2/Pt memory devices. Journal of Applied Physics, 105(6), 1–5.

[Sun2017] Sun, H., Zhang, M., Li, Y., Long, S., Liu, Q., Lv, H., ... & Liu, M. (2017). A cell-based clustering model for the reset statistics in RRAM. Applied Physics Letters, 110(12), 123503.

[Tang2013] Tang, G. S., Zeng, F., Chen, C., Liu, H. Y., Gao, S., Li, S. Z., ... & Pan, F. (2013). Resistive switching with self-rectifying behavior in Cu/SiO x/Si structure fabricated by plasma-oxidation. Journal of Applied Physics, 113(24), 244502.

[Tang2013b] Tang, G. S., Zeng, F., Chen, C., Gao, S., Fu, H. D., Song, C., ... & Pan, F. (2013). Resistive switching behaviour of a tantalum oxide nanolayer fabricated by plasma oxidation. physica status solidi (RRL)–Rapid Research Letters, 7(4), 282-284.

[Tseng2021] Tseng, P. H., Lee, M. H., Lin, Y. H., Lung, H. L., Wang, K. C., & Lu, C. Y. (2021). ReRAM-Based Pseudo-True Random Number Generator With High Throughput and Unpredictability Characteristics. IEEE Transactions on Electron Devices, 68(4), 1593-1597.

[TSMC2020] TSMC offers 22nm RRAM, taking MRAM on to 16nm | eenewsanalog. (n.d.). Retrieved October 29, 2021, from https://www.eenewsanalog.com/news/tsmc-offers-22nm-rram-taking-mram-16nm

[Valov2011] Valov, I., Waser, R., Jameson, J. R., & Kozicki, M. N. (2011). Electrochemical metallization memories—fundamentals, applications, prospects. Nanotechnology, 22(25), 254003.

[Vandelli2015] A. Padovani, L. Larcher, O. Pirrotta, L. Vandelli, G. Bersuker, "Microscopic Modeling of HfO x RRAM Operations: From Forming to Switching", IEEE Transactions on Electron Devices, 62(6), pp. 1998-2006, 2015.

[videoSimulator] Complementary material to "D. Maldonado, F. Gómez-Campos, M.B. González, A. Roldán, F. Jiménez-Molinos, F. Campabadal, J. B. Roldán, "Comprehensive study on unipolar RRAM charge conduction and stochastic features, a simulation approach", Journal of Physics D: Applied Physics, 55, 155104, 2022". Video link. URL: https://youtu.be/-kq6-5k2-HY

[Villena2015] Villena Sánchez, M. A. (2015). Estudio, modelado y simulación de memorias RRAM.

[Villena2016] Villena, M. A., Roldán, J. B., González, M. B., González-Rodelas, P., Jiménez-Molinos, F., Campabadal, F., & Barrera, D. (2016). A new parameter to characterize the charge transport regime in Ni/HfO2 /Si-n+ -based RRAMs. Solid-State Electronics, 118, 56–60. DOI: 10.1016/j.sse.2016.01.007

[Villena2017] Villena, M. A., Roldán, J. B., Jiménez-Molinos, F., Miranda, E., Suñé, J., & Lanza, M. (2017). SIM^2RRAM: a physical model for RRAM devices simulation. Journal of Computational Electronics, 16(4), 1095-1120. DOI: 10.1007/s10825-017-1074-8

[Walczyk2009] Walczyk, C., Wenger, C., Sohal, R., Lukosius, M., Fox, A., Dąbrowski, J., ... & Schroeder, T. (2009). Pulse-induced low-power resistive switching in Hf O 2 metal-insulator-metal diodes for nonvolatile memory applications. Journal of Applied Physics, 105(11), 114103.

[Wang2010a] Wang, S. Y., Lee, D. Y., Huang, T. Y., Wu, J. W., & Tseng, T. Y. (2010). Controllable oxygen vacancies to enhance resistive switching performance in a ZrO2-based RRAM with embedded Mo layer. Nanotechnology, 21(49).

[Wang2013] Wang, J. C., Jian, D. Y., Ye, Y. R., & Chang, L. C. (2013). Platinum–aluminum alloy electrode for retention improvement of gadolinium oxide resistive switching memory. Applied Physics A, 113(1), 37-40.

[Wang2018] Wang, M., Cai, S., Pan, C., Wang, C., Lian, X., Zhuo, Y., ... & Miao, F. (2018). Robust memristors based on layered two-dimensional materials. Nature Electronics, 1(2), 130-136.

[Wang2019] Wang, Z., Li, C., Song, W., Rao, M., Belkin, D., Li, Y., ... & Strachan, J. P. (2019). Reinforcement learning with analogue memristor arrays. Nature Electronics, 2(3), 115-124.

[Wang2019b] Wang, Y., Kang, K. M., Kim, M., Lee, H. S., Waser, R., Wouters, D., ... & Park, H. H. (2019). Mott-transition-based RRAM. Materials today, 28, 63-80.

[Waser2007] Waser, R., & Aono, M. (2007). Nanoionics-based resistive switching memories. Nature Materials, 6(11), 833–840.

[Waser2009] Waser, R., Dittmann, R., Staikov, G., & Szot, K. (2009). Redox-based resistive switching memories–nanoionic mechanisms, prospects, and challenges. Advanced materials, 21(25-26), 2632-2663.

[Waser2010] Waser, R., & Aono, M. (2010). Nanoionics-based resistive switching memories. In Nanoscience And Technology: A Collection of Reviews from Nature Journals (pp. 158-165).

[Waser2012] R. Waser, “Nanoelectronics and Information Technology”, 3rd ed., Wiley-VCH, Berlin, 2012.

[Wei2020] Hu, Wei & Yang, Ben & Zhang, Yanming & She, Yin. (2020). Recent progress in physically transient resistive switching memory. Journal of Materials Chemistry C. 8. 14695-14710.

[Wong2010] Wong, H. S. P. et al. (2010). Phase Change Memory. Proceedings of the IEEE, vol. 98, no. 12, pp. 2201-2227

[Wong2012a] Wong, H. S. P., Lee, H. Y., Yu, S., Chen, Y. S., Wu, Y., Chen, P. S., ... & Tsai, M. J. (2012). Metal–oxide RRAM. Proceedings of the IEEE, 100(6), 1951-1970.

[Wong2015] Wong, H.S.P., Salahuddin, S. Memory leads the way to better computing. Nature Nanotech 10, 191–194 (2015).

[Woo2016] Woo, J., Belmonte, A., Redolfi, A., Hwang, H., Jurczak, M., & Goux, L. (2016). Introduction of WO 3 layer in a Cu-based Al_2O_3 conductive bridge RAM system for robust cycling and large memory window. IEEE Journal of the Electron Devices Society, 4(3), 163-166.

[Wu2010] Wu, Y., Lee, B., & Wong, H. S. P. (2010). Al_2O_3-Based RRAM Using Atomic Layer Deposition (ALD) With 1-$\mu\hbox {A} $ RESET Current. IEEE electron device letters, 31(12), 1449-1451.

[Wu2016] Yu, Hanming & Liao, Yan & Gao, Bin & Jana, Debanjan & Qian, He. (2016). RRAM cross-point arrays. 10.1007/978-94-017-7512-0_8.

[Xie2013] Xie, Y. (Ed.). (2013). Emerging Memory Technologies: Design, Architecture, and Applications. Springer Science & Business Media.

[Xie2014] Xie, Y. (2014). Introduction. In Emerging Memory Technologies (pp. 1–14). New York, NY: Springer New York.

[Xue2019] Xue, W., Xu, X. H., & Liu, G. (2019). Solid-state electrochemical process and performance optimization of memristive materials and devices. Chemistry, 1(1), 44-68.

[Yang2006] Yang, H., Kim, H., Park, S. I., Kim, J., Lee, S. H., Choi, J. K., ... & Kong, J. T. (2006, October). Reliability issues and models of sub-90nm NAND flash memory cells. In 2006 8th International Conference on Solid-State and Integrated Circuit Technology Proceedings (pp. 760-762). IEEE.

[Yang2009] Yang, J. J., Miao, F., Pickett, M. D., Ohlberg, D. A., Stewart, D. R., Lau, C. N., & Williams, R. S. (2009). The mechanism of electroforming of metal oxide memristive switches. Nanotechnology, 20(21), 215201.

[Yang2009b] Yang, M. K., Park, J. W., Ko, T. K., & Lee, J. K. (2009). Bipolar resistive switching behavior in Ti/MnO 2/Pt structure for nonvolatile memory devices. Applied Physics Letters, 95(4), 042105.

[Yang2009c] Yang, L., Kuegeler, C., Szot, K., Ruediger, A., & Waser, R. (2009). The influence of copper top electrodes on the resistive switching effect in TiO 2 thin films studied by conductive atomic force microscopy. Applied physics letters, 95(1), 013109.

[Yang2021] Yang, B., Arumí, D., Manich, S., Gómez-Pau, Á., Rodríguez-Montañés, R., González, M. B., ... & Fang, L. (2021). RRAM Random Number Generator Based on Train of Pulses. Electronics, 10(15), 1831.

[Yao2020] Yao, P., Wu, H., Gao, B., Tang, J., Zhang, Q., Zhang, W., ... & Qian, H. (2020). Fully hardware-implemented memristor convolutional neural network. Nature, 577(7792), 641-646.

[Ye2016] Ye, C., Wu, J., He, G., Zhang, J., Deng, T., He, P., & Wang, H. (2016). Physical mechanism and performance factors of metal oxide based resistive switching memory: a review. Journal of Materials Science & Technology, 32(1), 1-11.

[Yoshida2007] Yoshida, C., Tsunoda, K., Noshiro, H., & Sugiyama, Y. (2007). High speed resistive switching in Pt⁄Ti O 2⁄Ti N film for nonvolatile memory application. Applied Physics Letters, 91(22), 223510.

[You2014] You, T., Du, N., Slesazeck, S., Mikolajick, T., Li, G., Bürger, D., ... & Volz, K. (2014). Bipolar electric-field enhanced trapping and detrapping of mobile donors in BiFeO3 memristors. ACS applied materials & interfaces, 6(22), 19758-19765.

[Yu2011] S. Yu, Y. Wu, R. Jeyasingh, D. Kuzum, H.-S. Wong. An electronic synapse device based on metal oxide resistive switching memory for neuromorphic computation. IEEE Trans. Electron Devices, 58 (8), pp. 2729–2737, 2011.

[Yu2016] Yu, S., & Chen, P. Y. (2016). Emerging memory technologies: Recent trends and prospects. IEEE Solid-State Circuits Magazine, 8(2), 43-56.

[Zahoor2020] Zahoor, F., Zulkifli, T. Z. A., & Khanday, F. A. (2020). Resistive random access memory (RRAM): an overview of materials, switching mechanism, performance, multilevel cell (MLC) storage, modeling, and applications. Nanoscale research letters, 15(1), 1-26.

[Zahurak2014] Zahurak, J., Miyata, K., Fischer, M., Balakrishnan, M., Chhajed, S., Wells, D., ... & Nakazawa, K. (2014, December). Process integration of a 27nm, 16Gb Cu ReRAM. In 2014 IEEE International Electron Devices Meeting (pp. 6-2). IEEE.

[Zeng2019] Zeng, B., Liao, M., Peng, Q., Xiao, W., Liao, J., Zheng, S., & Zhou, Y. (2019). 2-bit/cell operation of Hf 0.5 Zr 0.5 O 2 based FeFET memory devices for NAND applications. IEEE Journal of the Electron Devices Society, 7, 551-556.

[Zhang2020] Zhang, Y., Wang, Z., Zhu, J., Yang, Y., Rao, M., Song, W., ... & Joshua Yang, J. (2020). Brain-inspired computing with memristors: Challenges in devices, circuits, and systems. Applied Physics Reviews, 7(1), 011308.

[Zheng2011] Zheng, K., Sun, X. W., Zhao, J. L., Wang, Y., Yu, H. Y., Demir, H. V., & Teo, K. L. (2011). An indium-free transparent resistive switching random access memory. IEEE electron device letters, 32(6), 797-799.

[Zhang2018] Zhang, R., Jiang, H., Wang, Z. R., Lin, P., Zhuo, Y., Holcomb, D., ... & Xia, Q. (2018). Nanoscale diffusive memristor crossbars as physical unclonable functions. Nanoscale, 10(6), 2721-2726.

[Zhou2019] Zhou, G., Ren, Z., Wang, L., Wu, J., Sun, B., Zhou, A., ... & Song, Q. (2019). Resistive switching memory integrated with amorphous carbon-based nanogenerators for self-powered device. Nano Energy, 63, 103793.

[Zhu2008] Zhu, J. (2008). Magnetoresistive Random Access Memory: The Path to Competitiveness and Scalability. Proceedings of the IEEE, vol. 96, no. 11, pp. 1786-1798.

[Zidan2018] Zidan, M. A., Strachan, J. P., & Lu, W. D. (2018). The future of electronics based on memristive systems. Nature electronics, 1(1), 22-29.